

HE  
18.5  
.A37  
no.  
DOT-  
TSC-  
UMTA-  
75-13

78-244-507

REPORT NO. UMTA-MA-06-0025-75-12

NOISE PREDICTION MODELS FOR  
ELEVATED RAIL TRANSIT STRUCTURES

Dept. Of Transportation



Library

J. E. Manning  
D. C. Hyland  
J. J. Fredberg  
N. Senapati



AUGUST 1975  
FINAL REPORT

DOCUMENT IS AVAILABLE TO THE PUBLIC  
THROUGH THE NATIONAL TECHNICAL  
INFORMATION SERVICE, SPRINGFIELD,  
VIRGINIA 22161

Prepared for  
U.S. DEPARTMENT OF TRANSPORTATION  
URBAN MASS TRANSPORTATION ADMINISTRATION  
Office of Research and Development  
Washington DC 20590

#### NOTICE

This document is disseminated under the sponsorship of the Department of Transportation in the interest of information exchange. The United States Government assumes no liability for its contents or use thereof.

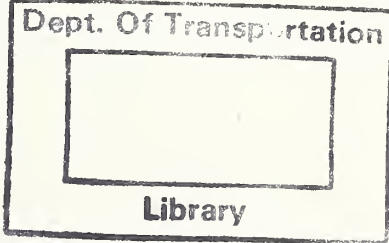
#### NOTICE

The United States Government does not endorse products or manufacturers. Trade or manufacturers' names appear herein solely because they are considered essential to the object of this report.

8.5  
A37

0 DOT-TSC-UMTA-75-13

TECHNICAL REPORT STANDARD TITLE PAGE

1. Report No. UMTA-MA-06-0025-75-12		2. Government Accession No.		3. Recipient's Catalog No.	
4. Title and Subtitle NOISE PREDICTION MODELS FOR ELEVATED RAIL TRANSIT STRUCTURES				5. Report Date August 1975	
				6. Performing Organization Code	
7. Author(s) J. E. Manning, D. C. Hyland, J. J. Fredberg, N. Senapati				8. Performing Organization Report No. DOT-TSC-UMTA-75-13	
9. Performing Organization Name and Address Cambridge Collaborative, Inc.* 238 Main Street Cambridge MA 02142				10. Work Unit No. UM504/R6747	
				11. Contract or Grant No. DOT-TSC-643	
				13. Type of Report and Period Covered Final Report July 1973 - June 1975	
12. Sponsoring Agency Name and Address U.S. Department of Transportation Urban Mass Transportation Administration Office of Research and Development Washington DC 20590				14. Sponsoring Agency Code	
15. Supplementary Notes *Under contract to:		U.S. Department of Transportation, Transportation Systems Center, Kendall Square Cambridge MA 02142			
16. Abstract <p>This report presents the theoretical development of a model for the prediction of noise radiated by elevated structures on rail transit lines. It is one of three reports prepared by Cambridge Collaborative under the UMTA Urban Rail Supporting Technology Program, dealing with noise and vibration control for urban rail transit track and elevated structures. The model described here allows for the prediction of both the vibration transmission between elements of the structure and the resulting noise radiation from each major structural element, in terms of design parameters for the different elements. Thus the potential effectiveness of various alternative methods for noise control can be evaluated. Results of a field study of three different types of elevated structure on the MBTA Rapid Transit System are also summarized. These results support the validity of the prediction model. The engineering application of the prediction model is discussed in another report.</p>					
<div style="text-align: center;">  <p>Dept. Of Transportation Library</p> </div>					
17. Key Words Noise, Transportation Noise, Mass Transit, Rail Noise, Community Noise, Vibration Analysis				18. Distribution Statement  DOCUMENT IS AVAILABLE TO THE PUBLIC THROUGH THE NATIONAL TECHNICAL INFORMATION SERVICE, SPRINGFIELD, VIRGINIA 22161	
19. Security Classif. (of this report) Unclassified		20. Security Classif. (of this page) Unclassified		21. No. of Pages 250	
				22. Price	





## PREFACE

This report has been prepared by Cambridge Collaborative, Inc. (CC), under Contract DOT-TSC-643 as part of the Urban Rail Supporting Technology Program managed by the Transportation Systems Center, Cambridge, Massachusetts, under the sponsorship of the Rail Technology Division, Urban Mass Transportation Administration, Washington, D.C.

The authors express their gratitude to Dr. Leonard Kurzweil of TSC who provided much assistance and encouragement during the course of the work in the preparation of this report.

The work described includes extensive field measurements on elevated structures that are in typical service. The measurements were carried out by Mr. Gregory Tocci of Cambridge Collaborative. However, they would not have been possible without the help of the MBTA in Boston. In particular, we wish to thank Mr. Jack O'Hara of the MBTA who made all necessary arrangements for our many hours of measurements.



	Page
4. COMPARISON OF PREDICTION WITH DATA.....	112
4.1 Data Collection and Reduction.....	112
4.2 Anderson Bridge on MBTA Red Line Extension.....	121
4.3 Elevated Structure near Green Street on MBTA Orange Line.....	131
4.4 Elevated Structure Near Hathon Square on MBTA Orange Line.....	142
5. CONCLUSIONS.....	149
5.1 Critical Review of the Prediction Model.....	149
5.2 Noise Control Techniques.....	151
APPENDIX I. REFINED MODELS FOR STUDYING RAIL VIBRATION.....	153
I.1 Discrete Rail Support Points and Multiple Excitation Points.....	154
I.1.1 Theoretical Developments for a Periodically Supported Beam.....	157
I.1.1.1 Free-Wave Propagation.....	157
I.1.1.2 Forced Response.....	167
I.1.1.3 Wheel-Rail Roughness Excitation.....	172
I.1.2 Computer Program.....	173
I.1.3 Computational Results.....	191
I.2 A Refined Model for Rail Damping.....	201
I.3 Effect of Shear Deformations in the Rail.....	211
I.4 Effect of a Nonrigid Support Under the Fasteners.....	213
APPENDIX II. PREDICTION MODEL FOR LOW FREQUENCIES.....	217
APPENDIX III. COMPILATION OF COUPLING LOSS FACTORS.....	220
APPENDIX IV. REPORT OF INVENTIONS APPENDIX.....	237
REFERENCES.....	238

## LIST OF FIGURES

<u>Figure</u>	<u>Page</u>
1.1 Vibration Transmission Paths and Noise Radiation for Elevated Track Structures.....	3
1.2 Vibratory Energy Transmission Between Elements of an Elevated Structure.....	8
2.1 Vertical Vibratory Velocity Levels for the Rail Measured on BART Test Track .....	17
2.2 Vertical and Torsional Velocity Levels for the Rail Measured on MBTA Red Line.....	18
2.3 Integrated Rail Response Spectrum.....	26
2.4 Radiation Efficiency for the Rail.....	28
2.5 Cylinder Coordinates.....	30
2.6 Directivity of the Rail Radiation.....	34
3.1 Elements of an Elevated Structure Contributing to the Radiated Noise.....	36
3.2 Typical Lattice or Open-Web Girder, Open Tie Deck Elevated Structure.....	38
3.3 Typical Plate-Web Girder, Open Tie Deck Elevated Structure.....	40
3.4 Typical Steel Plate-Web Girder, Concrete Slab Deck Elevated Structure.....	42
3.5 Concrete ELevated Structures.....	43
3.6 Two Connected Plate Structures.....	50
3.7 Rail Dispersion Curve.....	58
3.8 Idealized Model of an Elevated Structure with a Concrete Deck on Steel-Plate Girders.....	64
3.9 Force and Velocity Conventions Used in the Calculation of Slab and Web Impedances.....	65
3.10 Interaction Diagram for Concrete Deck on Steel Plate Girder Structure.....	68
3.11 Sketch of the Vertical Web Stiffeners.....	74

3.12	Idealized Model of an Elevated Structure with a Wood Tie Deck on Steel-Plate Girders.....	76
3.13	Force and Velocity Conventions for Calculations of Tie Deck and Girder Web Impedances.....	79
3.14	Interaction Diagram for Open Tie Deck on Steel Plate Girder Structure.....	80
3.15	Idealized Model of Elevated Structure with Wood Tie Deck on Open-Web Steel Girders.....	84
3.16	Interaction Diagram for Open Tie Deck on Open Web Steel Girder Structure.....	86
3.17	Sketch of a Typical Open Web Steel Girder, Showing the Configuration of One Bay.....	89
3.18	Baffled Simply Supported Plate Vibrating Below the Critical Frequency with Uncancelled Volume Velocity at the Edge.....	96
3.19	The Functions $g_2$ and $g_3$ .....	98
3.20	Vibrating Plate with a Wedged Baffle.....	99
3.21	Vibrating Plate with a Finite Baffle.....	99
3.22	Radiation Efficiency for One Tie.....	102
3.23	Typical Steel Plate Girder Dimensions for a New Structure.....	104
3.24	Measured Elevated Structure Noise Data.....	106
3.25	Comparison of Predicted and Measured Radiation Efficiency for the Plate Webs of the Anderson Bridge on the MBTA.....	107
3.26	Typical Steel Plate Girder Dimensions for an Older Structure.....	109
3.27	Comparison of Predicted and Measured Radiation Efficiency for an Older Elevated Structure Near Green Street on the MBTA Orange Line..	111
4.1	Instrumentation Used to Collect and Analyze Noise and Vibration Data.....	113
4.2	Instrumentation Set-Up on the Anderson Bridge of the MBTA Red Line..	114
4.3	Instrumentation Set-Up on the Green Street Structure of the MBTA Orange Line.....	115
4.4	Recorded Time Histories of Acoustic and Vibration Levels in the 500 Hz Octave Band for the Anderson Bridge.....	117
4.5	Recorded Time Histories of Acoustic and Vibration Levels in the 500 Hz Octave Band for the Green Street Structure.....	118
4.6	Cross Section of the Anderson Bridge (Neponset River Bridge) on the MBTA Red Line.....	123
4.7	Empirically Predicted and Measured Maximum Rail Vibration Levels for the Anderson Bridge.....	125
4.8	Predicted and Measured Values of Spatially Averaged Energy for the Anderson Bridge (A Concrete Deck, Plate-Web, Steel Girder Structure)	127

4.9	Predicted and Measured Noise Radiation Levels from Elements on the Anderson Bridge.....	130
4.10	Comparison of Predicted Wayside Noise Levels with Measured Levels	132
4.11	Cross Section of the Green Street Structure (An Open Wood Tie Deck, Plate-Web, Steel-Girder Structure).....	133
4.12	Time Histories of the Rail Vibration Level.....	135
4.13	Predicted and Measured Values of Spatially Averaged Energy for the Green Street Structure (An Open Wood Tie Deck, Plate-Web, Steel-Girder Structure).....	137
4.14	Predicted and Measured Noise Radiation Levels from Elements on the Green Street Elevated Structure.....	140
4.15	Cross Section and Side View of the Elevated Structure Near Hathon Square on the MBTA Orange Line.....	143
4.16	Predicted and Measured Values of Spatially Averaged Energy for the Hathon Square Structure (An Open Wood Tie Deck, Open-Web Steel-Girder Structure).....	146
4.17	Predicted and Measured Noise Radiation Levels from Elements on the Hathon Square Elevated Structure.....	147
I.1	Discrete Model of the Rail and Fastener System.....	156
I.2	A Single Bay.....	158
I.3	Location of the Excitation Points.....	168
I.4	Flow Chart for Computer Program.....	177
I.5	Propagation Constants for Case 1.....	192
I.6	Real Part of the Displacement Phasor $u(x)$ for Case 1 at $\omega = 1000$ Radians/Second.....	194
I.7	Propagation Constants for Case 2.....	196
I.8	Spatial Distribution of the Acceleration Level for Case 2 at Three Frequencies.....	197
I.9	Spatial Distribution of the Acceleration Levels for Case 2 at Two High Frequencies.....	198
I.10	Propagation Constants for the Case in Which the Fastener Stiffness of Case 2 Is Increased by a Factor of 10.....	200
I.11	Typical Rail Fastener Configuration.....	202
I.12	Sketch of the Rail Mounted on the Effective Load Bearing Section of the Fastener Pad.....	203
I.13	Shear Deformation in Pad Due to Rail Bending Motion.....	207
I.14	Predicted and Measured Values for Rate of Attenuation of the Rail Vibration.....	210



III.1	Coupled Beam and Plate.....	221
III.2	Two Plates Connected Through a Rigid, Right-Angled Junction.....	225
III.3	Coordinate and Moment Sign Conventions.....	228
III.4	Coordinate, Moment, and Force Sign Conventions.....	233

#### LIST OF TABLES

1.1	Effect of Wheel-Rail Condition on Radiated Noise.....	7
4.1	Parameter Values for the Anderson Bridge on the MBTA Red Line....	124
4.2	Parameter Values for the Elevated Structure Near Green Street on the MBTA Orange Line.....	138
4.3	Parameter Values for the Elevated Structure Near Hathon Square on the MBTA Orange Line.....	144

## 1. INTRODUCTION

Recent years have seen a renewed interest in urban rail transit systems for public transportation. In part this interest has come about because of the many environmental problems associated with the automobile. However, environmental problems are also associated with rail transit systems. This report focuses on one problem of particular concern: noise near elevated rail transit structures. Those who have lived or worked near an old (all-steel structure) elevated transit line do not need to be convinced that this problem must be solved before rail transportation can be a viable alternative to the automobile.

### 1.1 Background

As systems manager for the U.S. Urban Mass Transportation Administration (UMTA) Urban Rail Supporting Technology Program, the Transportation Systems Center (TSC) is conducting research, development and demonstration efforts directed towards the introduction of improved technology in urban rail systems applications. As part of this program, TSC is conducting analytical and experimental studies directed towards noise and vibration reduction in urban rail systems.

The UMTA Rail Noise Abatement effort will bring together and improve existing and new elements into a unified technology consisting of: design criteria for establishing goals, noise control theory, design methods, test procedures, and appropriate documentation. The program has been organized into four concurrent and interrelated parts which will be closely coordinated with each other by TSC. They are:

1. Assessment of Urban Rail Noise and Vibration Climates and Abatement Options;
2. Test and Evaluation of State-of-the-Art Urban Rail

Noise Control Techniques;

3. Wheel/Rail Noise and Vibration Control Technology;
4. Track and Elevated Structure Noise and Vibration Control Technology.

The contract under which this report was prepared deals with Part 4 of the overall program. This report deals with the development and use of analytical models for predicting elevated structure noise.

## 1.2 Program Objectives

The noise and vibration generated by rail transit vehicles on an elevated structure are the result primarily of wheel/rail interactions. The fluctuating forces generated at the wheel/rail interface due to surface roughness, impact at rail joints, and wheel flat spots or other irregularities result in vibrations of the wheel and the rail. These vibrations, in turn, result in radiated noise from the rails and the wheels and transmission of vibration into the supporting track structure as shown in Fig. 1.1. When the vehicles are on an elevated structure, the sound radiation from the supporting structure often exceeds the radiation from the rails, wheels, and other vibrating surfaces of the vehicles. Thus, we refer to the noise as elevated structure noise even though the rail vehicle is the cause of the noise.

Many miles of elevated track structure are used in densely populated urban areas. The noise generated by these structures can be quite intense. In addition, the distance from the structure to the nearest residential dwelling is often small. These two factors combine so that many people are exposed to noise levels which they find annoying. In addition, the problem is made even more complex by the limited capability of many older structures to withstand the added weight of a noise control treatment. A study is presently being conducted for the NYCTA to assess the structural status of their elevated structures.

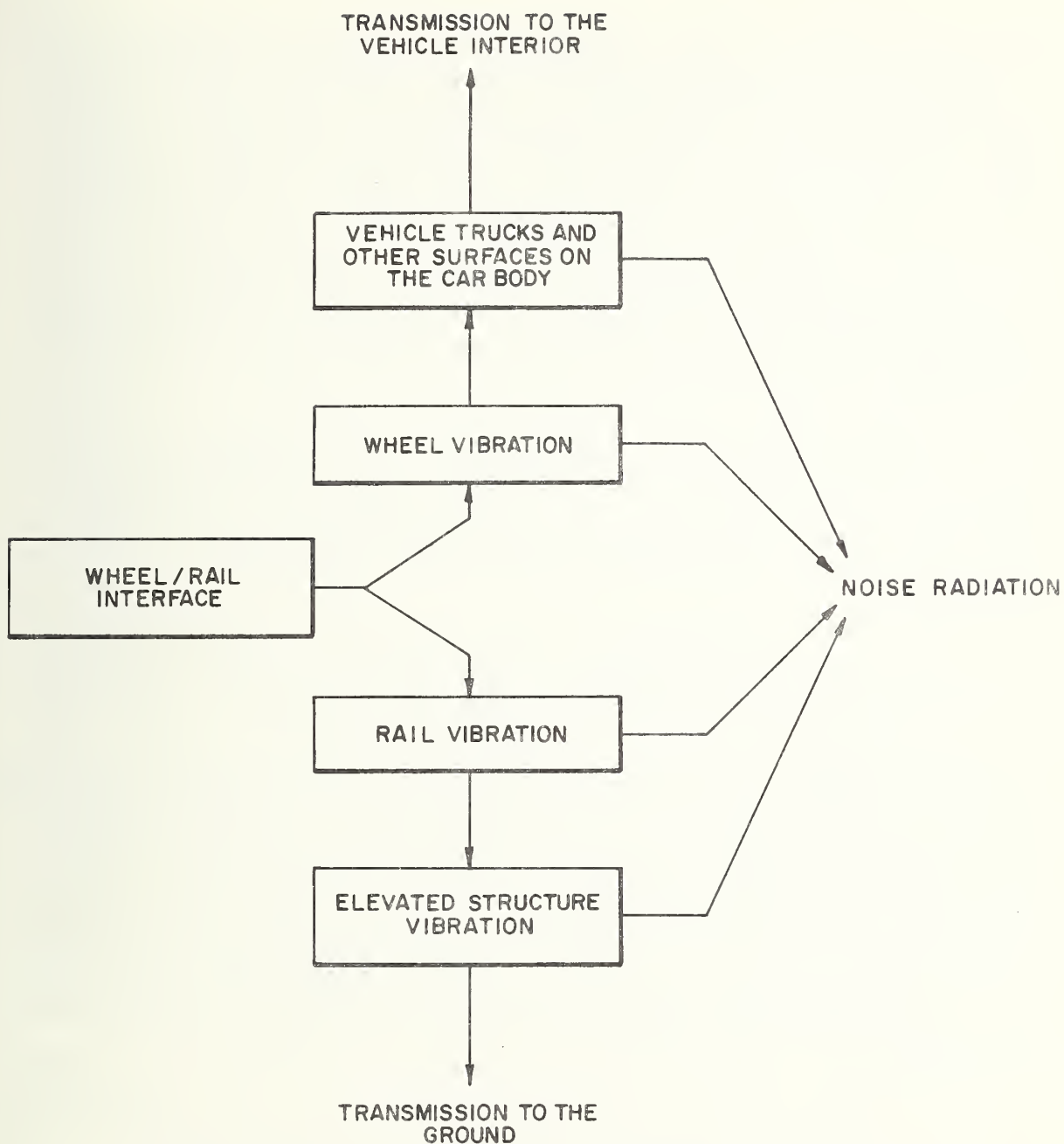


FIG. 1.1 VIBRATION TRANSMISSION PATHS  
AND NOISE RADIATION FOR ELEVATED TRACK STRUCTURES

Elevated structure noise is also a problem for those planning new systems or line extensions. In most cases the wayside noise is an issue of great concern to those communities near the proposed right-of-way. Therefore, every effort must be made to insure that reasonable noise criteria are met. See Reference [1] for a more detailed discussion of criteria. Since modifications to an operating line are extremely expensive, it is important that noise control be incorporated into the initial design of these structures.

Several techniques have appeared over the years for the prediction and control of radiated noise from rail vehicles and structures. These techniques are reviewed in an Interim Report prepared earlier during the course of this study [1].

The noise from elevated structures that are presently in use by the various rail transit properties can be predicted with sufficient accuracy to allow one to estimate the noise impact from proposed systems using the same types of structure. However, the prediction methods are empirical and do not allow one to predict the effect of design changes on the radiated noise. Thus, without a more detailed prediction model it is impossible to proceed with a well defined systematic program to reduce the noise. A primary objective of this study has been to develop a model for predicting noise from elevated structures. It is anticipated that this model will allow the design of reliable and cost effective noise control procedures.

A second objective of our study has been to investigate the noise and vibration problems associated with underground transit lines. When the line is located underground in a tunnel, wayside noise problems are largely eliminated. However, two new problems arise. The passengers of the transit vehicles may be exposed to high noise levels because of reverberant buildup of the sound levels in the tunnel and transmission of acoustical energy into the vehicle interiors through vents, windows, doors, etc. Also,

the vibration induced by the wheel/rail interaction is transmitted to the tunnel wall and through the soil to adjacent buildings where it is felt or heard as a low frequency rumbling noise. A detailed discussion of these two problems is presented in Reference [1].

The vibration problem has been of particular concern in the construction of new subway lines because of anticipated public complaints. In an effort to reduce the vibration transmission a number of techniques have been suggested and tried. The most successful of these is to isolate the vibrations of the rail from the tunnel floor by means of resilient rail fasteners and floating track slabs. A second report prepared by Cambridge Collaborative presents mathematical models for predicting the performance of floating slabs [2].

### 1.3 State of the Art in Elevated Structure Noise Control

The dominant source of elevated structure noise is known to be the wheel/rail interaction. It is known that wheel and rail roughness along the rolling surface lead to random forces that excite the rail into vibration with a broad range of frequencies. These forces also excite the car wheels into vibration. Both the wheels and rails radiate noise. However, at present, techniques to predict the relative contribution to the total wayside noise from these sources are not refined. A specific accomplishment of this report is to present a method for predicting the noise radiated by the rail.

It is also known that rail joints and wheel flats produce impact forces that set the rail and wheels into vibration. In this report we do not distinguish between the different mechanisms by which the rail is excited into vibration. We know that the elevated structure noise is to first approximation directly proportional to the rail vibration levels. Therefore, noise control



programs for wheel trueing and rail grinding and for replacement of jointed rail with continuously welded rail where possible will lead both to reductions in rail vibration and elevated structure noise. An estimate of the magnitude of the reductions is indicated in Table 1.1

The rail vibration acts through the rail fasteners to apply fluctuating forces to the deck of the elevated structure, as shown schematically in Fig. 1.2. The vibrations of the deck increase in level until the vibratory power transmitted from the rail to the deck is balanced by the sum of the power dissipated in the deck due to damping, the power radiated as noise, and the power transmitted from the deck to the supporting girders. Similarly, the vibration levels of the girders build up until a power flow balance is achieved. The state-of-the-art allows a prediction of the noise radiation from the entire structure[1]. However, since the prediction procedure is empirical, the radiation from the individual components of the structure and the transmission of vibration from one component to another cannot be determined without further analysis.

In this report we advance the state-of-the-art by presenting a generalized prediction model. In this model the vibration and noise radiation of each component is considered. The model allows us to predict the effect of increasing the damping of individual components or of changing the structural design so that the vibration transmission from one structural component to another is reduced.

#### 1.4 Summary of Results

The noise prediction model presented in this report has been developed analytically and validated by comparison of the predictions with results of field measurements for three types of elevated structure in Boston. The comparisons are sufficiently good that we have some confidence for using the models to predict the results of various noise and vibration control modifications. On the other hand, we must admit to some uncertainty. The elevated structure noise prediction model has given reasonably accurate

CORRECTION FACTORS *	
	ADD
JOINTED RAIL	8 to 10 dBA
WHEEL FLATS	8 to 10 dBA
NEW OR ROUGH RAILS	3 to 6 dBA
ROUGH WHEELS	3 to 6 dBA
CORRUGATIONS	UP to 15 dBA

NOTE : CORRECTION FACTORS ARE TO BE ADDED TO  
NOISE LEVELS EXPERIENCED WITH SMOOTH  
WHEELS ON SMOOTH JOINTLESS RAIL .

\* ADD ONLY ONE CORRECTION FACTOR —  
THE LARGEST APPLICABLE

TABLE 1.1 EFFECT OF WHEEL - RAIL CONDITION ON RADIATED NOISE

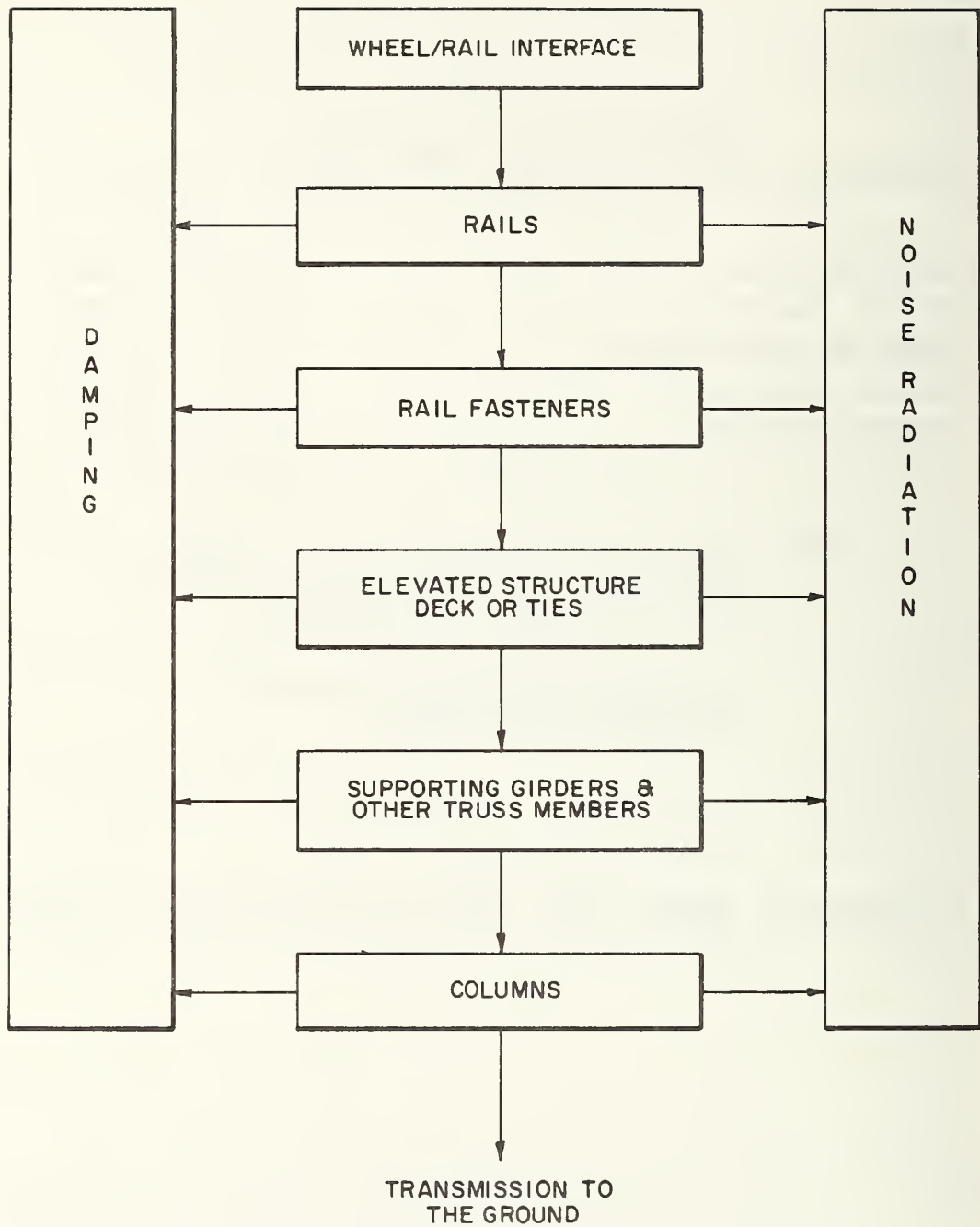


FIG. 1.2 VIBRATORY ENERGY TRANSMISSION  
BETWEEN ELEMENTS OF AN ELEVATED STRUCTURE

predictions only for the three structures studied. This is no absolute guarantee that the model will work for other types of structures. Also, we should point out that the field data we obtained was used both to evaluate and to improve preliminary versions of the model and to validate the final version. In spite of these uncertainties the authors of this report have confidence in the general validity of the model.

Use of the prediction model to evaluate various noise control options indicate that steel plate girders\* are the single most important noise source. A reduction in girder-web radiation can be achieved either by application of a damping treatment to increase the damping of the webs (and thus reduce their vibration) or by enclosing the girders to reduce their radiation efficiency.

The model indicates that use of vibration isolation materials between the deck and the girders would be effective only after the web damping is increased.

The model indicates that the use of very soft resilient rail fasteners can reduce the transmission of vibration to the elevated structure. However, by using fasteners that are too soft the effective damping of the rail vibrations by the fastener is decreased and the noise radiation by the rail is increased. In addition, requirements for good ride and safety impose a lower limit on fastener stiffness.

## 1.5 Organization of the Report

Rail vibration plays a major role in determining the elevated structure noise. For this reason, we start, in Section 2 of this report, with a complete discussion of models for predicting rail vibration.

---

\* A description of terms for elevated structures is given in Section 3.1

We continue in Section 3 with a description of the different types of elevated structure that are in use and show the development of a model for predicting vibration and noise radiation levels for different components of the structure.

A comparison of prediction with measured levels for three types of structure used on the Boston MBTA is presented in Section 4. Finally, in Section 5, we review the prediction model and discuss how it can be used to design effective noise control treatments. Engineering prediction procedures based on the model developed in this report are presented in a separate report [3].

## 2. RAIL VIBRATION

We start our discussion by considering the vibrations of the rail. During a train pass-by, the force on the rail at each wheel/rail contact point is made up of three components: a steady DC force due to the static load of the train; a slowly fluctuating force due to gross vehicle motions; and, finally, a rapidly fluctuating force due to the interaction of wheel and rail roughness, wheel flat spots, rail joints, and wheel slip. In this report we are primarily interested in the rapidly fluctuating forces, since the vibrations due to these forces generate noise that is in the audible range of frequencies.

The high frequency, rapidly fluctuating forces due to the wheel/rail interaction impart energy to the rail in the form of bending and torsional vibrations. This energy propagates along the rail away from the wheel/rail contact point. During propagation part of the rail vibrational energy is dissipated by various damping mechanisms in the rail and in the rail fasteners. A second part is radiated as noise. And, finally, a third part is transmitted to the track support structure.

In our study of elevated structure noise, we consider the rail vibration as the source of excitation for the remaining structure. Also, since the maximum rail vibration levels during a pass-by are 10 to 15 dB higher than levels observed for other components of the structure, the rail must be considered as a potentially important noise source in spite of its small radiating area. Our approach will be to determine first the maximum vibration levels during a pass-by, and then to relate the maximum levels to the spatial distribution of the levels. Both the maximum levels and the spatial distribution of the levels are needed to calculate the vibrational energy transmitted to the structure and the noise radiated by the rail.



## 2.1 Basic Wheel-Rail Interaction Mechanisms

The basic mechanisms of the wheel/rail interaction are being studied under a parallel effort funded by the U. S. Department of Transportation. Based on the results of this study [4], at least a qualitative understanding of the different mechanisms has been achieved. Three distinct mechanisms are involved:

- (1) "Roar": The broadband noise during a train pass-by is due to the roughness of the wheel and the rail. This roughness imposes a small relative displacement between the wheel and the rail which gives rise to rapidly fluctuating forces at the wheel/rail contact point.
- (2) Impact: Rail joints, switches, and other rail discontinuities lead to impact noise. Similarly, wheels that are "out of round" or have "flats" cause an impact to occur for each revolution of the wheel.
- (3) Squeal: When a train is on curved track, an intense squeal can occur. This noise is due to a number of mechanisms which cause the wheels to slide on the rail. During the sliding, stick-slip mechanisms lead to large fluctuating forces and intense noise radiation.

## 2.2 Prediction of Maximum Response

In past studies the vibratory response of the rail to wheel and rail roughness has been formulated in terms of the wheel and rail roughness spectrum, the vehicle speed, and the driving point impedances of the wheel and the rail [5]. The spectrum of the vibratory velocity of the rail at the wheel/rail contact point is given by

$$S_v(\omega) = \frac{\omega^2}{S} \left| \frac{Z_w}{Z_r + Z_w} \right|^2 \left[ \phi_w(k=\frac{\omega}{S}) + \phi_r(k=\frac{\omega}{S}) \right] \quad (2.1)$$

where  $S_v(\omega)$  is the spectrum of the vibratory velocity,  $\omega$  is the radian frequency,  $S$  is the vehicle speed,  $Z_r$  is the point impedance of the rail,  $Z_w$  is the point impedance of the wheel,  $\phi_w(k)$  is the roughness spectrum of the wheel,  $\phi_r(k)$  is the roughness spectrum of the rail,  $k$  is the wavenumber, and  $| |$  signifies the magnitude of a complex number.

A direct verification of Eq. 2.1 requires measurement of the wheel and rail roughness spectra. A device to accomplish this measurement is being developed [4]. However, at present the prediction of maximum rail vibration levels during a train pass-by is not within the state-of-the-art. Therefore, we must rely on an empirical approach based on measured data.

Equation 2.1 can be used to infer the effect of various parameters on the maximum vibratory level of each rail during a pass-by. At intermediate frequencies, in the approximate range 100 to 1500 Hz, the wheel impedance,  $Z_w$ , is believed to be higher than the rail impedance,  $Z_r$  [5]. In this case the rail response spectrum given by Eq. 2.1 is independent of the rail impedance to first approximation. Thus, we can assume that the maximum vibratory levels for the rails do not depend on track design or the design of the elevated structure in the frequency range 100 to 1500 Hz\*. Use of resilient wheels decreases the wheel impedance and this general assumption is invalid. See Ref. [4] for a more detailed discussion.

Vehicle speed affects both the magnitude and frequency of the fluctuating forces at the wheel/rail interface and the value of

---

\* We do not mean to imply that the complete spatial history of the rail vibration is independent of track design.

the rail impedance. However, in Ref. [6] it is shown that the effect of vehicle speed on impedance can be neglected as long as the speed is much less than the propagation velocity of free bending and torsional waves in the rail. This result is used to great advantage in our remaining work, since it allows us to study the dynamic response of elevated structures in terms of their response to fluctuating forces that do not move along the track.

Assuming that the impedances are not affected by vehicle speed, we see from Eq. 2.1 that the dependence of the response spectrum on speed is determined by the term  $1/S$  and by the dependence of the roughness spectra on wavenumber. The limited data that is available show that the roughness spectra tend to decrease in amplitude with increasing wavenumber [4]. Although general trends are difficult to identify, the average trend is for the amplitudes to decrease with between a third and fourth power of wavenumber.\* In this case, the rail response spectrum in any given band should increase with between a second and third power of vehicle speed. A third power speed dependence for A-weighted wayside noise levels is commonly observed [1]. Thus, for the purposes of this report we will assume that the maximum vibratory levels of the rail also show a third power dependence on vehicle speed.

Mechanisms leading to impact at the wheel/rail interface are also affected by vehicle speed. Field data for rail vehicles on jointed rail or with wheel flats indicate that the wayside noise level exhibits a third power dependence on vehicle speed.† This suggests that the maximum vibratory levels of the rail due to impact mechanisms also exhibit a third power dependence. In the work to

---

\*Many exceptions to this general trend have been observed. The reader should see Ref. [4] for a more complete discussion.

†Individual events show a second power dependence [4] but the number of impacts per unit time increases linearly with speed giving an overall third power dependence.

follow we assume this to be the case.

Based on empirical evidence we know that impact noise mechanisms can increase the A-weighted noise level from at-grade track 10 dB(A) above levels for smooth continuously welded rail with trued wheels. We assume that the rail vibration increases by a similar amount. In the following Sections we do not treat the vibration and noise due to impact separately. We assume that the levels discussed are average levels with the averaging time being long enough to average over impacts.

### 2.2.1 Review of Reported Data

Extensive data on rail vibration were taken during tests of the BART vehicles [7]. The purpose of the tests was to investigate the effects of four different rail fasteners on radiated noise and vibration. The rail was continuously welded and in a reasonably smooth condition as were the vehicle wheels (although no roughness measurements were taken).

The maximum vertical vibratory velocity levels,  $L_v$ , during pass-bys at 60 mph (96 km/hr) were in the range 108 to 114 dB referenced to  $5 \times 10^{-8}$  m/sec\*, i.e.

$$108 \leq L_v \leq 114 \text{ dB} \quad (2.2a)$$

with

$$L_v = 20 \log_{10} \frac{v_{\text{rms}}}{5 \times 10^{-8}} \quad (2.2b)$$

and  $v_{\text{rms}}$  is the maximum rms (root-mean-square) velocity of the rail vibration in meters per second. The octave band frequency spectra

---

\* ISO Standard TC 43/SC 2/WG 2.

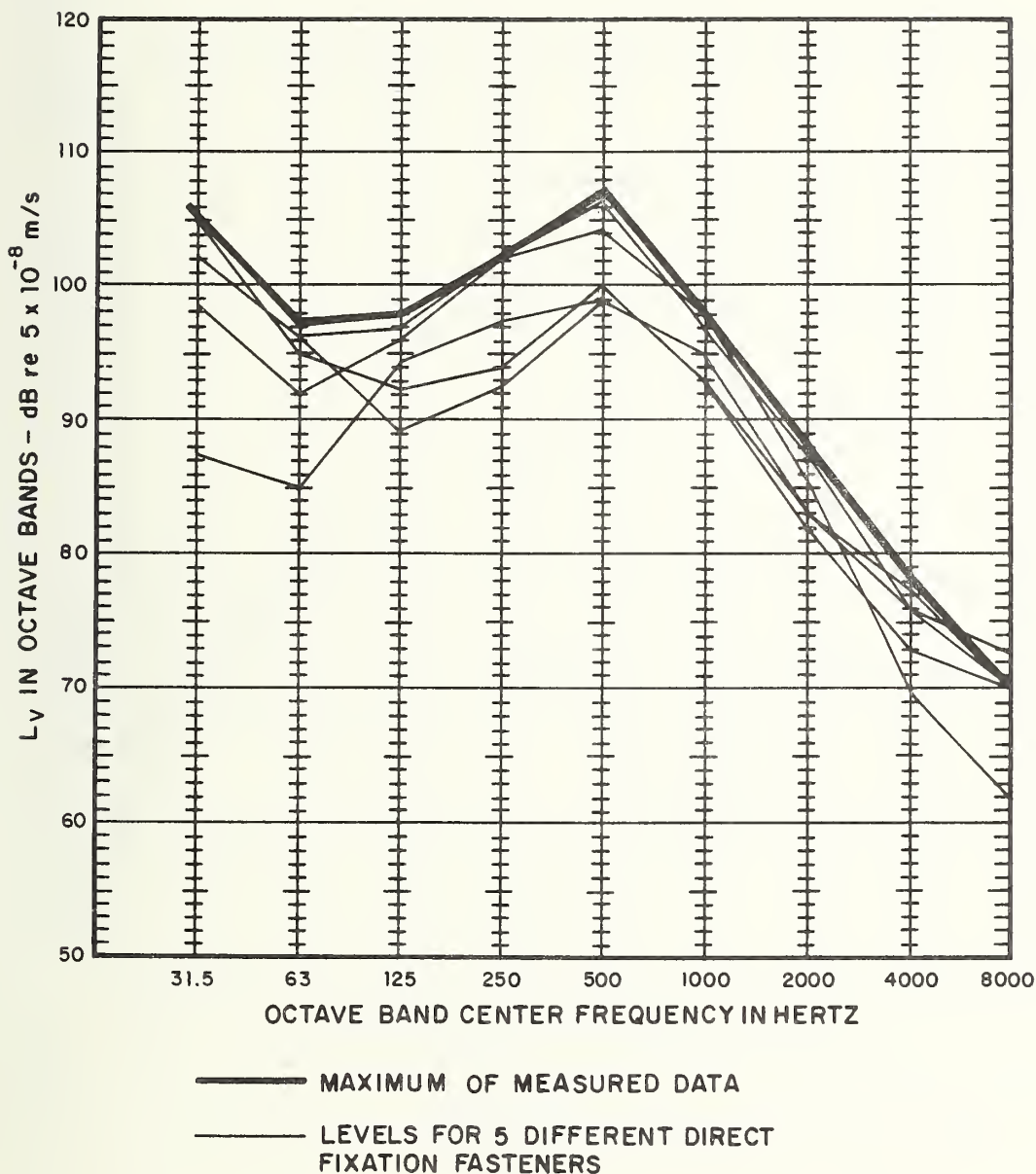
are shown in Fig. 2.1 These show maxima in the 31.5 Hz band and the 500 Hz band. However, from the point of view of predicting elevated structure noise the levels in the 500 Hz band are much more important.

The range of octave band levels for the five types of rail fastening is quite large, particularly at lower frequencies. Based on the discussion of the previous Section we would expect the levels in the 125, 250, 500, and 1000 Hz octave bands to be the same, since the wheel impedance is supposedly higher than the rail impedance in this frequency range. The range of levels in these bands must be attributed to unknown effects and considered in our evaluation of the accuracy of the prediction model that uses these measured levels as input data. The range of values at low frequencies, below 125 Hz, may indeed be due to the differences in rail fastener properties, since the rail impedance typically exceeds the wheel impedance at these low frequencies.

Torsional vibration levels for the rail are usually not reported. For this reason we have instrumented a rail on a section of track of the MBTA Red Line Quincy Extension. The rail was continuously welded. Maximum levels during a pass-by for vertical and torsional vibration are shown in Fig. 2.2. Note that the vibrational levels of the rail foot due to vertical motion are significantly larger than levels due to torsional motion in the octave bands centered at frequencies below 2000 Hz. In addition, the noise radiation and transmission of vibration to the structure is much less for torsion than for vertical vibration at these frequencies. Based on this fact we can ignore the contribution of torsional vibration to the overall wayside noise levels in the lower frequency bands. At higher frequencies, 2000 Hz and above, radiation due to torsional vibration will increase the total rail radiation by approximately 3 dB.

Our approach in the work to follow will be to use the maximum octave band levels shown in Fig. 2.1 as a basic input to our prediction model except for specific comparisons with experimental

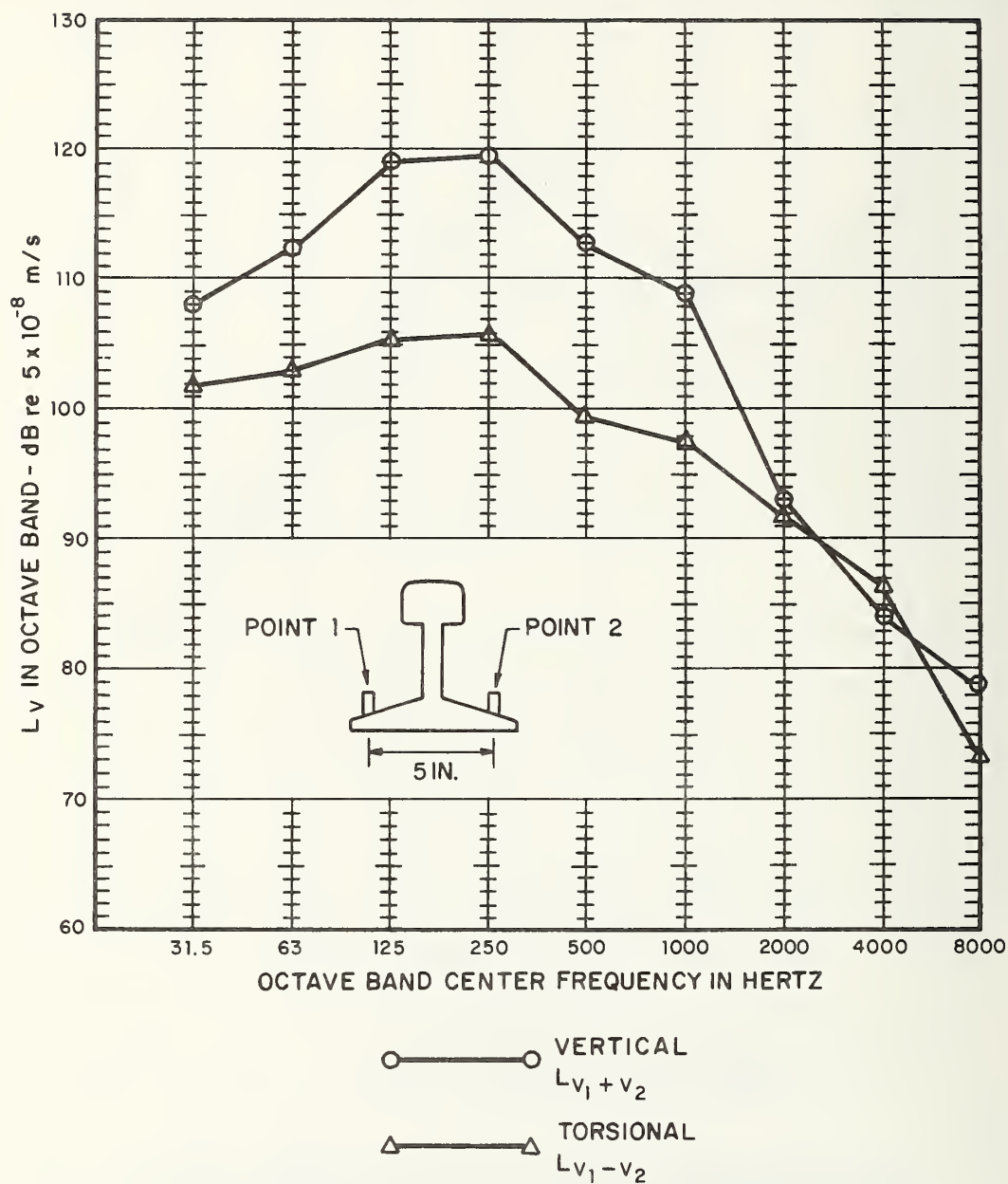




NOTE: LEVELS ARE THE MAXIMUM LEVEL OBSERVED DURING THE PASS-BY OF A SINGLE CAR AT 60 MPH (100 km/h) ON SMOOTH CONTINUOUSLY-WELDED RAIL

FIG. 2.1 VERTICAL VIBRATORY VELOCITY LEVELS FOR THE RAIL MEASURED ON BART TEST TRACK [7]





NOTE: LEVELS ARE THE MAXIMUM LEVEL OBSERVED DURING THE PASS-BY OF A FOUR-CAR TRAIN WITH WHEEL FLATS ON CONTINUOUSLY-WELDED RAIL

FIG. 2.2 VERTICAL AND TORSIONAL VELOCITY LEVELS FOR THE RAIL MEASURED ON MBTA RED LINE

data where measured rail vibration levels are available. We are assuming, in essence, that changes in rail fastener or elevated structure design do not change the maximum rail vibration level. It will be possible to reduce the errors caused by assumption when a model for predicting the maximum rail vibration levels during a pass-by is available.

The vibration levels used as an input to our prediction model will be taken as representative of continuously welded rail with both wheels and rails in good condition, i.e. smooth. The effects of rail joints, roughness, and wheel flats will be taken into account by raising the levels in Fig. 2.1 by the amount indicated in Table 1.1.

## 2.3 A Simplified Vibration Prediction Model

The simplest model for studying the rail vibration is an infinitely long beam on a continuous elastic foundation. The dynamic properties of the beam are set to represent those of the rail. The stiffness of the foundation is set to represent the stiffness of the rail fasteners. We assume that the rail fasteners are mounted on a rigid support. We also ignore shear deformations in the rail and the effect of non-continuous fasteners, i.e. the effect of fastener spacing. The excitation of the rail will be modeled as a stationary point force.

A detailed study of more refined models for predicting the rail vibration is presented in Appendix I. As a result of this detailed study we have concluded that the simple model presented in this Section gives sufficiently accurate results that it can be used as the basis for an elevated structure noise prediction model.

The equation of motion for bending of the beam on an elastic foundation is given by

$$m_r \frac{\partial^2 u}{\partial t^2} + B_r \frac{\partial^4 u}{\partial x^4} + K_\ell u = f(t) \delta(x) \quad (2.3)$$

where  $m_r$  is the mass of the rail per unit length,  $u$  is the downward rail displacement,  $B_r$  is the bending stiffness of the rail\*,  $K_l$  is the effective stiffness of the fasteners per unit length of rail,  $f(t)$  is the downward force applied to the rail,  $t$  is the time coordinate,  $x$  is a spatial coordinate down the track, and  $\delta(x)$  is the Dirac Delta function, where

$$\int dx \ u(x) \ \delta(x) = u(0) \quad (2.4)$$

The solution to Eq. 2.3 is found by using Fourier transforms. If we define the transform pair,

$$f(t) = \frac{1}{2\pi} \int d\omega \ F(\omega) \ e^{i\omega t} \quad (2.5a)$$

$$F(\omega) = \int dt \ f(t) \ e^{-i\omega t} \quad (2.5b)$$

then the transform of the rail response at point  $x$  is given by

$$U(x, \omega) = \frac{F(\omega)}{4 B_r} \cdot \frac{1}{k_r^3} \{-i e^{-ik_r x} - e^{-k_r x}\} \quad (2.6a)$$

for  $x > 0$  and  $\omega > \omega_r$

and

$$U(x, \omega) = \frac{F(\omega)}{2\sqrt{2} B_r} \cdot \frac{1}{k_r^3} e^{-\frac{k_r x}{\sqrt{2}}} \left( \cos \frac{k_r x}{\sqrt{2}} + \sin \frac{k_r x}{\sqrt{2}} \right) \quad (2.6b)$$

for  $x > 0$  and  $\omega < \omega_r$

---

\*  $B_r = EI$  where  $E$  is Young's Modulus and  $I$  is the cross-section moment of inertia.

where

$$k_r^4 = \frac{K_\ell}{B_r} \left| \left( \frac{\omega}{\omega_r} \right)^2 - 1 \right| \quad (2.7a)$$

$$\omega_r^2 = \frac{K_\ell}{m_r} \quad (2.7b)$$

and  $| |$  signifies the absolute value. The parameter  $k_r$  is the wavenumber of freely propagating bending waves in the rail. It is reciprically related to the vibration wavelength,  $\lambda$ , by

$$\lambda = \frac{2\pi}{k_r} \quad (2.8)$$

Equation 2.6a shows two terms. The first represents a bending wave traveling away from the excitation point at the free bending-wave speed for the beam,  $c_r$ , where

$$c_r = \frac{\omega}{k_r} \quad (2.9)$$

The second term represents a near field term that decays rapidly as we move away from the excitation point. The beam behavior changes at frequencies below the rail resonance frequency,  $\omega_r$ . For these frequencies, both terms decay exponentially and a traveling wave term does not exist.

The effects of damping in the rail fasteners and in the rail are accounted for by letting the foundation stiffness,  $K_\ell$ , and the rail bending stiffness,  $B_r$ , be complex,

$$B'_r = B_r(1 + i \eta_r) \quad (2.10)$$

and

$$K'_\ell = K_\ell(1 + i \eta_f) \quad (2.11)$$

where  $B_r$  and  $K_\ell$  are now real quantities,  $\eta_r$  is the damping loss factor of the rail, and  $\eta_f$  is the damping loss factor of the foundation.

When damping is included, the rail response is given for  $x \geq 0$  and all values of  $\omega$  by Eq. 2.6a with  $k'_r$  substituted for  $k_r$ , where

$$k'_r = k_m \left\{ \sin \frac{\theta}{4} - i \cos \frac{\theta}{4} \right\} \quad (2.12a)$$

$$k_m^4 = \frac{K_\ell}{B_r} \left[ \frac{\left( 1 - \frac{\omega^2}{\omega_r^2} \right)^2 + \eta_f^2}{1 + \eta_r^2} \right]^{1/2} \quad (2.12b)$$

and  $\theta$  is defined to be in the range 0 to 360 degrees so that

$$\sin \theta = \frac{K_\ell}{B_r} \frac{1}{k_m^4} \left[ \frac{\eta_r \left( 1 - \frac{\omega^2}{\omega_r^2} \right) + \eta_f}{1 + \eta_r^2} \right] \quad (2.12c)$$

and

$$\cos \theta = \frac{K_\ell}{B_r} \frac{1}{k_m^4} \left[ \frac{\frac{\omega^2}{\omega_r^2} - (1 + \eta_r \eta_f)}{1 + \eta_r^2} \right] \quad (2.12d)$$

The magnitude of the response at the point of excitation is found from Eq. 2.6a to be

$$|U(0, \omega)|^2 = \frac{|F(\omega)|^2}{8 B_r^2 k_m^6} \quad (2.13)$$

To calculate the transmission of vibration from the rail to other structures and to calculate the sound radiation, we require the amplitude of vibration along the entire length of rail. Substituting  $k_r'$  for  $k_r$  in Eq. 2.6a we find

$$\begin{aligned} \frac{|U(x, \omega)|^2}{|U(0, \omega)|^2} &= \frac{1}{2} e^{-2k_m x \sin \frac{\theta}{4}} + \frac{1}{2} e^{-2k_m x \cos \frac{\theta}{4}} \\ &+ e^{-k_m x (\sin \frac{\theta}{4} + \cos \frac{\theta}{4})} \sin k_m x (\sin \frac{\theta}{4} + \cos \frac{\theta}{4}) \end{aligned} \quad (2.14)$$

where  $k_m$  and  $\theta$  are given by Eqs. 2.11. At high frequencies,  $\omega \gg \omega_r$ , and for small values of damping, the following approximations are possible,

$$k_m^4 \approx \frac{\omega^2 m_r}{B_r} \quad (2.15a)$$

$$\sin \frac{\theta}{4} \approx 1, \quad (2.15b)$$

and

$$\cos \frac{\theta}{4} \approx \frac{\eta_r}{4} + \frac{\eta_f}{4} \frac{\omega_r^2}{\omega^2} \quad (2.15c)$$

Equation 2.14 can be written as

$$\begin{aligned} \frac{|U(x, \omega)|^2}{|U(0, \omega)|^2} &\approx \left( \frac{1}{2} + \sin k_m x \right) e^{-k_m x} + \frac{1}{2} e^{-\alpha x} \\ &\text{for } \omega \gg \omega_r \end{aligned} \quad (2.16)$$



where

$$\alpha = k_m \left( \frac{\eta_r}{2} + \frac{\eta_f}{2} \frac{\omega_r^2}{\omega^2} \right) \quad (2.17)$$

The first term in Eq. 2.16 decays very rapidly at an average rate of 55 dB per wavelength,  $\lambda$ , where for small damping and high frequencies

$$\lambda \approx \frac{2\pi}{k_m} \approx 2\pi \left[ \frac{B_r}{\omega^2 m_r} \right]^{1/4} \quad (2.18)$$

At 500 Hz, the wavelength for a typical rail is approximately 6.5 ft (2 meters). The second term in Eq. 2.16 decays at a slower rate that is governed by the damping. It is this term which dominates the vibration transmission and sound radiation for small values of damping.

In the work to follow we will formulate the vibration transmission in terms of the rail response spectrum,  $S_{u(x)}(\omega)$ , where

$$S_{u(x)}(\omega) = \frac{1}{2} |U(x, \omega)|^2 \quad (2.19)$$

and  $U(x, \omega)$  is the Fourier transform of the displacement at point  $x$ . We will also make use of an integrated displacement spectrum,  $I_u(\omega)$ , where

$$I_u(\omega) = \int dx S_{u(x)}(\omega) \quad (2.20)$$

and the integration is over all values of  $x$ . From Eq. 2.14 we find

$$\frac{I_u(\omega)}{S_{u(o)}(\omega)} = \frac{1}{2k_m} \left\{ \frac{1}{\sin \frac{\theta}{4}} + \frac{1}{\cos \frac{\theta}{4}} + \frac{1}{\sin \frac{\theta}{4} + \cos \frac{\theta}{4}} \right\} \quad (2.21)$$

At high frequencies and for light damping Eq. 2.21 can be written as

$$\frac{I_u(\omega)}{S_{u(o)}(\omega)} \approx \left[ \frac{B_r}{\omega^2 m_r} \right]^{1/4} \frac{2}{\eta_{eff}} \quad \text{for } \omega \gg \omega_r \quad (2.22)$$

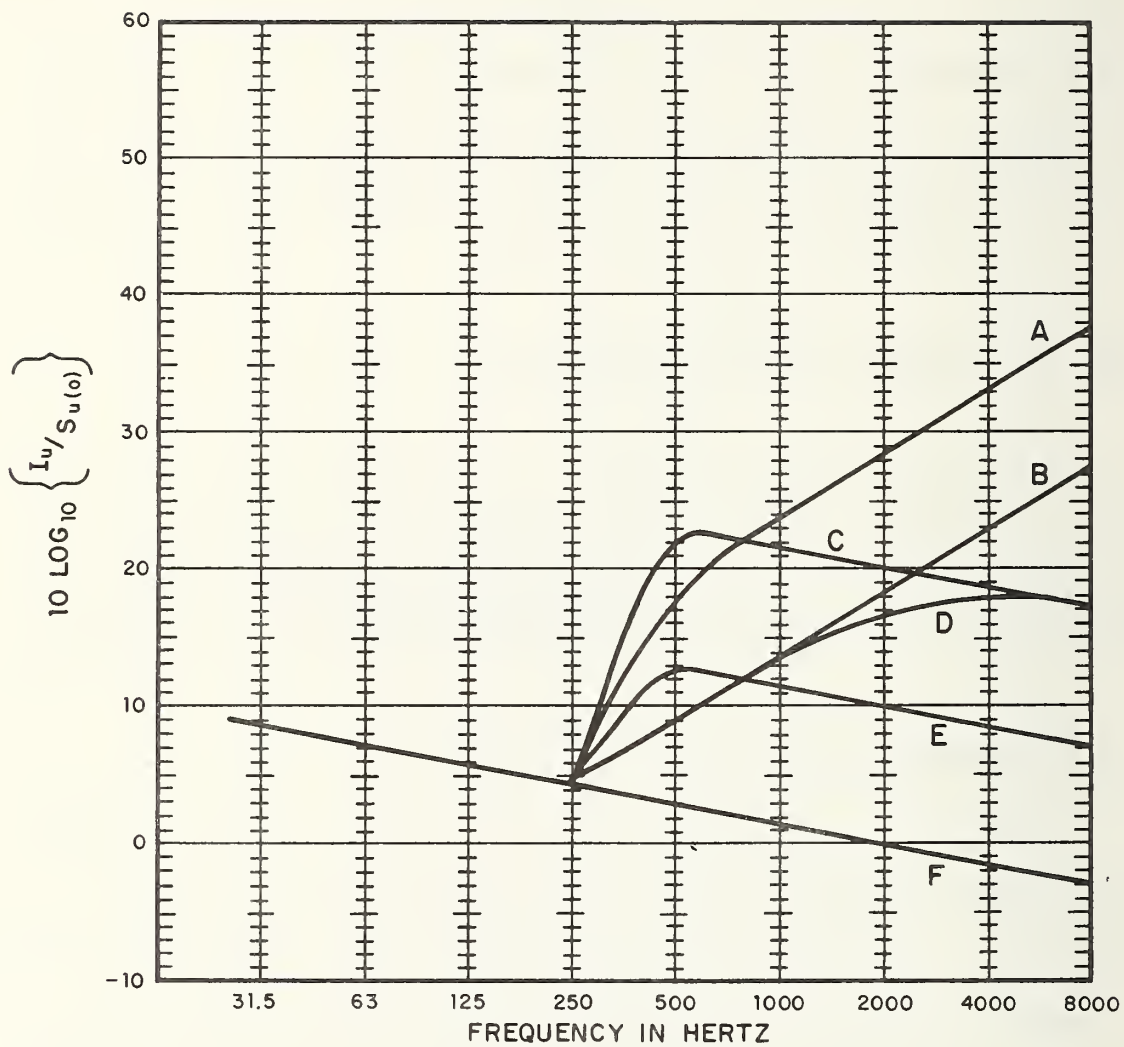
where the effective damping is given by

$$\eta_{eff} = \eta_r + \eta_f \frac{\omega_r^2}{\omega^2} \quad (2.23)$$

Figure 2.3 shows the total integrated rail response spectrum for a broad range of frequencies and damping values.

## 2.4 Rail Radiation

The rail is a radiating surface of complex cross-sectional shape, high vibrational levels, and relatively small radiating area (that is, compared to the rest of the track support structure). From an acoustical point of view, the rail can be modeled with reasonable accuracy as a long cylinder. The effective diameter of this equivalent cylinder can be determined by two methods. First, the effective radius,  $a$ , could be taken to be 1/2 of the largest rail cross-sectional dimension (i.e. rail height), which implies  $a = 3.3$  inches for 115 RE rail, and an effective radiating perimeter of 1.7 ft. Using this radius, the theoretical result from Ref. [8] for the radiation efficiency of a vibrating cylinder can be used to predict the radiated acoustic power from the rail. The alternate technique, which provides a higher degree of confidence in the result, determines the effective cylinder radius by fitting



RAIL FASTENER RESONANCE FREQUENCY IS 250 Hz  
CALULATIONS FOR RE 115 RAIL,UNITS ARE IN FT.

#### DAMPING LOSS FACTOR VALUES

- |                                |                                |
|--------------------------------|--------------------------------|
| A. $\eta_r = 0, \eta_f = 0.1$  | B. $\eta_r = 0, \eta_f = 1.0$  |
| C. $\eta_r = 0.01, \eta_f = 0$ | D. $\eta_r = 0.01, \eta_f = 1$ |
| E. $\eta_r = 0.1, \eta_f = 0$  | F. $\eta_r = 1.0, \eta_f = 0$  |

FIG. 2.3 INTEGRATED RAIL RESPONSE SPECTRUM

the theoretical result to actual measurements.

#### 2.4.1 Radiation Efficiency

The rail radiation efficiency,  $\sigma$ , is defined by Eq. 2.24,

$$\sigma(\omega) = \frac{W_{\text{rad}}(\omega)}{\rho_o c_o P I_v(\omega)} \quad (2.24)$$

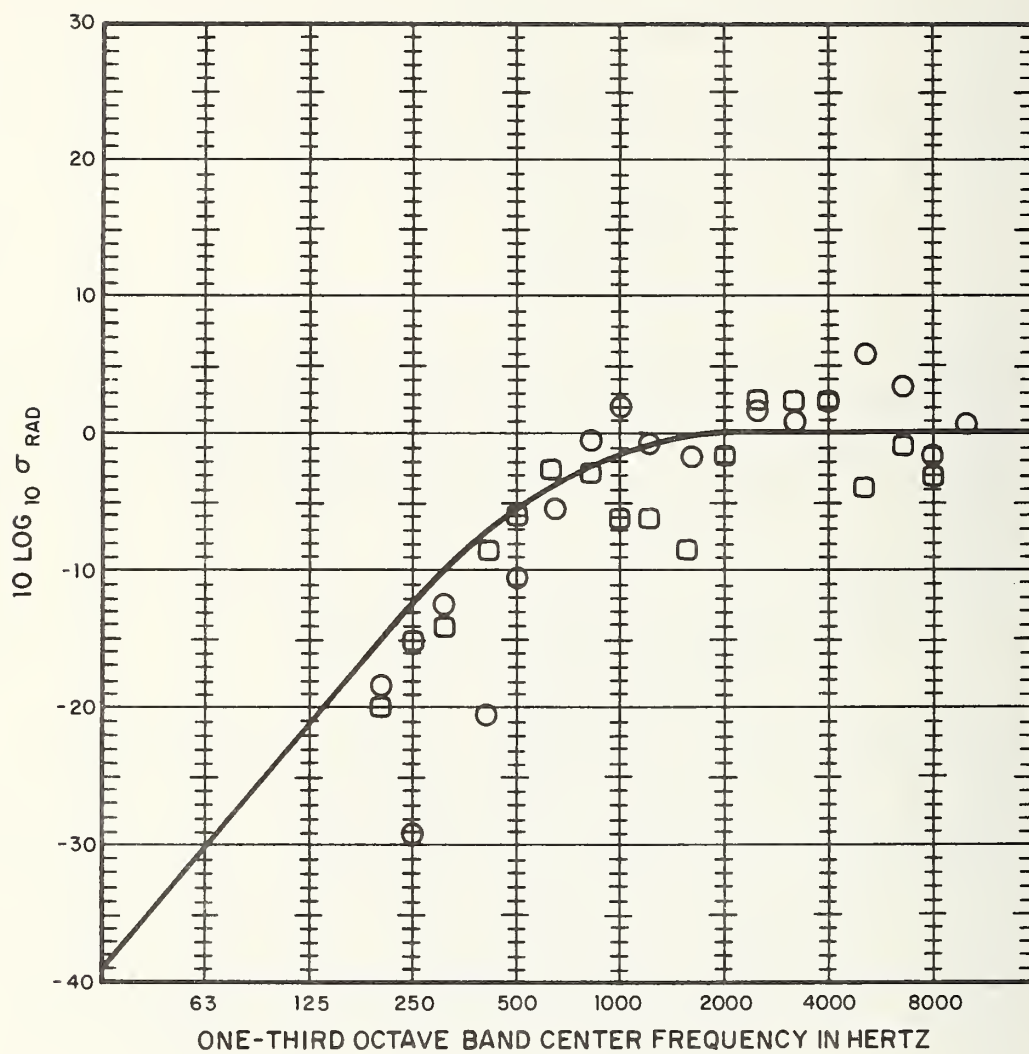
where  $W_{\text{rad}}(\omega)$  is the spectrum of radiated acoustic power,  $\rho_o c_o$  is the characteristic impedance of air,  $P$  is the radiating perimeter, and  $I_v(\omega)$  is the integrated spectrum of the rail vibratory velocity. The theoretical expression for radiation efficiency is taken from Ref. [8]\*,

$$\sigma(\omega) = \frac{2}{\pi} \{k_o a [J_1'(k_o a) + N_1'(k_o a)]\}^{-1} \quad (2.25)$$

where  $k_o$  is the acoustic wavenumber,  $a$  is the cylinder diameter,  $J_1'$  is the derivative of the 1<sup>st</sup> order Bessel Function, and  $N_1'$  is the derivative of the 1<sup>st</sup> order Neumann Function. Values for the radiation efficiency can be inferred from data obtained by exciting a finite length of rail into vibration in a reverberant room and measuring radiated power. Values based on data from Ref. [5] are shown in Fig. 2.4. The solid line represents the theory fitted to the data with  $a = 2.9$  in., and  $P = 1.5$  ft. The agreement of the data with theory appears quite good, certainly within the scatter of the data. Note that data is presented for both vertical and horizontal excitation and that there is no appreciable difference between the results. In light of this agreement the radiation

---

\* A slight error exists in the result given by Ref. [8]. The correct expression is given above.



———— THEORETICAL PREDICTION FROM  
Eq. 2.25 WITH  $a = 2.9$  in.

○ DATA DERIVED FROM REVERBERATION  
ROOM MEASUREMENT [5]  
○ VERTICAL EXCITATION OF RAIL  
□ HORIZONTAL EXCITATION OF RAIL

FIG. 2.4 RADIATION EFFICIENCY FOR THE RAIL

efficiency of Fig. 2.4 will be used for all rail radiation calculations and the effective radiating perimeter of the equivalent radiating cylinder will be taken to be 1.5 ft. The integrated velocity spectrum is found by multiplying the integrated displacement spectrum given by Eq. 2.21 or 2.22 by  $\omega^2$ .

## 2.4.2 Directivity

In addition to the power radiated by the rail, its directivity in the horizontal plane is also of interest. Consider an infinite cylinder lying along the  $x_2$  axis whose vibration is confined to the  $x_3$  direction, as shown in Fig. 2.5.

The vector  $\underline{x}$  represents the position of the observer relative to some arbitrary origin. The vector  $\underline{y}$  represents the vector from the origin to a radiating element of the cylinder. The scalar parameter  $r$  is the distance from the radiating element to the observer. The Fourier transform of the pressure at  $\underline{x}$  is given by [9]

$$P(\underline{x}, \omega) = - \int_{-\infty}^{\infty} \frac{i k_o \cos \theta_3 e^{-i k_o r}}{4 \pi r} F_3(y_2, \omega) dy_2 \quad (2.26)$$

where  $r = |\underline{x} - \underline{y}|$ ,  $\cos \theta_3 = (\partial r)/(\partial x_3)$  is the direction cosine,  $k_o$  is the acoustic wavenumber, and  $F_3(y_2, \omega)$  is the Fourier transform of the force exerted by the cylinder on the acoustic medium.

We now define the angle  $\phi$  which is the angle between the vector  $\underline{x}$  and the  $x_1, x_3$  plane. If the distance from the observer to the cylinder is much larger than the spatial extent of vibration on the cylinder\* the far field approximation

---

\*This can be shown to be true in time histories of rail vibration with realistic values for rail damping at all frequencies of importance, since the spatial extent of the vibration due to each point force at the wheel/rail contact points is on the order of a few feet in length.



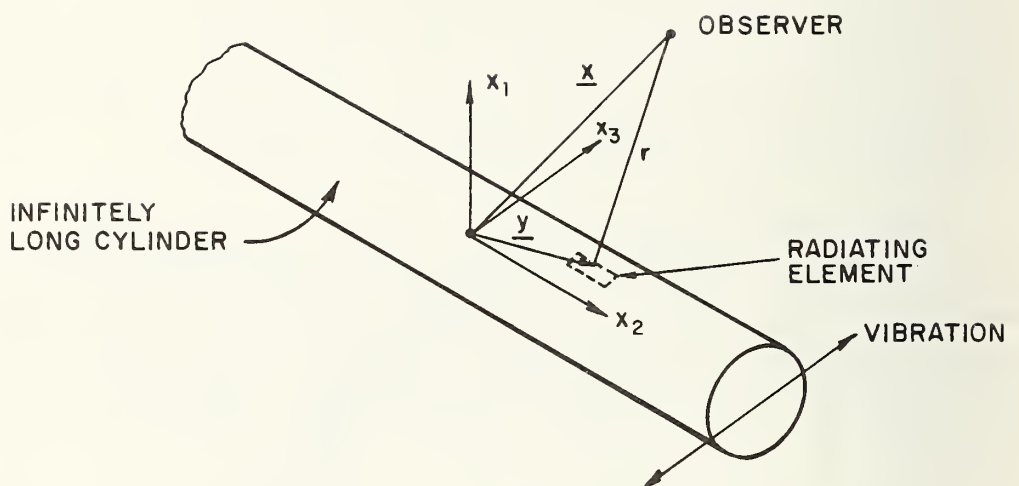


FIG. 2.5 CYLINDER COORDINATES

$$r \cong |\underline{x}| + y_2 \sin \phi \quad (2.27)$$

can be used and the transform of the pressure is given by

$$P(\underline{x}, \omega) = - \frac{i k_0 \cos \theta_3 e^{-ik_0 |\underline{x}|}}{4 \pi |\underline{x}|} \int_{-\infty}^{\infty} dy_2 e^{-ik_0 y_2 \sin \phi} F_3(y_2, \omega) \quad (2.28)$$

We observe that the integral of Eq. 2.28 is in the form of an Fourier transform over  $y_2$ . Thus,

$$P(\underline{x}, \omega) = - \frac{i k_0 \cos \theta_3 e^{-ik_0 |\underline{x}|}}{4 \pi |\underline{x}|} \cdot \hat{F}_3(k_0 \sin \phi, \omega) \quad (2.29)$$

where  $\hat{F}_3$  is the wavenumber transform of  $F_3(y_2, \omega)$ ,

$$\hat{F}_3(k, \omega) = \int_{-\infty}^{\infty} dy_2 F_3(y_2, \omega) e^{iky_2} \quad (2.30)$$

The dependence of the radiation on the angle  $\phi$  is given by  $\hat{F}_3(k_0 \sin \phi, \omega)$ . The dependence of the radiation given by  $\cos \theta_3$  is due to the dipole nature of the vibrating cylinder, and is multiplicative with  $\phi$  dependence.

Assuming the force on the rail due to the surrounding fluid is proportional to the rail velocity, we can obtain the directivity of rail radiation from the wavenumber dependence of the transform of the rail vibrational velocity,  $\hat{V}_r(k, \omega)$ . To find  $\hat{V}_r(k, \omega)$  we

Fourier transform the equation of motion for the rail displacement, Eq. 2.3, in both time and space and multiply by  $i\omega$ . The result is

$$\hat{V}_r(k, \omega) = \frac{i\omega}{K'_\ell + k^4 B_r - \omega^2 m_r} F(\omega) \quad (2.31)$$

where the effective stiffness of the fasteners per unit length of rail,  $K'_\ell$ , is allowed to be complex to include the effects of damping,

$$K'_\ell = K_\ell (1 + i \eta_f), \quad (2.32)$$

and where  $\eta_f$  is the fastener damping loss factor. The dependence of radiation upon  $\phi$  is given by  $\hat{V}_r(k_o \sin \phi, \omega)$ , and the directivity function,  $D(\phi, \omega)$ , is given by

$$D(\phi, \omega) = \frac{|P(r, \phi, \omega)|^2}{|P(r, 0, \omega)|^2} = \frac{|\hat{V}_r(k_o \sin \phi, \omega)|^2}{|\hat{V}_r(0, \omega)|^2} \quad (2.33)$$

where  $|P(r, \phi, \omega)|^2$  is the magnitude squared of the complex pressure amplitude at a point in the far field a distance  $r$  from the rail at an angle  $\phi$  from a line perpendicular to the rail and  $|P(r, 0, \omega)|^2$  is the magnitude-squared of the pressure at a point, the same distance from the excitation point on the rail and at right angles to the line of travel. Using Eq. 2.31 in Eq. 2.33 we find

$$D(\phi, \omega) = \frac{1 + \left(\frac{K_\ell}{B_r k_r^4} \eta_f\right)^2}{\left(1 - \frac{k_o^4 \sin^4 \phi}{k_r^4}\right)^2 + \left(\frac{K_\ell}{B_r k_r^4} \eta_f\right)^2} \quad (2.34)$$

where

$$k_r^4 = \frac{K_\ell}{B_r} \left( \frac{\omega^2}{\omega_r^2} - 1 \right) \quad (2.35)$$

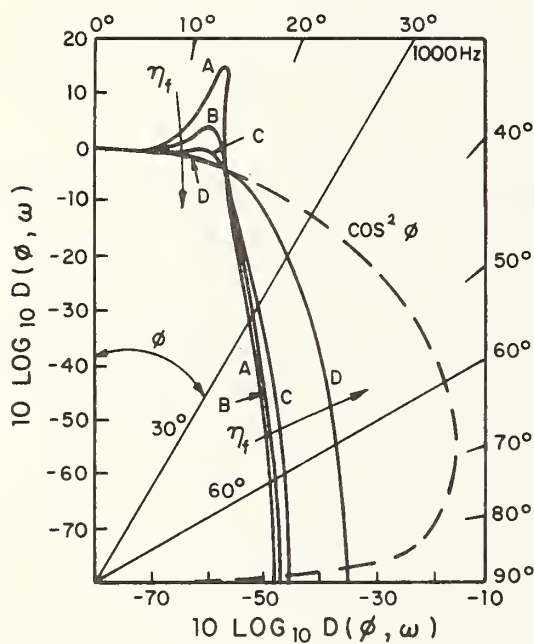
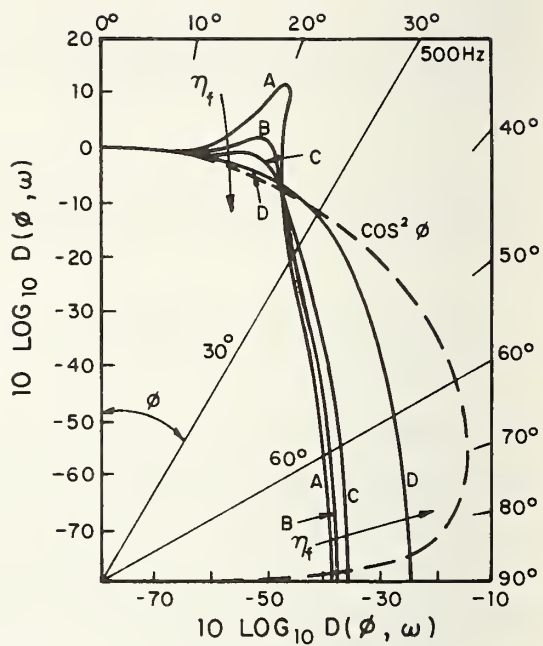
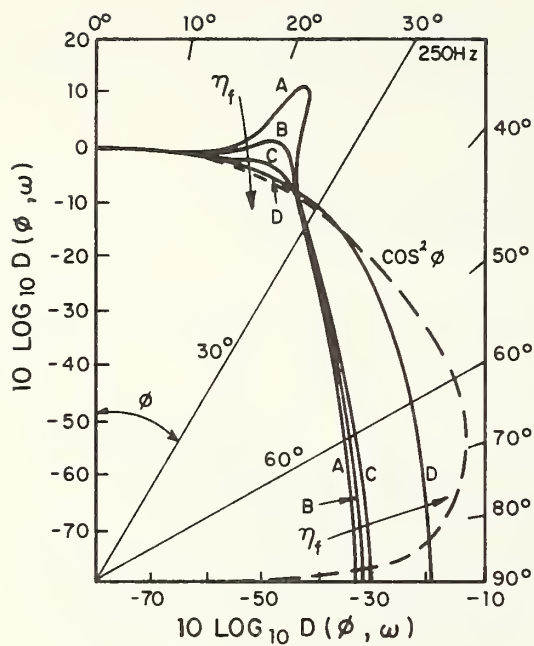
and  $\omega_r$  is the resonance of the rail on its fasteners,

$$\omega_r^2 = \frac{K_\ell}{m_r} \quad (2.36)$$

This directivity function is plotted in Fig. 2.6 with frequency and damping as parameters. The cosine-squared directivity is plotted for comparison. Notice that rail radiation can be quite directive, and that damping plays an important role. The direction of maximum intensity changes with frequency, since the rail is a dispersive medium.

Past data studies have shown that the wayside noise from rail vehicles on at-grade track is directive with the direction of maximum radiation being at right angles to the line of travel,  $\phi = 0$  [1]. Based on this observation, it was suggested that the noise radiation was predominantly from the wheels, which were expected to radiate as acoustic dipoles. Recent measurements have shown the wheels to be fairly omnidirectional radiators [4].

Based on the above work, we note that the radiation from the rail is also directive, with the direction of maximum radiation being frequency dependent. Although the past measurements of wayside noise have not been sufficiently detailed as to allow confirmation of the directivity patterns shown in Fig. 2.6, we suggest that the observed directivity in wayside noise may be due to the directivity of the noise radiated by the rail.



VALUES OF  $\eta_f$   
 $A=0.1, B=0.5, C=1.0, D=5.0$   
 $\eta_f$  IS THE DAMPING LOSS  
 FACTOR OF THE RAIL FASTENERS  
 RAIL / FASTENER RESONANCE  
 FREQUENCY,  $\omega_r = 1257$  (200Hz)  
 PLOTS ARE FOR AREA 115 RAIL

FIG. 2.6 DIRECTIVITY OF THE RAIL RADIATION

### 3. ELEVATED STRUCTURE NOISE

The elements of the elevated structure that contribute to the wayside noise are shown in Fig. 3.1. The most significant of these are the rail, the deck, longitudinal girder webs, and girder flanges. A description of these terms and of the different types of elevated structure will be given in Section 3.1. The columns of the elevated structure may be significant noise sources if they are steel plate. However, since their total surface area is much less than that of the structure spans, we can ignore the column radiation until the elevated structure noise is reduced approximately 10 dB(A) from a base condition of no noise control treatment.

This Section of the report is organized into four basic subsections. In Section 3.1 we describe the different types of elevated structure that will be considered. Section 3.2 discusses in general the possible methods of analysis. Then, in Sections 3.3 and 3.4 we describe the development of a model to predict the vibrational levels of the structure and the resulting noise radiation. In Section 4 we will describe the application of the prediction model for elevated structure noise to three actual structures.

#### 3.1 Classification of Elevated Structures

The type of structure used on an elevated transit right-of-way has a significant effect on the wayside noise levels. The most influential variables are the type of construction material and the method of track fastening. Variables that have great significance with regard to the basic design of the structure such as span length and design load have little direct influence on noise.

The elevated structures currently being used by transit properties in the United States were constructed over a time period



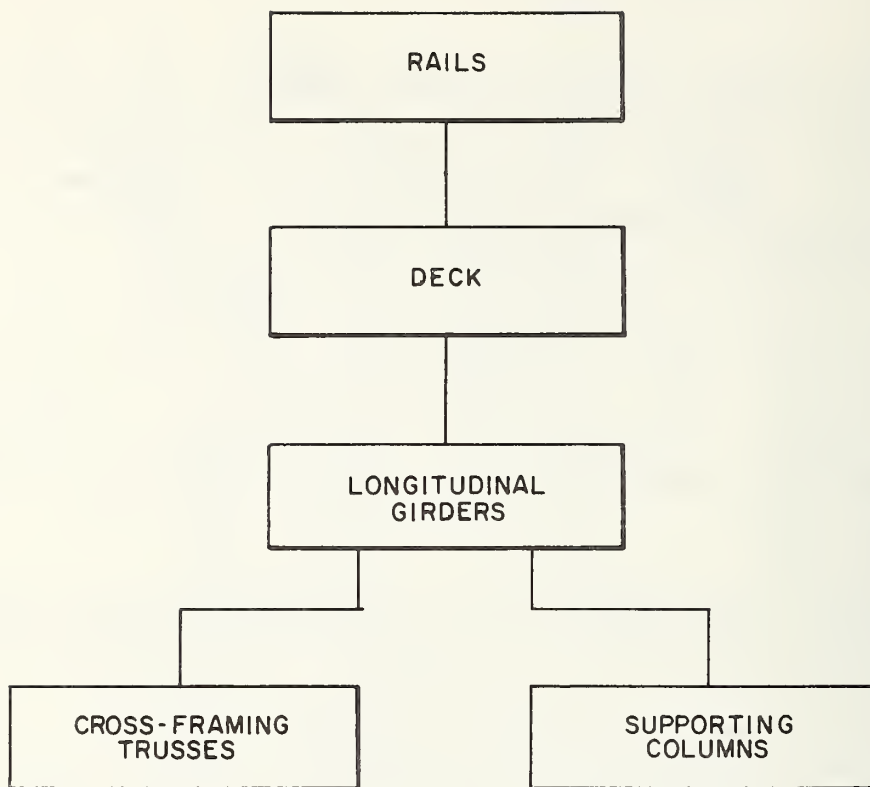


FIG. 3.1 ELEMENTS OF AN ELEVATED STRUCTURE  
CONTRIBUTING TO THE RADIATED NOISE

covering almost 100 years. Due to changes in technology, materials availability, and construction techniques during this period, the types of structure in use are quite varied. In this report we are concerned with the noise from all types of structure. The results are applicable both for the modification of older structures to reduce noise and for the design of new structures so that they generate less noise.

For the purposes of this study the following general classification of elevated structures has been helpful.

#### lattice-web girder, open deck

This type of structure is shown in Fig. 3.2. It consists of an open deck of wooden ties supported by two longitudinal girders. The girders are fabricated by bolting or riveting together a number of angle-section steel beams. The web of the girder is formed by a lattice of beams.

The ties in this type of structure are clamped to the top flange of each girder. The rails are fastened directly to the ties using tie plates and a variety of fastener designs. In typical cases the spacing between the girders is slightly greater than the track gauge so that the rails are approximately over the inside edges of the girder flanges.

The lattice-web, open deck structure has been used extensively in New York and Chicago. However, the method of construction required by this type of structure has been obsolete and uneconomical for many years. Our interest in these structures is therefore limited to methods by which existing structures can be modified to reduce noise.

The most significant feature of the lattice-web, open deck structure with regard to noise is its openness. By use of a lattice type of girder fabrication the noise radiating area is

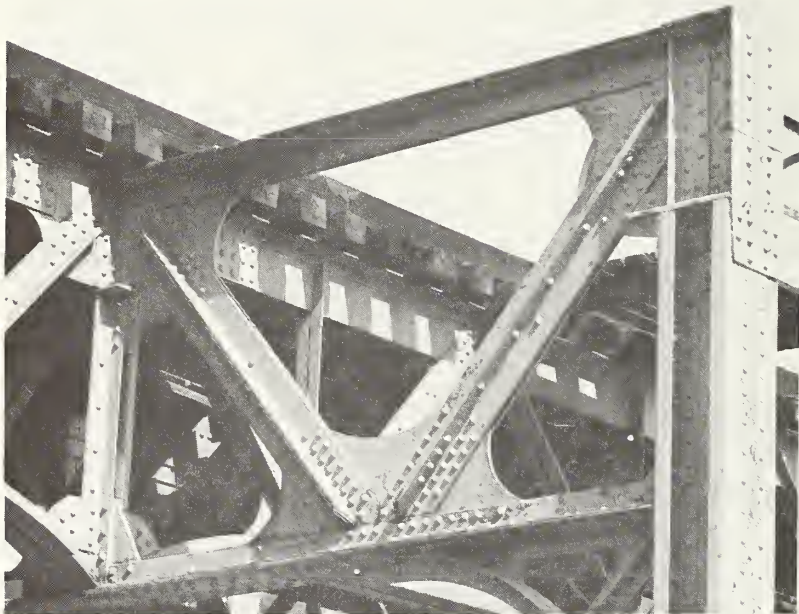
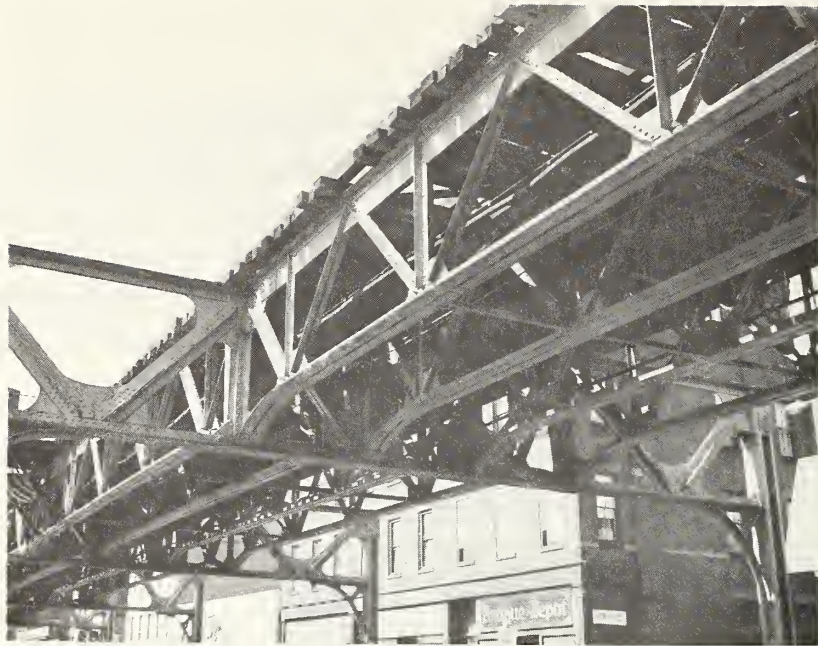


FIG. 3.2 TYPICAL LATTICE OR OPEN-WEB GIRDER, OPEN TIE  
DECK ELEVATED STRUCTURE

kept to a minimum. Also by use of riveted or bolted junctions the damping of the structure is increased to values well above those experienced in welded junctions. On the other hand, the openness of the structure provides no shielding for noise radiated by the rails, wheels, and other surfaces on the vehicle.

Wayside noise measurements indicate that the noise levels for this type of structure are approximately 10 dB(A) above levels for at-grade operation.\* The increase is most pronounced in the lower frequencies. However, because of the small radiating area the increase at very low frequencies, below 100 Hz, is not as great for this type of structure as for others described below.

#### plate-web girder, open deck

This type of structure is very similar to the lattice-web, open deck structure. The difference is in the construction of the girder webs. Instead of a lattice of angle-section beams, steel plates are used. In older structures of this type the girder flanges are formed by bolting or riveting angle-section beams to the web plates. In newer structures the girders are formed by welding the flanges to the web plate.

A typical plate-web, open deck structure is shown in Fig. 3.3. Although this type of structure is no longer used for new construction, we are interested in it because of the many miles of guideway that exist on this type of structure.

The most significant feature of the plate-web, open deck structure with regard to noise is the plate web. Vibrations of

---

\*Noise levels given in this Section are based on the limited amount of data that appears in the literature [1] and a few of the measurements that we have taken during the course of this study.





FIG. 3.3 TYPICAL PLATE-WEB GIRDER, OPEN TIE DECK  
ELEVATED STRUCTURE

the web are high and because of its large area it is an efficient radiator of noise. When the flanges are joined by bolts or rivets, the damping is greater than when the flanges are welded. For the bolted or riveted construction, the wayside noise levels are increased approximately 10 dB(A) above levels for at-grade operation due to radiation from the structure [1]. For welded construction, with its lower damping levels, the elevated structure noise levels can be expected to be even higher. In both cases the most significant increase is at the lower frequencies.

#### steel girder, concrete deck

The steel girder, concrete deck structure is commonly used in new construction. In this type of structure, a concrete deck is supported by steel girders in one of a number of different configurations as shown in Fig. 3.4. The rails are supported directly on the concrete deck by means of resilient rail fasteners.

In the newer constructions the girders are fabricated from welded plate. Because the damping with this type of fabrication is very low, the increase in wayside noise is again approximately 10 dB(A) above levels for at-grade operation [10].

#### concrete girder, concrete deck

This type of structure consists of a concrete deck supported by solid or hollow-section concrete girders. A number of different configurations are shown in Fig. 3.5. In all cases the rails are directly fastened to the deck using resilient rail fasteners.

The concrete girder, concrete deck structure has been extensively used for the BARTD system. Wayside noise measurements for this system show that the radiation from the structure causes a very small increase in noise relative to at-grade levels. A study of the data indicates that the noise level from structural



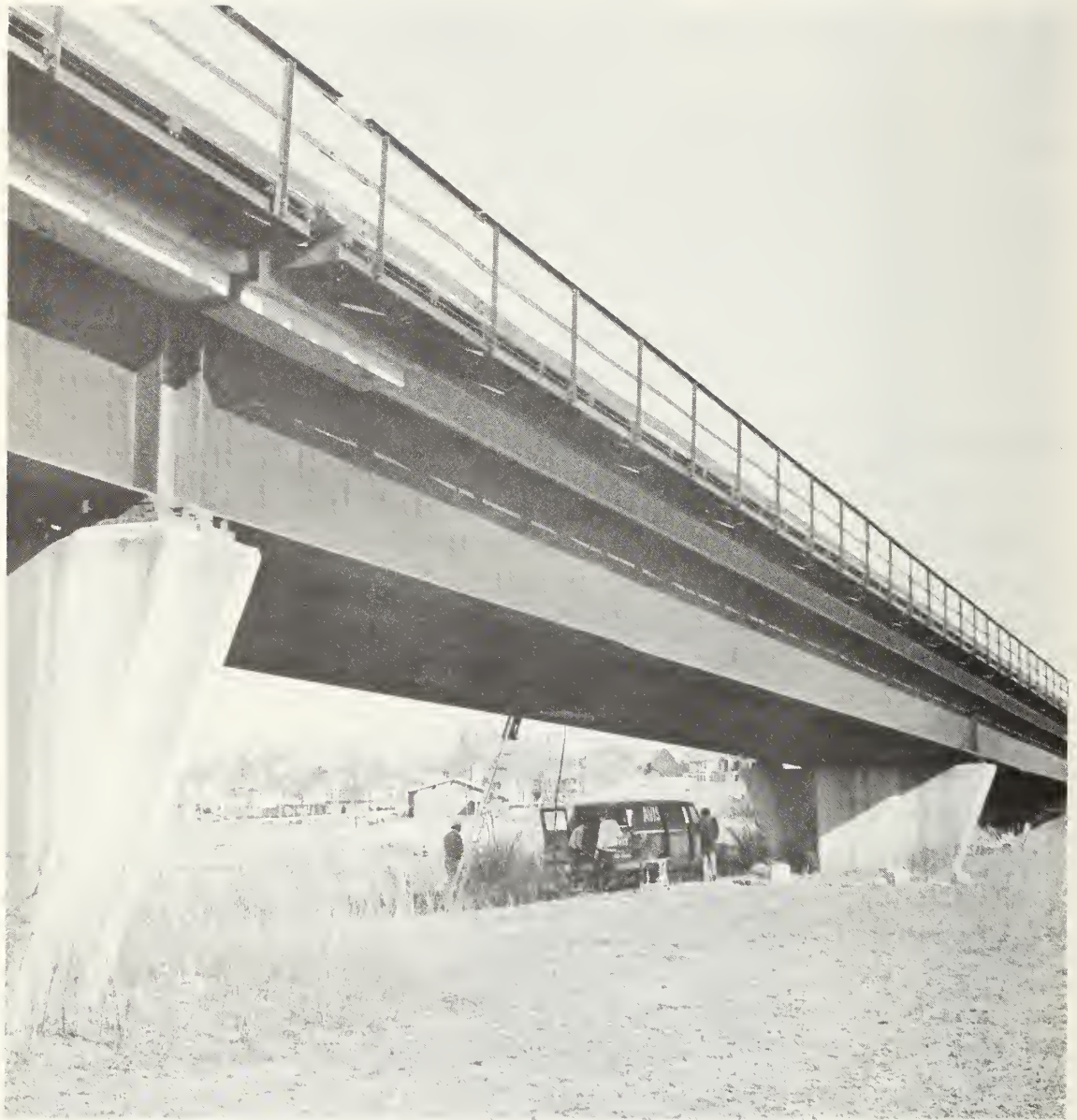


FIG. 3.4 TYPICAL STEEL PLATE-WEB GIRDER, CONCRETE SLAB  
DECK ELEVATED STRUCTURE



FIG. 3.5 CONCRETE ELEVATED STRUCTURES

radiation is 5 to 10 dB(A) below direct radiation from the rails, the wheels, and other vibrating surfaces of the train cars [1].

Because of the low level of structural radiation, it was possible in the BARTD system to reduce the wayside noise by using noise barriers extending up from the concrete deck.

All-concrete structures are markedly quieter than all-steel structures to which no noise control treatment has been added. Thus, in noise critical areas where elevated structures are to be used on a new system, it is common practice to specify that all concrete structures be used.

The most significant feature of the all-concrete structure is its weight. The high mass per unit surface area of the structure and the relatively high damping of concrete compared to steel explain the lower noise radiation of the concrete structure.

#### structures with ballasted track

On some elevated structures the track is laid on tie and ballast. Noise studies have indicated that when ballast track is used the increased noise due to radiation from the structure is small. This conclusion has been found to be true both for all-steel supporting structures and for concrete structures.

Use of ballasted track is one method of noise control for elevated structures. However, it is impractical for existing structures because of the very large increase in the loading of the structure.

In this report we give little attention to structures with ballasted track since the elevated structure noise should not be a problem.\*

---

\* Noise from the rails and the car itself may, however, be a problem in some cases.



## other types of structures

Many other types of elevated structures exist on transit systems in the U.S. However, the number of miles of right-of-way on these structure types is small compared to that of the five types described above.

### 3.2 Methods of Analysis

Prediction of the vibration and noise radiation for the types of structure introduced in the previous Section is difficult because of the complexity of the structures and the large frequency range of interest (50 to 5,000 Hz). Several prediction techniques have been considered. We have selected a type of Statistical Energy Analysis (SEA) in our development of a general prediction model because of fundamental limitations in the other techniques.

#### 3.2.1 Review of the Different Methods

Classical normal mode analysis requires that the vibrations of the track structure be described in terms of the response of the different modes of vibration. Typically, the mode shapes and resonance frequencies are calculated for the undamped system. Modal damping loss factors are then applied in an ad-hoc fashion. When damping is included in the calculation of mode shapes, the shapes can become frequency dependent unless the damping is uniformly distributed throughout the structure. The complexity of the analysis is greatly increased for frequency dependent mode shapes.

The classical normal mode analysis is not generally useful for track structures. Many reasons can be given. First, the number of modes participating in the vibration of a typical section of track structure or elevated structure span is so large that even

new computer techniques cannot handle the problem over the complete frequency-range of interest. Second, the modes of adjacent track sections are coupled so that the vibration is transmitted from one section to the next. And third, the damping is not uniformly distributed throughout the structure so that the mode shapes are frequency dependent. Practical problems also exist. The accuracy with which parameters describing the structure and its boundary conditions is not sufficient to allow an accurate determination of mode shapes and resonance frequencies beyond the first few modes of the structure.

Finite element techniques are potentially useful for the analysis of track structures, but have been ruled out because of the large number of elements required to determine the vibration over the complete frequency range of interest. For example, in the analysis of noise radiation from elevated steel structures, the spacing of the elements on the webs of the supporting girders must be less than one-half of the bending wavelength at the highest frequency of interest. Field data indicate significant noise radiation from a structure with one-half inch thick webs at frequencies up to 1000 Hz. For this case the finite element spacing must be less than 8 inches so that approximately 750 elements are required to study the vibration of just one web on a typical 80 ft long span.

Many of the limitations of the normal mode approach can be eliminated by allowing the modes to be coupled. The procedure is to divide the complete track structure into its individual structural elements: e.g. for the case of an elevated structure: rail and fasteners, track slab or ties, supporting girders, and supporting columns. The mode shapes and resonance frequencies of each element are then found. Boundary conditions are required to calculate the mode shapes and resonance frequencies are obtained by assuming the vibration of all other structural elements to be zero. The modes of the individual structural elements are used in the

equations of motion for the complete structure to obtain a series of coupled equations in the modal amplitudes. The physical interpretation is that the complete structure is represented by a set of coupled single-degree-of-freedom oscillators.

The methods used to analyze the coupled oscillator set depends on the strength of the coupling. For very light coupling, the calculations can be cascaded. First, the response of each oscillator that is directly excited by external forces is calculated. Then, this calculated response is used as an input to determine the excitation forces on indirectly excited oscillators. In studying track structure vibration, the cascading approach is equivalent to the assumption that the rail vibration is unaffected by the track structure under the rail fasteners. For example, to study the vibration transmitted to an elevated structure one would calculate the rail response assuming the deck to be motionless; use the calculated rail vibration to determine forces acting through the rail fastener onto the deck; calculate the deck response to these forces assuming the supporting girders to be motionless; use the calculated deck vibration to determine forces and moments acting on the girders; and finally, calculate the girder vibration.

When the coupling between oscillators representing the complete structure is moderately large, the effect is to cause a small shift in resonance frequencies and a large increase in the effective damping due to energy transmission between oscillators. In this case the cascade approach cannot be used. However, when the excitation is a broadband random process, a technique referred to as Statistical Energy Analysis can be used [11]. In this technique the interaction between oscillators is studied in terms of time-average power and energy variables. At high frequencies, where each structural element has many modes with resonances in each octave band of frequencies, the exact mode shapes and resonance frequencies are replaced by statistical averages — the averages



being taken over structures that are generally similar but not identical. At low frequencies, the exact values for mode shapes and resonance frequencies are used to calculate the energy-flow between each pair of oscillators.

When the coupling between oscillators is very large, the shift in resonance frequencies becomes large. It has been shown that Statistical Energy Analysis can be used to study the vibrations of a single pair of strongly-coupled oscillators [12]. However, the use of SEA when there are many strongly coupled oscillators is questionable. Unfortunately, there is no satisfactory technique for studying strongly coupled oscillators. The best approach in this case is to redefine the structural components so that the representative oscillators are no longer strongly coupled.

Statistical Energy Analysis can be used both when the coupling is moderately strong and when it is weak. However, a basic assumption in past uses of SEA has been that the response of each structural component be described in terms of the resonant response of each mode of the component. This assumption is generally not met in track structures.

The length of a typical track segment is sufficiently long that the vibration of each structural element is best described in terms of vibrational waves travelling away from the excitation points at each wheel location. As the waves propagate away from the excitation points, their amplitude is changed because of energy dissipation due to damping and because of energy flow between waves in the different structural elements.

As in the case of normal mode analysis, a classical travelling-wave analysis cannot be used because the different waves in the structure are coupled. What must be done in studying the vibrations of track structures is to extend the chaining procedure and Statistical Energy Analysis so that they can be used to predict

the response and interaction of travelling waves in coupled structures.

Many aspects of the required extensions, which will be described in the following Sections, represent new work. Therefore, in developing a complete and reliable prediction model for track vibration and noise radiation, we will make frequent use of the field data that we have obtained on three Boston MBTA elevated structures.

### 3.2.2 General Formulation of Coupled Oscillator Equations

In general we model the track structure as an assemblage of beam and plate elements that are infinite and homogeneous along the track direction (the x-axis). For example, two plate elements, "a" and "b", may be visualized in cross-section as shown in Fig. 3.6. In the development of this Section we consider for sake of example the interaction of only two members vibrating in flexure. The analysis can be extended to any number of interacting elements vibrating both in flexure and in-plane.

We shall find it convenient to define for each element a local coordinate along the cross-sectional length, call it  $y$ . Mostly, we deal with the space and time Fourier transforms of response, defined for structure "a" by

$$\tilde{u}_a(k_x, y, t) = \int dx e^{ik_x x} u_a(x, y, t) \quad (3.1a)$$

$$U_a(x, y, \omega) = \int dt e^{-i\omega t} u_a(x, y, t) \quad (3.1b)$$

$$\hat{U}_a(k_x, y, \omega) = \int dt e^{-i\omega t} \tilde{u}_a(k_x, y, t) \quad (3.1c)$$

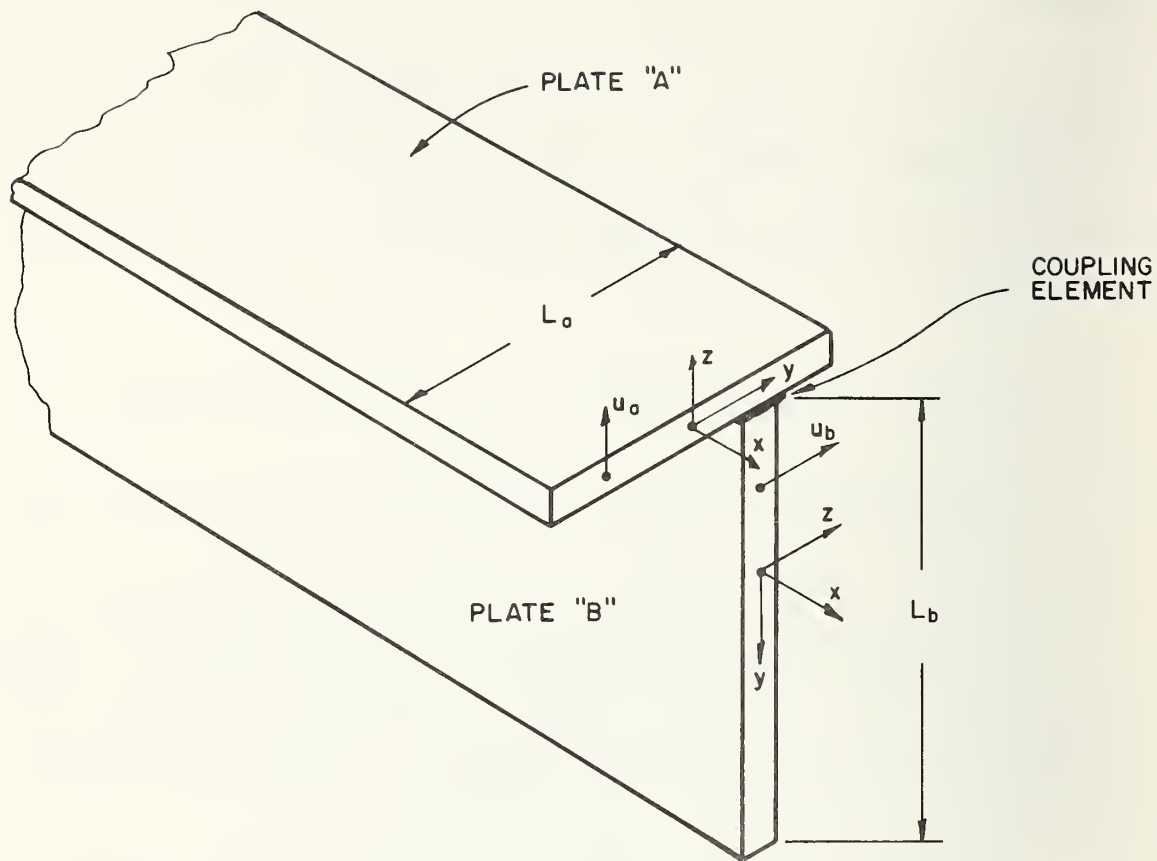


FIG 3.6 TWO CONNECTED PLATE STRUCTURES

where  $u_a(x,y,t)$  is the displacement of structure a at a point  $x,y$  at time  $t$ ,  $k_x$  is the wavenumber in the  $x$  direction, and  $\omega$  is the radian frequency. Note that  $\tilde{u}_a$ ,  $U_a$ , and  $\hat{U}_a$  are all complex numbers with real and imaginary parts.

The transform of the response of each structural element may be decomposed into a sum of eigenfunction amplitudes, i.e.

$$\tilde{u}_a(k_x, y, t) = \sum_{n=1}^{\infty} \tilde{u}_{an}(k_x, t) \psi_{an}(k_x, y) \quad (3.2a)$$

$$\tilde{u}_b(k_x, y, t) = \sum_{n=1}^{\infty} \tilde{u}_{bn}(k_x, t) \psi_{bn}(k_x, y) \quad (3.2b)$$

where the  $\psi_{an}(k_x, y)$  are appropriately chosen cross-wise eigenfunctions for structure "a" and  $\psi_{bn}(k_x, y)$  are the eigenfunctions for structure "b". These are to be defined such that the square of their norm equals the cross-sectional length, i.e.

$$\int_{-L_a/2}^{L_a/2} \psi_{an} \psi_{am} dy = L_a \delta_{mn} \quad (3.3a)$$

$$\int_{-L_b/2}^{L_b/2} \psi_{bn} \psi_{bm} dy = L_b \delta_{mn} \quad (3.3b)$$

where  $\delta_{mn} = 1$  if  $m = n$  and is zero otherwise. In the case of beam structures (with zero cross-sectional length)  $\psi_{an}$  or  $\psi_{bn}$  is to be taken to equal to one.

The  $\tilde{u}_{an}$ 's may be termed the modal coordinates of structure a. They represent the time varying part of the transform of the structural response at a particular  $k_x$ . The eigenfunctions,  $\psi_{an}$  and  $\psi_{bn}$ , represent the spatial variation in y of the  $n^{\text{th}}$  cross-wise mode. In general, the eigenfunctions are functions of both y and  $k_x$  [13].

Using the orthogonality of the eigenfunctions and the definition of their norm, the equations of motion can be recast into a set of coupled ordinary differential equations for the modal coordinates,

$$m_a \ddot{\tilde{u}}_{an} + C_{an} \dot{\tilde{u}}_{an} + K_{an} \tilde{u}_{an} - \sum_{m=1}^{\infty} \beta_{n,m} \tilde{u}_{bm} = \tilde{f}_{an}(k_x, t) \quad (3.4a)$$

$$m_b \ddot{\tilde{u}}_{bn} + C_{bn} \dot{\tilde{u}}_{bn} + K_{bn} \tilde{u}_{bn} - \sum_{m=1}^{\infty} \beta_{m,n} \tilde{u}_{am} = \tilde{f}_{bn}(k_x, t) \quad (3.4b)$$

$$(n = 1, 2, \dots)$$

where  $m_a$ ,  $m_b$  are the masses per unit length (along x) of structures "a" and "b";  $C_{an}$ ,  $C_{bn}$  are the damping coefficients;  $K_{an}$ ,  $K_{bn}$  are the stiffness coefficients, and  $\beta_{n,m}$  is the coupling coefficient. All coefficients can be functions of wavenumber,  $k_x$ .

Equations 3.4 describe a system of coupled oscillators. This analogy will prove particularly useful when we consider response calculations, since we can use many of the ideas of Statistical Energy Analysis.

### 3.2.3 The Integrated Spectrum

In practice the solution of Eqs. 3.4 can be carried out when only a few modes participate in the response. The solution is difficult to find for even simple track structures in the frequency

range of interest because of the large number of cross-wise modes contributing to the response. Our approach and the key to the prediction procedure developed in this report is to describe the response in terms of the integrated spectrum, which is related to the total vibratory energy in the structure.

By definition the integrated displacement response spectrum for a two-dimensional structure,  $I_u(\omega)$ , is given by

$$I_u(\omega) = \int_{-L_y/2}^{L_y/2} dy \int_{-\infty}^{\infty} dx S_u(x,y,\omega) \quad (3.5)$$

where  $L_y$  is the width of the structure in the y direction,  $S_u(x,y,\omega)$  is the spectrum of the response, u, at point x,y on the structure. The spectrum  $S_u(x,y,\omega)$  can also be written in terms of the Fourier transform of the response  $u(x,y,t)$  as

$$S_u(x,y,\omega) = \frac{1}{2} |U(x,y,\omega)|^2, \quad (3.6)$$

By expanding the response into its modal coordinates  $\tilde{u}_n$  and using the Fourier transform relationships we find

$$U(x,y,\omega) = \frac{1}{2\pi} \sum_{n=1}^{\infty} \int_{-\infty}^{\infty} dk_x e^{-ik_x x} \hat{U}_n(k_x,\omega) \psi_n(k_x,y) \quad (3.7)$$

where  $\hat{U}_n$  is the Fourier transform in time of the  $n^{\text{th}}$  modal coordinate transform  $\tilde{u}_n$ . Combining Eqs. 3.5, 3.6, and 3.7 we find

$$I_u(\omega) = \frac{L_y}{2\pi} \sum_{n=1}^{\infty} \int_{-\infty}^{\infty} dk_x S_{u_n}(k_x,\omega) \quad (3.8)$$



where  $S_{u_n}$  is the spectrum of the response of the  $n^{\text{th}}$  oscillator, which is given by

$$S_{u_n}(k_x, \omega) = \frac{1}{2} |\hat{U}_n(k_x, \omega)|^2. \quad (3.9)$$

The Eqs. 3.8 and 3.9 will be used extensively in the remaining Sections of this report. Use of the integrated spectrum limits our ability to predict in detail the vibration at different points on a track structure. We will show, however, that the noise radiation from elevated structures can be adequately defined in terms of the integrated spectrum. We will also show that a general prediction procedure based on the integrated spectrum can be used to investigate the effectiveness of various noise and vibration control treatments.

#### 3.2.4 Characterization of the Excitation

The analytical model developed in this Section treats the excitation due to the wheel/rail interaction as a series of point forces at the wheel/rail contact points. Two mechanisms of force generation are considered: roar\* due to the random roughness of the wheel and rail surfaces and impact due to the crossing of rail joints, and impact due to wheel flats. Squeal mechanisms will not be considered. The forces associated with roar will be taken as continuously-fluctuating random point forces with the forces generated by different wheels being uncorrelated. Because the forces are uncorrelated we can calculate the total integrated spectrum as a sum of the integrated spectra due to each wheel, i.e.

$$I_u^{\text{roar}}(\omega) = \sum_i I_u^{(i)}(\omega) \quad (3.10)$$

---

\*See Section 2.1 for a definition of terms.

where  $I_u^{(i)}$  is the integrated spectrum due to forces generated by wheel  $i$  and the summation is over all wheels. The motion of the transit vehicle is important in determining the level of the fluctuating forces under each wheel and the shape of the force spectrum. However, once the forces have been determined the motion of the vehicle can be neglected in calculating the integrated spectrum of response, since the vehicle speed is much less than the phase velocity of the different cross modes of the track structure. By ignoring the vehicle motion we eliminate the Doppler shift in the vibration frequencies. The shift in frequencies is much less than an octave over most of the frequency range of interest so that it is not important in our general prediction.

The forces due to impact at rail joints and due to wheel flats occur as a series of impulsive events with one event occurring each time a wheel crosses a joint or for each wheel revolution. However, if we select a sufficiently long averaging time the series of impulsive forces can be replaced by a number of equivalent continuously fluctuating forces which have the same spectrum. Furthermore, if we limit our attention to the integrated spectrum, we can neglect the distinction between forces that move along with the wheel and forces that occur at the fixed location of each rail joint.

In the remaining Sections of this report we will assume that the integrated spectrum of the rail vibration under each wheel is known either from measurement or empirical prediction.\* With this assumption we do not need to identify the specific excitation mechanism.

---

\*See Section 2.

### 3.2.5 Application of Statistical Energy Analysis

To use Statistical Energy Analysis (SEA) we study the time-average vibratory power balance for each oscillator in the set described by Eqs. 3.4. For the  $n^{\text{th}}$  mode of a particular structure "a", we balance the power input from external forces,  $W_{an}^{(\text{in})}$ , with the power dissipated,  $W_{an}$ , and the net power transmitted to other modes in structure a and to other directly or indirectly connected structures,  $\sum_m W_{an,m}$ ,

$$W_{an}^{(\text{in})} = W_{an} + \sum_m W_{an,m} \quad (3.11)$$

The power dissipated and the power transmitted between modes are then expressed in terms of modal energies,

$$W_{an} = \phi_{an} T_{an} \quad (3.12)$$

and

$$W_{an,m} = \phi_{an,m} [T_{an} - T_m] \quad (3.13)$$

where  $T_{an}$  and  $T_m$  are the time average energies of the  $n^{\text{th}}$  mode in structure a and the  $m^{\text{th}}$  mode respectively,  $\phi_{an}$  is a modal damping coefficient, and  $\phi_{an,m}$  is a modal coupling coefficient.

Equations 3.11, 3.12 and 3.13 form a set of linear algebraic equations which can theoretically be solved for the modal energy of each mode in terms of the power input from external sources. It is common practice, however, to make simplifying assumptions. The validity of the assumptions has been generally supported by comparison of predicted vibration levels with data from laboratory experiments and field tests.

Many past applications of SEA have used assumptions that are valid only when there are many resonance frequencies in each narrow band of frequencies, e.g. a high modal density. The density of cross-mode resonances for elements of a typical elevated structure is not large. In general, for any given wavenumber,  $k_x$ , the separation between adjacent resonance frequencies is large compared to the damping bandwidth,  $\omega_{n,d}$ . In this case we can neglect the coupling between modes of the same structure with little error. Furthermore, in studying the interaction between the  $n^{\text{th}}$  mode of structure a and the modes of structure b we need consider only the interaction with that mode in structure b whose resonance frequency is closest to the resonance frequency of the  $n^{\text{th}}$  mode in structure a. These assumptions greatly simplify the power balance equations and allow a straightforward solution for the modal energies.

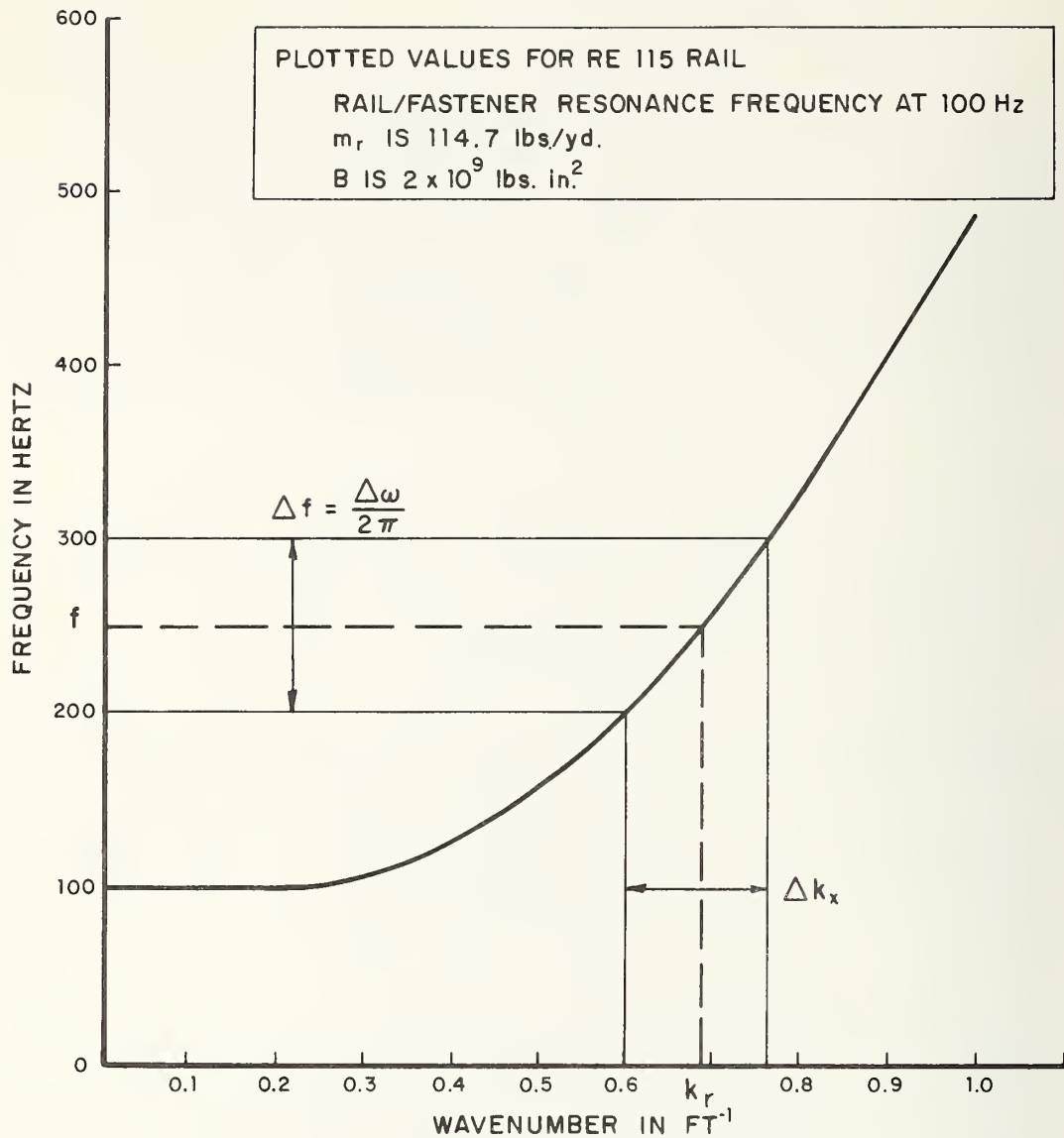
In applying S.E.A. to rail structures we can take advantage of the fact that the rail is a one-dimensional wave-bearing structure. For each value of wavenumber,  $k_x$ , the rail has a single cross-mode with a resonance frequency,  $\omega_{r1}$ , given by the dispersion relation for freely propagating waves in the rail,

$$\omega_{r1}^2 = \frac{B_r}{m_r} k_x^4 + \omega_r^2 \quad (3.14)$$

where  $B_r$  is the bending stiffness of the rail,  $m_r$  is the mass per unit length of the rail, and  $\omega_r$  is the resonance of the rail on its resilient fasteners.\* The dispersion relation is plotted for a typical rail in Fig. 3.7.

---

\* Interpretation of the meaning of  $\omega_r$  when the rail is fastened directly to a wood tie deck will be given in Section 3.3.2.



$f$  BAND CENTER FREQUENCY  
 $k_r$  FREE BENDINGWAVE NUMBER FOR FREQUENCY  $f$

FIG. 3.7 RAIL DISPERSION CURVE

If we consider the vibration in a band of frequencies  $\Delta\omega$ , the rail will have one cross-mode resonance frequency within  $\Delta\omega$  when  $k_x$  is in the range  $\Delta k_x$  and none otherwise, where  $\Delta k_x$  is obtained from the dispersion relation as shown in Fig. 3.7.

In studying the interaction of the rail with other components of the elevated structure, we need consider only those cross-modes whose resonance frequencies for values of  $k_x$  in the range  $\Delta k_x$  are in the range  $\Delta\omega$ . Furthermore, since the resonance frequencies of the cross-modes are well separated for typical elevated structure components, we need consider for each value of  $k_x$  in the range  $\Delta k_x$  only a single cross-mode for each component: the one having a resonance frequency nearest the resonance frequency of the rail cross-mode. If the frequency band  $\Delta\omega$  is narrow, say an octave or less, the interaction between the rail and other components can be studied in terms of the cross-modes for  $k_x$  equal to  $k_r$ , where from the dispersion relation,

$$\frac{B_r}{m_r} k_r^4 = \omega^2 - \omega_r^2 \quad (3.15)$$

and  $\omega$  is the center frequency of the band  $\Delta\omega$ .

As an example, we consider the interaction between two structures - a rail on resilient fasteners and a concrete slab deck. For each frequency band the time-average power exchange between the rail and the deck can be given in terms of a difference in modal energies,

$$W_{r,d} = \omega \eta_{r,d} (T_r - T_d) \quad (3.16)$$

where  $\omega$  is the band center frequency,  $T_r$  is the time-average modal energy of the rail,  $T_d$  is the time-average energy of that cross-mode in the deck for  $k_x$  equal  $k_r$  which has a resonance frequency nearest to  $\omega$ , and  $\eta_{r,d}$  signifies the coupling loss



factor between the rail mode and the deck mode with the nearest resonance frequency. The power exchange between modes has been written in terms of a coupling loss factor rather than a coupling coefficient to agree with the conventionally used notation. Since we are considering a band of frequencies,  $\Delta\omega$ , the relationship between these two factors is simply  $\omega\eta_{r,d} = \phi_{r,d}$ . By balancing the power transmitted from the rail to the deck,  $W_{r,d}$ , with the power dissipated in the deck due to damping,  $W_d$ , we find a relationship between the modal energies in the deck and in the rail,

$$\frac{T_d}{T_r} = \frac{\eta_{r,d}}{\eta_{r,d} + \eta_d} \quad (3.17)$$

where  $\eta_d$  is the damping loss factor for the deck. As a final step we must relate the modal energies to the vibratory velocity levels. In the general case, the modal energies are functions of frequency,  $\omega$ , and wavenumber,  $k_x$ . To find the integrated velocity spectrum for a particular structural component we use Eqs. 3.8 and 3.9 to find

$$I_V(\omega) = \frac{L_y}{2\pi} \int_{-\infty}^{\infty} dk_x \sum_n \frac{1}{2} |\hat{v}_n(k_x, \omega)|^2 \quad (3.18)$$

where the summation is over all modes of the structure. The average integrated velocity spectrum over a frequency band,  $\Delta\omega$ , is obtained by integrating the spectrum over the band and dividing by bandwidth,

$$\bar{I}_V(\omega) = \frac{1}{\Delta\omega} \int_{\Delta\omega} d\omega I_V(\omega) \quad (3.19)$$

where  $\bar{I}_v(\omega)$  signifies the average integrated velocity spectrum. Using Eq. 3.19 in Eq. 3.18 and rearranging order of integration we find

$$\bar{I}_v(\omega) = \frac{L_y}{2\pi} \int_{-\infty}^{\infty} dk_x \sum_n \frac{1}{\Delta\omega} \int_{\Delta\omega} d\omega \frac{1}{2} |\hat{v}_n(k_x, \omega)|^2 \quad (3.20)$$

If we limit the summation for each value of  $k_x$  to modes with resonance frequencies within the band  $\Delta\omega$  and if we assume the bandwidth  $\Delta\omega$  to be large compared to the damping bandwidth  $\omega \eta_n$ , the limits of integration over  $\omega$  can be replaced by infinite limits with only a small error. Eq. 3.20 can then be written

$$\bar{I}_v(\omega) = \frac{L_y}{4\pi^2} \int_{-\infty}^{\infty} dk_x \frac{1}{\Delta\omega} \sum_n \langle |\tilde{v}_n(k_x, t)|^2 \rangle_t \quad (3.21)$$

where  $\langle |\tilde{v}_n(k_x, t)|^2 \rangle_t$  is the mean-square velocity of the  $n^{\text{th}}$  mode, which is simply related to the modal kinetic energy. If we take the time average kinetic and potential energies of the resonant vibration to be equal, the average integrated velocity spectrum for structure a can be related to the total (kinetic plus potential) modal energy by

$$\bar{I}_{v_a}(\omega) = \frac{L_a}{4\pi^2 m_a} \int_{-\infty}^{\infty} dk_x \frac{1}{\Delta\omega} \sum_n T_{an}(k_x, \omega) \quad (3.22)$$

where for each value of  $k_x$  the summation is over all modes with resonance frequencies in the band  $\Delta\omega$ .

In accordance with the discussion earlier in this Section we can limit the summation to one mode. Furthermore, the modal energy in other structural elements is nonzero only in the range of wavenumbers  $\Delta k_x$  as shown in Fig. 3.7. Thus, if the band  $\Delta\omega$  is narrow we can write Eq. 3.22 as

$$\bar{I}_{v_a}(\omega) = \frac{L_a}{4\pi^2 m_a} \frac{\partial k_r}{\partial \omega} T_a(k_r, \omega) \quad (3.23)$$

where  $k_r$  is given by Eq. 3.15.

Use of Eq. 3.23 allows us to use the modal energies obtained from S.E.A. in calculating the integrated velocity spectrum for each component of the elevated structure. For the example cited earlier in this Section we use Eq. 3.23 in Eq. 3.17 to find

$$\frac{\bar{I}_{v_d}(\omega)}{\bar{I}_{v_r}(\omega)} = \frac{L_d m_r}{m_d} \frac{\eta_{r,d}}{\eta_{r,d} + \eta_d} \quad (3.24)$$

where  $L_d$  is the width of the deck,  $m_r$  is the mass per unit length of the rail, and  $m_d$  is the mass per unit length of the deck. Further applications of S.E.A. and calculations of the loss factors will be given in the next Section.

### 3.3 Analysis of the Response of Idealized Rail Structures

In the following Sections, we present analyses of various idealized structures representative of those commonly appearing in practice. The basic approach is as outlined in Section 3.2. All structures are considered to be infinite and homogeneous along the track direction. Since the response of rails during a train passage has already been fully discussed, it will be assumed that the rail vibration is known. Major emphasis will be placed on predicting the response of those structural elements that contribute most to the acoustic radiation.

### 3.3.1 Concrete Deck on Steel Plate Girders

The geometry and nomenclature of this idealized structure are as shown in Fig. 3.8. It is meant to represent the type of structure shown in Fig. 3.4. The rails are mounted on resilient fasteners to a concrete slab deck which is typically 1 ft thick and 8 to 10 ft wide. The deck is supported by two steel I-beams consisting of a plate web approximately 1/2 in. thick and steel flanges. In addition to these main elements there are often vertical stiffeners placed periodically on the I-beam web. Also, there are usually truss members connecting the two longitudinal I-beam girders. Often, as indicated in Fig. 3.8 the rails are mounted directly over the I-beams.

To apply S.E.A. we divide the structure into the following elements:

1. rail and fasteners (denoted by subscript "r")
2. concrete slab deck (subscript "s")
3. I-beam girders (subscript "g")
4. additional truss members (subscript "t").

The rail and fasteners are idealized by a Bernoulli-Euler beam on an elastic foundation, while the slab deck can be modeled as a Bernoulli-Euler plate. The motions of the I-beam web is modeled by a Bernoulli-Euler plate.

We must now decide what dynamical interactions exist among the above elements. Of greatest importance is the rate of vibratory energy flow from the rails to the deck and girders. The situation is shown in Fig. 3.9, where  $F_r$  is the force amplitude on the deck due to the rail vibration and  $V_s$  is the resulting deck velocity.

The forces under the rail transmit power to the deck and to the girders. The ratio of the power transmitted to these two structures is equal to the ratio of the magnitudes of their input

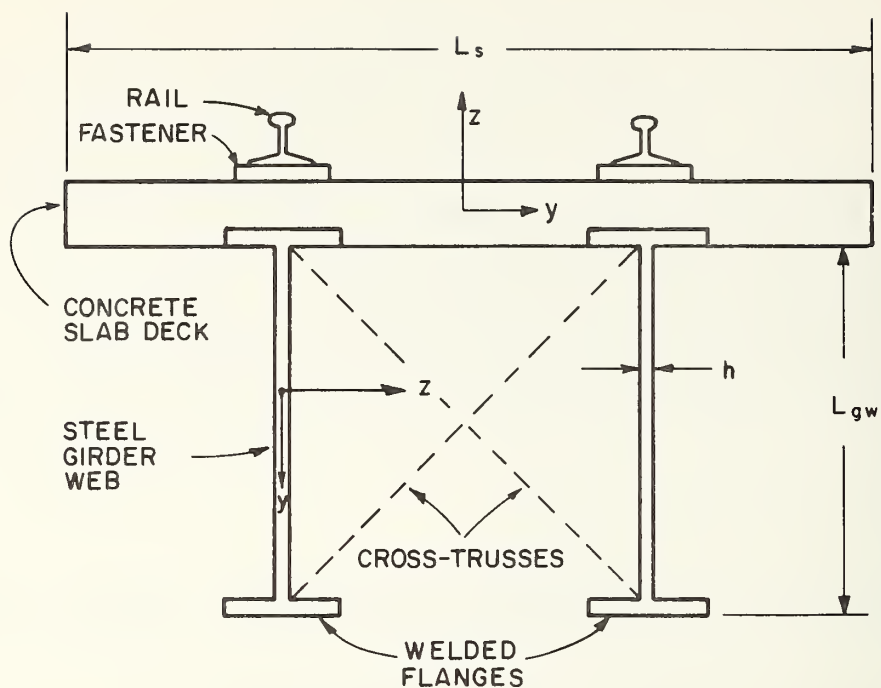
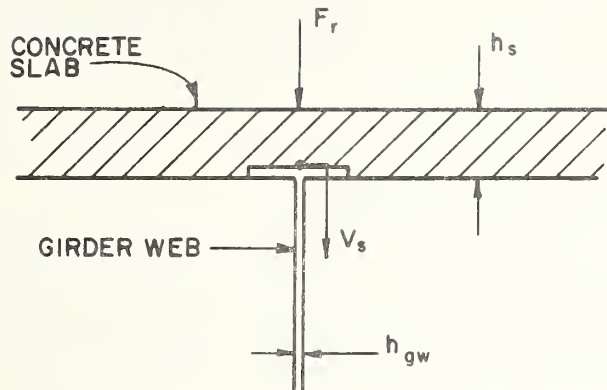


FIG. 3.8 IDEALIZED MODEL OF AN ELEVATED STRUCTURE WITH A CONCRETE DECK ON STEEL-PLATE GIRDERS



TYPICAL PARAMETER VALUES	
SURFACE DENSITIES	
$\rho_s$	$= 3.5 \text{ SLUG / FT.}^2$
$\rho_{gw}$	$= 0.776 \text{ SLUG / FT.}^2$
BENDING STIFFNESSES	
$D_s$	$= 1.77 \times 10^7 \text{ LB. FT.}$
$D_{gw}$	$= 5.08 \times 10^4 \text{ LB. FT.}$
THICKNESSES	
$h_s$	$= 9 \text{ IN.}$
$h_{gw}$	$= 0.625 \text{ IN.}$

FIG.3.9 FORCE AND VELOCITY CONVENTIONS USED  
IN THE CALCULATION OF SLAB AND WEB IMPEDANCES



impedances. The impedance of the deck averaged over bands of frequency containing several cross-mode resonances is equal to the line impedance of an infinite plate, [11]

$$|Z_s| = |Z_{s,inf}| = 2\sqrt{2} \rho_s \sqrt{\omega \kappa_s c_{l,s}} \quad (3.25a)$$

where  $\rho_s$  is the surface density of the deck material,  $h_s$  is the thickness of the deck,  $\kappa_s = h_s/\sqrt{12}$  is the radius of the gyration for the deck, and  $c_{l,s}$  is the longitudinal wavespeed in the deck material. For a typical concrete deck one ft thick with  $\rho_s = 150 \text{ lbs/ft}^2$ , and  $c_{l,s} = 9,800 \text{ ft/sec}$ ,

$$|Z_s| \approx 700 \sqrt{\omega} \frac{\text{lb sec}}{\text{ft}} \quad (3.25b)$$

The frequency average impedance of a typical girder to forces in line with the plane of the web is given by the impedance of a semi-infinite plate; i.e., a semi-infinite web plate,

$$|Z_u| = |Z_{u,inf}| = \rho_{gw} c_{l,gw} \approx 13,500 \frac{\text{lb sec}}{\text{ft}} \quad (3.26)$$

where  $\rho_{gw}$  is the surface density of the girder web and  $c_{l,gw}$  is the longitudinal wavespeed in the girder web material, 17,000 ft/sec for steel. For frequencies above 60 Hz the average impedance of the deck is greater than that of the girder so that power transmitted to the deck is much greater than that transmitted to the girder. Hence, the rail can be assumed to be coupled only to the deck. The dominant path of energy transmission is from the rails to the deck to the girders.

The vertical forces acting on the web plate excite vibratory deformations of the web-plate that are in the plane of the plate; i.e., longitudinal wave motion. On the other hand, moments acting on the web plate excite deformations that are normal to the plane of the plate in the form of bending wave motion.

Normally, in an analysis of noise radiation the in-plane longitudinal vibration is neglect since the acoustic radiation from this type of vibration is negligible. However, in the present case, we recognize that in-plane vibration is coupled to the bending vibration, which does cause significant acoustic radiation, by the trusses. Therefore, in setting up the SEA equations we distinguish between longitudinal web motion, denoted by "u", and bending motion of the web, denoted "w".

With the above preface, the structural interactions may be diagrammed as in Fig. 3.10. All parameters shown are functions of wavenumber,  $k_x$ . However, as discussed in Section 3.2.5, we set  $k_x$  equal to the wavenumber of free bending wave vibration in the rail,  $k_r$ , at the center frequency of the band of frequencies being studied. In this Report we will study the vibration in octave bands. Vibration levels may now be computed on the basis of the interaction shown in Fig. 3.10. We consider first the high frequency vibration, above the rail/rail fastener resonance,  $\omega_r$ .

The first step in the analysis is to formulate the power flow relations corresponding to each element and vibration type. Written in full, these are:

$$\begin{aligned} \eta_s T_s + \eta_{s,r} (T_s - 2T_r) + \eta_{s,w} (T_s - 2T_w) \\ + \eta_{s,u} (T_s - 2T_u) = 0 \end{aligned} \quad (3.27a)$$

$$\eta_w T_w + \eta_{w,s} (T_w - T_s) + \eta_{w,t} (T_w - T_t) = 0 \quad (3.27b)$$

$$\eta_u T_u + \eta_{u,s} (T_u - T_s) + \eta_{u,t} (T_u - T_t) = 0 \quad (3.27c)$$

$$\eta_t T_t + \eta_{t,u} (T_t - 2T_u) + \eta_{t,w} (T_t - 2T_w) = 0 \quad (3.27d)$$

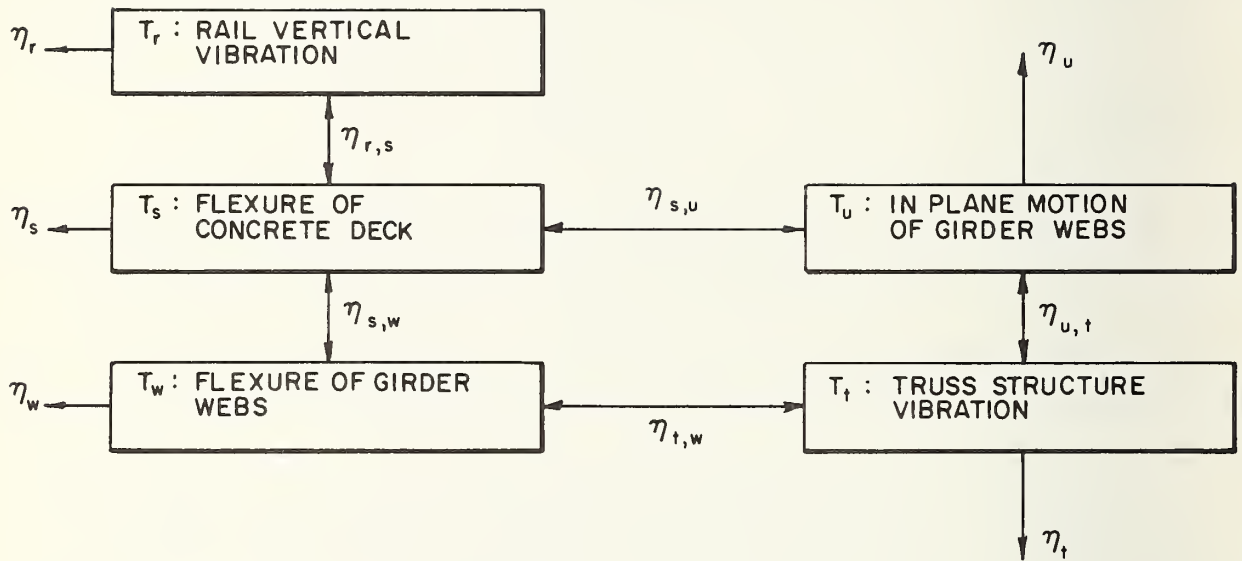


FIG. 3.10 INTERACTION DIAGRAM FOR CONCRETE DECK ON STEEL PLATE GIRDER STRUCTURE

The rail energy,  $T_r$ , is assumed to be known. Factors of two enter because there are two rails and two girder webs. Because we have considered the modes in each element to be coupled only to one mode in the adjacent elements, the coupling loss factors are symmetric, i.e.

$$\eta_{r,s} = \eta_{s,r}, \text{ etc.} \quad (3.28)$$

The truss members couple in-plane motion of the web to web flexure. In its details, this interaction is very difficult to formulate. However, the calculation is greatly simplified by making a few reasonable assumptions. First, we can solve Eqs. 3.27(c) and 3.27(d) for  $T_u$  and  $T_t$  in terms of  $T_s$  and  $T_w$ , by neglecting the damping loss factors,  $\eta_u$  and  $\eta_t$  in comparison with the coupling loss factors,  $\eta_{t,u}$ ,  $\eta_{t,w}$ , and  $\eta_{u,s}$ . This gives:

$$\eta_{w,t}(T_w - T_t) \approx \eta_{u,s}(T_w - T_s)\left(1 + \frac{\eta_{u,s}}{\eta_{w,t}} + \frac{\eta_{u,s}}{\eta_{t,u}}\right)^{-1} \quad (3.29a)$$

$$\eta_{s,u}(T_s - T_u) \approx \eta_{u,s}(T_s - T_w)\left(1 + \frac{\eta_{u,s}}{\eta_{t,w}} + \frac{\eta_{u,s}}{\eta_{t,u}}\right)^{-1} \quad (3.29b)$$

It will also be assumed that  $\eta_{w,t}$  and  $\eta_{t,u}$  are at least as large as  $\eta_{u,s}$ . Then, from Eqs. 3.29 the error incurred by taking

$$\eta_{w,t}(T_w - T_t) \approx \eta_{u,s}(T_w - T_s) \quad (3.30a)$$

$$\eta_{s,u}(T_s - T_u) \approx \eta_{u,s}(T_s - T_w) \quad (3.30b)$$

is no more than a factor of 3, i.e. 5 dB. This margin of error is considered to be acceptable, since we anticipate the actual error for rail structures to be small.

Support for the above assumptions is difficult to quantify. In general, we do expect the damping loss factors to be small in rail structures, particularly for the in-plane web vibration. We also expect the coupling between the slab deck and in-plane motion of the web to be small because of the difference in impedances. Therefore, we proceed with some confidence, even though a quantitative estimate of the error introduced by these assumptions cannot be made.

Substituting Eqs. 3.30 into Eqs. 3.27, we have

$$\eta_s T_s + \eta_{r,s} (T_s - 2T_r) + (\eta_{s,w} + \eta_{s,u}) (T_s - 2T_w) = 0 \quad (3.31a)$$

$$\eta_w T_w + (\eta_{w,s} + \eta_{u,s}) (T_w - T_s) = 0 \quad (3.31b)$$

The interpretation of Eqs. 3.31 is that the slab and web flexure are coupled with an augmented coupling loss factor  $(\eta_{s,w} + \eta_{s,u})$ . This comes about because the vibration of the truss members serves to convert the energy of in-plane web motion to web flexure. The solution of Eqs. 3.31 for the slab and web energies is

$$T_s = \frac{2 \eta_{r,s}}{\eta_s + \eta_{r,s} + \eta_{s,w} + \eta_{s,u} - \frac{2 (\eta_{s,w} + \eta_{s,u})^2}{\eta_w + \eta_{s,w} + \eta_{s,u}}} T_r \quad (3.32a)$$

$$T_w = \frac{\eta_{s,w} + \eta_{s,u}}{\eta_w + \eta_{s,w} + \eta_{s,u}} T_s \quad (3.32b)$$

These equations represent our analytical predictions based on known rail response, which are valid for frequencies above the rail fastener resonance frequency.



For frequencies below the rail resonance, the wavenumber for free bending waves in the rail, given by Eq. 3.15, becomes an imaginary number, meaning that all the vibration waves decay rapidly in amplitude as the distance from the excitation point increases. Analysis for this case is quite difficult, as is shown in Appendix II. Fortunately, the total radiated acoustic power in the frequency range below the rail/fastener resonance frequency makes little contribution to the A-weighted noise level. Our approach, therefore, will be to limit our analysis to frequencies at or above the rail/fastener resonance frequency. Prediction in the low frequency range could be based on the work in Appendix II.

As the final step we must calculate the loss factors. The damping loss factors can be obtained from available tables on the damping loss factors of materials and on the basis of the acoustic radiation losses to be expected. However, for the coupling loss factors, detailed determinations must be made.

The basic calculations of coupling losses are carried out in Appendix III for typical configurations and are all based on wave calculations. Below, we discuss these results as applied to each loss factor of the particular elevated structure considered in this Section.

$\eta_{r,s}$ : The coupling loss factor between the rail and slab can be obtained by considering the power flow from a beam (representing the rail) connected to an infinite plate through a continuous elastic layer (the rail fasteners). The result presented in Appendix III can be immediately adapted to the present case to yield:

$$\eta_{r,s} = \frac{\frac{4}{k_s} \frac{\rho_s}{m_r} \sqrt{1-s^2}}{\left| 1 + i\sqrt{1-s^2} \left( \frac{2}{k_{rs}} - \frac{1}{\sqrt{1+s^2}} \right) \right|^2} \quad (3.33)$$

where

$$s \equiv \sin \theta = k_r/k_s$$

$$\kappa_{rs} = \frac{K_\ell}{2 D_s k_s^3}$$

$$k_s^4 = \omega^2 \frac{\rho_s}{D_s}$$

and where  $k_s$  is the free bending wavenumber of the slab,  $\rho_s$  and  $D_s$  are the mass density per unit surface area and bending rigidity ( $E_s I_s$ ) of the slab, and  $k_r$  is the free bending wavenumber of the rail. Note that in the general case, the fastener stiffness per unit length of rail,  $K_\ell$ , must be modeled by a complex number taking into account the fastener damping, see Section 2.

$\eta_{s,w}$ : The interaction between the slab and I-beam web bending may be idealized by two plates forming a rigid right angled T junction. For the purpose of calculating this coupling loss factor, the in-plane motions of slab and web can be neglected to obtain

$$\eta_{s,w} = \frac{\left(\frac{\psi}{k_s L_s}\right)(1 - s^2) \sqrt{\kappa^2 - s^2}}{\psi^2/2 + \psi[\sqrt{1-s^2}\sqrt{\kappa^2-s^2} + \sqrt{1+s^2}\sqrt{\kappa^2+s^2}] + 2 \kappa^2} \quad (3.34)$$

where

$$s = k_r/k_s$$

$$\kappa = k_w/k_s$$

$$\psi = \kappa^2 D_{gw}/D_s$$

$$k_w^4 = \omega^2 \frac{\rho_{gw}}{D_{gw}}$$

and  $k_w$  is the free bending wavenumber of the girder web,  $\rho_{gw}$  is the

girder web mass per unit area, and  $D_{gw}$  is the girder web bending rigidity ( $E_{gw} I_{gw}$ ).

One must note, in calculating  $\eta_{s,w}$ , the effect of the vertical web stiffeners (a typical example is shown in Fig. 3.11). Usually, bending waves transmitted to the web from the slab propagate in a direction nearly normal to the structural junction. Thus, the effect of stiffeners is to augment  $\rho_{gw}$  and  $D_{gw}$  by their mass and bending stiffness. We may think of this added stiffness and mass density as being uniformly distributed over the whole web length (along the track). Thus  $\rho_{gw}$  must be increased by adding:

$$\rho_{stiff} / \Delta X_{stiff}$$

where  $\rho_{stiff}$  is the mass of a stiffener per unit length and  $\Delta X_{stiff}$  is the distance between the centerline of adjacent stiffeners.

Also,  $D_{gw}$  must be increased by

$$D_{stiff} / \Delta X_{stiff}$$

where  $D_{stiff}$  is the bending rigidity of the stiffener. From the dimensions shown in Fig. 3.11, these parameters are given by:

$$D_{stiff} = E_{steel} I \quad (3.35)$$

where

$$I = \frac{1}{3} (B c_1^3 - b h^3 + a c_2^3)$$

$$c_1 = \frac{1}{2} \frac{aH^2 + bd^2}{aH + bd}$$

$$c_2 = H - c_1, \quad h = c_1 - d$$

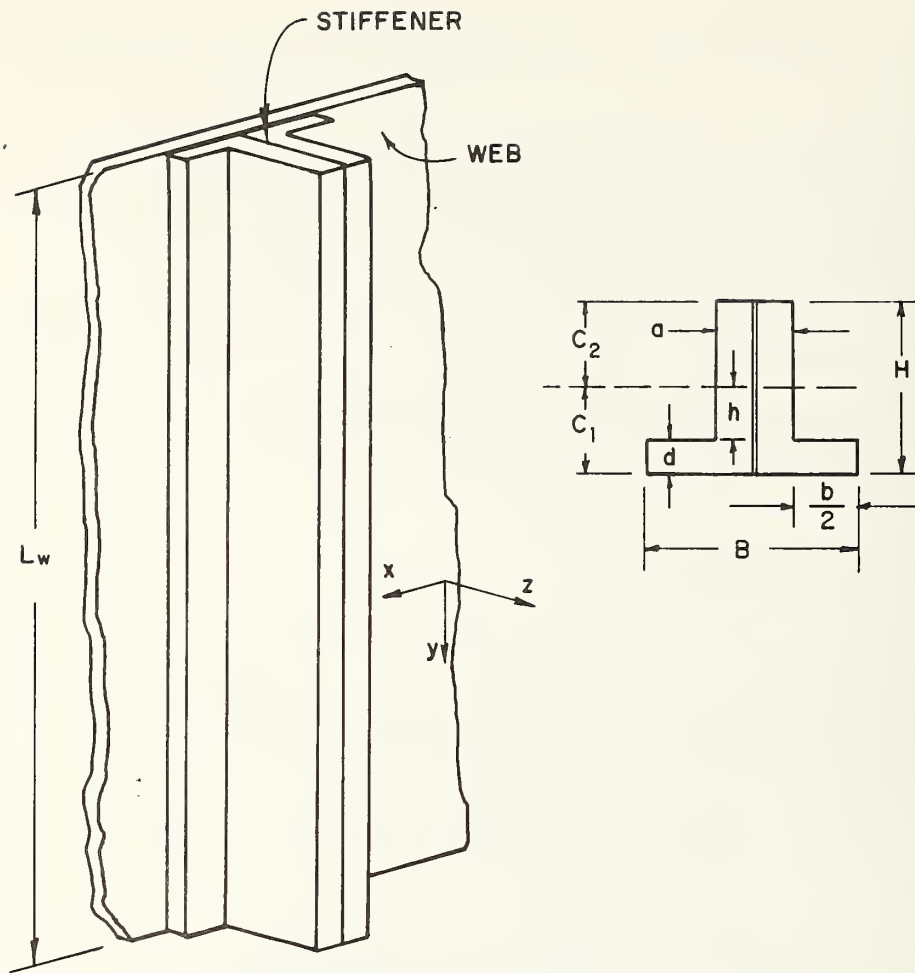


FIG. 3.11 SKETCH OF THE VERTICAL WEB STIFFENERS

$\eta_{s,u}$ : This is the loss factor for the coupling between bending waves in the slab and in-plane motion of the I-beam web. To a first approximation the in-plane motion can be modeled as longitudinal waves in the web propagating normal to the structural junction. The resulting coupling loss factor is

$$\eta_{s,u} = \frac{\rho_{gw} c_{l,gw}}{2\rho_s \omega L_s} \frac{1 - s^4}{(\sqrt{1-s^4} + \frac{\lambda}{4} \sqrt{1+s^2})^2 + \frac{\lambda^2}{16} (1-s^2)} \quad (3.36)$$

where

$$\lambda = \frac{c_{l,gw} \rho_{gw} \omega}{k_s^3 D_s}$$

$c_{l,gw}$  is the longitudinal wave speed in the steel girder web and other parameters are defined earlier.

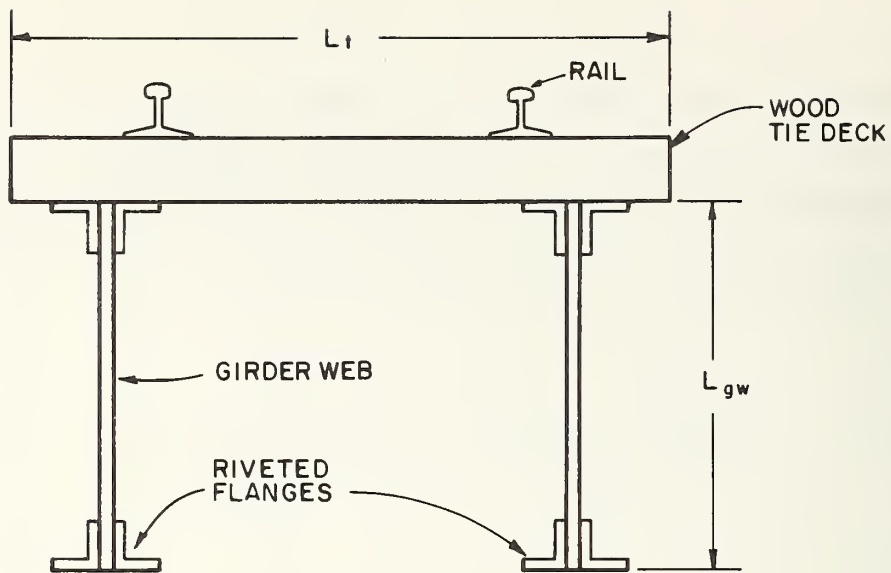
This concludes the analysis of the concrete deck on steel plate girders. A typical application of the analysis will be given in Section 4.

### 3.3.2 Open Tie Deck on Steel Plate Girders

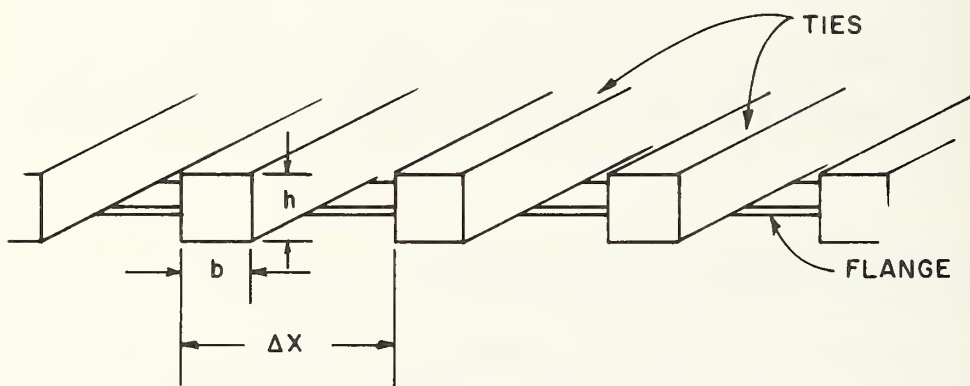
The geometry and nomenclature associated with this type of structure are shown in Fig. 3.12. The structure consists of rails directly mounted on an open deck of wooden ties which are in turn supported by two steel plate I-beam girders. As in the previous structure the girder webs may have vertical stiffeners periodically placed along their length. Furthermore the rails are typically placed almost directly above the girder webs.

The compressional stiffness offered by the ties to relative motion of rail and I-beam is modeled by a continuous elastic





(a) CROSS- SECTIONAL VIEW



(b) WOOD TIE DECK

FIG.3.12 IDEALIZED MODEL OF AN ELEVATED STRUCTURE WITH A WOOD TIE DECK ON STEEL-PLATE GIRDERS .

layer, with stiffness per unit rail length  $K_t$ . In many practical situations the rails are not rigidly bolted to the ties, so that estimation of  $K_t$  is problematical. This is because the static loading of the rails by the mass of the cars can cause the rail to deflect upward at some points and break contact with the tie deck. At these locations, the rail is essentially unsupported. Therefore, the value of  $K_t$  to which we here refer is the spatial average of the stiffness over the whole train length, including those locations where rail and ties are uncoupled. The rational calculation of this average stiffness is very difficult, and one must therefore often rely on intuitive reasoning. This will be done in Section 4, where we apply the analysis to a specific case.

The bending motion of the ties is modeled by Bernoulli-Euler beams. However, to preserve our picture of an assemblage of homogeneous, infinite structural elements, we may think of the tie deck as an orthotropic grillage with vanishingly small bending rigidity along the track direction. Referring to Fig. 3.12, the mass density per unit surface area,  $\rho_d$ , and the bending rigidity along the y axis,  $D_d$ , given by

$$\rho_d = \rho_{\text{wood}} \frac{hb}{\Delta x}, \quad D_d = \frac{E_{\text{wood}}}{\Delta x} \frac{bh^3}{12} \quad (3.37)$$

where  $\rho_{\text{wood}}$  and  $E_{\text{wood}}$  are the density and Young's modulus of wood.

Finally, the bending motion of the girder web is modeled by a Bernoulli-Euler plate and its in-plane deformation is idealized as longitudinal wave motion.

As the result of the above idealizations, the whole structure can be divided into the following elements:

1. rails on the compressional stiffness of ties (denoted by subscript "r")

2. flexure of tie deck (subscript "t")
3. I-beam girders — girder web properties (subscript "gw")
  - , — web flexure (subscript "w")
  - in-plane motion (subscript "u")
4. additional structural members (subscript "o").

Item 4 may include, for example, the longitudinal and bending motion of the trusses, columns or any other element tending to couple flexural and in-plane motion of the webs.

Now consider the nature of coupling between the rail and the other structural elements. Suppose that  $F$  is the force exerted on the ties by the rail, as shown in cross-section in Fig. 3.13. The ties act as point driven beams with impedance,  $Z_t$

$$Z_t = \hat{F}/\hat{V}_t = 2 D_t k_t^3 (1 - j)/\omega \quad (3.38)$$

where

$$k_t = (m_t/D_t)^{1/4} \sqrt{\omega}$$

$m_t$  is the mass density per unit length of a tie, and  $D_t$  is its bending rigidity. Similarly, the impedance for in-plane motion of the I-beam web to a vertical force is

$$Z_u = \hat{F}/\hat{V}_u = c_{\ell, gw} \rho_{gw} \quad (3.39)$$

where  $c_{\ell, gw}$  is the longitudinal wave speed in steel, and  $\rho_{gw}$  is the mass per unit area of girder web. With wooden ties 8" square, a 3/8" thick steel web, and typical values of mass densities and elastic moduli, one finds that  $|Z_t| < |Z_u|$  for frequencies up to approximately 5000 Hz. Hence, in considering the power flow from rail to ties and I-beams, we can neglect the coupling between rail and ties. This is the opposite conclusion to that reached for the concrete deck on steel plate girders. The resulting "interaction diagram" is as shown in Fig. 3.14.

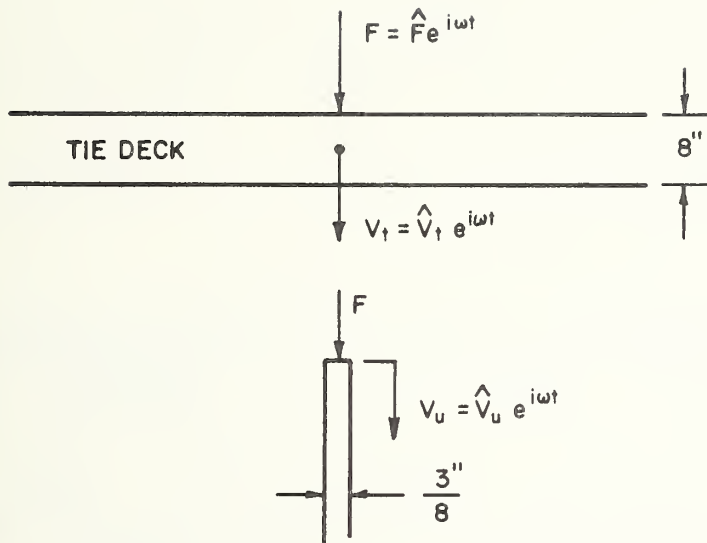


FIG. 3.13 FORCE AND VELOCITY CONVENTIONS FOR CALCULATIONS OF TIE DECK AND GIRDER WEB IMPEDANCES

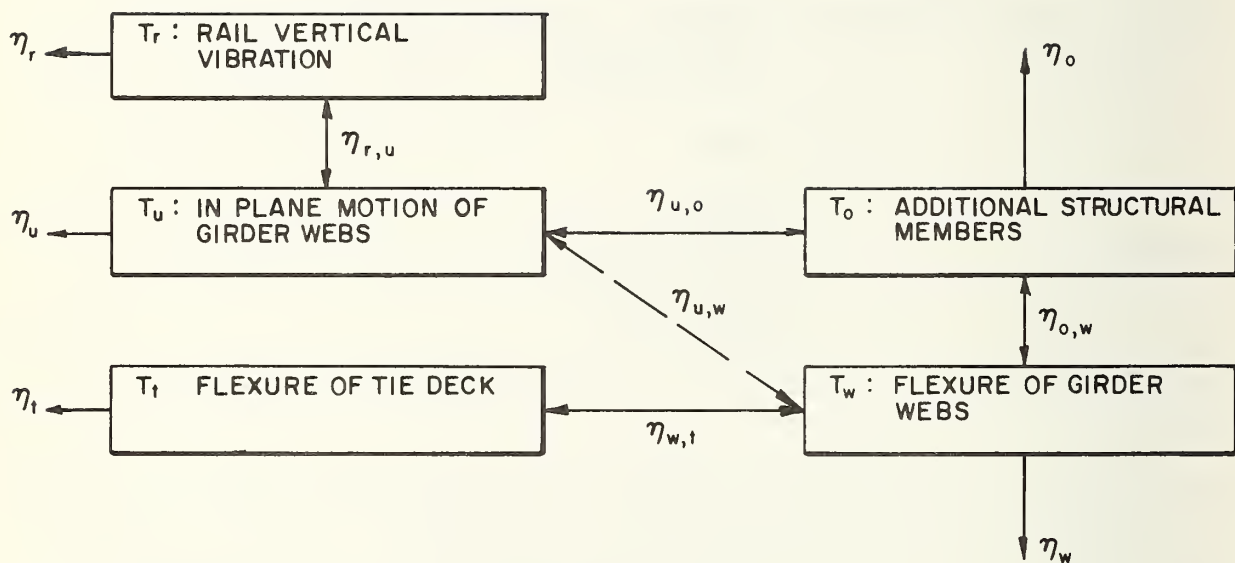


FIG.3.14 INTERACTION DIAGRAM FOR OPEN TIE DECK ON STEEL PLATE GIRDER STRUCTURE

The behavior of the secondary structural elements is very difficult to calculate. However, we may assume that  $\eta_o$ , and  $\eta_u$  are small compared with  $\eta_{u,o}$  and  $\eta_{o,w}$  and that  $\eta_{u,o}$  and  $\eta_{o,w}$  are no smaller than  $\eta_{w,t}$ . Then, the interaction among the "u", "o" and "w" systems may be modeled by the short circuited path shown as the dotted line in Fig. 3.14. Finally, the assumptions that  $\eta_{u,o}, \eta_{o,w} > \eta_{w,t}$  imply that  $\eta_{u,w} < \eta_{w,t}$ , so that one incurs little error by taking

$$T_w \approx T_u \quad (3.40)$$

With this result, the steady state power flow relations can be expressed solely in terms of the energies of the rail, ties, and I-beam webs,

$$(\eta_w + \eta_u)T_w + \eta_{u,r}(T_w - T_r) + \eta_{w,t}(T_w - T_t) = 0 \quad (3.41a)$$

$$\eta_t T_t + \eta_{w,t} (T_t - 2T_w) = 0 \quad (3.41b)$$

Eqs. 3.41 can be solved to find

$$T_w = \frac{\eta_{u,r}}{(\eta_w + \eta_u) + \eta_{u,r} + \frac{\eta_t \eta_{w,t}}{\eta_t + \eta_{w,t}}} T_r \quad (3.42a)$$

$$T_t = \frac{2\eta_{w,t}}{\eta_t + \eta_{w,t}} T_w \quad (3.42b)$$

The remaining step is to calculate the two loss factors  $\eta_{r,u}$  and  $\eta_{w,t}$ . Results from Appendix III are as follows:



$\eta_{r,u}$ : From Appendix III we find the coupling loss factor between bending of the rail and in-plane motion of the I-beam, to be

$$\eta_{r,u} = \frac{m_r}{2} \left( \frac{\omega_r}{\omega} \right)^3 \frac{\omega_r}{\rho_{gw}^c \ell_{gw}} \quad (3.43)$$

where

$$\omega_r^2 = \frac{K_t}{m_r}$$

It is to be noted that  $\eta_{r,u}$  decreases very rapidly with frequency.

$\eta_{w,t}$ : This is the loss factor between bending waves in the tie deck and bending of the I-beam web. The situation may be idealized as a rigid right angled T junction between a grillage (the tie deck) and a Bernoulli-Euler plate (the I-beam web). By the very nature of the tie deck, only waves normal to the structural junction may propagate on it. Accounting for this fact, assuming incident waves on the tie deck and calculating the resulting power flow to the web, one recovers the result given in Appendix III for normal incidence ( $s = 0$ ):

$$\eta_{w,t} = \frac{\frac{\kappa}{k_t} \frac{\psi}{L_t}}{\frac{1}{2} \psi^2 + 2 \kappa \psi + 2 \kappa^2} \quad (3.44)$$

where

$$\kappa = k_w / k_t$$

$$\psi = \kappa^2 D_{gw} / D_t$$

$$k_w = (\rho_{gw} / D_{gw})^{1/4} \sqrt{\omega}$$

$$k_t = (\rho_t / D_t)^{1/4} \sqrt{\omega}$$

$k_w$  and  $k_t$  are the wavenumbers of free bending waves on the web and the ties, respectively. The coupling loss factor given by Eq. 3.44 is typically quite small. Since the damping losses of wooden ties is fairly large, the average energy of ties will generally be much less than that of the I-beam webs.

### 3.3.3 Open Tie Deck on Open Web Steel Girders

As in the previous example, the rails are supported by an open tie deck. Here, however, the girders have open webs, as shown in Fig. 3.15. The girders consist of a horizontal flange, supporting the tie deck, connected to a lower flange by vertical columns. The girder is stiffened with respect to shear deflections by diagonally placed truss members. Clearly, this assemblage is not homogeneous along the track, however, one can obtain crude but serviceable estimates by modeling it by an "equivalent" continuum, as will be discussed below.

We will divide the structure into the following elements:

1. rail on the compressional stiffness of the ties  
(denoted by subscript "r")
2. flexure of the tie deck (subscript "t")
3. Girder structural members — local z component of  
vibration ("w")  
— local y component of  
vibration ("u").

We characterize the open web girder structures by the average of their vibratory energy over all their structural members, distinguishing only between motions in the y-direction and in the z-direction, as shown in Fig. 3.15. The manner in which these elements interact must now be determined. Since most ties are supported by the upper flange at points where vertical columns in the web trusses are not present, we may assume that the force impedance of the flange is typically much less than that of the ties. Thus, the energy flow from rail to girder may be neglected in



comparison with the energy flow directly from the rail to the tie deck. Furthermore, similar to what has been done in the preceding examples, various mechanisms are postulated which account for a conversion of the energy of y-component girder vibration to energy of the z-component. We model these mechanisms by a direct coupling between system elements "u" and "w", although in fact the coupling may be through other structural elements.

On the basis of the above remarks, the interaction scheme is as shown in Fig. 3.16. Proceeding as before, we assume that  $\eta_{w,u}$  is sufficiently large that  $T_u \approx T_w$ . Also, note at the outset that since the tie deck and horizontal flange are connected with the vertical and diagonal girder members only at discrete points, the energy flow from the ties to the z-component of vibration of the girders is negligible. Therefore,  $\eta_{t,w}$  is neglected in our analysis. The resulting energy flow relations corresponding to each system element are:

$$\eta_t T_t + \eta_{r,t}(T_t - 2T_r) + \eta_{t,u}(T_t - T_w) = 0 \quad (3.45a)$$

$$(\eta_w + \eta_u) T_w + \eta_{t,u}(T_w - T_t) = 0 \quad (3.45b)$$

The resulting solutions for  $T_t$  and  $T_w$  are

$$T_t = \frac{2 \eta_{r,t}}{\eta_t + \eta_{r,t} + \frac{\eta_{t,u}(\eta_w + \eta_u)}{\eta_w + \eta_u + \eta_{t,u}}} T_r \quad (3.46a)$$

$$T_w = \frac{\eta_{t,u}}{\eta_w + \eta_u + \eta_{t,u}} T_t \quad (3.46b)$$

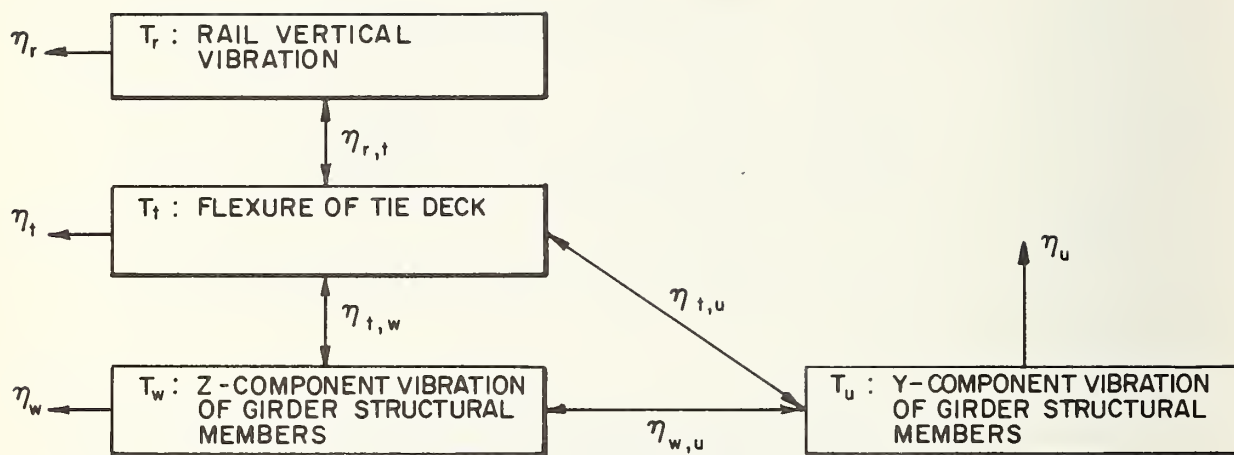


FIG.3.16 INTERACTION DIAGRAM FOR OPEN TIE DECK ON OPEN WEB STEEL GIRDER STRUCTURE

Eqs. 3.46 are for frequencies at or above the rail/tie resonance,  $\omega_r$ , where

$$\omega_r^2 = \frac{K_t}{m_r}$$

and  $K_t$  is the effective stiffness of the ties (see Section 4). We do not consider the low frequency regime in detail, but proceed to determine the coupling loss factors appearing in Eqs. 3.46.

$\eta_{r,t}$ : As in the previously discussed example, Section 3.3.2, the tie deck can be modeled as an orthotropic grillage with zero bending rigidity in the track direction. The rail is first coupled to the compressional stiffness of the ties and then to the tie flexure. This is the same situation as is considered in Appendix III, except that only waves normal to the rail-tie junction can propagate in the ties. Thus,  $\eta_{r,t}$  is the result found in Appendix III, evaluated for normal wave propagation ( $s = 0$ ):

$$\eta_{r,t} = \frac{(2\rho_t \kappa_{rt}^2)/(k_t m_r)}{\kappa_{rt}^2 + 2(1 - \kappa_{rt})} \quad (3.47)$$

where

$$\kappa_{rt} = \frac{m_r \omega_r^2}{2 D_t k_t^3}$$

$$k_t = \left(\frac{\rho_t}{D_t}\right)^{1/4} \sqrt{\omega}$$

and where  $\rho_t$  and  $D_t$  are the mass per unit area of the tie deck and



bending rigidity of the tie-grillage system and  $\omega_r$  is the resonance frequency of the rail on the compressional stiffness of the ties.

$\eta_{t,u}$ : This is the coupling loss factor for bending waves in the tie deck and the y-component of girder vibration. Here we face the difficulty that the girder structure is not homogeneous in the track direction. However, one notes that the most significant contribution to the spatially averaged energy of response comes from the low wavenumber components of vibration. That is, we need consider only the coupling between those tie bending wave motions and girder vertical vibrations which are very slowly varying along the track direction. Hence one may crudely approximate  $\eta_{t,u}$  by calculating the power transmitted by tie-deck bending waves (at normal incidence) to longitudinal waves in the vertical columns and diagonal truss members of the girder. This procedure is tantamount to replacing the open web by a thin plate having a mass density per unit area equal to the average mass density of the columns and diagonal elements. A typical open-web girder is shown in Fig. 3.17. The web structure is periodically repeated, the basic pattern being the "bay" indicated by the dashed lines in the figure. The mass surface density of the plate equivalent to the open web can be estimated as

$$\rho_{gw} = \frac{1}{L_w L_b} (M_2 + M_4) \quad (3.48)$$

where  $M_2$  and  $M_4$  are the masses of the column and truss members, respectively, and  $L_w$  and  $L_b$  are the height of the web and the length of a bay.

To conclude, we consider the coupling loss factor for bending waves in a grillage connected through a right angled junction to a plate with mass density given by Eq. 3.48 undergoing in-plane motion. Since only waves normal to the junction can propagate in the tie deck,  $\eta_{t,u}$  is the result from Appendix III,

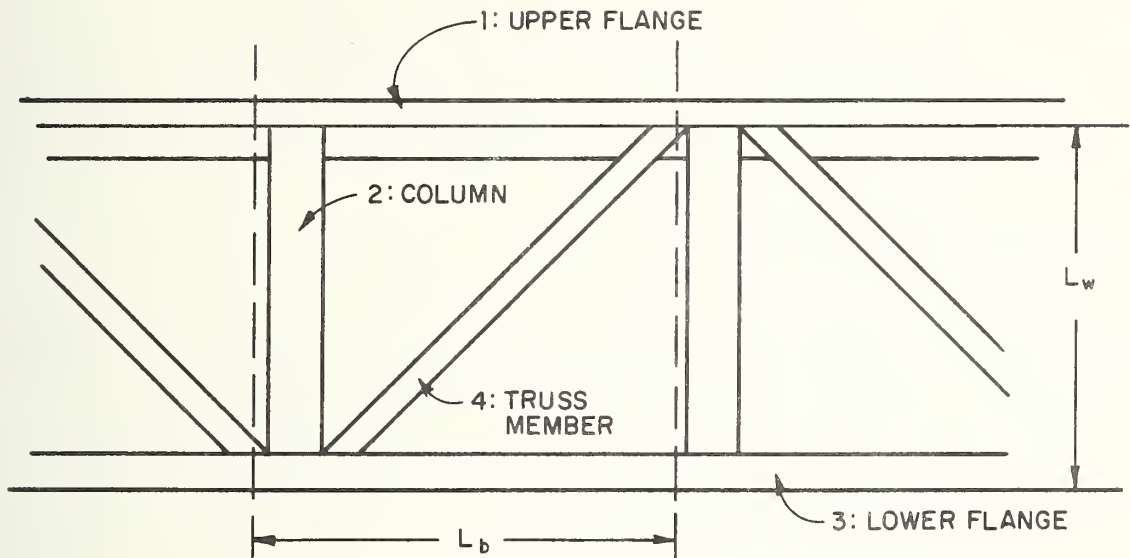


FIG. 3.17 SKETCH OF A TYPICAL OPEN WEB STEEL GIRDER, SHOWING THE CONFIGURATION OF ONE BAY

evaluated at normal incidence:

$$\eta_{t,u} = \frac{\rho_{gw} c_{l,gw}}{2 \rho_t \omega L_t} \left[ \left(1 + \frac{\lambda}{4}\right)^2 + \frac{\lambda^2}{16} \right]^{-1} \quad (3.49)$$

where

$$\lambda = \frac{c_{l,gw} \rho_{gw} \omega}{k_t^3 D_t}$$

$$k_t = \left(\frac{\rho_t}{D_t}\right)^{1/4} \sqrt{\omega}$$

and  $c_{l,gw}$  is the longitudinal wave speed in steel,  $L_t$  is the length of ties, and  $k_t$  is the free-bending wavenumber of the ties.

Examples of the use of the equations presented in this Section will be given in Section 4.

### 3.4 Analysis of the Acoustic Radiation

During the passage of a train on an elevated structure, acoustical power is radiated from elements of the structure due to their vibration. This radiated power, which we call elevated structure noise, adds to the power radiated by the wheels, rails, and other vehicle surfaces so that the total wayside noise when the train is on an elevated structure is greater than when the same train is on at-grade tie and ballast track.

As a train passes by, vibrational energy due to wheel/rail interactions is transmitted to the structure at each wheel/rail contact point. As this energy propagates away from the contact points and distributes itself throughout the structure, the vibration amplitudes become smaller due to the spreading of the energy within the structure and due to damping. However, as the amplitudes diminish, the net surface area participating in the vibration grows, providing a greater radiating area. Since the radiated acoustic power is proportional to the product of area and vibration amplitude, prediction of the noise radiation requires a detailed knowledge of both the radiative properties of each element of the elevated structure and the distribution of vibration throughout the structure.

#### 3.4.1 Basic Approach

The acoustic power radiated by a vibrating surface that is infinite in one dimension can be expressed in terms of the radiation efficiency by

$$W_{\text{rad}}(\omega) = \rho_o c_o \sigma_{\text{rad}}(\omega) I_v(\omega) P_{\text{rad}} \quad (3.50)$$

where  $W_{\text{rad}}(\omega) \Delta\omega$  is the total power radiated by the surface in the narrow band of frequencies  $\Delta\omega$ ,  $\rho_o c_o$  is the acoustic wave impedance,

$\sigma_{\text{rad}}$  is the radiation efficiency,  $I_v(\omega)$  is the integrated velocity spectrum, and  $P_{\text{rad}}$  is the cross-sectional length of the structure from which acoustic power can be radiated. The units of the integrated spectrum are  $L^3/T$  where  $L$  is a unit of length and  $T$  is a unit of time. The radiation efficiency is dimensionless.

If we define power level,  $L_w$ , and integrated velocity spectrum level,  $L_{I_v}$ , according to

$$L_w = 10 \log_{10} \frac{W_{\text{rad}}(\omega) \Delta\omega}{10^{-12}} \text{ with } W_{\text{rad}}(\omega) \Delta\omega \text{ in watts} \quad (3.51)$$

and

$$L_{I_v} = 10 \log_{10} \frac{I_v(\omega) \Delta\omega}{2.5 \times 10^{-15}} \text{ with } I_v(\omega) \Delta\omega \text{ in meters}^3/\text{sec}^2 \quad (3.52)$$

then Eq. 3.51 becomes

$$L_w = L_{I_v} + 10 \log_{10} \sigma_{\text{rad}}(\omega) + 10 \log_{10} P_{\text{rad}} \quad (3.53)$$

where  $P_{\text{rad}}$  is in meters. For the purposes of this report the bandwidth  $\Delta\omega$  is taken to be an octave and the radiation frequency will be evaluated at the band center frequency. Variations of the radiation efficiency within an octave band are not large enough to be of concern.

The reference quantities in Eqs. 3.51 and 3.52 correspond to international standards, ISO TC 43/SC 2/WG2. However, we should point out that the integrated spectrum is unique to this report. Therefore, we have used the ISO standard for velocity,  $5 \times 10^{-8}$  m/sec, with an area of 1 meter squared to derive a reference for the integrated spectrum.

The objective of this report is to develop methods to predict and control elevated structure noise. This objective is

carried out in terms of the total radiated power,  $L_w$ , in frequency bands relevant to annoyance. Of course, users of the prediction methods are also interested in predicting the sound pressure levels (or A-weighted noise levels) at various distances from the track. This variation is discussed below.

As part of our earlier work [1] a model was developed for predicting the noise level from trains on at-grade track in terms of levels at a distance of fifty feet from the track centerline. The model represented the train as a series of point sources with dipole directivity located at each truck. Data we have taken confirms this model for predicting noise from wheels, rails, and other vehicle surfaces. However, noise radiated from elements of the elevated structure is not concentrated at and near the vehicle trucks but is distributed more uniformly. If we restrict our attention to predicting noise levels at a distance of 50 ft or more from the track centerline, then the structure can be modeled as a line source — the length of the line being equal to the length of the train. The elements of the line source are taken to have uniform radiation in all directions, i.e. non-directional sources.

The models used for elevated structure noise and wheel/rail noise are similar but not identical. However, the elevated structure noise model can also be used to predict the maximum wheel/rail noise during a train pass-by at distances equal to or greater than 50 ft from the train. The maximum sound pressure level,  $L_p$ , is given by [14]

$$L_p = L_w - 20 \log_{10} D + 10 \log_{10} \left\{ \frac{2D}{L} \arctan \frac{L}{2D} \right\} \quad (3.54)$$

where  $D$  is the distance in meters from the measurement point to the track centerline and  $L$  is the train length in meters.



### 3.4.2 Radiation From Simple Elements

We model elevated structures as a collection of plates and beams. Therefore, an initial step in the development of a prediction model is to review the radiation from these simple structural elements.

#### Plates

The radiation efficiency of plates that are larger than  $1/3$  of an acoustic wavelength is essentially one at frequencies above their critical frequency. The critical frequency is defined as the frequency at which waves on the plate become supersonic,\* or equivalently, the frequency at which the wave-number of flexural waves in the plate equals the acoustic wave-number. This frequency is given by

$$f_c = \frac{c_o^2}{2\pi} \sqrt{\frac{\rho_s}{B}} \quad (3.55)$$

where  $f_c$  is the critical frequency in Hz,  $c_o$  is the speed of sound,  $B$  is the bending stiffness, and  $\rho_s$  is the density per unit area. For steel or aluminum plates

$$f_c = 500/h \quad (3.56)$$

where  $h$  is the plate thickness in inches.

---

\* In a dispersive system, such as a plate, the speed of propagating waves depends on the frequency.

At frequencies below the critical frequency the radiation laws become considerably more complicated and depend upon the details of the plate boundary conditions, baffling, and the location of stiffeners. Infinite homogeneous plates radiate no acoustic energy below the critical frequency because the spatial Fourier transform of the plate velocity has all its energy at a wavenumber greater than the acoustic wavenumber,  $k_0$ . However, when the plate is finite the spatial transform of the velocity does have energy at wavenumbers less than  $k_0$ . The details of the radiation depend upon the parameters mentioned above and can be found mathematically. For sake of discussion, however, we will base our discussion on simpler physical models [15].

### Simply supported baffled plate

Consider the simply supported baffled plate of Fig. 3.18 , vibrating at frequencies below the critical frequency in a typical modal pattern. Each of the cells creates motion of the air (volume velocity). However, for cells near the center of the plate, the air sloshes back and forth from cell to cell, radiating no net acoustical energy. At the edge of the plate the sloshing of volume velocity from the cells is not cancelled, and noise is radiated quite efficiently. The radiation efficiency for this "edge mode" radiation is given by\*

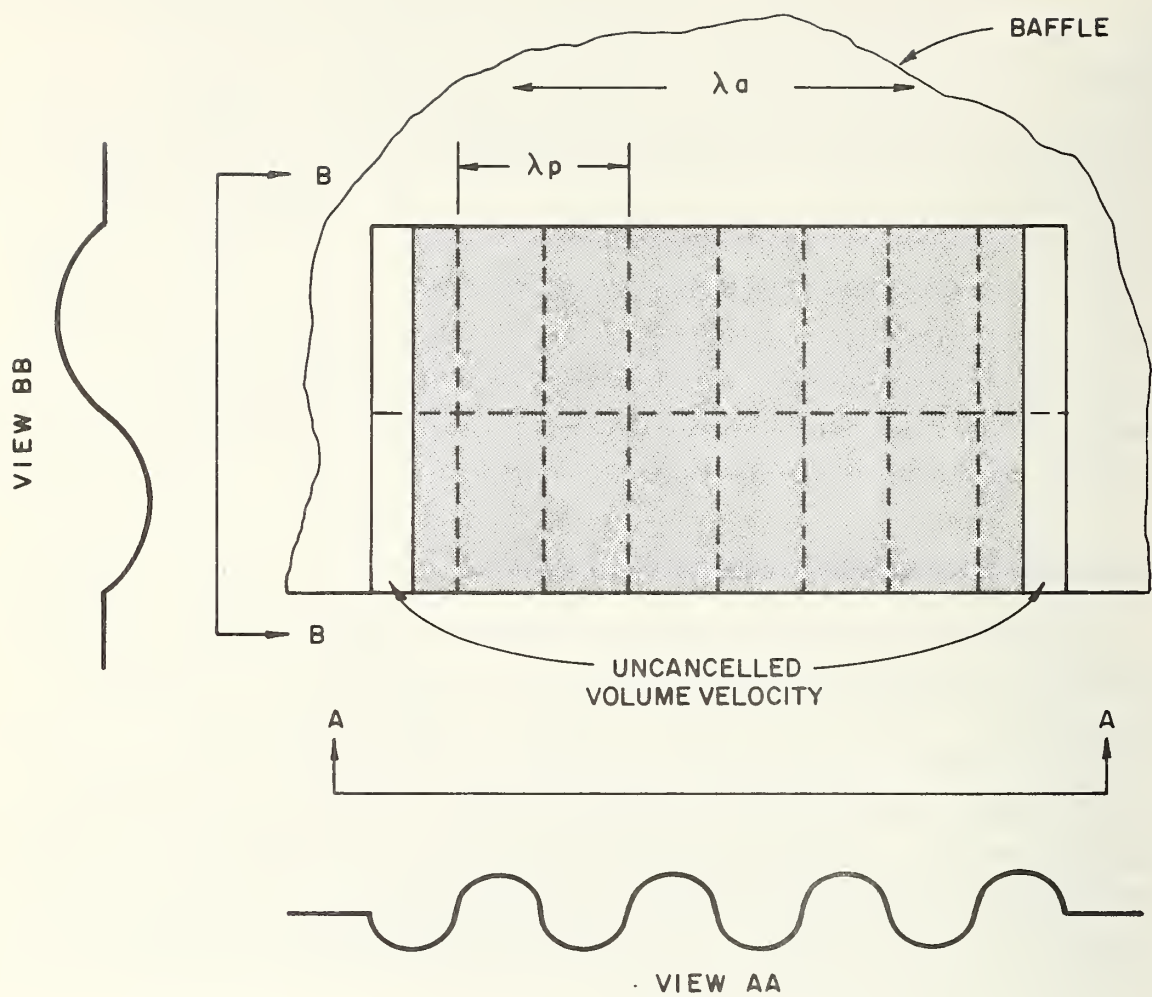
$$\sigma_{\text{rad}} = \frac{P \lambda_p}{A} g_2(f/f_c) \quad f < f_c \quad (3.57)$$

where  $P$  is the perimeter of the plate,  $A$  is its area,  $\lambda_p$  is the wavelength of flexural waves at critical frequency,

$$\lambda_p = \frac{c_0}{f_c} = \left( \frac{4\pi^2 B}{f_c^2 \rho_s} \right)^{1/4} \quad (3.58)$$

---

\*with the limitation that the plate perimeter is greater than an acoustic wavelength. This is generally true for the structures of interest in this report.



ACOUSTIC WAVELENGTH  $\lambda_a$   
 VIBRATION WAVELENGTH  $\lambda_p$

$$\lambda_a > \lambda_p$$

FIG.3.18 BAFFLED SIMPLY SUPPORTED PLATE VIBRATING BELOW THE CRITICAL FREQUENCY WITH UNCANCELLED VOLUME VELOCITY AT THE EDGE

and the function  $g_2$  is plotted in Fig. 3.19.

### Baffled plates with beam stiffeners

Stiffening or ribbing the plates alters the simple mode shapes of Fig. 3.18 and increases the radiation by causing the volume velocity near the stiffeners not to cancel out. Although this problem has not been solved exactly, a good approximation for the radiation from such structures has been obtained by considering a flexural wave incident upon an infinite beam coupled to an infinite plate [15]. The resulting radiation efficiency is given by

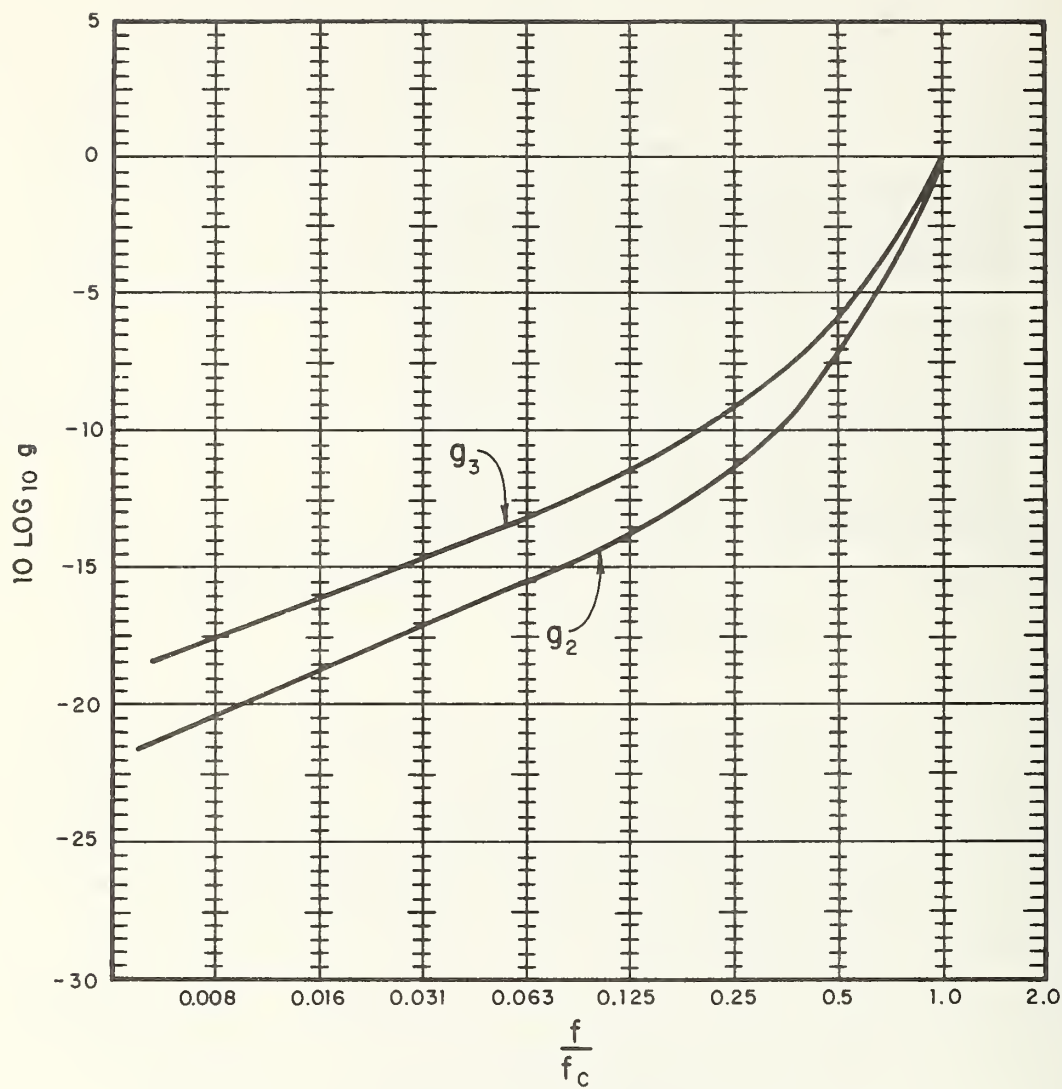
$$\sigma_{\text{rad}} = \frac{P \lambda_p}{A} g_3(f/f_c) \quad f < f_c \quad (3.59)$$

where  $g_3$  is given in Fig. 3.19,  $P$  is the total perimeter of all subpanels formed by the stiffeners, and  $A$  is the plate area.

### Baffling effects

The baffling at the edges of a plate plays an important role in its radiation below the critical frequency. If the baffling is removed the previously uncanceled volume velocity along the edges of the plates is now cancelled, or short circuited, since air can slosh around the edge from one side of the plate to the other. Radiation from the unbaffled edge will be considerably less than the baffled edge due to this short circuiting effect. The radiation from the unbaffled edges of plates vibrating below the critical frequency has not been given a great deal of attention in the literature. However, the radiation from these edges is dipole in nature and radiates less efficiently by a factor of  $(h/\lambda_0)^2$  than the baffled edge, which is monopole in nature. The parameter  $h$  is the plate thickness and  $\lambda_0$  is the acoustic wavelength.

When the edges are baffled by a wedge, as shown in Fig. 3.20 the radiation can be greater or less than the planar baffle case



$f_c$  IS THE CRITICAL FREQUENCY

FIG.3.19 THE FUNCTIONS  $g_2$  AND  $g_3$

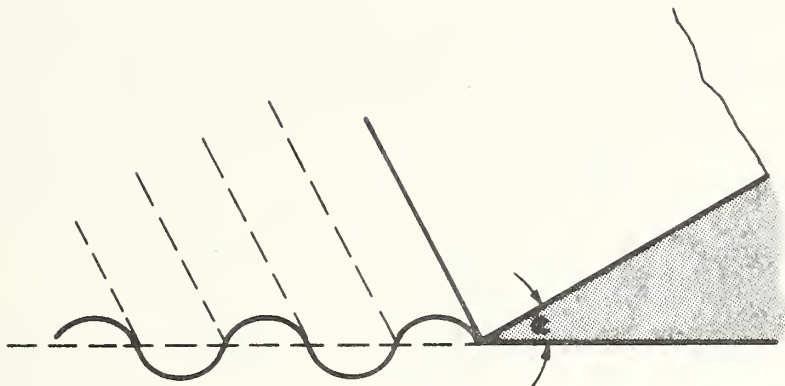


FIG. 3.20 VIBRATING PLATE WITH A WEDGED BAFFLE

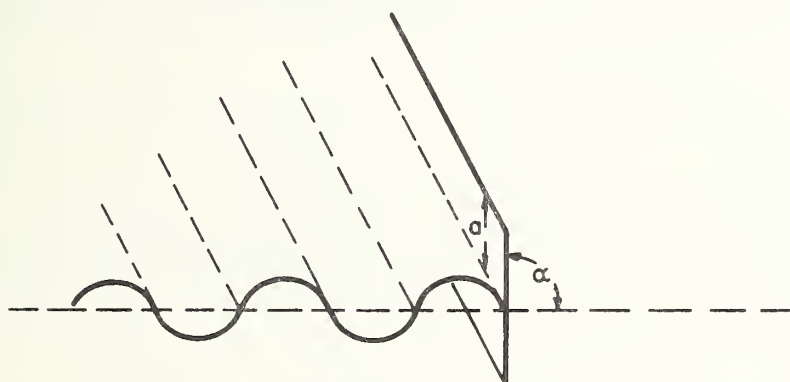


FIG. 3.21 VIBRATING PLATE WITH A FINITE BAFFLE



( $\alpha = 0$ ). The radiation impedance as seen by the radiating edge strip is increased (or decreased if  $\alpha < 0$ ) over the case when  $\alpha = 0$  by an amount given by  $(1 - \frac{\alpha}{\pi})^{-1}$  where the angle  $\alpha$  is in radians, because the same volume velocity is confined to a smaller (or larger) angle. This effect will become important in predicting the radiation from steel girder I-beams, since the flanges provide a baffle for the web edges.

When a wedged baffle is finite, as shown in Fig. 3.21, we can approximate the effect by considering the high and low frequency limits. At high frequencies, where  $k_0 a \gg 1$ , and  $a$  is one-half the baffle width, the effects discussed in the previous paragraphs apply, since the baffle is many wavelengths long. At low frequencies, where  $k_0 a \ll 1$ , the baffle is much smaller than an acoustic wavelength, so the wedge effect previously discussed is somewhat short circuited due to air sloshing around the baffle and volume velocity cancellation. The radiation from a baffled edge when  $k_0 a$  is less than one can be modeled as a line dipole source, with the radiation efficiency reduced by a factor of  $(k_0 a)^2$ .

### Beams

From an acoustical point of view we define a beam as a structure whose length is much greater than either transverse direction and whose cross-section does not deform. When these criteria are met, a structure of arbitrary cross-section can be modeled as a circular cylinder to calculate the acoustical radiation with reasonable accuracy. The equivalent diameter of the cylinder can be obtained either by rough approximation using the larger of the transverse dimensions or by fitting measured radiated efficiency to theoretical prediction of cylinder radiation efficiency.

At frequencies above the critical frequency where the bending wavespeed is greater than the speed of sound, the radiation efficiency of the beam can be represented by that of a cylinder

vibrating uniformly along its length.

The radiation efficiency of a freely suspended cylinder of radius  $a$  is given in Eq. 2.25. When  $k_0 a \ll 1$ , the cylinder radiates as a line dipole source, or vibrating wire, and has a radiation efficiency given by the asymptotic limit

$$\sigma_{\text{rad}} \approx \frac{\pi}{2} (k_0 a)^3 = \frac{\pi f^3 P^3}{2 c_0^3} \quad k_0 a \ll 1 \quad (3.60)$$

where  $P$  is the cylinder perimeter.

At high frequencies where  $k_0 a \gg 1$ , the radiation efficiency tends to unity,

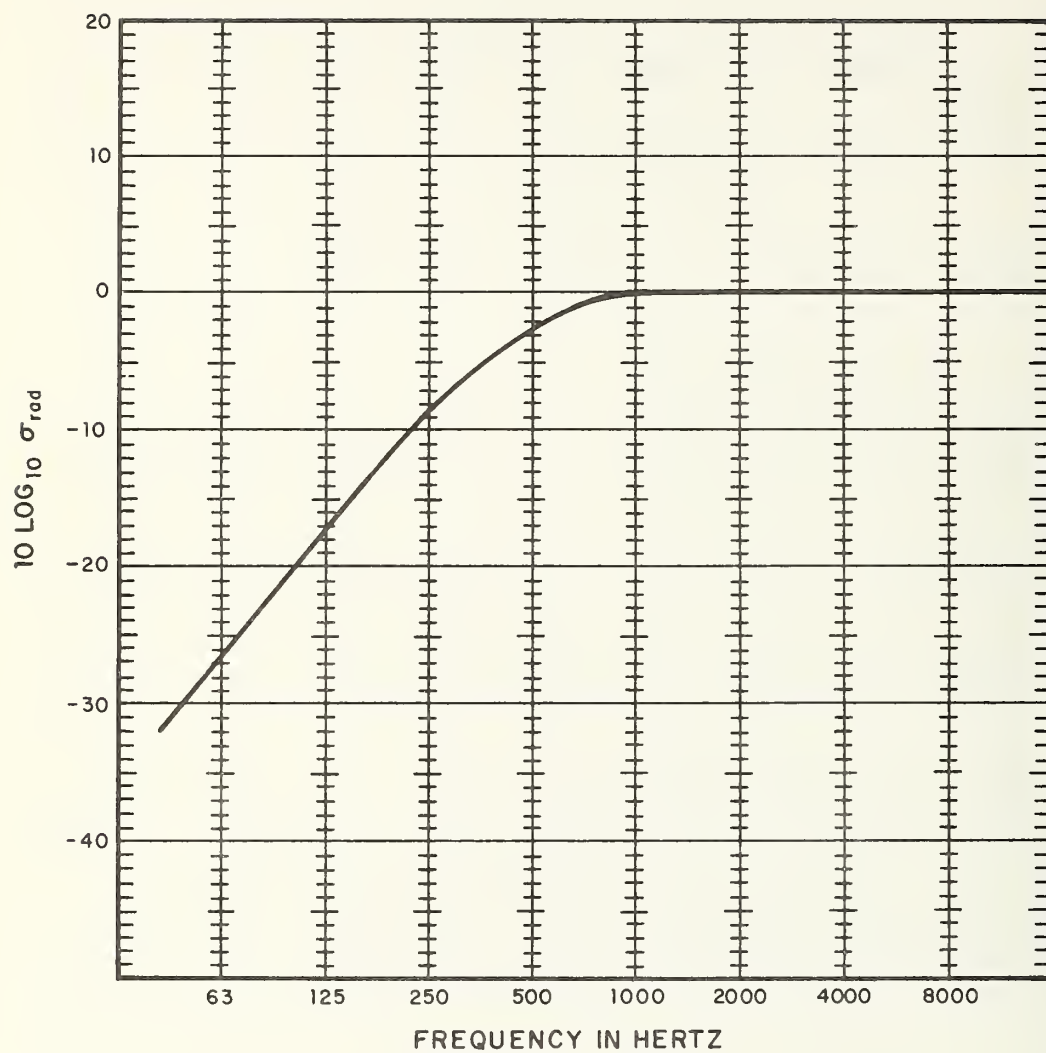
$$\sigma_{\text{rad}} \approx 1 \quad (3.61)$$

### 3.4.3 Application to Elements of an Elevated Structure

To apply the results presented in Section 3.4.2 to elements of an elevated structure, we must represent the elements by idealized models. The modeling is described in the following Sections and supported where necessary by comparisons of prediction with data from field measurements.

#### Ties

Tie are rectangular solids, generally made of wood, with dimensions that are typically 8 in. x 8 in. x 8 ft long. In the audible frequency range, ties conform to the definition of beams stated in Section 3.4.2. Since the critical frequency of a tie is approximately 60 Hz, the radiation efficiency given by Eqs. 3.60 and 3.61 will hold. The efficiency will increase with the third power of frequency. The diameter of the equivalent radiating cylinder is taken to be the tie height, 8 in. Tie radiation efficiency is plotted in Fig. 3.22.



TIE CROSS-SECTION 8"X8"

FIG 3.22 RADIATION EFFICIENCY FOR ONE TIE

### Deck slabs

Large concrete slabs have come into common usage in newer elevated structures. These slabs extend the length of the structure span and are typically 9 to 12 in. thick. Since the critical frequency of a 9 in. concrete slab is 90 Hz, the radiation efficiency can be taken to be unity for all of the bands of interest in calculating radiated noise.

$$\sigma_{\text{slab}} = 1 \quad (3.62)$$

### Steel plate girders

Steel plate girders are commonly used to support elevated structures. However, due to their large surface area and low damping they are significant noise radiators. We model these structural elements by baffled plates.

The dimensions of typical steel plate girders in a recently designed structure are shown in Fig. 3.23 . The critical frequency of the web is calculated to be 800 Hz. Thus, the radiation efficiency in octave bands centered at 1000 Hz and above is approximately one. At lower frequencies the radiation is due to edge radiation at the top and bottom flanges and at vertical stiffeners. The radiation efficiency is the sum of three factors. The first factor is radiation from the vertical stiffeners and is given by Eq. 3.59 with the perimeter  $P$  set to equal twice the stiffener length and  $A$  set to be the area of the subpanel formed by the stiffeners and flanges. The second factor is radiation from the upper flange edge and, due to baffling by the concrete deck, is equal to twice the radiation efficiency given by Eq. 3.57 with the ratio of  $P/A$  equal to the depth of the web,  $L_w$ . The third term is due to radiation from the lower flange edge. However, the radiation from this edge becomes short circuited at low

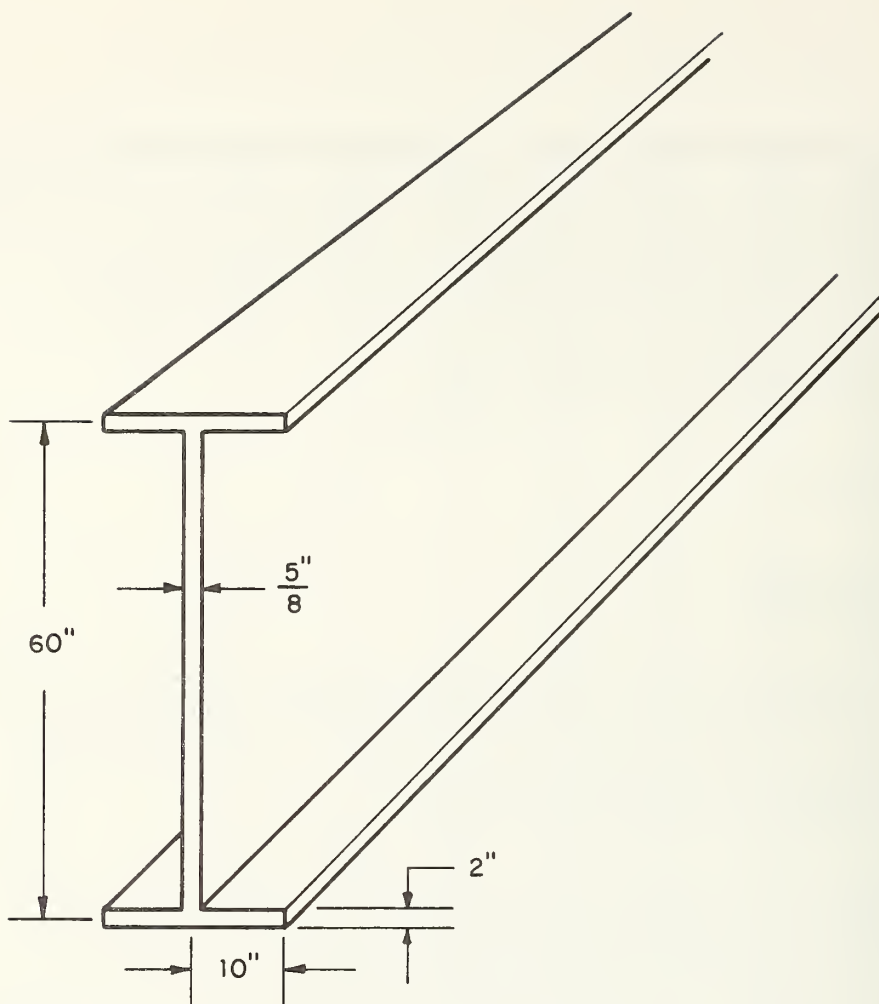


FIG. 3.23 TYPICAL STEEL PLATE GIRDER DIMENSIONS  
FOR A NEW STRUCTURE

frequencies, below 200 Hz for the dimensions given, due to air sloshing around the flange. Therefore, as a general procedure we set the third term equal to zero for frequencies below the frequency at which  $k_0 a$  equals one. For higher frequencies we treat the lower range as an infinite baffle so that the third term can be set to be equal to the second term. The transition from the lower frequency region to the higher frequency region is assumed to take place over an octave centered at the frequency where  $k_0 a = 1$ .

Due to the importance of noise radiation from steel girders, we have collected extensive field data with which to check the validity of the noise radiation prediction. In one series of measurements accelerometers were placed at seven points along a 140 ft span of a steel girder. The time histories of the vibration levels in octave bands were nearly the same for each accelerometer. As would be expected the only difference was a shift in time corresponding to the distance between measurement points divided by train speed. In the same series of measurements microphones were located five feet from the web at three points along the span and at a point 50 ft from the track centerline. The web radiation efficiency can be inferred from these measurements in two ways. Below 1000 Hz the time history of the octave band web vibration level has the same slope as the time history of the sound pressure level five feet from the web. This is shown in Fig. 3.24. The sudden jump in vibration and sound pressure levels occurs when the train passes from at-grade track onto the elevated structure. We infer from this data that the sound radiation measured five feet from the web is due to web vibration. Calculations of radiation efficiency are compared with prediction in Fig. 3.25. The comparison shows reasonably good agreement. The differences between calculated values and prediction are believed to be due to errors in relating acoustic power levels to measured sound pressure levels five feet from the web.



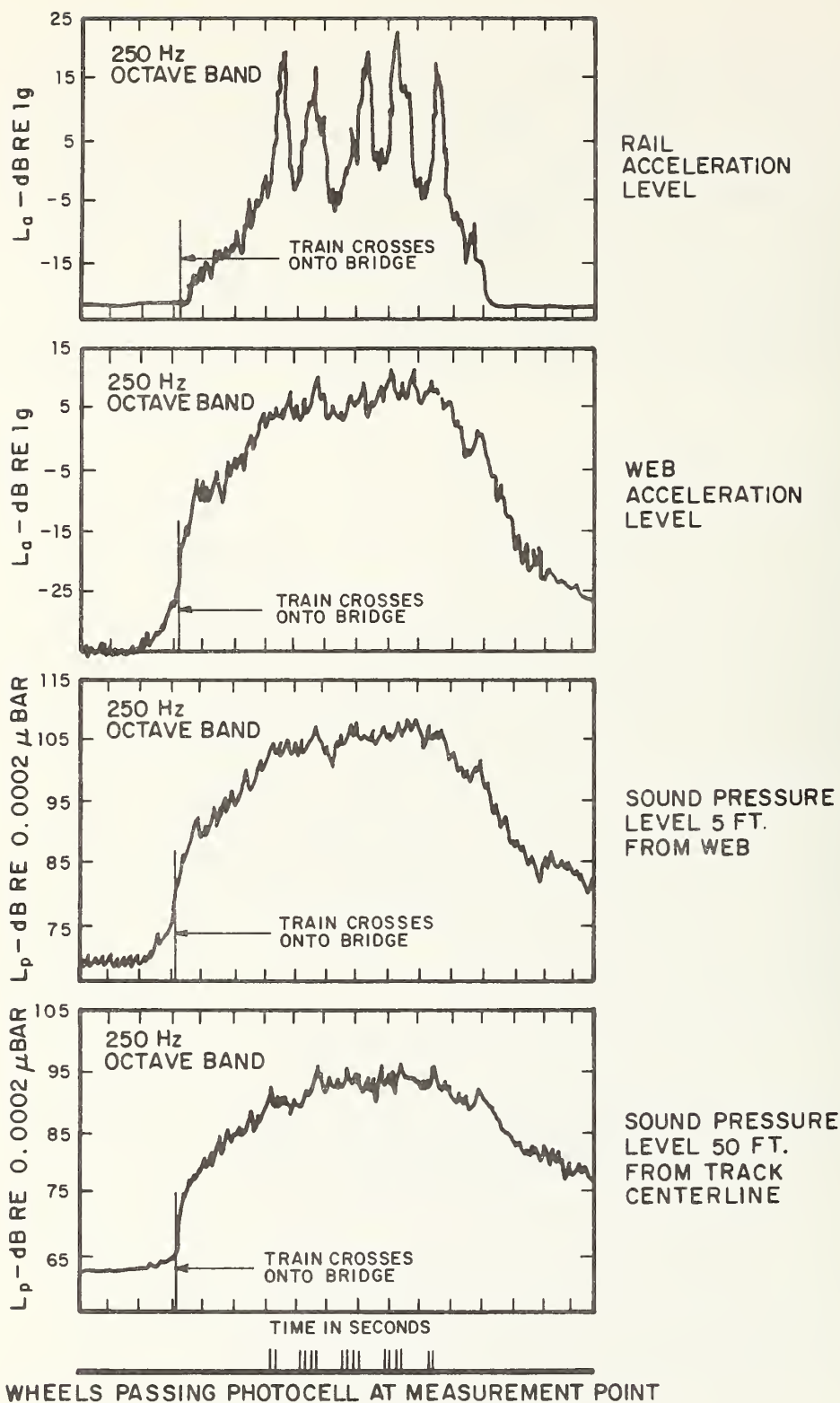
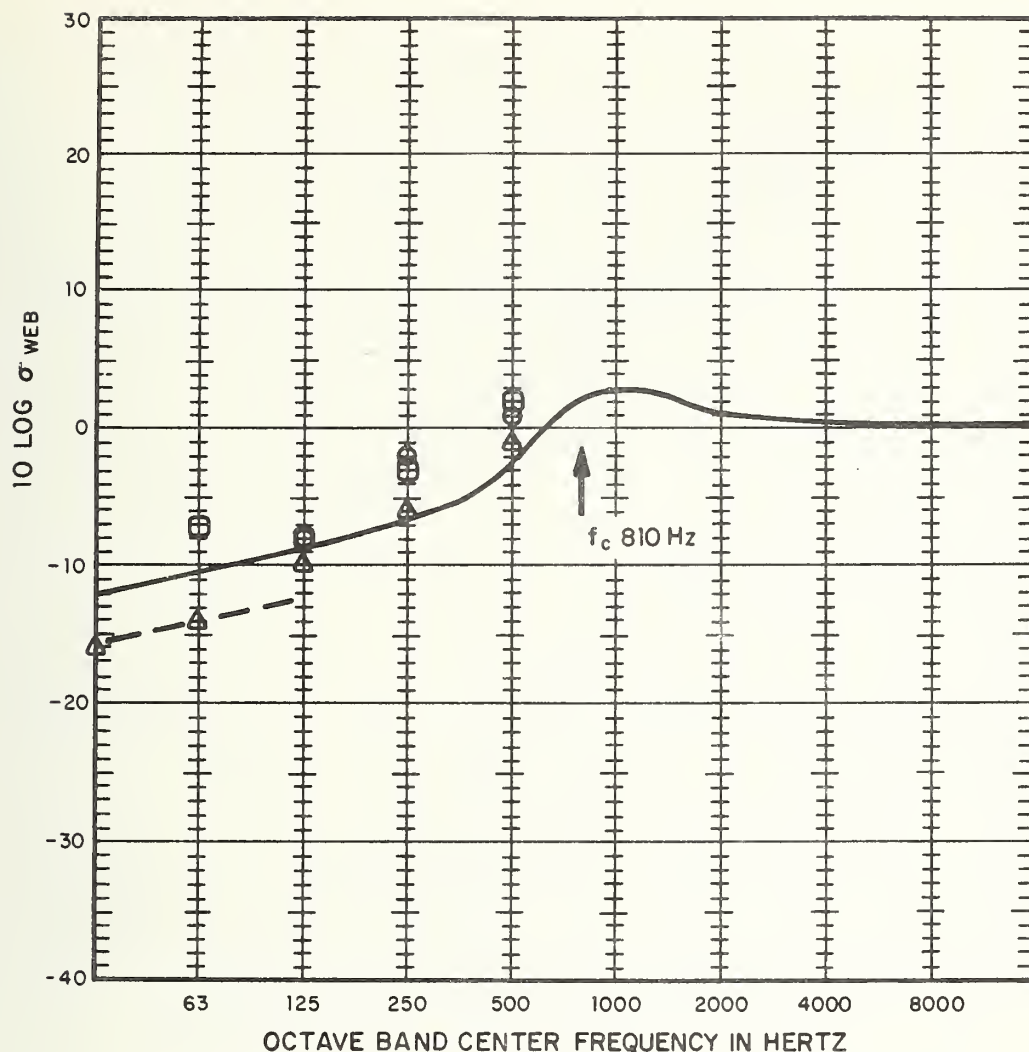


FIG. 3.24 MEASURED ELEVATED STRUCTURE NOISE DATA



#### THEORETICAL PREDICTION

————  $K_0 a \gg 1$   
 - - - -  $K_0 a \ll 1$

#### MEASURED VALUES

- INFERRED FROM SOUND LEVELS 5 FT. FROM WEB, APRIL 22 DATA
- INFERRED FROM SOUND LEVELS 5 FT. FROM WEB, MAY 16 DATA
- △ INFERRED FROM SOUND LEVELS AT 50 FT.

$f_c$  IS THE CRITICAL FREQUENCY OF THE WEB

FIG. 3.25 COMPARISON OF PREDICTED AND MEASURED RADIATION EFFICIENCY FOR THE PLATE WEBS OF THE ANDERSON BRIDGE ON THE MBTA

The radiation efficiency of the girder webs can also be inferred from the measurements 50 ft from the track in those frequency bands where the total noise radiation is dominated by web radiation. It is shown in Fig. 3.24 that when the train passes from at-grade track to the elevated structure, the sound pressure level at 50 ft increases suddenly in all frequency bands below 1000 Hz. This implies that elevated structure noise radiation dominates the overall noise radiation in these bands. Since the web vibration levels are much greater than level of the deck, we assume the elevated structure noise is from the webs. Therefore, the radiation efficiency of the girder webs was calculated from the 50 ft sound pressure levels and web vibration levels by summing the radiation from the entire length of the structure and assuming that both sides of each girder radiate equally into a hemispherical space with no directivity. The results of these calculations are also plotted in Fig. 3.25. The agreement between the calculated values and the prediction is good.

The radiation efficiency of steel plate girders on older elevated structures, with an open deck of wood ties, is reduced at low frequencies because the open deck does not serve as a baffle. Dimensions of a typical girder are shown in Fig. 3.26. The critical frequency for the web is found from Eq. 3.56 to be 1333 Hz. The radiation efficiency above this frequency is predicted to be one.

At frequencies below the critical frequency the radiation is from top and bottom edges of the web and from any web stiffeners. However, because of short-circuiting around the flanges, the radiation from the upper and lower edges is greatly reduced at low frequencies. The transition frequency, above which the flanges which can be treated as being infinite baffles, is found, by setting  $k_0 a = 1$ , to be equal to 360 Hz.

Two terms contribute with approximately the same weight to the radiation efficiency in the frequency range 360 to 1000 Hz.

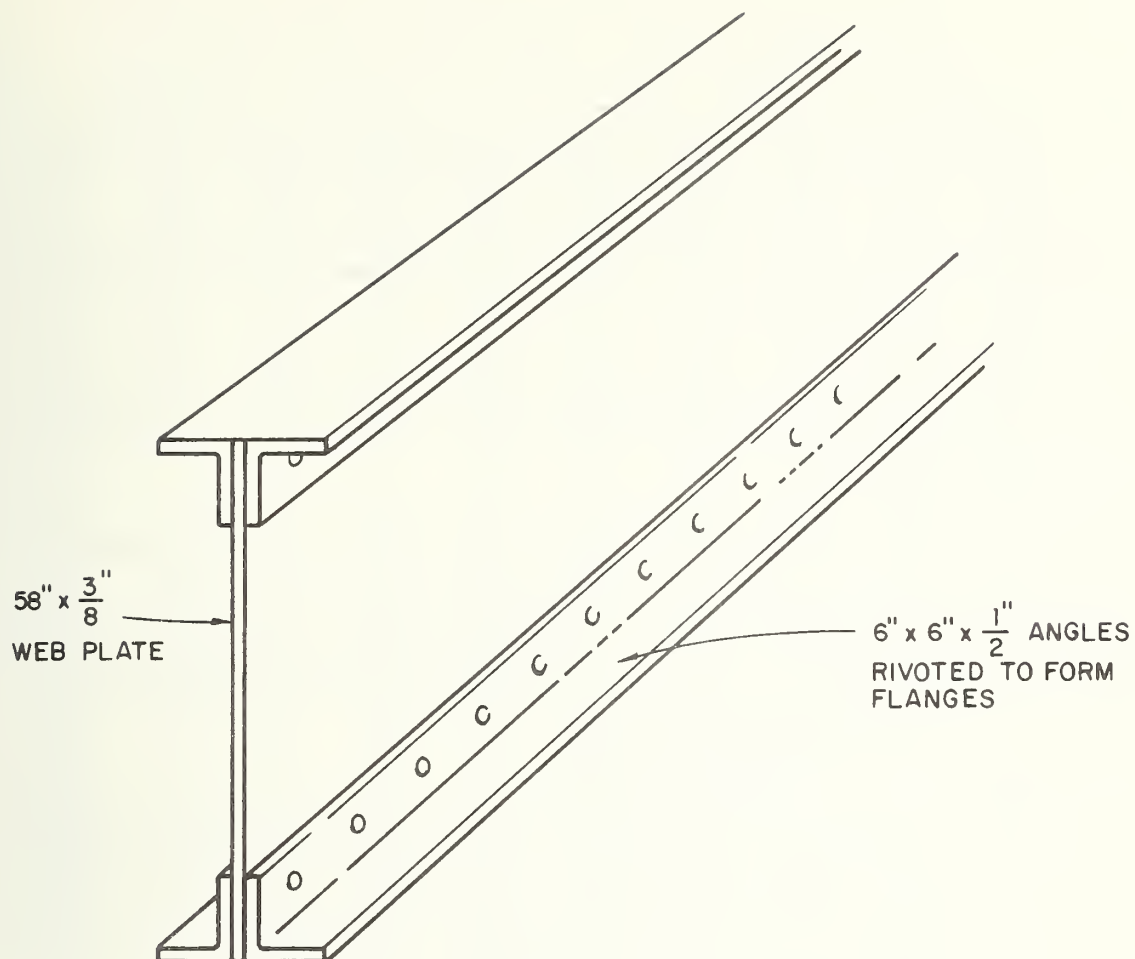


FIG. 3.26 TYPICAL STEEL PLATE GIRDER  
DIMENSIONS FOR AN OLDER STRUCTURE

The first is due to radiation from stiffeners and is given by Eq. 3.59 with the perimeter set to equal twice the length of one stiffener and the area  $A$  set to be the area of a subpanel formed by the stiffeners and flanges. The second term is due to the radiation from upper and lower edges of the girder web. Due to baffling by the flanges this term is twice the radiation efficiency given by Eq. 3.57 with the ratio of  $P/A$  equal to twice the depth of the web,  $L_w$ .

Below 360 Hz the second term must be multiplied by  $(f_t/f)^2$ , where  $f_t$  is the transition frequency 360 Hz and  $f$  is the frequency under consideration.

Predicted values for the radiation efficiency are shown in Fig. 3.27. Also shown are values inferred from field data. The values compare well considering the difficulty in using an acoustic measurement 5 ft from the web as a measure of radiated power.

#### open web girders

Open web girders are elements in which the web and flanges are fabricated from beams of various cross-sections. This type of girder is found only in very old elevated structures. To calculate the radiation efficiency of these girders, we model them as an array of beam elements. Then, the radiation efficiency is given by Eqs. 3.60 and 3.61 with  $2a$  equal to the maximum cross-section width of a typical element.

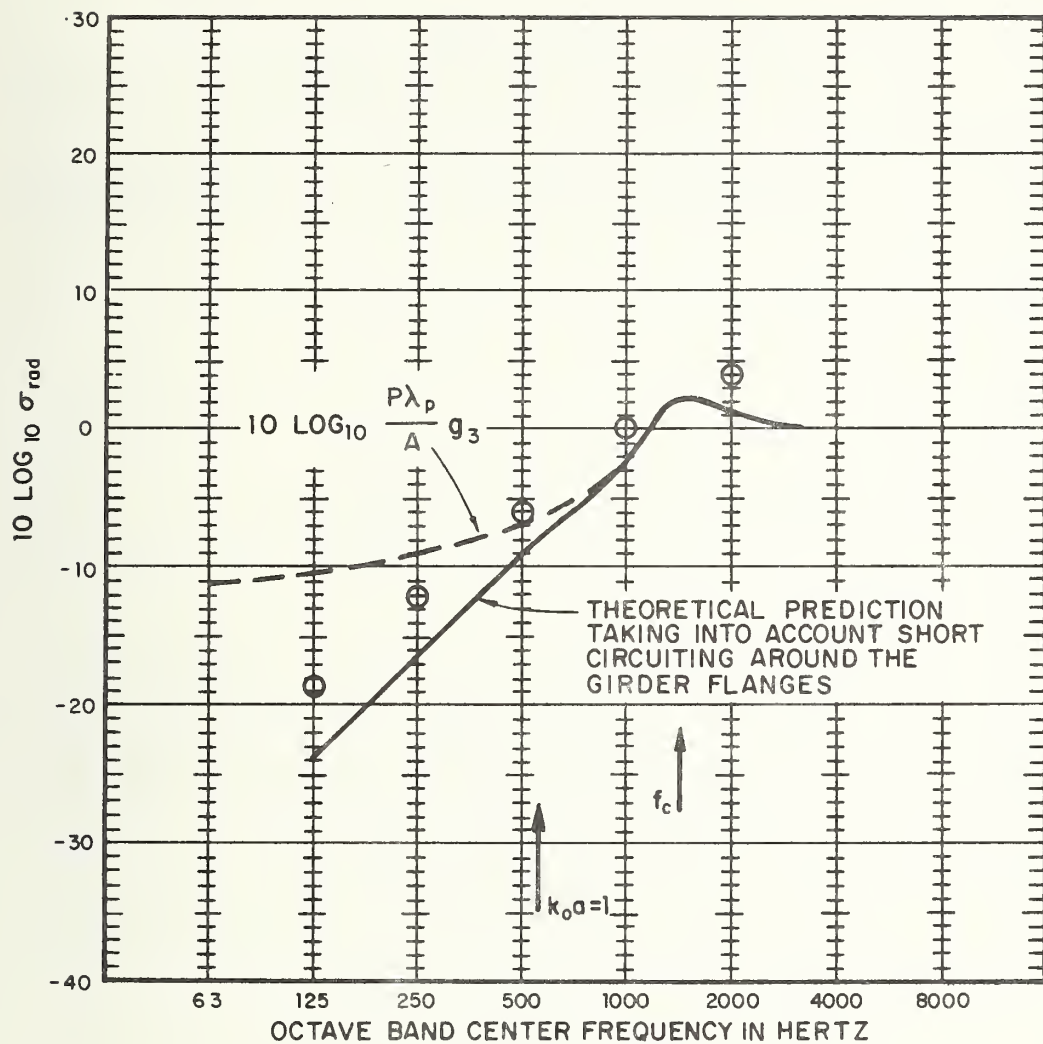


FIG.3.27 COMPARISON OF PREDICTED AND MEASURED RADIATION EFFICIENCY FOR AN OLDER ELEVATED STRUCTURE NEAR GREEN STREET ON THE MBTA ORANGE LINE



## 4. COMPARISON OF PREDICTION WITH DATA

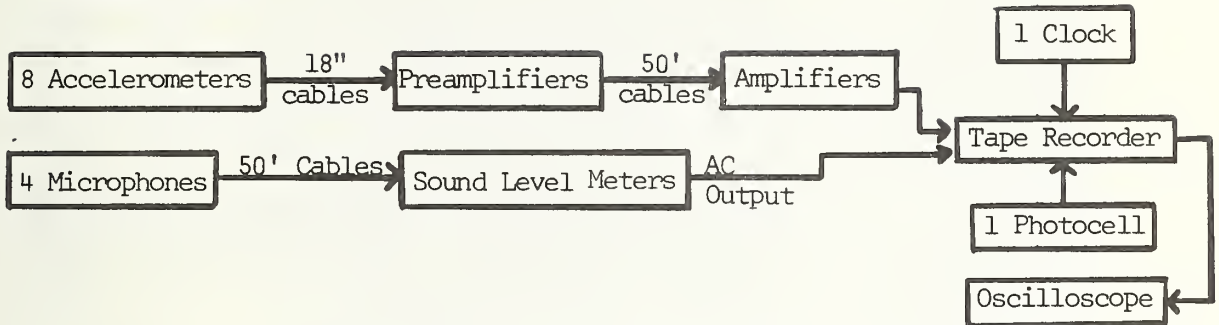
In this Section we proceed to compare the theoretical predictions developed in earlier Sections with data from field measurements. Three types of elevated structure will be considered: 1) a structure with steel plate girders, a concrete deck, and direct fixation resilient rail fasteners; 2) a structure with steel plate girders supporting an open deck of wood ties with direct rail fastening; and 3) a structure with open web steel girders supporting an open deck of wood ties with direct rail fastening. Structures representative of these three types exist on the Boston MBTA and are shown in Figs. 3.2, 3.3 and 3.4.

### 4.1 Data Collection and Reduction

Data on elevated structure noise that have been reported in the literature are limited by and large to measurements of the maximum noise level during a train pass-by at a fixed distance from the track. In a few studies data are also given for the maximum vibration levels at two or three points on the structure [7, 16]. Although these reported data allow one to gain a general understanding of elevated structure noise, they do not make it possible to verify the prediction model developed in this report. To do this we have carried out an extensive program of field measurements.

Instrumentation for the measurements is shown in Figs. 4.1, 4.2, and 4.3. Eight calibrated accelerometer channels and four acoustic channels were recorded simultaneously on a 14-channel wide-band FM tape recorder. For each set of measurement points, at least 5 train pass-bys were recorded to determine the repeatability of the measured levels. Train position and speed information was also recorded on the data tape using a photocell and reflector. The photocell beam was directed across the track at a height of 3 inches above the rail head, so that the train wheels would interrupt the beam as they passed by. The train speed was obtained

### DATA COLLECTION



### DATA ANALYSIS



ACCELEROMETERS: 8 Bruel & Kjaer Model 4333 and 4344

MICROPHONES: 4 General Radio 1962-9801

PREAMPLIFIERS: 8 Ithaco Model 125L and 143L

AMPLIFIERS: 4 Ithaca Model 451 and 4 Dana Model #2820

SOUND LEVEL METERS: 4 General Radio 1933

TAPE RECORDER: Honeywell 14 Channel 5600, FM wideband at 15 ips

OSCILLOSCOPE: Tektronix 5103N storage scope

CLOCK: Systron-Donner 8350

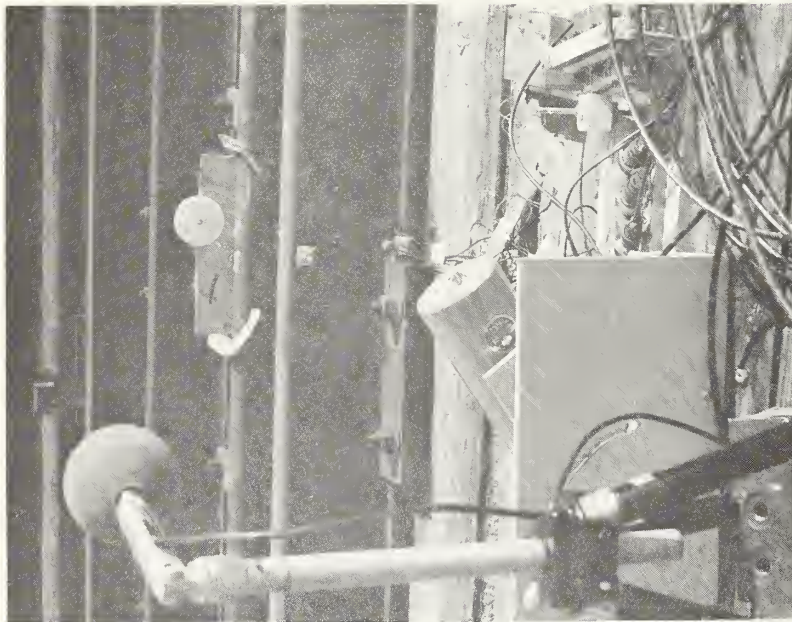
PHOTOCELLS: Photoswitch 42RL1

CHART RECORDER: Gulton Industries Model 444

FIG. 4.1 INSTRUMENTATION USED TO COLLECT AND  
ANALYZE NOISE AND VIBRATION DATA



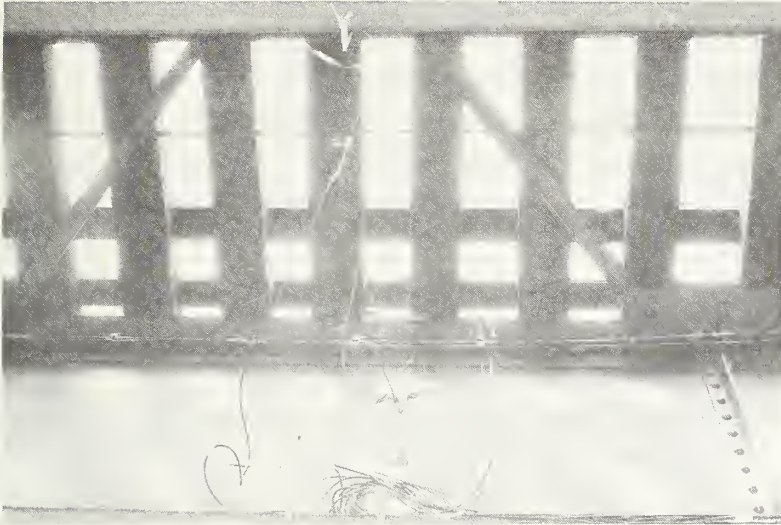
Accelerometer on the Girder-Web  
Microphone 4' from the Web



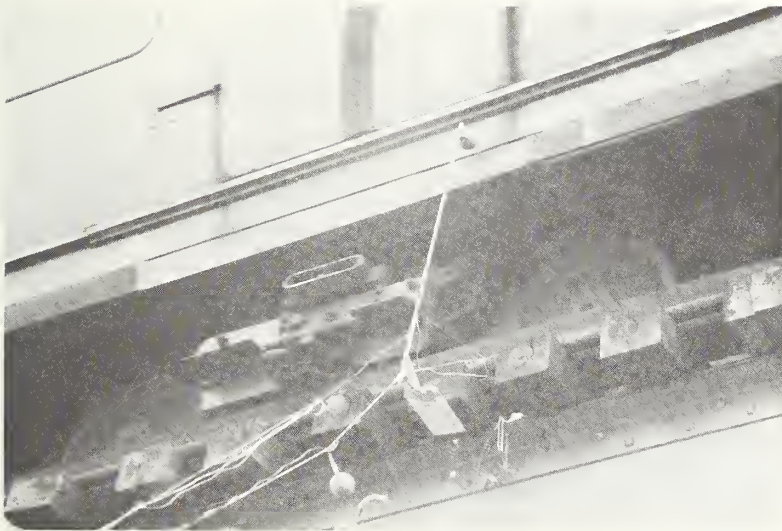
Accelerometers on the Rail  
Microphone 3' from Rail Head  
Photocell and Reflector

FIG. 4.2 INSTRUMENTATION SET-UP ON THE  
ANDERSON BRIDGE OF THE MBTA RED LINE





Accelerometers on the  
Girder-Web



Microphones near the  
Girder-Web and the  
Rail Head

FIG. 4.3 INSTRUMENTATION SET-UP ON THE  
GREEN STREET STRUCTURE OF THE MBTA  
ORANGE LINE

from the measured time interval between the passage of two wheels and the distance between the wheels.\*

The overall accuracy of the measurement system was  $\pm 1/2$  dB. Frequency response was flat within  $\pm 2$  dB from 1 Hz to 15,000 Hz on the accelerometer channels and 20 Hz to 15,000 Hz on the acoustic channels. Accelerometers were fastened to the structure using mounting studs and epoxy to insure a good bond between the accelerometer and the measurement point. A windscreen was used on each microphone.

The recorded data were analyzed in our laboratory using conventional filters and level recorders. Since the recorded noise and vibration signals were random transient events, a single frequency spectrum or a single time history is not sufficient to present the data from a complete train pass-by. As a compromise, we have obtained strip chart recordings of the time histories of the octave band noise and vibration levels. The readings on the strip chart recordings correspond closely to the reading that would be found with a Precision Sound Level Meter with fast meter response. Examples of the recorded time histories are shown in Figs. 4.4 and 4.5. Note that the vibration levels of the rail show the passage of each wheel pair by the measurement point. The noise level 3 ft from the rail also shows the passage of each wheel pair, suggesting that the wheels and the rail near the wheel/rail contact point are the sources of noise at this point. Vibration levels at points on the deck of the structure and on the steel girders show a typical crescendo-decrescendo time history. The individual wheel and trucks do not stand out.

Further data processing is required to find the integrated spectrum. Although the integrated spectrum is defined as an integration over the spatial extent of the structural component,

---

\* We used the distance between leading wheels on the two trucks of a single car.

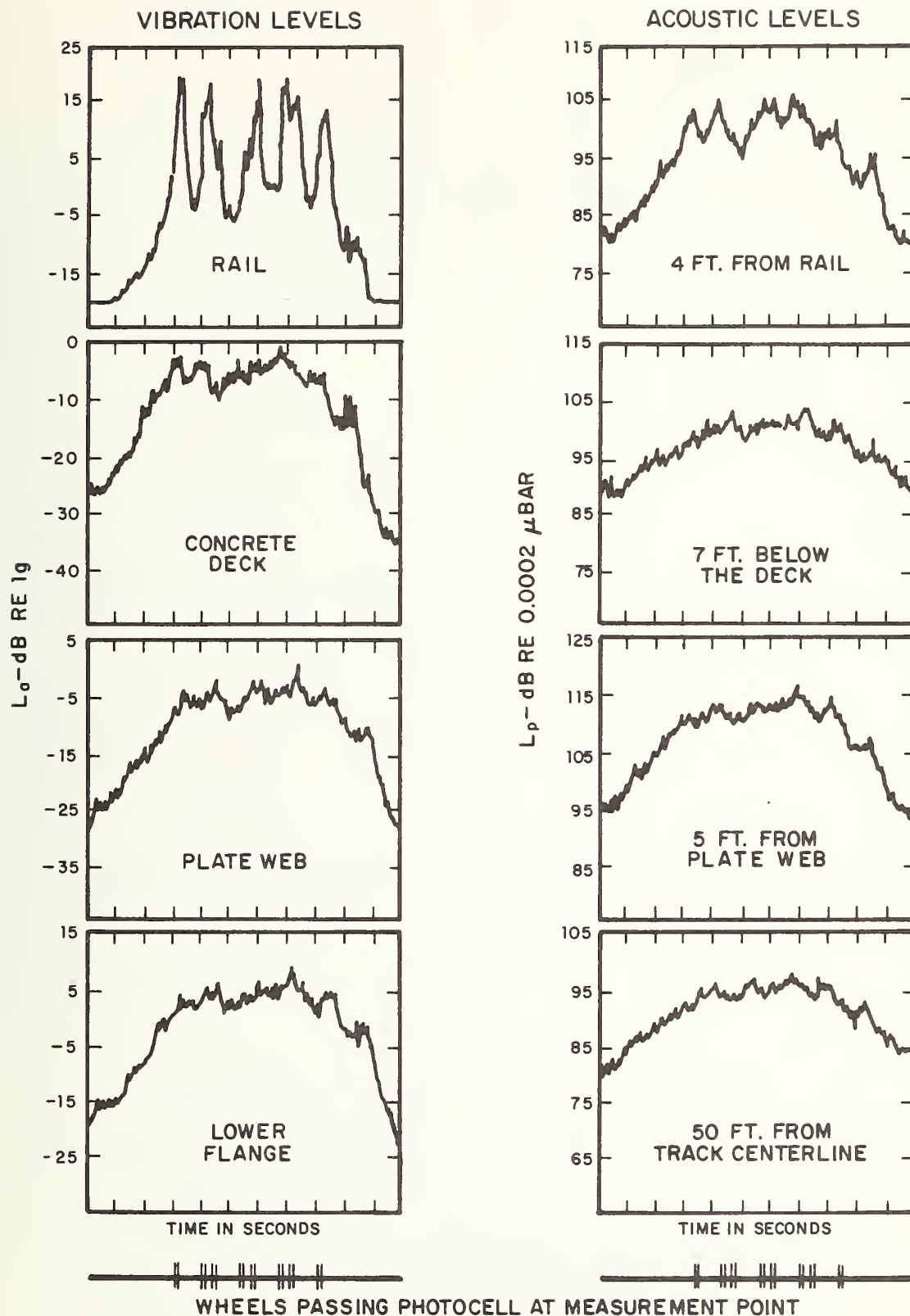


FIG. 4.4 RECORDED TIME HISTORIES OF ACOUSTIC AND VIBRATION LEVELS IN THE 500 HZ OCTAVE BAND FOR THE ANDERSON BRIDGE



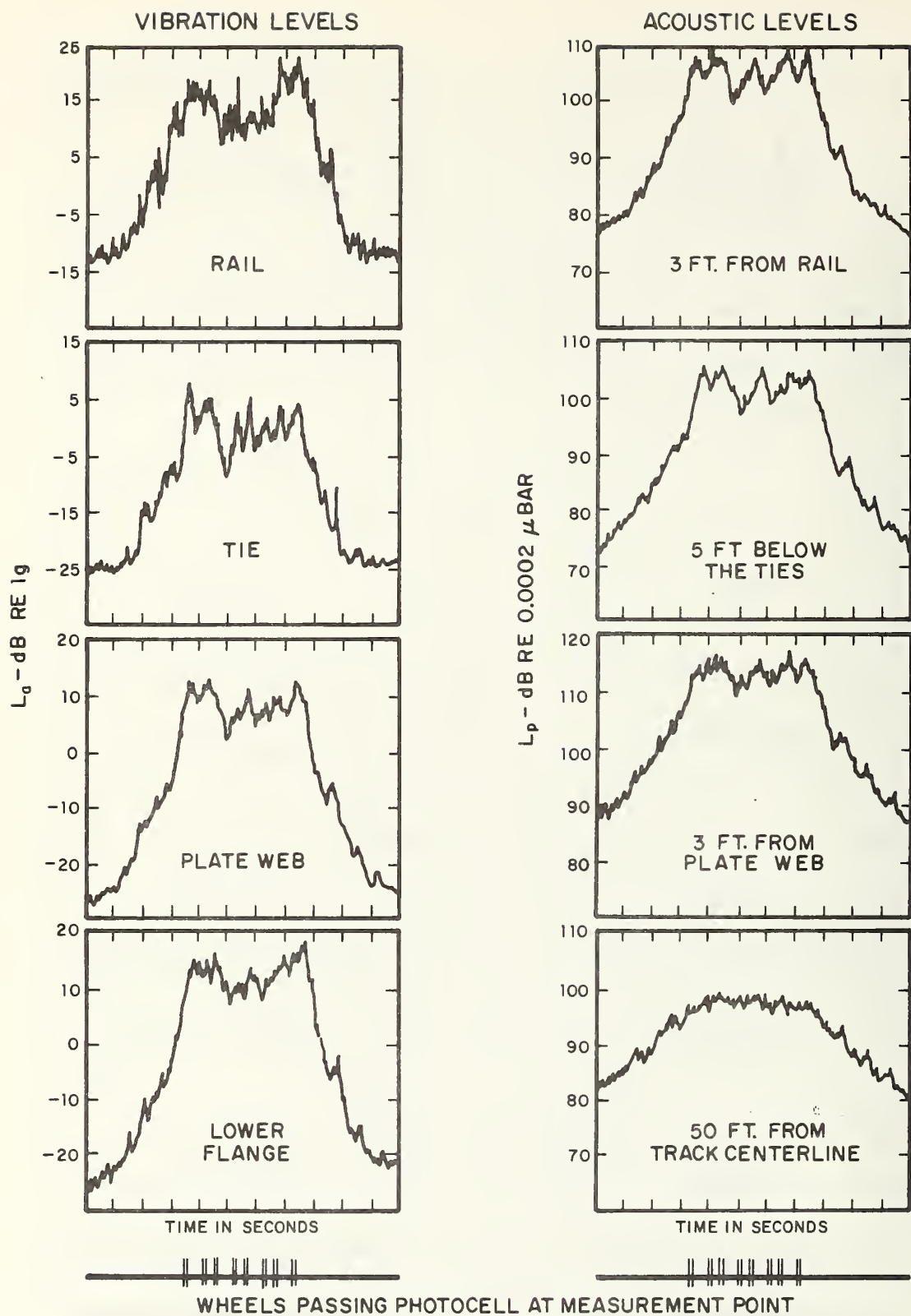


FIG. 4.5 RECORDED TIME HISTORIES OF ACOUSTIC AND VIBRATION LEVELS IN THE 500 HZ OCTAVE BAND FOR THE GREEN STREET STRUCTURE

we assume that it is equivalently equal to the spectrum integrated in time during a train pass-by. The accuracy of this assumption depends on the uniformity of the structure along the track. It is expected to be quite good when continuously welded rail is used on structures with long spans. Less accuracy is expected for older structures where jointed rail is used and the spans are short.

Many measurements were taken to verify the use of a single time history in computing the integrated spectrum. In one set of measurements seven accelerometers were placed along the span on the web of a steel girder structure with a concrete deck and continuously-welded rail. The time histories of the octave band vibration levels for five pass-bys were nearly the same although displaced slightly in time to account for the train passage. The picture of a stationary vibration pattern convected along with the train appears to be valid. It follows, therefore, that an integration of the time history at a single point is equivalent to an integration in space along the span of the structure.

Span-wise measurements were also carried out on the web of an elevated structure with steel girders supporting an open wood tie deck with jointed rail. As for the first structure that was studied, the time histories of the vibration levels at the different points are nearly the same and show a vibration pattern that is convected along with the train.

The prediction model developed in earlier Sections gives the total vibrational energy levels in octave bands for each element of the structure. To obtain these energy levels from the measured data we use the relationship that the time-average kinetic energy equals the time-average potential energy in resonant vibration. Thus, the total energy in a given band of frequencies,  $E$ , can be related to the mass per unit length of structure,  $m$ , and the integrated velocity spectrum,  $I_v(\omega)$ ,

$$E = m I_v(\omega) \Delta\omega \quad (4.1)$$

where  $\Delta\omega$  is the frequency bandwidth. For convenience in presenting the data we define a normalized integrated spectrum level,  $L_{N_n}$ , such that

$$L_{N_v} = 10 \log_{10} \frac{1}{L_t} \frac{I_v(\omega) \Delta\omega}{2.5 \times 10^{-15}} \quad (4.2)$$

where  $L_t$  is the train length in meters and  $I_v(\omega) \Delta\omega$  is in meter<sup>3</sup>/sec<sup>2</sup>. Note that for a long train the normalized integrated spectrum level is simply the average velocity level during the pass-by. If we divide the total energy by the train length, then the energy density level can be written as

$$L_{E_\ell} = L_{N_v} + 10 \log_{10} m - 26 \text{ dB} \quad (4.3)$$

where

$$L_{E_\ell} = 10 \log_{10} \frac{1}{L_t} \frac{E}{10^{-12}} \quad (4.4)$$

and  $E$  is in joules,  $L_t$  is in meters, and  $m$  is in kilograms per meter.

In reducing the vibration and acoustic data, we have used the following procedure. The strip chart recordings of the time histories of the octave band acceleration levels were graphically approximated by a series of straight line segments. Within a given segment, from time  $t_i$  to time  $t_{i+1}$ , the mean-square acceleration\*,  $a^2(t)$ , is given by

---

\* We refer here to the mean-square value based on an average over a period of time that is small compared to the duration of the segment.

$$a^2(t) = a^2(t_i) e^{\frac{s_i}{4.34} (t - t_i)}, \quad t_i < t < t_{i+1} \quad (4.5)$$

where  $s_i$  is the slope of the  $i^{\text{th}}$  segment in dB/second. The integrated acceleration spectrum,  $I_a(\omega)$ , is found by integrating Eq. 4.5 and summing over all segments of the time history and multiplying by the train speed,  $V_t$ ,

$$I_a(\omega) \Delta\omega = V_t \sum_i \frac{4.34 a^2(t_i)}{s_i} \left[ e^{\frac{s_i}{4.34} (t_{i+1} - t_i)} \right] \quad (4.6)$$

where  $\Delta\omega$  is the bandwidth of the octave band being studied. Then, the integrated acceleration spectrum is simply related to the integrated velocity spectrum by

$$I_v(\omega) = \frac{I_a(\omega)}{\omega^2} \quad (4.7)$$

where  $\omega$  is the center frequency of the band. Finally, we substitute the calculated value for the integrated velocity spectrum in Eq. 4.2 to find the normalized integrated spectrum level,  $L_{N_v}$ , and then we use Eq. 4.3 to find the energy density level,  $L_{E_\ell}$ . Comparisons can then be made between data and prediction for the energy density level of each element of the elevated structure.

## 4.2 Anderson Bridge on MBTA Red Line Extension

The Anderson Bridge is a relatively new elevated structure crossing the Neponset River on the MBTA Red Line South Shore Extension. It is an example of a structure with steel plate girders supporting a concrete deck. A photo of the structure is shown in Figs. 3.4 and 4.2. A sketch of the cross-section of the

structure with major dimensions is shown in Fig. 4.6. Other relevant parameters are given in Table 4.1.

The rail used on the Anderson Bridge is continuously welded AREA 115 rail with New York type Liberty rail fasteners. The resilient material used in the fasteners is 70 durometer butyl so that the fastener damping loss factor is quite high and is frequency dependent. Based on a study of rail vibration attenuation data, we have estimated that the fastener damping can be represented by a viscous damping coefficient of 1.3. Then, the damping loss factor is  $\eta_f = 1.3 (\omega/\omega_r)$ , where  $\omega_r$  is the resonancy frequency of the rail on its fasteners, which is estimated to be 1728 rad/sec (275 Hz). However, the dynamic stiffness of the fastener was not known by the manufacturer and we did not take measurements.

In comparing predictions with data we will base our calculations of the elevated structure vibration and noise on measured values of rail vibration. This method of comparison no doubt improves the apparent accuracy of the prediction model. However, until an accurate method for predicting rail vibration is developed in other DOT research activities, we are unable to advance a complete prediction model that starts from a basic description of the wheel/rail interaction. For situations in which measured values of rail vibration are not available, the semi-empirical procedure described in Section 2 must be used. Results for the maximum velocity level of the rail vibration obtained using the procedure of Section 2 are shown in Fig. 4.7 and compared with measured values. The comparison is reasonable considering the lack of precision in the empirical prediction of the maximum rail vibration during the pass-by.

The predicted energy density for the concrete deck and for the steel girder webs are given by Eqs. 3.32a and b. To evaluate these equations we require the damping loss factors for the deck,  $\eta_s$ , and the web,  $\eta_w$ , the coupling loss factor between the rail and the slab,  $\eta_{r,s}$ , the coupling loss factor between the slab and bending vibration of the web,  $\eta_{s,w}$ , and the coupling loss factor between the slab and in-plane vibration of the web,  $\eta_{s,u}$ . Values for the damping loss factors taken from Ref. [17] are listed in Table 4.1. Values for the coupling loss factors are obtained

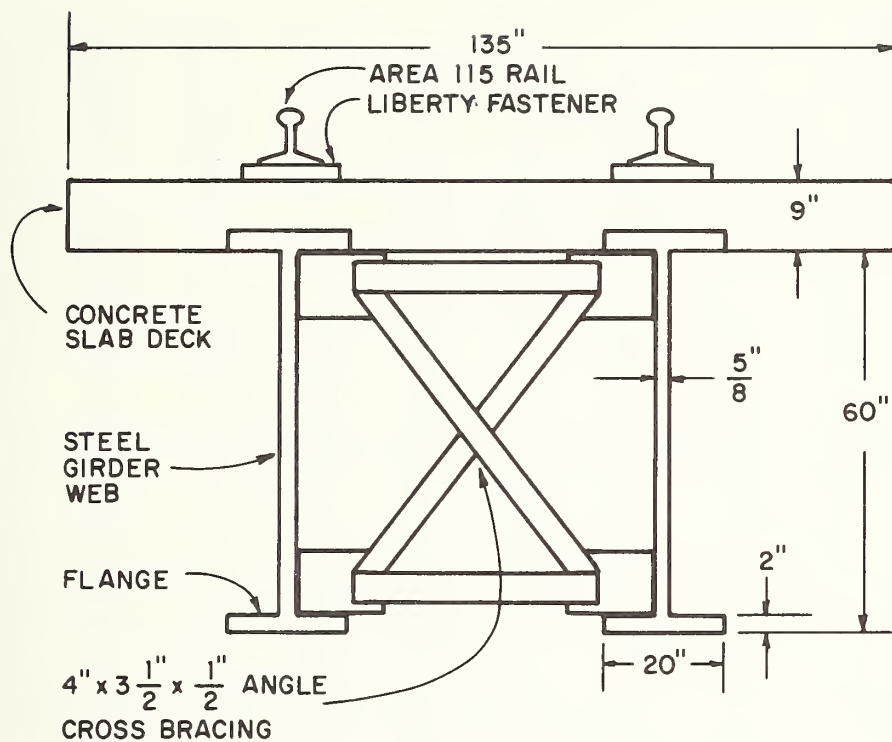


FIG. 4.6 CROSS SECTION OF THE ANDERSON BRIDGE (NEPONSET RIVER BRIDGE) ON THE MBTA RED LINE



RAIL:

RE 115 continuously welded rail on Liberty fasteners

$$m_r = 38.3 \text{ lb/ft} = 1.19 \text{ slugs/ft}$$

$$B_r = E_r I_r = 1.35 \times 10^7 \text{ ft}^2\text{-lbs}$$

$$n_r = 0$$

$$\omega_r = 1728 \text{ rad/sec}; f_r = 275 \text{ Hz}$$

$$\eta_f = 1.3 \times (\omega/\omega_r)$$

$$K_\ell = 3.55 \times 10^6 \text{ lb/ft/ft}$$

DECK:

concrete slab deck (9" thick, 150 lbm/ft<sup>3</sup>)

$$\rho_s = 112.5 \text{ lb/ft}^2 = 3.49 \text{ slugs/ft}^2$$

$$D_s = E_s I_s = 2.03 \times 10^7 \text{ ft-lbs}$$

$$\eta_s = 0.02$$

GIRDER WEB:

$$\rho_{gw} = 25.5 \text{ lb/ft}^2 = 0.792 \text{ slugs/ft}^2 \quad (\text{includes effective mass of stiffeners})$$

$$D_{gw} = E_{gw} I_{gw} = 2.03 \times 10^5 \text{ ft-lbs} \quad (\text{includes effective stiffness of stiffeners})$$

$$\eta_w = 0.002$$

$$\rho_{\text{stiff}} = 18.41 \text{ lb/ft}$$

$$\Delta X_{\text{stiff}} = 12 \text{ ft}$$

$$D_{\text{stiff}} = 1.83 \times 10^6 \text{ ft}^2\text{-lbs}$$

$$c_{\ell, gw} = 1.7 \times 10^4 \text{ ft/sec}$$

TABLE 4.1 PARAMETER VALUES FOR THE  
ANDERSON BRIDGE ON THE MBTA RED LINE

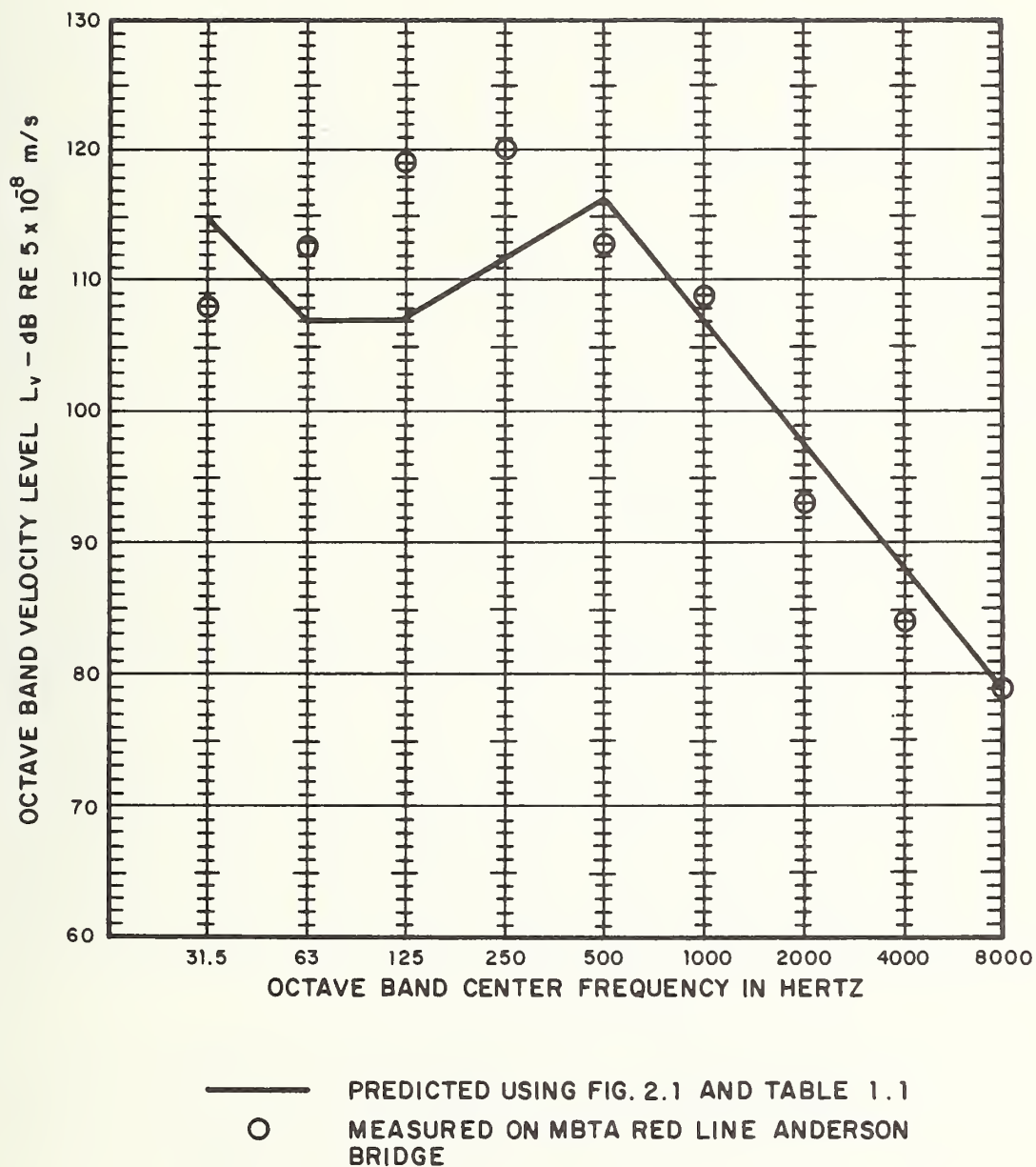


FIG. 4.7 EMPIRICALLY PREDICTED AND MEASURED MAXIMUM RAIL VIBRATION LEVELS FOR THE ANDERSON BRIDGE

from Eqs. 3.33, 3.34, and 3.36. Numerical values for these coupling loss factors are given below:

$$\eta_{r,s} = \left(\frac{\omega}{103,171}\right)^{\frac{1}{2}} \left(\frac{\omega_r}{\omega}\right)^4 (1 + \eta_f^2) \quad (4.8a)$$

$$\eta_{s,w} = \left(\frac{4.84 \times 10^{-4}}{\omega}\right)^{\frac{1}{2}} \quad (4.8b)$$

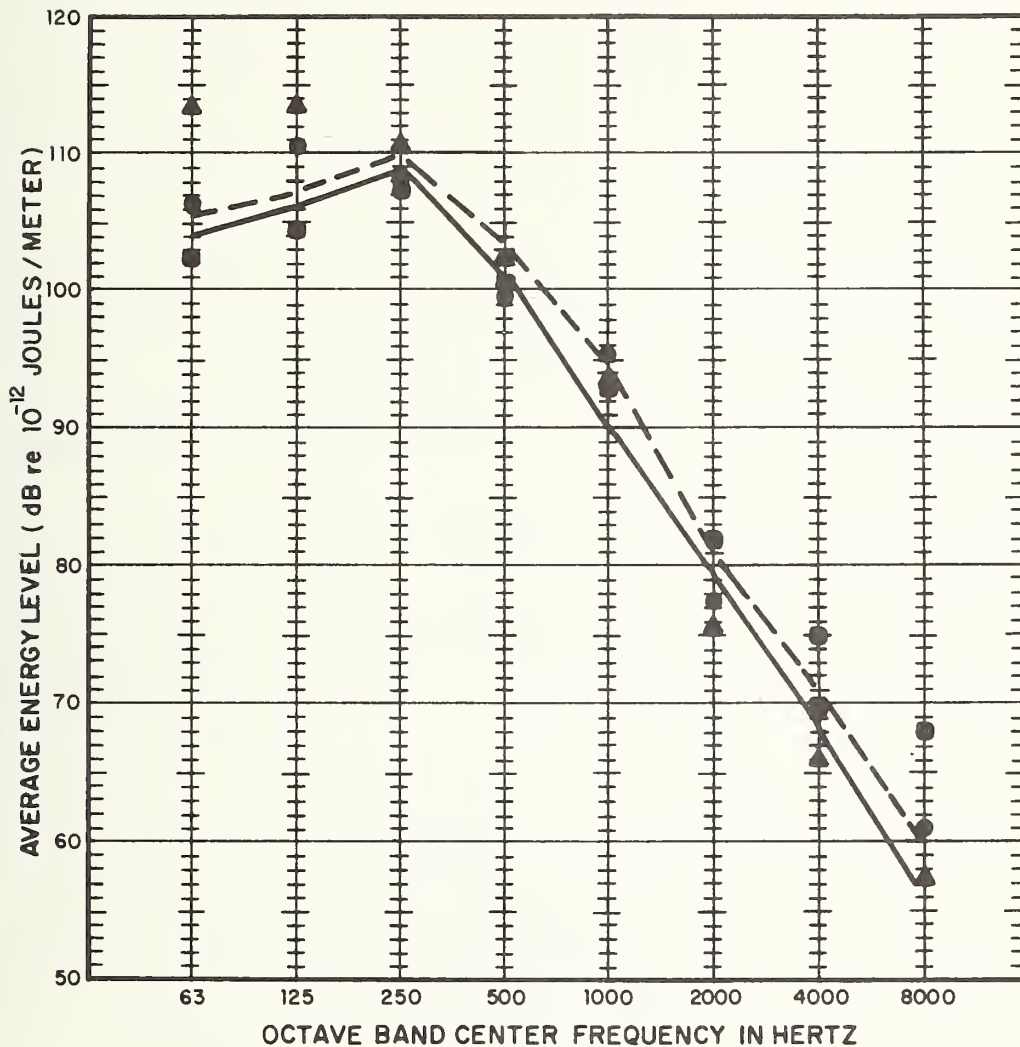
$$\eta_{s,u} = \frac{\left(\frac{145}{\omega}\right)}{1 + \left(\frac{3563}{\omega}\right)^{\frac{1}{2}} + \left(\frac{660}{\omega}\right)} \quad (4.8c)$$

where  $\omega_r$  is the resonance frequency of the rail on its fasteners,  $\omega$  is the center frequency of the octave band being considered, and  $\eta_f$  is the fastener damping loss factor. For comparison with data we take the resonance frequency  $\omega_r$  to be 1728 rad/sec (275 Hz), and  $\eta_f$  to be  $1.3 \times (\omega/\omega_r)$ .

Energy levels obtained from Eqs. 3.32 are shown in Fig. 4.8 and compared with data. At high frequencies, at and above 250 Hz, the predicted energy levels are within 3 dB of the measured data for almost every frequency. We consider this accuracy to be representative to the accuracy generally expected for the prediction model.

At lower frequencies, below 250 Hz, predicted values are well below the measured data. This inaccuracy is due to the improper use of Eqs. 3.32 for the frequency range below the rail fastener resonance frequency. However, since the contribution to the A-weighted noise radiation from these low frequency bands is not significant, we have not tried to obtain a more accurate prediction at these frequencies.

Investigation of Eqs. 3.32 which give the deck and web energies and Eqs. 4.8 for the coupling loss factors lead to some interesting conclusions for this structure. First, we note that



	MEASURED DATA	PREDICTION USING MEASURED RAIL VIBRATIONAL ENERGY
RAIL	■	
DECK	●	— — —
WEB	▲	—————

FIG.4.8 PREDICTED AND MEASURED VALUES OF SPATIALLY AVERAGED ENERGY FOR THE ANDERSON BRIDGE (A CONCRETE DECK, PLATE -WEB, STEEL GIRDER STRUCTURE )

the coupling loss factors for the web are comparable to or much greater than the damping loss factor of the web. This means that effective control of the web vibration must first include a web damping treatment. Only after the web damping loss factor has been increased can the web vibration be reduced by decreasing the coupling between the deck and the web. The coupling loss factors in Eqs. 4.8 show that the dominant mechanism of vibration transmission from the deck to the web is the transmission of energy from bending vibrations of the deck to in-plane vibration of the web. Energy due to in-plane motion is then transmitted to bending motion by coupling mechanisms at cross bracing and elsewhere. For equal levels of vibratory energy noise radiation from the bending motion of the web is greater than from in-plane motion. Coupling between the deck and in-plane motion of the web could be reduced by using a resilient material between the deck and the upper flange of the girders. However, this approach may not be practically feasible, since the load bearing capability of the structure could be reduced. The coupling loss factors can also be reduced by lowering the resonance frequency of the rail on its fasteners. As a general rule, the fastener stiffness should be as low as possible within constraints of vehicle ride comfort and safety. However, some caution must be used in applying this rule since use of a soft fastener can result in lower effective rail damping and consequently higher rail vibrational energy and more noise radiation from the rail. The fastener stiffness and damping should be selected to minimize the total noise radiation from the rail and structure. A second way of lowering the rail resonance frequency is to increase the mass of the rail. Actual use of a heavier rail is probably not economically feasible. However, it is possible to add mass to the rail by mounting the rail on wood or concrete ties and then using a resilient fastener under the ties. This arrangement may not appreciably change the rail vibration velocity levels.

The maximum wayside noise levels are predicted by using the calculated integrated velocity spectrum levels for each component

of the elevated structure together with calculated values for the radiation efficiencies from Section 3.4 to find the total radiated acoustic power,

$$W_{\text{rad}}(\omega) \Delta\omega = \rho_o c_o \sum_i I_{v_i}(\omega) \Delta\omega \sigma_{\text{rad},i}(\omega) P_{\text{rad},i} \quad (4.9)$$

where  $W_{\text{rad}}(\omega) \Delta\omega$  is the total power radiated in the frequency band  $\Delta\omega$ ,  $I_{v_i}$  is the integrated velocity spectrum of element  $i$  of the elevated structure,  $\sigma_{\text{rad},i}$  is the radiation efficiency for element  $i$ , and  $P_{\text{rad},i}$  is the radiating perimeter of element  $i$ . The radiated power level  $L_w$  is given by

$$L_w = 10 \log_{10} \frac{W_{\text{rad}}(\omega) \Delta\omega}{10^{-12}} \quad \text{with } W_{\text{rad}}(\omega) \Delta\omega \text{ in watts} \quad (4.10)$$

Finally, the maximum noise level during the pass-by,  $L_p$ , is given by

$$L_p = L_w - 20 \log_{10} D + 10 \log_{10} \left\{ \frac{2D}{L} \arctan \frac{L}{2D} \right\} \quad (4.11)$$

where  $L$  is the train length in meters and  $D$  is the distance from the measurement point to the track centerline in meters. When  $D$  is much less than  $L$ , Eq. 4.11 becomes

$$L_p = L_w - 10 \log_{10} D + 10 \log \frac{\pi}{L} \quad \text{for } D \ll L \quad (4.12)$$

As one check on the accuracy of the prediction model, we use measured values for the integrated velocity spectrum level in predicting the wayside noise level. Results are shown in Fig. 4.9. Comparisons between predicted and measured levels are within 2 dB



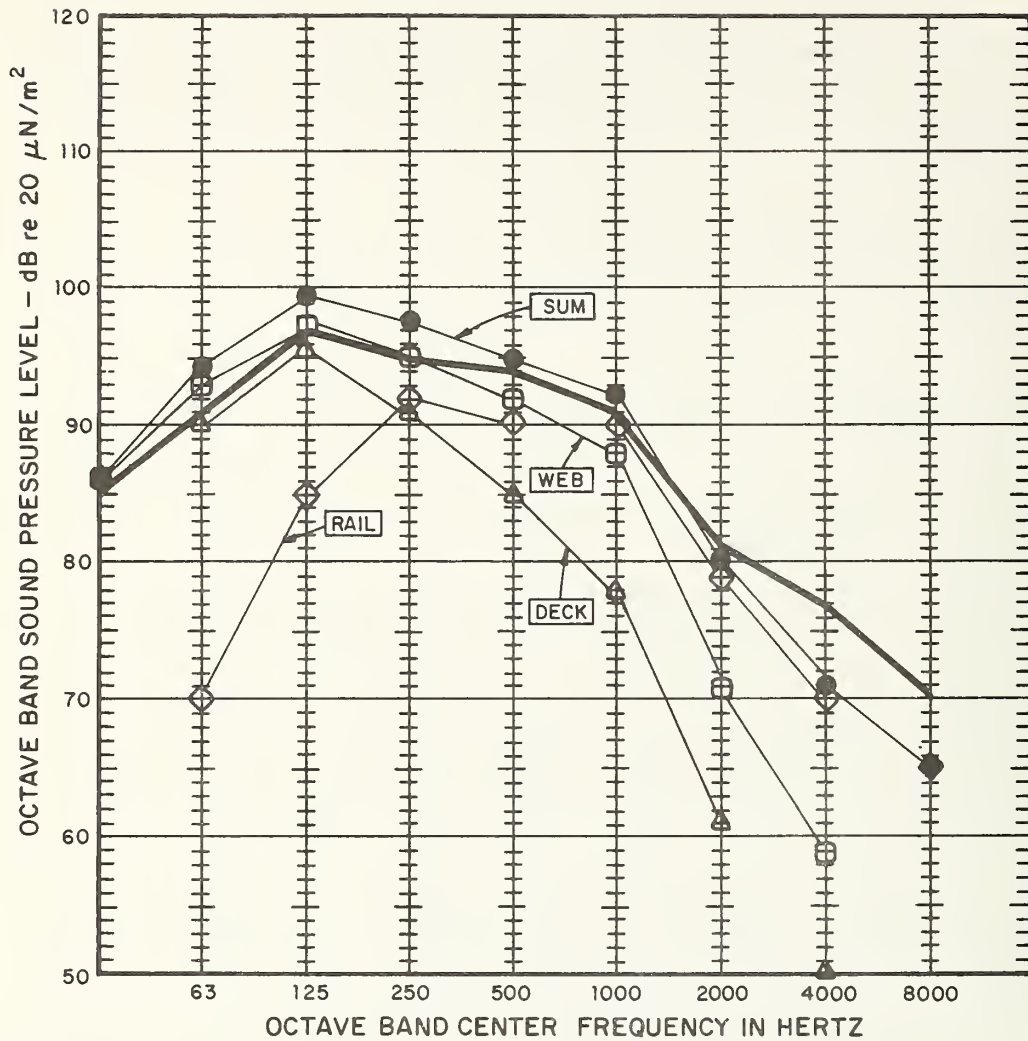


FIG. 4.9 PREDICTED AND MEASURED NOISE RADIATION LEVELS FROM ELEMENTS ON THE ANDERSON BRIDGE

for the most important frequency bands contributing to the A-weighted noise. However, at high frequencies, above 2000 Hz, the measured levels are higher than prediction. This result is believed to be due to radiation from the wheels and other car surfaces which has not been included in the prediction model.

Below 1000 Hz the dominant sources of elevated structure noise are the webs of the steel girders. At higher frequencies the dominant sources are the rails. Elimination of the webs and the rail as noise sources by reducing their vibration level or by enclosures, coverings and barriers would reduce the noise levels in the frequency bands centered at 250, 500, 1000 and 2000 Hz. The noise in the lower frequency bands would not be reduced because of slab radiation. Noise in the higher frequency bands would not be reduced because of sources on the vehicle itself.

Eliminating the rails as significant noise sources would reduce wayside noise levels by only 2 dBA. Eliminating only the webs as significant sources would also provide only a 2 dBA reduction in noise. However, elimination of both the rail and webs as sources would provide 10 dBA of noise reduction, although the noise radiation from the vehicle may prevent this degree of noise reduction from actually being achieved.

The overall accuracy of the prediction model for the particular structure being studied is shown in Fig. 4.10. Agreement between prediction and measured data is limited by the accuracy with which rail vibration levels have been predicted, see Fig. 4.7.

#### 4.3 Elevated Structure near Green Street on MBTA Orange Line

The elevated structure near Green Street on the MBTA Orange Line is typical of older structures that are in use in New York, Chicago, Boston, and Philadelphia. A photo of the structure is shown in Fig. 3.3. Other relevant information is shown in Fig. 4.11 and in Table 4.2.

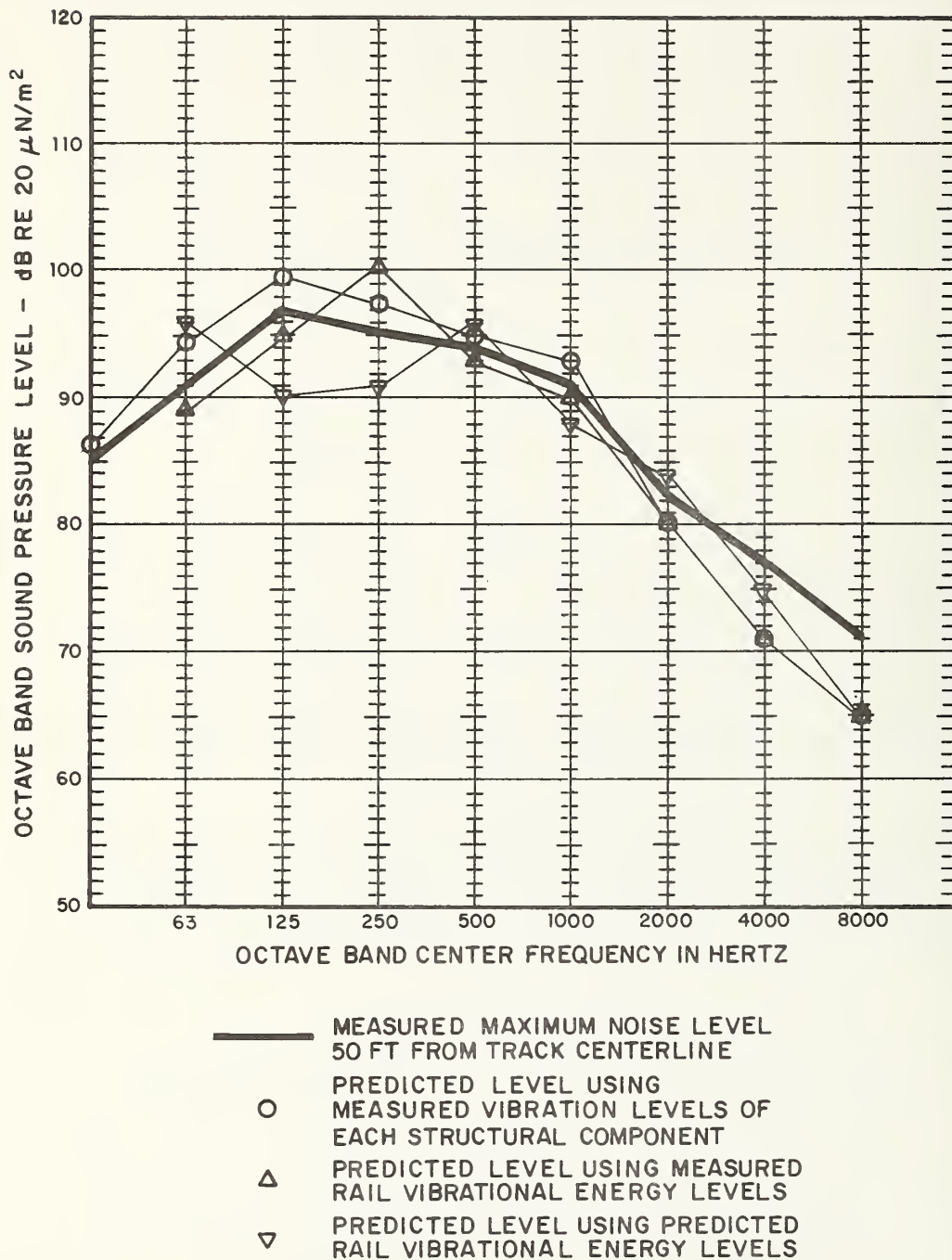


FIG. 4.10 COMPARISON OF PREDICTED WAYSIDE NOISE LEVELS WITH MEASURED LEVELS

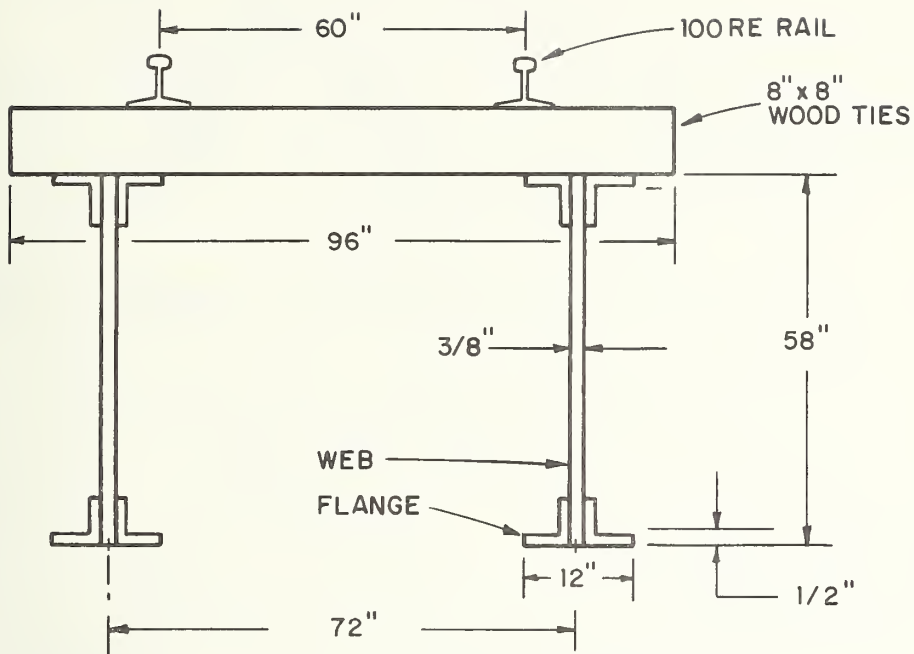
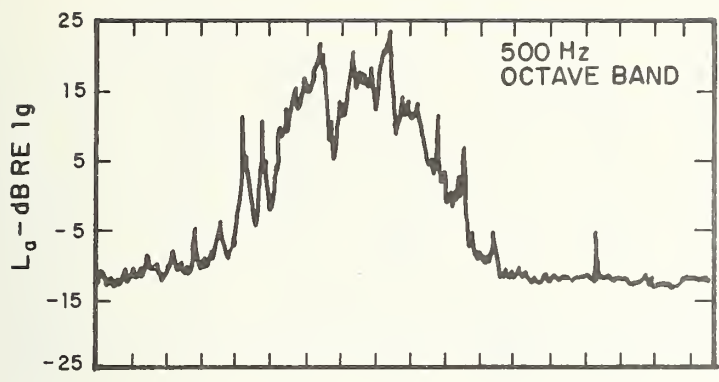


FIG.4.11 CROSS SECTION OF THE GREEN STREET STRUCTURE  
(AN OPEN WOOD TIE DECK, PLATE-WEB, STEEL-GIRDER STRUCTURE)

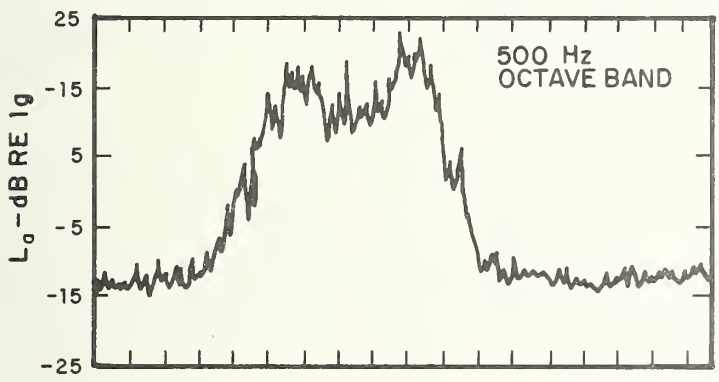
The rail used on the Orange Line is jointed AREA 100 rail fastened directly to wood ties. The ties form an open deck which is supported by steel I-beam girders with plate webs. Because of the age of the structure, many of the ties were not rigidly connected to the upper flanges of the girders. We assume, however, that the weight of the deck and the loading by the vehicle is sufficient to maintain the contact between the tie and the girder flange so that the system dynamics are linear.

The resonance frequency of the rail on its supports is determined by the compressional stiffness of the ties and the degree to which contact is maintained between the rail and the ties. If we assume that perfect contact is always maintained along the entire length of track then the rail resonance obtained using the static stiffness of the ties is 470 Hz. However, we do not believe that perfect contact is maintained. We estimate the effective contact area is approximately one fourth of the nominal contact area between the rails and the ties. Thus, we expect that the stiffness calculated by assuming perfect contact between rail and ties should be reduced by a factor of four to obtain the average stiffness over the length of the train. In this case the average resonance frequency is approximately 235 Hz. We will use this value in our calculations. Clearly, our approach here cannot be completely justified without further work.

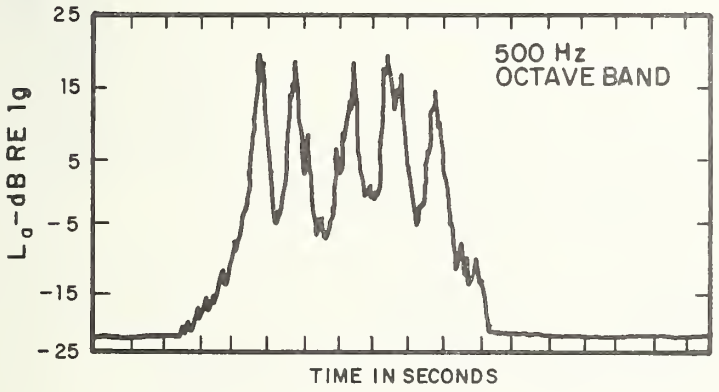
As in the previous Section we will base our calculations of elevated structure noise and vibration on measured values of rail vibration. Time histories of typical octave band acceleration levels for the rail are shown in Fig. 4.12. The measured levels peak each time a wheel passes the measurement point. However, as for the MBTA Red Line data the heights of the different peaks vary by up to 10 dB. This variation is probably due to variations in wheel condition. Other peaks in the time histories occur which do not correspond to the passage of a wheel. These are due to the impact of the wheels at the rail joints.



MBTA ORANGE LINE  
HATHON SQUARE  
ELEVATED STRUCTURE  
JOINTED RAIL



MBTA ORANGE LINE  
GREEN STREET  
ELEVATED STRUCTURE  
JOINTED RAIL



MBTA RED LINE  
ANDERSON BRIDGE  
CONTINUOUSLY - WELDED  
RAIL ON RESILIENT  
FASTENERS

FIG. 4.12 TIME HISTORIES OF THE RAIL VIBRATION LEVEL



Use of the measured rail vibration data to calculate a normalized integrated spectrum level according to the procedures of Section 4.1 is difficult because of the rapid fluctuation of the observed levels. Therefore, we did not use the described computational procedure and instead proceed directly to take a visual average of the levels. We estimate the accuracy of this visual averaging to be  $\pm 1\frac{1}{2}$  dB; within the expected range of accuracy for the prediction model. For other elements of the elevated structure we used the integration procedure described in Section 4.1 to find the integrated spectrum level and the energy density level in the different octave bands. Results are shown in Fig. 4.13 where they can be compared with values obtained using the prediction procedure.

The predicted energy density for the wood tie deck and for the steel girder webs are given by Eqs. 3.42. To evaluate these equations we require the damping loss factor for the ties,  $\eta_t$ ; the damping loss factors for in-plane and bending motion of the webs,  $\eta_u$  and  $\eta_w$ ; the coupling loss factor between the rail and in-plane motion of the web and the rail,  $\eta_{r,u}$ ; and the coupling loss factor between the ties and bending motion of the web,  $\eta_{w,t}$ . The damping loss factor for the ties is taken to be that of wood, while the loss factor for bending of the web is due almost entirely to radiation losses, since the material loss factor for steel is so small. The damping loss factor for in-plane motion of the web is taken to be that of steel and can be set to zero in the calculations since it is much smaller than the loss factor for bending of the web. The two coupling loss factors are given by Eqs. 3.43 and 3.44. Parameter values required to evaluate these equations are given in Table 4.2. Using these values we find

$$\eta_{r,u} = 6.52 \times 10^{-5} \omega_r \left( \frac{\omega}{\omega_r} \right)^3 \quad (4.13a)$$

and

$$\eta_{w,t} = \frac{0.0438}{\sqrt{\omega}} \quad (4.13b)$$

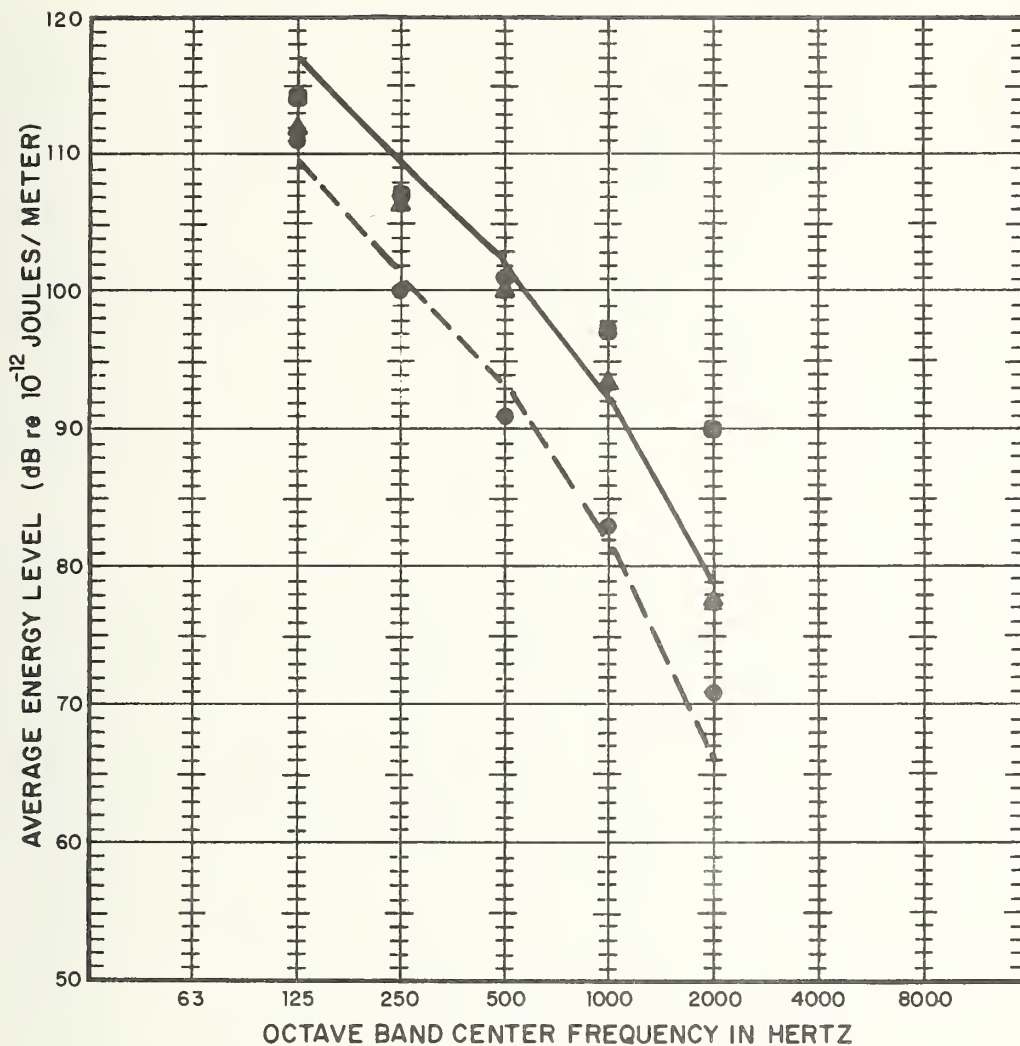


FIG. 4.13 PREDICTED AND MEASURED VALUES OF SPATIALLY AVERAGED ENERGY FOR THE GREEN STREET STRUCTURE (AN OPEN WOOD TIE DECK, PLATE-WEB, STEEL-GIRDER STRUCTURE)

#### RAIL:

RE 100 jointed rail on wood ties

$$m_r = 33.5 \text{ lb/ft} = 1.04 \text{ slugs/ft}$$

$$B_r = E_r I_r = 1.02 \times 10^7 \text{ ft}^2\text{-lbs}$$

$$\eta_r = 0$$

$$\omega_r = 1475 \text{ rad/sec}; f_r = 235 \text{ Hz}$$

$$\eta_f = 0.02$$

$$K_t = 2.26 \times 10^6 \text{ lb/ft/ft}$$

#### TIES:

8" by 8" by 8' long ties spaced 16" on centers

$$\rho_t = 16.7 \text{ lb/ft}^2 = 0.519 \text{ slugs/ft}^2$$

$$D_t = 3.20 \times 10^6 \text{ ft-lbs}$$

$$\eta_t = 0.06$$

#### GIRDER WEBS

3/8" thick steel plate webs

$$\rho_{gw} = 15.1 \text{ lb/ft}^2 = 0.469 \text{ slugs/ft}^2$$

$$D_{gw} = 1.10 \times 10^4 \text{ ft-lbs}$$

$$c_{l,gw} = 1.7 \times 10^4 \text{ ft/sec}$$

$$\eta_w = 0.002$$

TABLE 4.2 PARAMETER VALUES FOR THE ELEVATED  
STRUCTURE NEAR GREEN STREET ON THE MBTA ORANGE LINE

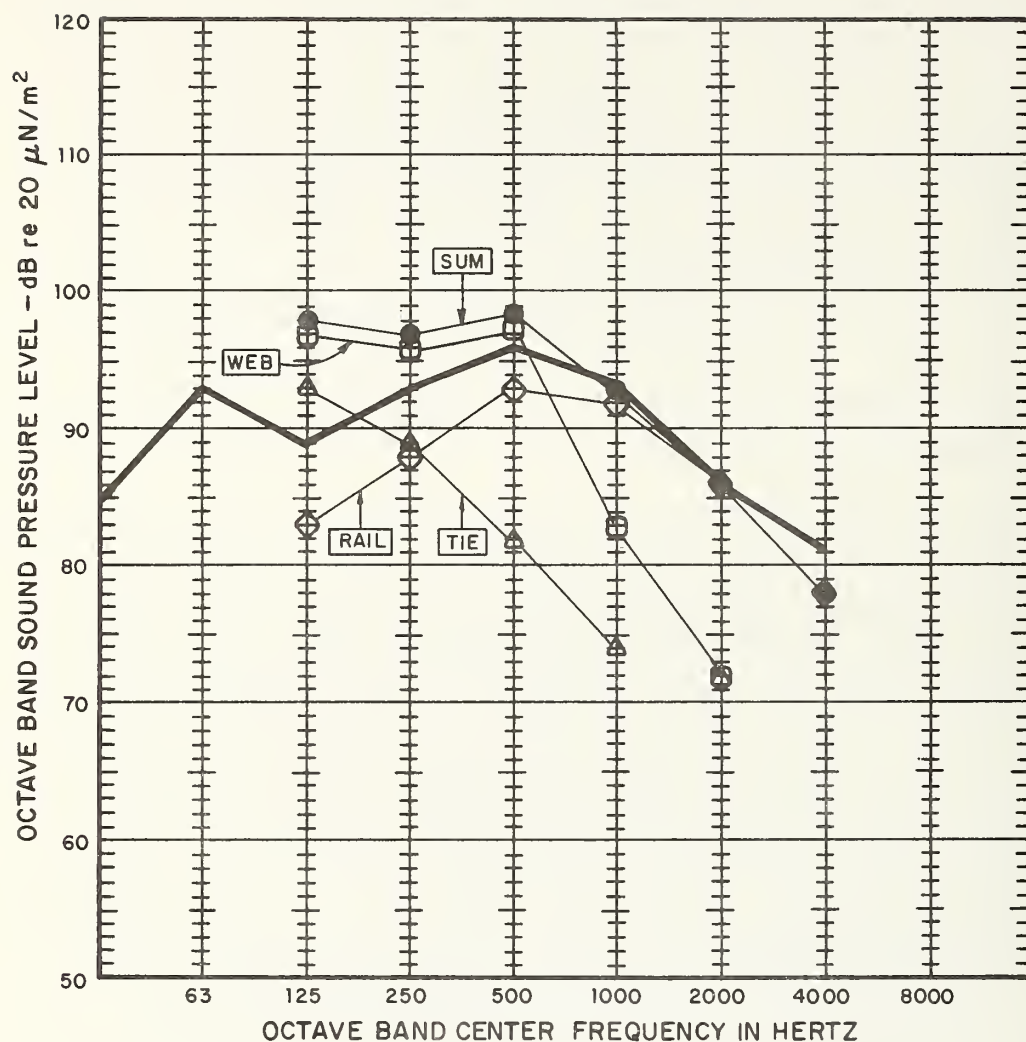
where  $\omega_r$  is the resonance frequency of the rail on the ties and  $\omega$  is the octave band center frequency.

The agreement between predicted values and measured data is within 3 dB for most frequency bands. However, at low frequencies, octave bands centered on 125 and 250 Hz, the prediction model gives values for the web energy density level that are too high. Since similar inaccuracies were observed for the Anderson Bridge we expect that the prediction model may consistently give values for the web vibration at low frequencies that are too high. This inaccuracy is not surprising since we have used a prediction model that is valid only at frequencies above the rail/fastener resonance frequency. Fortunately, the noise radiation in these low frequency bands does not contribute significantly to the A-weighted wayside noise levels.

Predicted noise levels 50 ft from the track centerline are shown in Fig. 4.14 and compared with measured data. The predicted levels have been obtained by using measured vibration levels for each element. Comparison of prediction with data again shows that the model predicts too much noise radiation at low frequencies. However, in spite of this inaccuracy the model allows us to gain a clear indication of the relative contribution of the different sources to the total radiated noise. At high frequencies the dominant noise source is the rail. At lower frequencies the webs become the dominant source. Thus, to be effective a noise control program must consider methods to reduce the noise radiation from both the web and the rail. Elimination of the web as a major source by reducing its vibration level or by use of an enclosure or covering would reduce overall noise levels by only 2 dBA. Similarly, elimination of the rail as a major source would reduce levels by only 3 to 4 dBA. However, if both sources were quieted the total noise would be reduced by over 10 dBA\*. Noise radiation from the ties is not a major problem because their vibration levels are well below those of the other elements due to the fairly high material damping of wood.

---

\* This level of noise reduction may not be achieved if the vehicle becomes significant. Further work on this matter is needed.



- MEASURED MAXIMUM NOISE LEVEL 50 FT. FROM TRACK CENTERLINE
- PREDICTED NOISE LEVEL USING MEASURED VIBRATION LEVELS
- ◇ RAIL RADIATION
  - UPPER FLANGE AND WEB RADIATION
  - △ TIE RADIATION
  - SUM OF PREDICTED RADIATION LEVELS

FIG. 4.14 PREDICTED AND MEASURED NOISE RADIATION LEVELS FROM ELEMENTS ON THE GREEN STREET ELEVATED STRUCTURE



Reduction of the noise radiation from the rail could be best accomplished by reducing the rail vibration. When possible, the rail joints should be eliminated and the wheels and rails kept in a smooth condition by periodic rail grinding. Use of resilient fasteners with high damping would provide damping to the rail and result in lower vibration levels. Also, it may be possible to apply a damping treatment directly to the rail. Reduction of the radiation from the rail by use of barriers would be difficult because of the openness of the tie deck.

Reduction of the noise radiation from the web could be accomplished by either reducing the web vibration levels or by use of an enclosure or covering. Investigation of Eqs. 3.42 which give the deck and web energies and Eqs. 4.13 for the coupling loss factor lead to the conclusion that a reduction of the web vibration can be obtained by two steps: first, the web damping must be increased; second, a resilient material should be used between the ties and the girders to reduce the coupling between the rail and in-plane motion of the web. A second equally valid approach would be to reduce the rail vibration so that the excitation of the web is decreased.

In our measured data we observed that the wayside noise levels jump approximately 10 dB(A) when the train crosses onto the bridge. Yet we conclude that the rail is as important to the total elevated structure noise as are the other components of the structure. We are led to the further conclusion that the rail vibration levels are higher when the train is on the elevated structure than when it is at-grade on tie and ballasted track. This conclusion may be unique to the specific case studied.



#### 4.4 Elevated Structure Near Hathon Square on MBTA Orange Line

The elevated structure near Hathon Square is similar to the structure near Green Street except that the girder webs are formed by bolting together various truss elements. A photo of the structure is shown in Fig. 3.2. Other relevant information is shown in Fig. 4.15 and in Table 4.3.

The rail used on the MBTA Orange Line is jointed AREA 100 rail fastened directly to wood ties. The ties form an open deck which is supported by steel girders. As in the case of the Green St. structure, we believe that the actual contact area between the rails and the ties is much less than if there were perfectly matching surfaces. Thus, in calculating the resonance of the rail we reduce the stiffness of the ties by a factor of four. As in the previous case, the resonance frequency is taken to be 235 Hz.

We will base our calculations of elevated structure noise and vibration on measured values of rail vibration. The time histories of the octave band acceleration levels for the rail were found to be quite similar to those found for the Green St. structure. Therefore, the procedure outlined in Section 4.3 was used to compute energy density levels for the rail.

The predicted energy density for the wood tie deck and for the girder elements is given by Eqs. 3.46. The coupling loss factors in these equations are given by Eqs. 3.47 and 3.49. Using the parameter values from Table 4.3 we find

$$\eta_{r,t} = \frac{\left(\frac{\omega_r}{\omega}\right)^4 (\omega)^{\frac{1}{2}}}{0.02 \left(\frac{\omega_r}{\omega}\right)^4 \omega - 2 \left(\frac{\omega_r}{\omega}\right)^2 (\omega)^{\frac{1}{2}} + 99.5} \quad (4.14a)$$

and

$$\eta_{t,u} = \frac{409}{\omega + 65.5 (\omega)^{\frac{1}{2}} + 2145} \quad (4.14b)$$

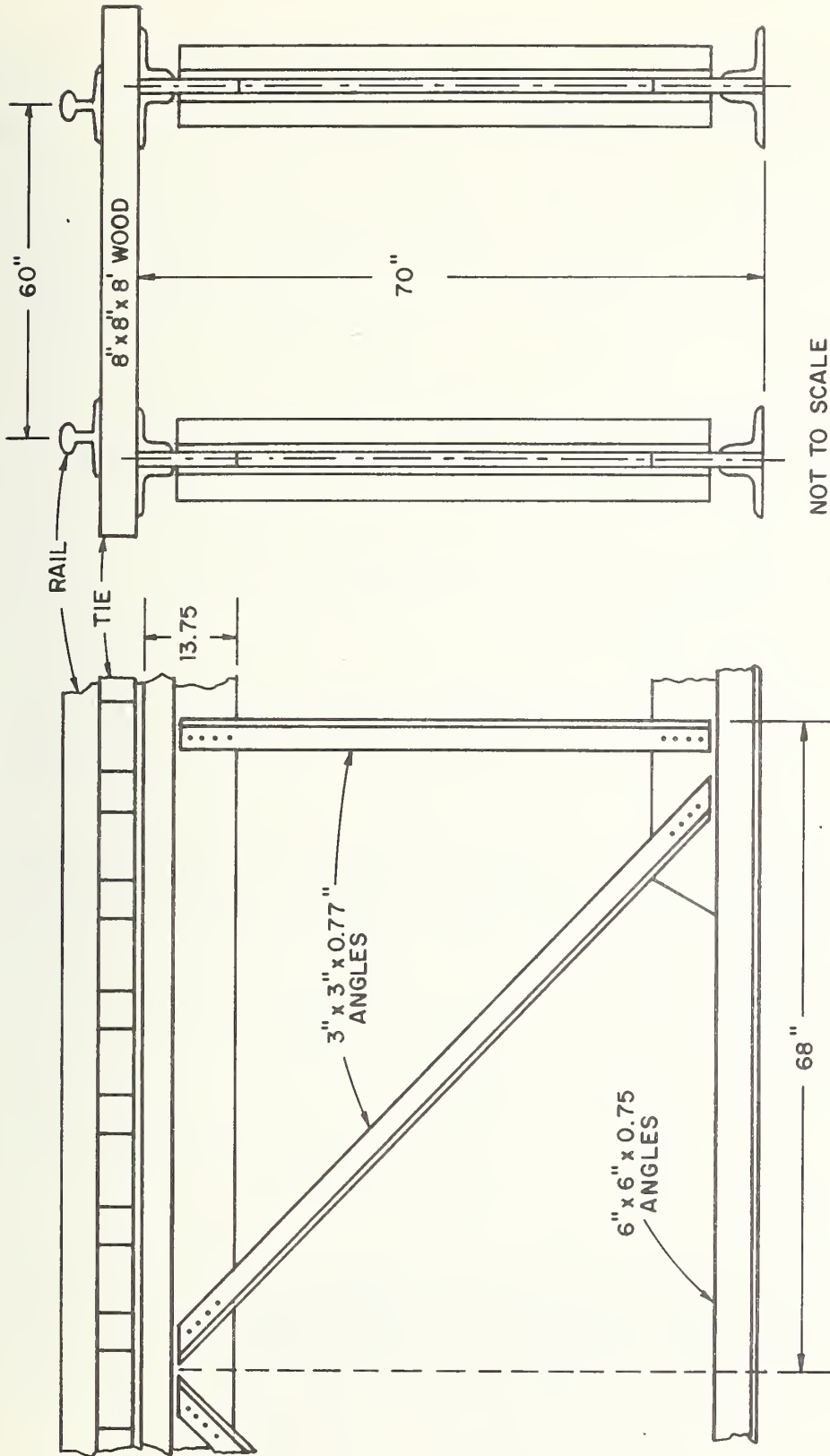


FIG. 4.15 CROSS SECTION AND SIDE VIEW OF THE ELEVATED STRUCTURE NEAR HATHON SQUARE ON THE MBTA ORANGE LINE

RAIL:

RE: 100 jointed rail on wood ties

$$m_r = 33.5 \text{ lb/ft} = 1.04 \text{ slugs/ft}$$

$$B_r = E_r I_r = 1.02 \times 10^7 \text{ ft}^2\text{-lbs}$$

$$\eta_r = 0$$

$$\omega_r = 1476 \text{ rad/sec}; f_r = 235 \text{ Hz}$$

$$\eta_f = 0.02$$

$$K_t = 2.26 \times 10^6 \text{ lb/ft/ft}$$

TIES:

8" by 8" by 8' long ties spaced 16" on centers

$$\rho_t = 16.7 \text{ lb/ft}^2 = 0.519 \text{ slugs/ft}^2$$

$$D_t = 3.20 \times 10^6 \text{ ft-lbs}$$

$$\eta_t = 0.06$$

GIRDER WEBS:

open webs comprised of steel beams (equivalent distributed properties are given below)

$$\rho_{gw} = 6.48 \text{ lb/ft}^2 = 0.20 \text{ slugs/ft}^2$$

$$c_{l,gw} = 1.7 \times 10^4 \text{ ft/sec}$$

$$\eta_w = 0.002$$

$$\eta_u = 0.002$$

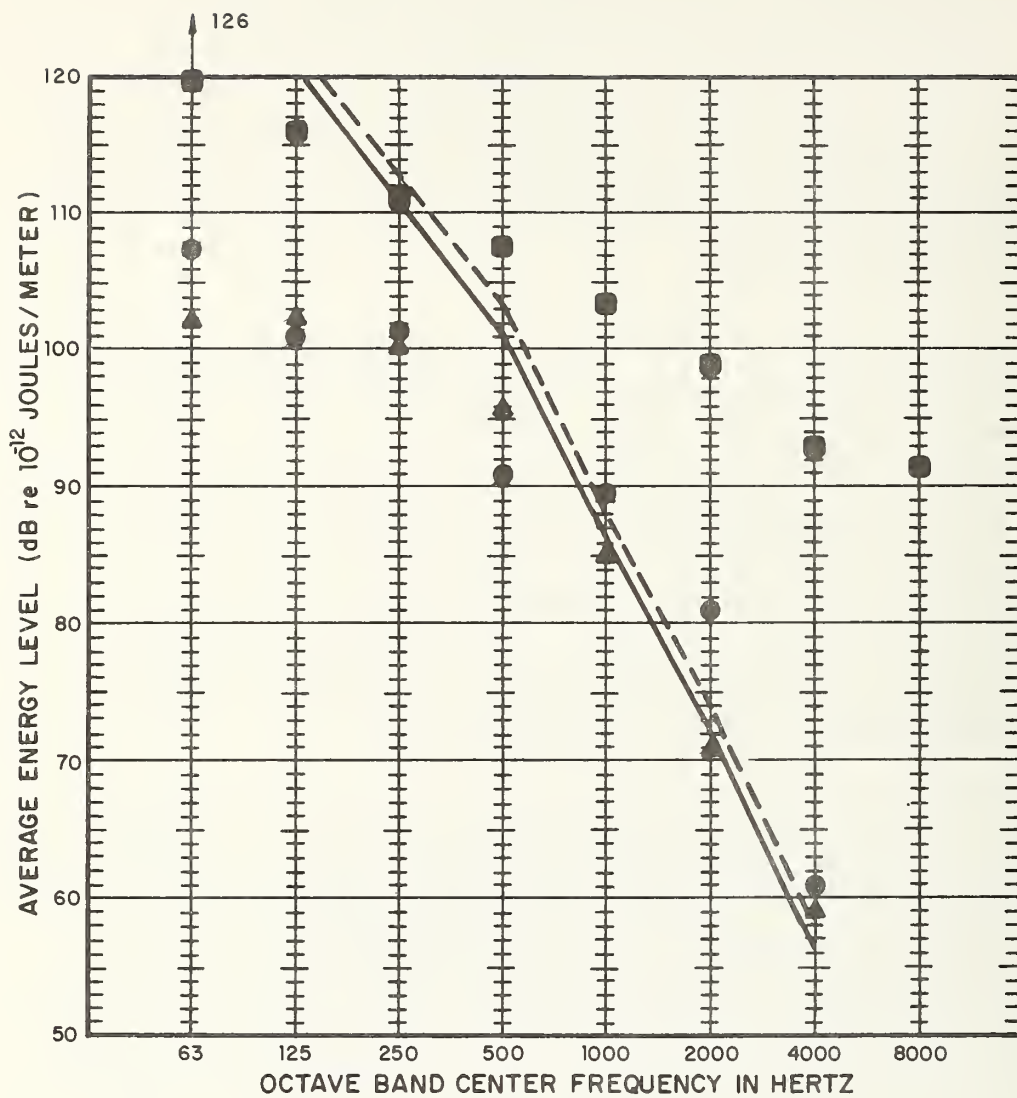
TABLE 4.3 PARAMETER VALUES FOR THE ELEVATED  
STRUCTURE NEAR HATHON SQUARE ON THE MBTA ORANGE LINE

where  $\omega_r$  is the resonance frequency of the rail on the tie deck, assumed to be 235 Hz ( $\omega_r = 1476$ ), and  $\omega$  is the band center frequency. Parameter values for the damping loss factors are given in Table 4.3. The damping loss factor for the tie deck,  $\eta_t$ , has been taken to be that for wood. The damping loss factors for the y and z components of the vibration for the structural members forming the web have been taken to be equal and due only to acoustic radiation losses.

The predicted energy density levels are shown in Fig. 4.16 and compared with measured levels. The agreement between theory and experiment is good above 500 Hz. However, at lower frequencies, the predicted levels are significantly higher than those measured. This error may be due to inaccuracies in prediction of the rail resonance frequency or to improper use of Eqs. 3.46 at frequencies below the rail resonance frequency. Fortunately, the contribution of the low frequency vibration to A-weighted levels is not large. Thus, in this report we will not attempt to improve the prediction at these low frequencies.

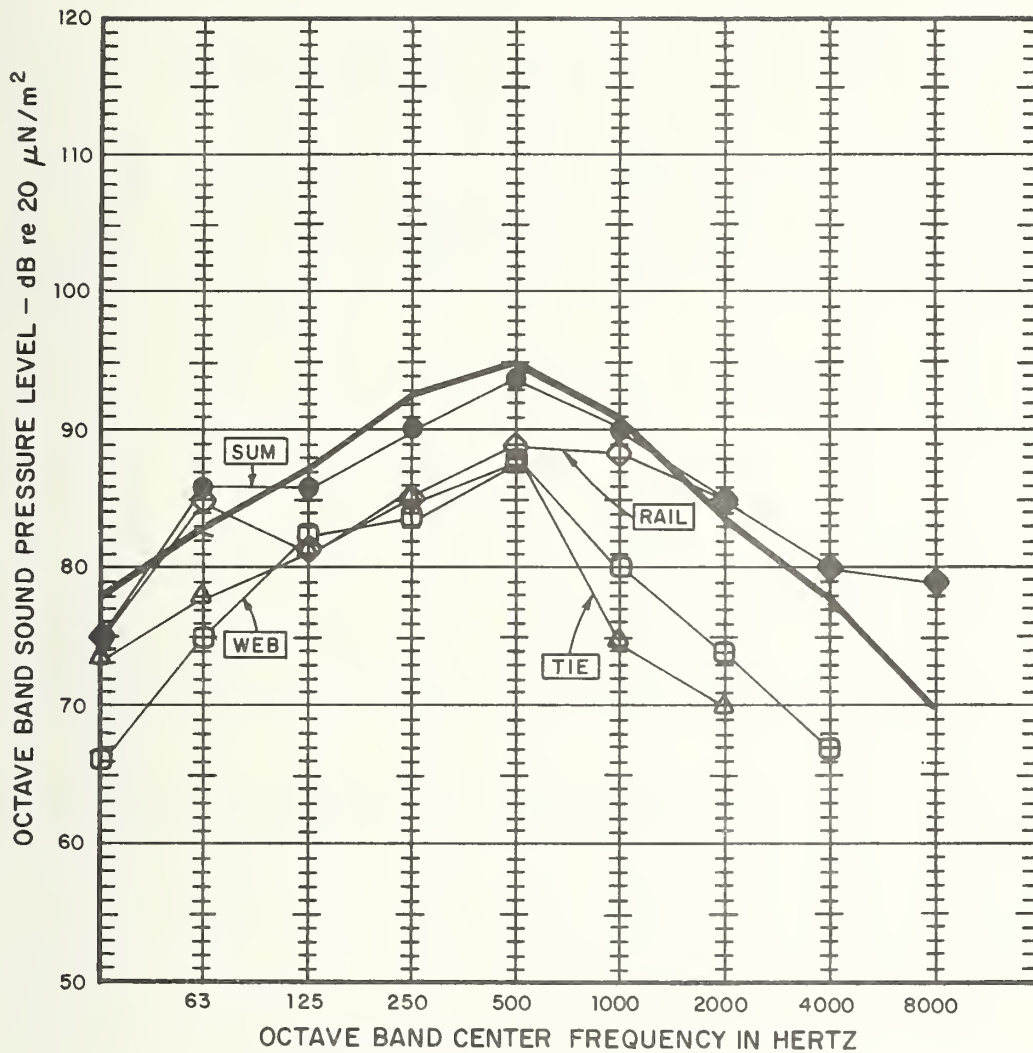
Predicted noise levels 50 ft from the track centerline are shown in Fig. 4.17 and compared with measured levels. The prediction, which is based on measured vibration levels for the different structural components, is in good agreement with the data at all frequencies. Thus, we conclude that the major errors in the overall prediction model for this type of structure will come either from errors in predicting the rail vibration or from errors in relating the low frequency component vibration levels to the rail vibration levels.

Fig. 4.17 shows that the rail is the major source of noise at and above 1000 Hz. Thus, an overall reduction of the elevated structure noise will require reduction of rail radiation. At lower frequencies all components contribute equally to the noise radiation. Thus, each component must be given attention. The



	MEASURED DATA	PREDICTION USING MEASURED RAIL VIBRATIONAL ENERGY
RAIL	■	
TIES	●	— — — — —
WEB	▲	—————

FIG. 4.16 PREDICTED AND MEASURED VALUES OF SPATIALLY AVERAGED ENERGY FOR THE HATHON SQUARE STRUCTURE (AN OPEN WOOD TIE DECK, OPEN-WEB STEEL-GIRDER STRUCTURE)



- MEASURED MAXIMUM NOISE LEVEL 50 FT. FROM TRACK CENTERLINE
- PREDICTED NOISE LEVEL USING MEASURED VIBRATION LEVELS
- ◇ RAIL RADIATION
  - FLANGE AND OPEN WEB RADIATION
  - △ TIE RADIATION
  - SUM OF PREDICTED RADIATION LEVELS

FIG. 4.17 PREDICTED AND MEASURED NOISE RADIATION LEVELS FROM ELEMENTS ON THE HATHON SQUARE ELEVATED STRUCTURE



prediction model and the measured levels show that the rail energy is greater than that of either the tie deck or the girders. The prediction model shows further that the coupling loss factors are smaller than the damping loss factors. Thus, reduction of tie and web vibration can be achieved either by reducing the coupling loss factors or by increasing the damping. This is a different result than that reached in the previous two cases where it was necessary first to increase the damping.

## 5. CONCLUSIONS

The elevated structure noise prediction model developed in the report requires five steps:

- 1) prediction of maximum vibration levels for the rails during a pass-by;
- 2) relating the maximum levels to the total vibratory energy for the rails;
- 3) relating rail energy to the vibratory energy of each component of the elevated structure (deck, girder, etc.);
- 4) calculation of radiated acoustic power;
- 5) relating the acoustic power to sound pressure levels at specified distances from the structure.

Each of the five steps is to be carried out in frequency bands. A-weighted sound pressure levels can then be calculated.

### 5.1 Critical Review of the Prediction Model

The field studies of three different types of elevated structure that were carried out as part of the program provide data which support to varying degrees the validity of the prediction procedures for each of the five steps above. That part of the prediction model, which involves using measured vibration levels for the different elevated structure components to predict the radiated acoustic power (step 4) and the sound pressure levels 50 ft from the track centerline (step 5), appears to be quite accurate. Comparison of prediction with data for the Anderson Bridge, Fig. 4.9, and for the Hathon Square structure, Fig. 4.17, show good agreement over almost the entire frequency range. Only at high frequencies do significant discrepancies occur. We believe that these are due to the fact that noise radiation from the wheels and other car surfaces has not been taken into account.

The agreement between prediction and data for the Green St. structure, Fig. 4.14, is not as good as for the other two structures. However, we consider it to be sufficiently good as to support the use of the prediction model for calculating A-weighted noise levels and for determining the value of proposed noise control treatments.

The procedure for relating the vibratory energies of each component of the elevated structure to measured rail vibrational energy (step 3) appears to be quite accurate at high frequencies but to be of very limited accuracy at low frequencies. This result is particularly evident in the case of the Hathon Sq. structure, see Fig. 4.16. In developing the theory two sources of inaccuracy were repeatedly noted. First, the formulation of the prediction model is based on assumptions that are valid only at frequencies that are above the resonance frequency of the rail on its fasteners or wood ties. Second, the calculation of the rail/fastener resonance frequency is based on a very qualitative argument with little precise data input. We have not tried to improve the accuracy of the prediction model at low frequencies, because the contribution from vibration at these frequencies to the A-weighted radiated noise level is not large. However, as the high frequency noise levels are reduced by addition of noise control treatments, it may be necessary to improve the accuracy of the prediction model at low frequencies. A general approach is outlined in Appendix II of this report.

The accuracy of the prediction model for calculating the rail vibrational energy (step 2) is limited by the inaccuracies in the prediction of maximum rail vibration levels (step 1) and by the lack of information and data on the damping provided by the rail fastener or the wood ties as the case may be. In the present program we have not collected this type of information.

The overall accuracy of the prediction model is adequate if the rail vibration levels are known. Of course, this is

usually not the case. Thus, in practice the accuracy of the model is limited by the accuracy with which the rail vibrational energy can be predicted.

## 5.2 Noise Control Techniques

A significant conclusion derived from the prediction model is the apparent importance of the rails as sources of elevated structure noise. For each of the three structures that were studied the rails are the dominant noise sources at high frequencies. Thus, complete elimination of the remaining structural components as significant noise sources would only reduce the A-weighted wayside noise levels by a few dB. At the same time elimination of the rail as a significant noise source would only reduce the A-weighted noise by a few dB, since the elevated structure steel girders dominate the noise radiation at the mid-frequencies in the approximate range 200 to 800 Hz. The concrete slab or wood tie decks do not contribute significantly to the A-weighted noise. Thus, the initial step in controlling elevated structure noise is to reduce the noise from the rails and steel girders.\*

The prediction model shows that one approach toward attaining this objective is to reduce the vibratory energy of the rails. This can be done by 1) adding a damping treatment to the rail, 2) increasing the damping of the rail fastener, and/or 3) decreasing the rail and wheel roughness and eliminating wheel flats and rail joints. The third technique is well known. However, the effective and practical use of the other two techniques should be studied further.

---

\* Available evidence indicates that noise from concrete girders is not significant compared to that from the rails.

The stiffness of the rail fastener (or wood tie) and the mass of the rail controls the rail/fastener resonance frequency. Reduction of this resonance frequency, by using softer fasteners or heavier rail, has two effects. First, the coupling between the rail and the other components of the elevated structure is reduced. However, the reduction in coupling will not result in a reduction in vibration if the damping of the elevated structure components is small. The second effect of decreasing the rail/fastener resonance is to decrease the effective rail damping and, thereby, increase the rail vibratory energy. Thus, the net effect of decreasing fastener stiffness on lightly damped elevated structures is to increase the noise. On the other hand, if the structure is well damped, the effects of increased rail radiation may be balanced by decreased vibration and noise radiation from other components of the elevated structure.

The prediction model indicates that steel girder vibration and noise radiation can be significantly reduced by damping the girder webs. Further study to develop effective and practical web damping treatments is needed.



## APPENDIX I. REFINED MODELS FOR STUDYING RAIL VIBRATION

The simple model of the rail as a beam on a continuous visco-elastic foundation excited by a point force does not take into account many factors that could conceivably affect the rail vibration. In reality, the rail fasteners are not continuous, but are a series of periodic supports. In addition, the excitation is not a single point force, but is a number of point forces at each wheel location. We explore the effects of these two related factors in Section I.1. It will be concluded that the effects are sufficiently small for typical rail parameters that they can be ignored.

In Section I.2 we will explore more precise models of rail damping. The simplified model of Chapter 2.3 uses the assumption that the rail fasteners have a frequency independent modulus of elasticity and damping loss factor. However, most fasteners use rubber-like materials in which both the modulus and loss factor are frequency dependent. The simplified model does not take into account the shear stiffness of the rail fastener. In Section I.2 we will also investigate the effect of fastener shear stiffness and explore the possibility that the rail and rail fastener act like a constrained damping layer.

The inclusion of frequency dependent fastener properties improves the prediction model and provides a more accurate picture of the decay in bending vibration levels with distance down the track.

In Section I.3 we study the effect of shear deformations on the rail vibration. We conclude that there is a significant effect, but only at high frequencies, above 2000 Hz.

Finally, in Section I.4 we consider the case in which the support under the fasteners is not rigid. We conclude that the rigid-support model can be used to study the rail vibration. Errors incurred using this model are significant only over a very limited range of frequencies.



## I.1 Discrete Rail Support Points and Multiple Excitation Points

The refinements of the rail vibration model to be discussed in this Section are concerned with effects of multi-wheel excitation and of the periodic nature of the rail supports. We wish to determine if there are any significant qualitative effects due to multi-wheel interaction that would invalidate the simple results of the single wheel model. Also, it is desired to find what role (if any) the wave propagation effects of periodic rail fastening have in vibration attenuation.

In general, the problem we wish to consider consists of a multi-car train with two trucks to each car passing over rails resiliently fastened by discrete supports to a supporting structure. The assumptions that will be made are:

- A. There is no dynamical coupling between rails due to wooden ties or other structural members;
- B. The input impedance of the track support structure is much larger than that of the rail;
- C. The rail is excited by the relative wheel-rail roughness and the roughness of different wheels are uncorrelated.
- D. Linearity

From assumptions A and B it is sufficient to determine the vibration of a single rail elastically mounted on a rigid foundation. Assumption C implies that one may synthesize a total solution by superimposing rail responses due to direct excitation by the roughness of one wheel with the other wheels acting as passive loads. Since the effects of multi-wheel interaction on rail vibration are likely to be greatest for wheels closest together, we consider just two wheels of a truck. Finally, since for the frequencies of interest bending wavelengths are much larger than the length of rail fasteners, we model the fasteners as point supports offering both vertical and torsional restraint.

The basic problem may be envisioned as in Fig. I.1. The impedance,  $Z_{w1}$ , of the first wheel is connected via a relative velocity source to the 0<sup>th</sup> bay of the rail fastener system, while the second wheel passively loads the p<sup>th</sup> bay through its impedance  $Z_{w2}$ . Here,  $V_{wR}(\omega)$  is the relative wheel-rail velocity amplitude due to wheel and rail roughness. The fasteners each with linear stiffness,  $K$ , and torsional stiffness,  $G$ , periodically support the rail with a separation distance,  $\ell$ . Furthermore, the rail itself is idealized as a Bernoulli-Euler beam with bending rigidity,  $B_r$ , and mass per unit length,  $m_r$ . In these calculations, we have followed Bender and Remington[5] and modeled the wheels by mass impedances including the wheel mass and an equivalent axle mass.

Among the specific questions we wish to answer with the above model are:

- (1) What are the effects on wave propagation and attenuation of the discrete nature of fasteners as opposed to the predictions of the continuous elastic support model?
- (2) What effects do wheel positions relative to fastener locations have on vibration excitation?
- (3) Is there significant build-up of vibration between truck wheels due to reflection of bending waves at wheel locations?

To answer these questions a computer program was developed for this problem. The analytical formulation and a listing of the program are in Sections I.1.1 and I.1.2.

As can be gathered from the above statement of the problem, we shall address ourselves primarily to the bending response of the rail. Time and cost constraints have prevented the inclusion of rail torsional motion in the computer calculation. However, the torsional vibrations of the rail are believed to be less important in predicting elevated structure noise.

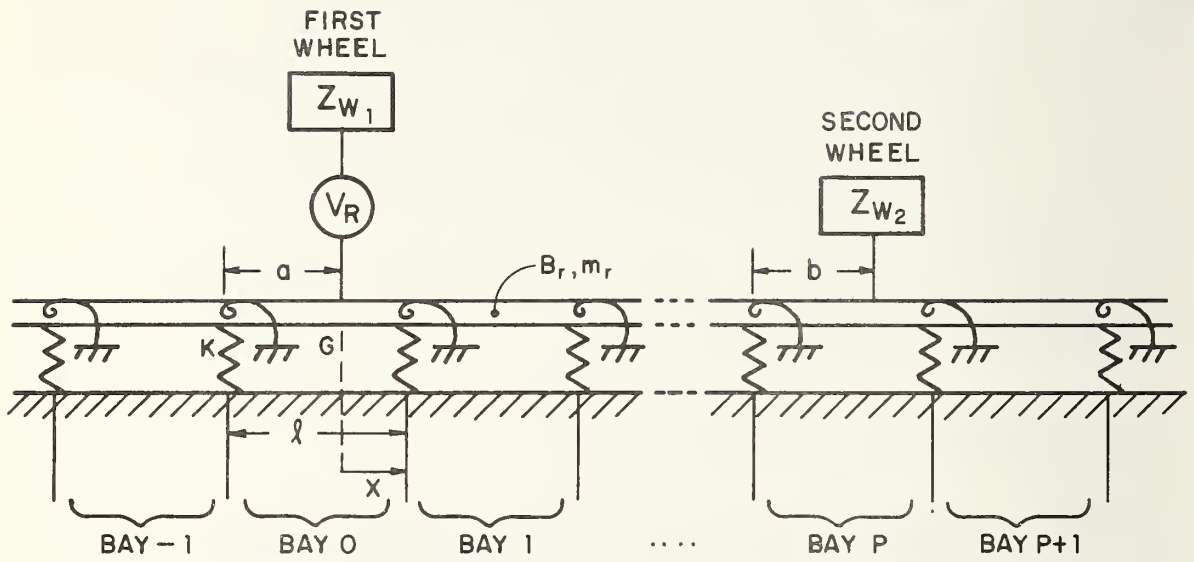


FIG. I. 1 DISCRETE MODEL OF THE RAIL AND FASTENER SYSTEM

In the following subsections, we discuss the underlying theoretical development and then present some computational results and conclusions.

#### I.1.1 Theoretical Developments for a Periodically Supported Beam

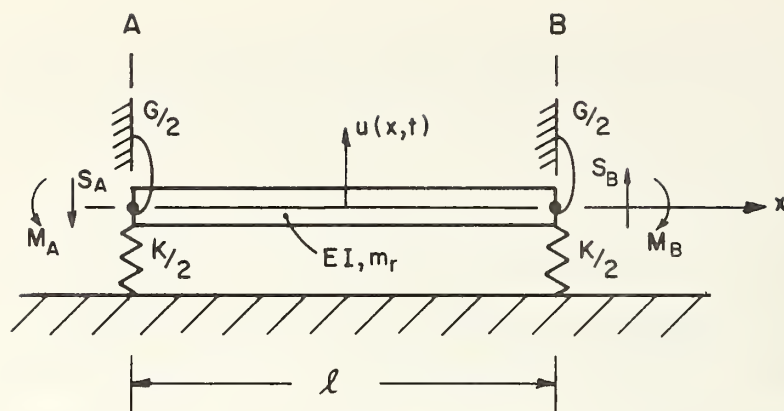
In this section we present the analytical results which form the basis for the computer program. The basic problem is shown schematically in Fig. I.1. The theory of free wave propagation is discussed first, and then the response relations for two different excitations are developed.

##### I.1.1.1 Free-Wave Propagation

In determining the characteristics of free wave propagation in the rail, we presume the displacement to have a harmonic time dependence of frequency  $\omega$ ,

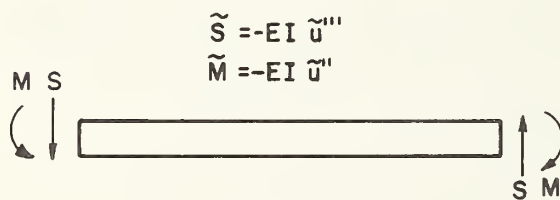
$$u = \tilde{u} e^{-j\omega t} \quad (I.1)$$

From Fig. I.1, it is apparent that the rail-fastener system may be divided into identical "bays" of length  $\ell$ . One of these is shown in Fig. I.2a. The motion of individual bays will be treated using a local  $x$  coordinate with its origin at the left end of the bay. Parameters  $S_A$ ,  $M_A$ , etc., denote the total applied shear force and moment due to both the beam segment and the linear and torsional stiffness of the fasteners. The remaining field variables



(a)

SKETCH OF ONE BAY OF THE RAIL FASTENER SYSTEM



(b)

SHEAR FORCE AND MOMENT SIGN CONVENTIONS

FIG. I. 2 A SINGLE BAY

at each end are the displacements  $u_A$ ,  $u_B$ , and the rotations  $\theta_A \equiv u'_A$ , and  $\theta_B \equiv u'_B$ , where "'" signifies differentiation with respect to  $x$ . Fig. I.2b shows the usual sign conventions and constitutive relations for shear force and moment within each beam segment. We note at the outset that  $K$  and  $G$  may have any frequency dependence and that  $K$ ,  $G$  and  $E$  may be assumed complex to account for solid-type damping in the rail or its fasteners.

Now we look at an individual bay. Within the endpoints  $A$  and  $B$ , the displacement phasor obeys the beam equation

$$\tilde{u}'''' = k^4 \tilde{u}, \quad k^4 \equiv \frac{\omega^2 m_r}{E I} \quad (I.2)$$

for which the general solution is

$$u(x) = A \cosh kx + B \sinh kx + C \cos kx + D \sin kx \quad (I.3)$$

where we have dropped the tilde.\* Imposing the conditions

$$\begin{aligned} u_A &= u(0), \quad u_B = u(\ell) \\ \theta_A &= u'(0), \quad \theta_B = u'(\ell) \end{aligned}$$

we find that the displacements and rotations at each end may be

---

\*In the following, the symbols for all fields variables denote the corresponding phasors.



related to the constants A, B, etc., by:

$$\begin{Bmatrix} \theta_A \\ \theta_B \\ u_A \\ u_B \end{Bmatrix} = \begin{bmatrix} 0 & k & 0 & k \\ k \text{ sh.} & k \text{ ch.} & -k \text{ s.} & k \text{ c.} \\ 1 & 0 & 1 & 0 \\ \text{ch.} & \text{sh.} & \text{c.} & \text{s.} \end{bmatrix} \begin{Bmatrix} A \\ B \\ C \\ D \end{Bmatrix} \quad (\text{I.4})$$

where  $s. \equiv \sin k\ell$ ,  $c. \equiv \cos k\ell$ ,  $\text{sh.} \equiv \sinh k\ell$  and  $\text{ch.} \equiv \cosh k\ell$ .

The inverse of this relation is

$$\begin{Bmatrix} A \\ B \\ C \\ D \end{Bmatrix} = \frac{1}{2(c.\text{ch.}-1)} \begin{bmatrix} \frac{1}{k}(\text{ch.s.}-c.\text{sh.}) & \frac{1}{k}(\text{sh.}-s.) & c.\text{ch.}+s.\text{sh.}-1 & c.-\text{ch.} \\ \frac{1}{k}(c.\text{ch.}-s.\text{sh.}-1) & \frac{1}{k}(c.-\text{ch.}) & -\text{sh.c.}-s.\text{ch.} & \text{sh.}+s. \\ \frac{1}{k}(c.\text{sh.}-s.\text{ch.}) & \frac{1}{k}(s.-\text{sh.}) & \text{ch.c.}-s.\text{sh.}-1 & \text{ch.}-c. \\ \frac{1}{k}(\text{ch.c.}+s.\text{sh.}-1) & \frac{1}{k}(\text{ch.}-c.) & \text{sh.c.}+s.\text{ch.} & -\text{sh.}-s. \end{bmatrix} \begin{Bmatrix} \theta_A \\ \theta_B \\ u_A \\ u_B \end{Bmatrix} \quad (\text{I.5})$$

Balancing forces and moments at the two ends and using the constitutive relations gives the conditions

$$u_A'' - \frac{\tilde{\gamma}}{2} u_A' = - \frac{M_A}{EI}$$

$$u_A''' + \frac{\tilde{\kappa}}{2} u_A = - \frac{S_A}{EI}$$

$$u_B'' + \frac{\tilde{\gamma}}{2} u_B' = - \frac{M_B}{EI} \quad (\text{I.6})$$

$$u_B''' - \frac{\tilde{\kappa}}{2} u_B = - \frac{S_B}{EI}$$

$$\text{where } \tilde{\gamma} \equiv \frac{G}{EI}, \quad \tilde{\kappa} \equiv \frac{K}{EI}$$

Using Eqs. I.4 gives the following relation between the shear forces and moments and the constants A, B, etc.:

$$\begin{bmatrix} 1 & -\frac{\lambda}{2} & -1 & -\frac{\lambda}{2} \\ \frac{\kappa}{2} & 1 & \frac{\kappa}{2} & -1 \\ \text{ch.} + \frac{\lambda}{2} \text{sh.} & \text{sh.} + \frac{\lambda}{2} \text{ch.} & -\text{c.} - \frac{\lambda}{2} \text{s.} & -\text{s.} + \frac{\lambda}{2} \text{c.} \\ \text{sh.} - \frac{\kappa}{2} \text{ch.} & \text{ch.} - \frac{\kappa}{2} \text{sh.} & \text{s.} - \frac{\kappa}{2} \text{c.} & -\text{c.} - \frac{\kappa}{2} \text{s.} \end{bmatrix} \begin{Bmatrix} A \\ B \\ C \\ D \end{Bmatrix} = \frac{-1}{EI\kappa^3} \begin{Bmatrix} kM_A \\ S_A \\ kM_B \\ S_B \end{Bmatrix} \quad (\text{I.7})$$

$$\text{where } \lambda = \frac{G}{EI\kappa} , \quad \kappa = \frac{K}{EI\kappa^3}$$

Finally, substitution of Eqs. I.5 into Eqs. I.7 gives the relation between shear and moments and displacements and rotations:

$$\begin{Bmatrix} M_A \\ S_A \\ M_B \\ S_B \end{Bmatrix} = \frac{EI\kappa^3}{1-\text{c.ch.}} \begin{bmatrix} \alpha_{11} & \alpha_{12} & \alpha_{13} & \alpha_{14} \\ -\alpha_{13} & \alpha_{14} & \alpha_{23} & \alpha_{24} \\ -\alpha_{12} & -\alpha_{11} & \alpha_{14} & \alpha_{13} \\ +\alpha_{14} & -\alpha_{13} & -\alpha_{24} & -\alpha_{23} \end{bmatrix} \begin{Bmatrix} \theta_A \\ \theta_B \\ u_A \\ u_B \end{Bmatrix} \quad (\text{I.8})$$

where

$$\alpha_{11} = \frac{1}{k^2} [\text{ch.s.} - \text{c.sh.} - \frac{\lambda}{2} (\text{c.ch.} - 1)]$$

$$\alpha_{12} = \frac{1}{k^2} [\text{sh.} - \text{s.}]$$

$$\alpha_{13} = \frac{1}{k} \text{s.sh.}$$

$$\alpha_{14} = \frac{1}{k} (\text{c.} - \text{ch.})$$

$$\alpha_{23} = \frac{k}{2} (\text{c.ch.} - 1) - \text{sh.c.} - \text{s.ch.}$$

$$\alpha_{24} = \text{s.} + \text{sh.}$$

At this point, note that Eqs. I.8 may be rearranged to read:

$$\begin{Bmatrix} u_B \\ \theta_B \\ S_B \\ M_B \end{Bmatrix} = \tilde{T} \begin{Bmatrix} u_A \\ \theta_A \\ S_A \\ M_A \end{Bmatrix} \quad (\text{I.9})$$

where  $\tilde{T}$  is constructed from the matrix in Eqs. I.8. Let us denote the state vectors at the right and left ends of bay  $n$  by

$\{u_{An}, \theta_{An}, S_{An}, M_{An}\}$  and  $\{u_{Bn}, \theta_{Bn}, S_{Bn}, M_{Bn}\}$ , respectively. For

the  $n^{\text{th}}$  and  $(n+1)^{\text{th}}$  bays, we must have  $\{u_{Bn}, \theta_{Bn}, S_{Bn}, M_{Bn}\} = \{u_{A(n+1)}, \theta_{A(n+1)}, S_{A(n+1)}, M_{A(n+1)}\}$ . Then, from Eqs. I.9

$$\begin{pmatrix} u_A \\ \theta_A \\ S_A \\ M_A \end{pmatrix}_{(n+1)} = \tilde{T} \begin{pmatrix} u_A \\ \theta_A \\ S_A \\ M_A \end{pmatrix}_{(n)} \quad (\text{I.10})$$

Hence,  $\tilde{T}$  is seen to be the transfer matrix of the system, relating the state vector at the left end of bay  $n+1$  to that at the left end of the preceeding bay. For future reference, we note that Eqs. I.10 may be expressed in another form. Let

$$\underline{\alpha}_n = \{A_n, B_n, C_n, D_n\} \quad (\text{I.11})$$

be the vector of coefficients appearing in Eqs. I.3 for the displacement of bay  $n$ . Then, using Eqs. I.4 and I.7 to express Eq. I.10 in terms of  $\underline{\alpha}_n$  and  $\underline{\alpha}_{n+1}$ , we have:

$$\underline{\alpha}_{n+1} = \mathbf{I} \underline{\alpha}_n \quad (\text{I.12})$$

where

$$\underline{I} = \begin{bmatrix} \text{ch.} + \frac{\lambda}{2} \text{sh.} & \text{sh.} + \frac{\lambda}{2} \text{ch.} & -\frac{\lambda}{2} \text{s.} & \frac{\lambda}{2} \text{c.} \\ \text{sh.} - \frac{\kappa}{2} \text{ch.} & \text{ch.} - \frac{\kappa}{2} \text{sh.} & -\frac{\kappa}{2} \text{c.} & -\frac{\kappa}{2} \text{s.} \\ -\frac{\lambda}{2} \text{sh.} & -\frac{\lambda}{2} \text{ch.} & \text{c.} + \frac{\lambda}{2} \text{s.} & \text{s.} - \frac{\lambda}{2} \text{c.} \\ \frac{\kappa}{2} \text{ch.} & \frac{\kappa}{2} \text{sh.} & -\text{s.} + \frac{\kappa}{2} \text{c.} & \text{c.} + \frac{\kappa}{2} \text{s.} \end{bmatrix}$$

Let us now consider the significance of the eigenvalue problem of  $\tilde{T}$ . Denoting these eigenvalues by  $e^{\mu_i}$  ( $i = 1, \dots, 4$ ), then

$$\begin{pmatrix} u_A \\ \theta_A \\ S_A \\ M_A \end{pmatrix}_{(n+1)} = e^{\mu_i} \begin{pmatrix} u_A \\ \theta_A \\ S_A \\ M_A \end{pmatrix}_{(n)} \quad (\text{I.13})$$

if  $\{u_A, \theta_A, S_A, M_A\}$  is the eigenvector corresponding to  $\mu_i$ . This equation shows that the eigenvector of  $\tilde{T}$  represents a distinct displacement shape which propagates undistorted from bay to bay with only a change in amplitude and phase, given by the factor  $e^{\mu_i}$ . The  $\mu_i$ 's are the propagation constants. The total beam displacement can be expressed in terms of an arbitrary linear

combination of the eigenvectors of  $\tilde{T}$ .

The propagation constants can be determined by setting  $\theta_B = e^\mu \theta_A$ ,  $u_B = e^\mu u_A$ , etc., in Eqs. I.8 to obtain a set of homogeneous equations in  $\theta_A$ ,  $u_A$ ,  $S_A$  and  $M_A$ . Requiring that the determinant of the coefficient matrix vanish gives the following condition determining the propagation constants:

$$(\cosh^2 \mu) [\alpha_{12} \alpha_{24} - \alpha_{14}^2] + (\cosh \mu) [\alpha_{23} \alpha_{12} + \alpha_{11} \alpha_{24}] + [\alpha_{11} \alpha_{23} + \alpha_{14}^2] = 0 \quad (I.14)$$

The four roots for  $e^\mu$  consist of two reciprocal pairs. We define our notation such that

$$\text{Re}(\mu_1), \text{Re}(\mu_2) > 0 \quad ; \quad \mu_3 = -\mu_1, \mu_4 = -\mu_2 \quad (I.15)$$

To obtain the corresponding eigenvector of  $T$ , we can impose the three conditions,  $\theta_B = x \theta_A$ ,  $u_B = x u_A$ ,  $S_B = x S_A$ , where  $x \equiv e^\mu$ , on Eqs. I.8. Using Eqs. I.4 and I.7, we find that  $B, C$ , and  $D$  may be expressed in terms of  $A$  by:

$$\begin{bmatrix} \text{sh.} & c.-x & s. \\ \text{ch.}-x & -s. & c.-x \\ 0 & s.-\frac{\kappa}{2}x & x-c. \end{bmatrix} \begin{Bmatrix} B_{\mu i} \\ C_{\mu i} \\ D_{\mu i} \end{Bmatrix} = A_{\mu i} \begin{Bmatrix} x-\text{ch.} \\ -\text{sh.} \\ \frac{\kappa}{2}x \end{Bmatrix} \quad (I.16)$$



where  $A_\mu$ ,  $B_\mu$ ,  $C_\mu$  and  $D_\mu$  are the constant coefficients in Eq. I.3 corresponding to propagation constant  $\mu$ . Solving these equations, one finds that the displacement,  $u$ , in any one bay may be written:

$$u(x) = [u_{\mu i}(x)] \{A_{\mu i}\},$$

where

(I.17)

$$[u_{\mu i}] \equiv [u_{\mu 1}, u_{\mu 2}, u_{\mu 3}, u_{\mu 4}]$$

$$[u_{\mu i}] = [\cosh kx, \sinh kx, \cos kx, \sin kx] [\underline{\Omega}].$$

$$[\underline{\Omega}] = \begin{bmatrix} 1 & 1 & 1 & 1 \\ b_{\mu 1} & b_{\mu 2} & b_{\mu 3} & b_{\mu 4} \\ c_{\mu 1} & c_{\mu 2} & c_{\mu 3} & c_{\mu 4} \\ d_{\mu 1} & d_{\mu 2} & d_{\mu 3} & d_{\mu 4} \end{bmatrix}$$

and where

$$\begin{aligned} b_{\mu i} &= \frac{1}{D} \{ s. [s. (s. - T_3) - \text{sh}. T_3] - T_1 [T_2 (s. - T_3) + T_1 (\text{sh}. - s. + T_3)] \} \\ c_{\mu i} &= \frac{1}{D} \{ T_1 [\text{sh}. (\text{sh}. - s. + T_3) - T_2^2] + s. T_2 (s. - T_3) \} \\ d_{\mu i} &= \frac{-1}{D} \{ T_2 [T_1 (s. - T_3) + T_2 T_3] + \text{sh}. [s. (s. - T_3) - \text{sh}. T_3] \} \\ D &= T_1 [T_1 T_2 + \text{sh}. (s. - T_3)] + s. T_2 T_3 \\ T_1 &= c. - x_i, \quad T_2 = \text{ch}. - x_i, \quad T_3 = s. - \frac{\kappa}{2} x_i \end{aligned} \quad (\text{I.18})$$

Eqs. I.14, I.17, and I.18 give the displacement within any non-excited bay. To obtain the variation of response from bay to bay note that

$$\{\alpha\} = \underline{\Omega} \{A_{\mu}\} \quad (I.19)$$

and since the eigenvector  $\{u_A, \theta_A, S_A, M_A\}$  of  $\mathbb{T}$  associated with  $\mu_i$  corresponds to  $u_{\mu i}$  given in Eq. I.17, we have

$$\underline{\Omega}^{-1} \mathbb{T} \underline{\Omega} = [\tilde{e}^{\mu}] \quad (I.20)$$

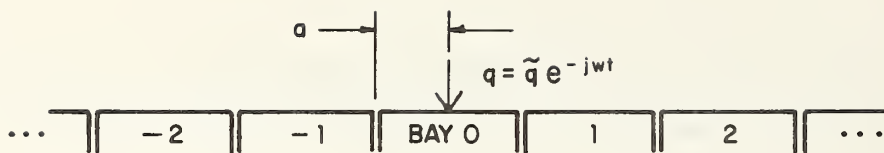
Thus, the columns of  $\underline{\Omega}$  are the eigenvectors of  $\mathbb{T}$  and both  $\mathbb{T}$  and  $\tilde{\mathbb{T}}$  have the same eigenvalues. Finally, combining Eqs. I.12, I.19, and I.20, we obtain:

$$\{A_{\mu(n+1)}\} = [\tilde{e}^{\mu}] \{A_{\mu(n)}\} \quad (I.21)$$

where  $[\tilde{e}^{\mu}]$  denotes a diagonal matrix (all off-diagonal terms zero). In conjunction with Eqs. I.17 and I.18, this relation gives us the displacement field in all non-excited bays once the response of one bay has been determined.

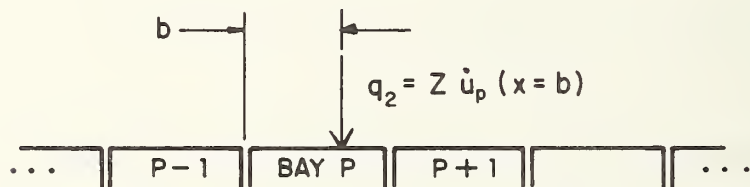
#### I.1.1.2 Forced Response

Now we must determine the displacement in bay 0, which is excited by the point force  $q(t)$ , as shown in Fig. I.3a.



(a)

POSITION OF THE POINT FORCE ON THE RAIL  
DUE TO EXCITATION BY THE FIRST WHEEL



(b)

LOCATION OF POINT FORCE ON THE RAIL DUE  
TO PASSIVE LOADING BY THE SECOND WHEEL

FIG. I.3 LOCATION OF THE EXCITATION POINTS

At the excitation point  $x_0 = a$  (where  $x_0$  denotes the local coordinate of bay 0), we have the conditions

$$u_{(+)} = u_{(-)} , \quad u'_{(+)} = u'_{(-)} , \quad u''_{(+)} = u''_{(-)} ,$$

$$u'''_{(+)} - u'''_{(-)} = -\tilde{q}/EI \quad (I.22)$$

where the subscripts (+) and (-) denote points immediately to the right or to the left of  $x_0 = a$ . Let

$$u = A_{(+)} \cosh kx + B_{(+)} \sinh kx + c_{(+)} \cos kx + D_{(+)} \sin kx \quad (I.23a)$$

for  $x_0 > a$  and

$$u = A_{(-)} \cosh kx + B_{(-)} \sinh kx + c_{(-)} \cos kx + D_{(-)} \sin kx \quad (I.23b)$$

for  $x_0 < a$ . Substitution of these into Eq. I.22 and use of Eq. I.19 yields:

$$\{A_{\mu(o+)}\} = \{A_{\mu(o-)}\} + \frac{\tilde{Q}}{2} \underline{\Omega}^{-1} \begin{Bmatrix} \text{sh.ka} \\ -\text{ch.ka} \\ -\text{s.ka} \\ \text{c.ka} \end{Bmatrix} \quad (I.24)$$

where

$$\tilde{Q} \equiv \tilde{q} \frac{1}{EI k^3}$$

The effects of the loading of the second wheel on the  $p^{\text{th}}$  bay (as shown in Fig. I.3b) may be handled similarly. The  $p^{\text{th}}$  bay is excited at  $x_p = b$  by the force  $q$ .

$$q_2 = Z \dot{u}_p(x_p=b) \quad (\text{I.25})$$

where  $Z$  is the impedance of the second wheel. Evaluating  $\dot{u}_p(x_p=b)$ , we get

$$q_2 = -Zj\omega \begin{bmatrix} \text{ch.kb} & \text{sh.kb} & \text{c.kb} & \text{s.kb} \end{bmatrix} \underline{\Omega} \{A_\mu(p-)\} \quad (\text{I.26})$$

where again there are two  $\{A_\mu\}$  vectors, one for the segment to the left of  $x_p = b$  and one for the segment to the right. The resulting conditions on the  $p^{\text{th}}$  bay are

$$\{A_\mu(p+)\} = \{A_\mu(p-)\} + \underline{\Lambda} \{A_\mu(p-)\} \quad (\text{I.27})$$

where

$$\underline{\Lambda} = -j\omega \frac{\tilde{Z}}{2} \underline{\Omega}^{-1} \begin{pmatrix} \text{sh.kb} \\ -\text{ch.kb} \\ -\text{s.kb} \\ \text{c.kb} \end{pmatrix} \begin{bmatrix} \text{ch.kb} & \text{sh.kb} & \text{c.kb} & \text{s.kb} \end{bmatrix} \underline{\Omega}$$

$$\tilde{Z} = \frac{Z}{EI k^3}$$

Finally, Eq. I.21 gives the additional condition:

$$\{A_\mu(p-)\} = [\tilde{e}^{p\mu}] \{A_\mu(o+)\} \quad (\text{I.28})$$

Eqs. I.24, I.27, and I.28 constitute a set of eight equations in twelve unknowns. However, since  $\mu_1$  and  $\mu_2$  were defined such that their real parts are positive we must have

$$A_{\mu 1}(p+) = A_{\mu 2}(p+) = A_{\mu 3}(o-) = A_{\mu 4}(o-) = 0$$

in order that the displacements remain finite at  $x = \pm\infty$ . Hence, Eqs. I.24, I.27, and I.28 may be rearranged into the following set of equations:

$$\begin{bmatrix} 0 & 0 & 0 & 0 \\ 0 & 0 & \underline{\Gamma} & 0 \\ 1 & 0 & (4 \times 4) & 0 \\ 0 & 1 & 0 & 0 \\ 0 & 0 & \underline{I} & -1 \\ 0 & 0 & (4 \times 4) & -1 \\ 0 & 0 & 0 & 0 \\ 0 & 0 & 0 & 0 \end{bmatrix} \begin{Bmatrix} A_{\mu 3}(p+) \\ A_{\mu 4}(p+) \\ A_{\mu 1}(o+) \\ A_{\mu 2}(o+) \\ A_{\mu 3}(o+) \\ A_{\mu 4}(o+) \\ A_{\mu 1}(o-) \\ A_{\mu 2}(o-) \end{Bmatrix} = \frac{\underline{\Omega}}{2} \begin{Bmatrix} 0 \\ 0 \\ 0 \\ 0 \\ \left. \begin{matrix} \text{sh.ka} \\ -\text{ch.ka} \\ -\text{s.ka} \\ \text{c.ka} \end{matrix} \right\} \underline{\Omega}^{-1} \end{Bmatrix} \quad (\text{I.29a})$$

$$\text{and} \quad \{A_{\mu}(p-)\} = [\underline{e}^{p\mu}] \{A_{\mu}(o+)\} \quad (\text{I.29b})$$

where

$$\underline{\Gamma} = -[\underline{I} - j\omega \frac{\underline{Z}}{2} \underline{\Omega}^{-1} \begin{Bmatrix} \text{sh.kb} \\ -\text{ch.kb} \\ -\text{s.kb} \\ \text{c.kb} \end{Bmatrix} [\text{ch.kb}, \text{sh.kb}, \text{c.kb}, \text{s.kb}] \underline{\Omega}] [\underline{e}^{p\mu}] \quad (\text{I.29c})$$



$\{A_{\mu}(p+)\}$ ,  $\{A_{\mu}(p-)\}$ ,  $\{A_{\mu}(o+)\}$  and  $\{A_{\mu}(o-)\}$  can now be obtained from Eqs. I.29. The  $\{A_{\mu}\}$  vector for any other bay can be calculated from Eq. I.21. Finally, the displacement in bay  $n$ ,  $u_n$ , can be obtained from

$$u_n(x) = [\cosh kx, \sinh kx, \cos kx, \sin kx] [\underline{\Omega}] \{A_{\mu}(n)\} \quad (I.30)$$

This completes the development of the solution procedure.

#### I.1.1.3 Wheel-Rail Roughness Excitation

When the excitation by the first wheel is a force source, the appropriate phasor,  $\tilde{Q}$ , of the exciting force can be employed directly in Eqs. I.29 to obtain the  $A_{\mu}$ 's and subsequently all response quantities. However, when the excitation is due to relative wheel-rail roughness, the phasor of the force on the rail is given by

$$\tilde{Q} = \frac{\omega^2}{S} \frac{Z_r Z_w}{Z_r + Z_w} [\phi_w(k=\frac{\omega}{S}) + \phi_r(k=\omega/S)] \quad (I.31)$$

where  $\omega$  is the radian frequency,  $S$  is the train speed,  $Z_w$  is the impedance of the wheel,  $Z_r$  is the driving point impedance of the rail, and  $[\phi_w(k) + \phi_r(k)]$  is the sum wavenumber spectra of the wheel and rail roughnesses. For frequencies in the range 100 to 1500 Hz, a reasonable approximation for  $Z_w$  is

$$Z_w \approx -j\omega M \quad (I.32)$$

where M is the mass of the wheel, bearing and an equivalent axle mass.

The rail impedance may be found by setting  $\tilde{Q} = 1$  in Eqs. I.29 and solving for the  $A_\mu$ 's. Then

$$\begin{aligned} Z_r^{-1} &= \frac{1}{\tilde{Q}} (-j\omega u_0(\omega, x_0 = a)) \\ &= \frac{-j\omega}{EI k^3} [\text{ch}.ka, \text{sh}.ka, \text{c}.ka, \text{s}.ka] \underline{\Omega} \{A_\mu(o-)\} \end{aligned} \quad (\text{I.33})$$

Using this value of  $Z_r$ , the final solution can be obtained by multiplying the solution with  $\tilde{Q}$  set equal to 1 by

$$\tilde{Q} = \frac{1}{EI k^3} \frac{\omega^2}{S} \frac{Z_r Z_w}{Z_r + Z_w} [\phi_w(k=\frac{\omega}{S}) + \phi_r(k=\frac{\omega}{S})] \quad (\text{I.34})$$

### I.1.2 Computer Program

A computer program, based on the above analysis, has been developed. The program is written in Fortran IV and has been run on a DEC 10 System. The program computes propagation constants and acceleration spectra for a rail-fastener system with specified material and geometric parameters. The calculations are performed for the desired range of frequencies and positions on the rail. Parameters are put into the program as part of the program listing either in data statements or under the section of

the program "parameters." As it is set up, the program must be recompiled for each new set of input parameters. A parameter listing is given below:

<u>Fortran Name</u>	<u>Variable Name</u>	<u>Input Line In Program</u>	<u>Description</u>
FL	$\ell$	4	fastener spacing
A	a	4	see Fig. I.1
IP	p	4	bay number, Fig. I.1
B	b	4	see Fig. I.1
FI	I	5	rail moment of inertia
RHO	$m_r$	5	rail mass per unit length
FM	M	5	wheel mass
MJ		5	number of bays for which calculation is carried out
FDL	$\Delta\xi$	6	length between computational points
RDOT(Z)	$\phi_w + \phi_r$	14	wheel and rail roughness spectrum
E	$E(1-j\eta_r)$	16	E, Youngs Modulus of rail material $\eta_r$ , rail damping
FKP	$\kappa'(1-j\eta_f)$	18	$\kappa' = K/(EI)$
FKC	$K(1-j\eta_f)$	19	K, fastener spring constant $\eta_f$ , fastener damping
FLP	$\lambda'(1-j\eta_f)$	20	$\lambda' = G/(EI)$
G	$G(1-j\eta_f)$	21	G, fastener torsional stiffness $\eta_f$ , fastener damping
INDQ	INDQ	26	
IOM	$\omega$	27	frequency
OMEGA	$\omega$	28	frequency
COM	$\omega(m_r \ell^4 / EI)^{1/2}$	35	dimensionless frequency

Units are in ft, lbs, slugs, and seconds. Computations are performed for bays - MJ/2 to + MJ/2 inclusive. In each bay, the acceleration is evaluated at  $\ell/\Delta\xi$  equidistant points. INDQ is a dummy variable offering the choice of one of two options:

INDQ = 1 : Rail response is computed for a force  
source excitation with magnitude such  
that  $\tilde{Q} = 1$ ,

INDQ = 2 : Computations are carried out for a  
relative wheel rail roughness excitation.

For each desired frequency, the program prints out the variables:

Name	Fortran Name	Evaluation Formula
$\omega$	OMEGA	
INDQ	INDQ	
k	K	$(\omega^2 m_r / EI)^{1/4}$
$\lambda$	LAMDA	$G / (EI k)$
$\kappa$	KAPPA	$K / (EI k^3)$
$Z_w$	ZW	$-j\omega M$
$\Omega$	COMEGA	$\omega \sqrt{m_r \ell^4 / EI}$

Thus, results can be expressed in terms of  $\omega$  or in terms of the dimensionless frequency parameter  $\Omega$ . Next, the real and imaginary

parts of the propagation constants are printed out. Finally, the program gives the acceleration level,  $L_{\ddot{u}}$ , where

$$L_{\ddot{u}} = 10 \log (| \ddot{u}(x, \omega) |^2) \quad (I.35)$$

for bay N ( $-MJ/2 \leq N \leq MJ/2$ ) at  $\ell/\Delta\xi$  stations within each bay. This entire process continues over all the desired values of  $\omega$  as specified in line 27 of the program.

The overall flow of the program is very simply illustrated in Fig. I.4. The frequency do-loop encompasses all calculations. Within this loop, the portion labeled MAIN calculates propagation constants and the quantities  $\{A_{\mu}(p+)\}$ ,  $\{A_{\mu}(o+)\}$ ,  $\{A_{\mu}(o-)\}$  for each frequency. The loop labeled X loops over all bays (from  $-MJ/2$  to  $MJ/2$ ) and over all stations within a bay (i.e., for  $\xi \in [0, \ell]$ ,  $\xi = n(\Delta\xi)$ ;  $n \in [0, \ell/\Delta\xi]$ ). The backsubstitution phase computes acceleration levels at these locations.

The MAIN portion carries out the following steps:

1.  $\alpha_{11}, \dots, \alpha_{24}$  are calculated from Eqs. I.8.
2. results of step 1 are used to calculate the coefficients of the characteristic equation for the propagation constants, Eqs. I.14, and this is solved to obtain  $\mu_1, \mu_2, \mu_3, \mu_4$ . Then the propagation constants are relabeled such that Eq. I.15 is satisfied.

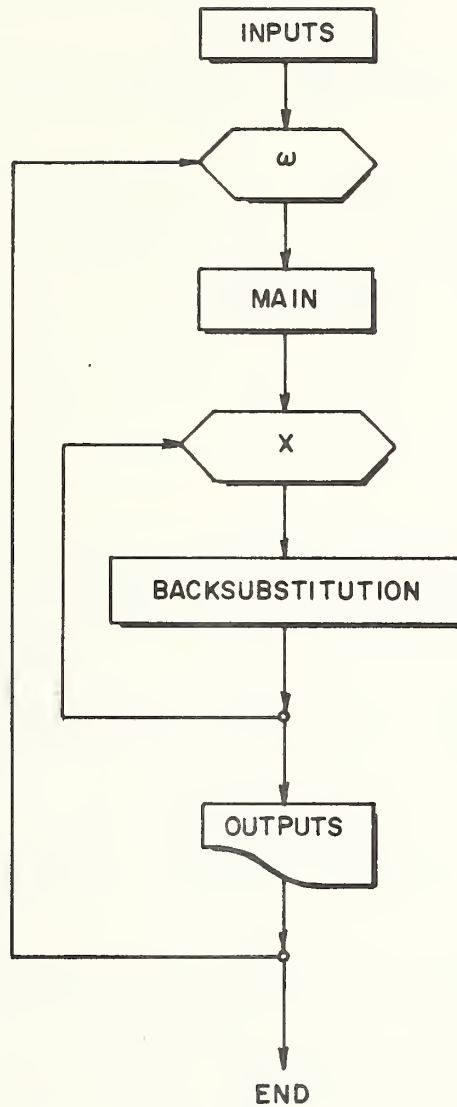


FIG. I. 4 FLOW CHART FOR COMPUTER PROGRAM



3. For each  $\mu$ ,  $x = e^\mu$ ,  $F_1$ ,  $F_2$ ,  $F_3$ ,  $D_\mu$ ,  $b_{\mu i}$ ,  $c_{\mu i}$  and  $d_{\mu i}$  are calculated following Eq. I.18, and the  $\underline{\Omega}$  matrix is assembled.
4. From step 3,  $\underline{\Omega}^{-1}$  is evaluated and the  $\underline{\Gamma}$  matrix is obtained from Eq. I.29c.
5. The system of eight linear algebraic Eqs. I.29a is solved, setting  $\tilde{Q} = 1$ .
6. If  $\text{INDQ} = 1$ ,  $\tilde{Q}$  is set = 1. If  $\text{INDQ} = 2$ ,  $Z_r$  is evaluated from Eq. I.33 and  $\tilde{Q}$  obtained from Eq. I.34. The solutions to Eq. I.29a previously obtained in step 5 are now multiplied by  $\tilde{Q}$ . Finally,  $\{A_{\mu(p-)}\}$  is evaluated from  $\{A_{\mu(p-)}\} = [\tilde{e}^{\mu p}] \{A_{\mu(o+)}\}$ .

The backsubstitution phase performs its computations for a given  $N$  and  $\xi$ . First, the following substitutions are made according to the contingencies indicated at the left hand margin below:

<u>Contingency</u>	<u><math>\{A\} =</math></u>
$N < o$	$[\tilde{e}^{\mu p}] \{A_{\mu(o-)}\}$
$N = o, \xi \leq a$	$\{A_{\mu(o-)}\}$
$N = o, \xi > a$	$\{A_{\mu(o+)}\}$
$o < N < p$	$\left\{ \begin{array}{l} e^{\mu 1(n-p)} A_{\mu 1(p-)} \\ e^{\mu 2(n-p)} A_{\mu 2(p-)} \\ e^{\mu 3N} A_{\mu 3(o+)} \\ e^{\mu 4N} A_{\mu 4(o+)} \end{array} \right\}$

$$\begin{array}{ll}
N = p, \xi < b & \{A_{\mu(p-)}\} \\
N = p, \xi > b & \{A_{\mu(p+)}\} \\
N > p & [e^{(n-p)\mu}] \{A_{\mu(p+)}\}
\end{array}$$

The substitution for the case  $0 < N < p$  avoids the numerical errors that would be produced by multiplying  $\{A_{\mu(o+)}\}$ , say, by

$$\begin{bmatrix}
e^{\mu 1N} & & & \phi \\
& e^{\mu 2N} & & \\
& & e^{\mu 3N} & \\
\phi & & & e^{\mu 4N}
\end{bmatrix}$$

where  $e^{N\mu 1}$  and  $e^{N\mu 2}$  can be very large numbers. Finally,  $u_N(\xi)$  is obtained from

$$u_N(\xi) = [\cosh k\xi, \sinh k\xi, \cos k\xi, \sin k\xi] [\underline{\Omega}] \{A\} \quad (I.36)$$

and the acceleration level,  $10 \log_{10} [\omega^4 |u_N(\xi)|^2]$  is determined.

The computer program, which embodies the theoretical scheme outlined above, consists of three main parts. The first part calculates, for each given frequency, the propagation constants and the corresponding wave components. The second part takes account of external loads on the rail and determines the coefficients  $A_{\mu i}^{(n)}$  for each bay. The final part generates  $u(x)$  for desired locations.

The dynamic properties of rail and fasteners, the fastener spacing, the locations of the wheels and their input impedance may be specified as desired. Either an exciting force at the first wheel of arbitrary spectrum or a wheel-rail roughness excitation for any desired roughness spectrum may be specified. As all arithmetic operations are carried out in the complex mode, damping may be included in any and all of the structural elements. The output includes both the propagation constants as functions of frequency and the velocity response of the rail at given frequencies and locations.

The program has been debugged and run for a number of cases. A listing follows.

```

      IMPLICIT COMPLEX(A-H,O-Z)
      DOUBLE PRECISION RR,RI,COR,COI
      COMPLEX CSINH,CCOSH,CCHIN,FZW,RDOT
      DATA FL,A,IP,B/(2.5,0.0),(1.25,0.0),3,(0.75,0.0)/
      DATA FI,RHO,FM,MJ/(3.13E-3,0.0),(1.1979,0.0),(1000.0,0.0),20/
      DATA FDL/(1.25,0.0)/
      DIMENSION FMU(4),DMU(4),BMU(4),CMU(4),OM(16),OMI(16),
1  V(4),DEL(4),EPMU(16),GAMMA(16),L(4),M(4),CO(64),
2  R(8),R1(12),FID(16),RR(8),RI(8),COR(64),COI(64)
      CSINH(Z)=(CEXP(Z)-CEXP(-Z))/(2.0,0.0)
      CCOSH(Z)=(CEXP(Z)+CEXP(-Z))/(2.0,0.0)
      CCHIN(Z)=CLOG(Z+CSQRT(Z*Z-(1.0,0.0)))
      FZW(Z,C)=C*Z
      RDOT(Z)=(1.0,0.0)
C.....PARAMETERS
      E=(4.32E9,0.0)
      EI=E*FI
      FKP=(0.3497,0.0)*((1.0,0.0)-(0.0,1.0))
      FKC=(4.729E6,0.0)*((1.0,0.0)-(0.0,1.0))
      FLP=(0.04861,0.0)*((1.0,0.0)-(0.0,1.0))
      G=(6.575E5,0.0)*((1.0,0.0)-(0.0,1.0))
C.....PRINT PARAMETERS INDEPENDENT OF OMEGA
      WRITE(3,108) FL,A,IP,B,E
      WRITE(3,109) FI,RHO,FM,MJ
      WRITE(3,112) G,FKP,FDL
      INDQ=2
      DO 1000 IOM=500,13000,500
      OMEGA=CMPLX(FLOAT(IOM),0.0)
      WRITE(3,111) OMEGA,INDQ
      FK=(OMEGA*OMEGA*RHO/EI)**0.25
      FLAMDA=G/(EI*FK)
      TERM=(1.0,0.0)/(EI*FK**3)
      FKAPPA=FKC*TERM
      ZW=(0.0,1.0)*OMEGA*FM
      COM=OMEGA*(1.860E-3,0.0)
C.....PRINT PARAMETERS DEPENDENT ON OMEGA
      WRITE(3,110) FK,FLAMDA,FKAPPA,ZW,COM
C.....CALCULATE ALPHA TERMS
      FKI=(1.0,0.0)/FK
      FKI2=FKI*FKI
      FKL=FK*FL
      S=CSIN(FKL)
      C=CCOS(FKL)
      SH=CSINH(FKL)
      CH=CCOSH(FKL)
      A11=FKI2*(CH*S-C*SH-FLAMDA/(2.0,0.0)*(C*CH-(1.0,0.0)))
      A12=FKI2*(SH-S)
      A13=FKI*S*SH
      A14=FKI*(C-CH)
      A23=FKAPPA/(2.0,0.0)*(C*CH-(1.0,0.0))-SH*C-S*CH
      A24=S+SH
C.....CALCULATE PROPAGATION CONSTANTS
      BT1=A12*A24-A14*A14
      BT2=A23*A12+A11*A24
      BT3=A11*A23+A14*A14
      IF(CABS(BT2*BT2/(BT1*BT3)) .LE. 1.0E4) GO TO 1
      FMU(1)=CCHIN(-BT3/BT2)
      FMU(2)=(10.0,0.0)
      GO TO 2
1  EP1=-BT2/((2.0,0.0)*BT1)
      EP2=CSQRT(BT2*BT2-(4.0,0.0)*BT1*BT3)/((2.0,0.0)*BT1)

```

```

FMU(1)=CCHIN(EP1+EP2)
FMU(2)=(10.0,0.0)
IF(CABS(EP1-EP2) .LT. 1.0E4) FMU(2)=CCHIN(EP1-EP2)
2  FMU(3)=-FMU(1)
   FMU(4)=-FMU(2)
   IF(REAL(FMU(1)) .GT. 0.0) GO TO 3
   SAVE=FMU(3)
   FMU(3)=FMU(1)
   FMU(1)=SAVE
3  IF(REAL(FMU(2)) .GT. 0.0) GO TO 8
   SAVE=FMU(4)
   FMU(4)=FMU(2)
   FMU(2)=SAVE
8  WRITE(3,115)
   WRITE(3,102) FMU
C.....LOOP FOR EACH MU
DO 9 K=1,4
  X=CEXP(FMU(K))
  F1=C-X
  F2=CH-X
  F3=S-FKAPPA/(2.0,0.0)*X
  SMF3=S-F3
  F23=F2+F3
  DMU(K)=F1*(F1*F2+SH*SMF3) + S*F23
  DMU(K)=(1.0,0.0)/DMU(K)
  BMU(K)=DMU(K)*(S*(S*SMF3-SH*F3)-F1*(F2*SMF3+F1*
1  (SH-S+F3)))
  CMU(K)=DMU(K)*(F1*(SH*(SH-S+F3)-F2**2)+S*F2*SMF3)
  DMU(K)=-DMU(K)*(F2*(F1*SMF3+F23)+SH*(S*SMF3-SH*F3))
9  CONTINUE
C.....FORM OMEGA MATRIX STORED AS VECTOR BY COLUMN
DO 10 K=1,4
  KK=4*(K-1)
  OM(KK+1)=(1.0,0.0)
  OM(KK+2)=BMU(K)
  OM(KK+3)=CMU(K)
  OM(KK+4)=DMU(K)
10 CONTINUE
C.....CALCULATE INVERSE OF OMEGA MATRIX
DO 11 K=1,16
11  OMI(K)=OM(K)
  CALL CMINV(OMI,4,D,L,M)
  IF(D .EQ. (0.0,0.0)) TYPE 113,D
C.....CALCULATE DEL VECTOR
  FKA=FK*A
  SA=CSIN(FKA)
  CA=CCOS(FKA)
  SHA=CSINH(FKA)
  CHA=CCOSH(FKA)
  V(1)=SHA
  V(2)=-CHA
  V(3)=-SA
  V(4)=CA
  CALL CMPRD(OMI,V,DEL,4,4,1)
DO 12 K=1,4
12  DEL(K)=(0.5,0.0)*DEL(K)
C.....FORM THE DIAGONAL-ELEMENTS-ONLY MATRIX EPMU
C.....AND THE IDENTITY MATRIX FID
  INDEXP=0
DO 13 K=1,4
  FID(4*(K-1)+K)=(1.0,0.0)

```



```

      EXPO=CMPLX(FLOAT(IP),0.0)*FMU(K)
      IF(ABS(REAL(EXPO)) .LT. 37.0) GO TO 13
      INDEXP=1
      EXPO=CMPLX(SIGN(37.0,REAL(EXPO)),0.0)
13     EPMU(4*(K-1)+K)=CEXP(EXPO)
C.....CALCULATE GAMMA MATRIX
      FKB=FK*B
      SB=CSIN(FKB)
      CB=CCOS(FKB)
      SHB=CSINH(FKB)
      CHB=CCOSH(FKB)
      V(1)=SHB
      V(2)=-CHB
      V(3)=-SB
      V(4)=CB
      CALL CMPRD(OMI,V,BMU,4,4,1)
      V(1)=CHB
      V(2)=SHB
      V(3)=CB
      V(4)=SB
      CALL CMPRD(BMU,V,OMI,4,1,4)
      CALL CMPRD(OMI,OM,GAMMA,4,4,4)
      DO 14 K=1,16
14     GAMMA(K)=-FID(K)-(0.0,1.0)*OMEGA*FZW(ZW,TERM)/
      1 (2.0,0.0)*GAMMA(K)
C.....SET UP COEFFICIENT MATRIX
      CO(3)=(1.0,0.0)
      CO(12)=(1.0,0.0)
      CO(53)=(-1.0,0.0)
      CO(62)=(-1.0,0.0)
      CALL CMPRD(GAMMA,EPMU,OMI,4,4,4)
      DO 15 K=3,6
      DO 15 KK=1,4
15     CO(8*(K-1)+KK)=OMI(4*(K-3)+KK)
      DO 16 K=3,6
      DO 16 KK=5,8
16     CO(8*(K-1)+KK)=FID(4*(K-3)+KK-4)
      DO 17 K=1,64
      COR(K)=DBLE(REAL(CO(K)))
17     COI(K)=DBLE(AIMAG(CO(K)))
C.....SET UP RIGHT-HAND-SIDE
      DO 18 K=5,8
18     R(K)=DEL(K-4)
      DO 19 K=1,8
      RR(K)=DBLE(REAL(R(K)))
19     RI(K)=DBLE(AIMAG(R(K)))
C.....SOLVE SYSTEM
C.....RESULT IS STORED IN RHS VECTOR R
      CALL CGELG(RR,RI,COR,COI,8,1,1,0D-15,IER)
      IF(IER.NE. 0) TYPE 100,IER
      DO 20 K=1,8
20     R(K)=CMPLX(SNGL(RR(K)),SNGL(RI(K)))
      DO 21 K=3,10
21     R1(K)=R(K-2)
      IF(INDEXP.EQ. 1) GO TO 23
      DO 22 K=1,4
22     V(K)=R(K+2)
      CALL CMPRD(EPMU,V,BMU,4,4,1)
      GO TO 24
23     BMU(3)=CEXP(CMPLX(FLOAT(IP),0.0)*FMU(3))*R1(7)
      BMU(4)=CEXP(CMPLX(FLOAT(IP),0.0)*FMU(4))*R1(8)

```



```

      COEFF=-(GAMMA(9)*GAMMA(14)-GAMMA(13)*GAMMA(10))
      BMU(1)=COEFF*BMU(3)
      BMU(2)=COEFF*BMU(4)
C.....CALCULATE OR SPECIFY Q DEPENDING ON VALUE OF INDQ.
C.....IF INDQ=1, SET Q=1. IF INDQ=2, CALCULATE Q.
24      GO TO(30,31),INDQ
30      Q=(1.0,0.0)
      GO TO 33
C.....CALCULATE DRIVING POINT IMPEDENCE
31      V(1)=CHA
      V(2)=SHA
      V(3)=CA
      V(4)=SA
      CALL CMPRD(V,OM,CMU,1,4,4)
      DO 32 K=1,4
32      V(K)=R1(K+8)
      CALL CMPRD(CMU,V,DMU,1,4,1)
      DELTA=+(0.0,1.0)*OMEGA*TERM*DMU(1)
      ZR=(1.0,0.0)/DELTA
      Q=TERM*(ZR*ZW/(ZR+ZW))*RDOT(OMEGA)
C.....MULTIPLY RESULTS OF SOL'N OF SYSTEM OF EQ'NS BY Q
33      DO 34 K=1,12
      IF(K.LE.4) BMU(K)=Q*BMU(K)
34      R1(K)=Q*R1(K)
C.....PRINT RESULTS
      WRITE(3,101)
      WRITE(3,102) (R1(K),K=1,4)
      WRITE(3,103)
      WRITE(3,102) BMU
      WRITE(3,104)
      WRITE(3,102) (R1(K),K=5,8)
      WRITE(3,105)
      WRITE(3,102) (R1(K),K=9,12)
C.....BACK SUBSTITUTION, CALCULATE FOR N=-MJ/2 TO MJ/2
C.....AND FOR XI=0 TO FL IN STEPS OF FDL
      KMAX=MJ+1
      DO 70 K=1,KMAX
      N=-MJ/2+(K-1)
      IF(N.GT. 0 .AND. N.LT. IP) GO TO 40
      IF(N.EQ. 0 .OR. N.EQ. IP) GO TO 43
      DO 35 KK=1,4
      IF(N.LT. 0) EXPO=CMPLX(FLOAT(N),0.0)*FMU(KK)
      IF(N.GT. IP) EXPO=CMPLX(FLOAT(N-IP),0.0)*FMU(KK)
      IF(ABS(REAL(EXPO)).GT. 37.0) EXPO=CMPLX(SIGN(37.0,
1 REAL(EXPO)),0.0)
35      EPMU(4*(KK-1)+KK)=CEXP(EXPO)
      IF(N.GT. IP) GO TO 38
      DO 36 KK=1,4
36      V(KK)=R1(KK+8)
37      CALL CMPRD(EPMU,V,CMU,4,4,1)
      GO TO 43
38      DO 39 KK=1,4
39      V(KK)=R1(KK)
      GO TO 37
40      DO 41 KK=1,2
      EXPO=CMPLX(FLOAT(N-IP),0.0)*FMU(KK)
      IF(ABS(REAL(EXPO)).GT. 37.0) EXPO=CMPLX(SIGN(37.0,
1 REAL(EXPO)),0.0)
41      CMU(KK)=CEXP(EXPO)*BMU(KK)
      DO 42 KK=3,4
      EXPO=CMPLX(FLOAT(N),0.0)*FMU(KK)

```

```

      IF(CABS(REAL(EXPO)) .GT. 37.0) EXPO=CMPLX(SIGN(37.0,
1      REAL(EXPO)),0.0)
42      CMU(KK)=CEXP(EXPO)*R1(KK+4)
C.....CALCULATE WN(XI) AND STORE IN VECTOR CO
43      MAXXI=(FL/FDL+(0.5,0.0))+1
      DO 60 KE=1,MAXXI
      XI=CMPLX(FLOAT(KE-1)*REAL(FDL),0.0)
      FKX=FK+XI
      IF(N .NE. 0 .AND. N .NE. IP) GO TO 51
      IF(N .EQ. IP) GO TO 47
      IF(CABS(XI) .GT. CABS(A)) GO TO 45
      DO 44 KK=1,4
44      CMU(KK)=R1(KK+8)
      GO TO 51
45      DO 46 KK=1,4
46      CMU(KK)=R1(KK+4)
      GO TO 51
47      IF(CABS(XI) .GT. CABS(B)) GO TO 49
      DO 48 KK=1,4
48      CMU(KK)=BMU(KK)
      GO TO 51
49      DO 50 KK=1,4
50      CMU(KK)=R1(KK)
51      V(1)=CCOSH(FKX)
      V(2)=CSINH(FKX)
      V(3)=CCQS(FKX)
      V(4)=CSIN(FKX)
      CALL CMPRD(V,OM,DMU,1,4,4)
      CALL CMPRD(DMU,CMU,V,1,4,1)
      CO(KE)=(10.0,0.0)*CMPLX(ALOG10(REAL(OMEGA))*4*
1      CABS(V(1))*2,0.0)
60      CONTINUE
C.....PRINT WN(XI) VALUES FOR SPECIFIED N
      WRITE(3,106) N
      WRITE(3,102) (CO(KK),KK=1,MAXXI)
70      CONTINUE
C.....ZERO THE VECTORS R,CO, AND CYCLE FOR NEXT OMEGA
      DO 80 K=1,64
      IF(K .LE. 8) R(K)=(0.0,0.0)
      CO(K)=(0.0,0.0)
80      CONTINUE
1000     CONTINUE
      STOP
100      FORMAT(' IER = ',I5)
101      FORMAT(' AMU(P+)' )
102      FORMAT(' (4(E15.4)) )
103      FORMAT(' AMU(P-)' )
104      FORMAT(' AMU(O+)' )
105      FORMAT(' AMU(O-)' )
106      FORMAT(' N = ',I5)
107      FORMAT(2F10.0,I5)
108      FORMAT(1H1,' L = ',2E10.4,' A = ',2E10.4,' & = ',
1      I5,' B = ',2E10.4,' E = ',2E10.4,/)
109      FORMAT(' I = ',2E10.4,' RHO = ',2E10.4,/,
1      ' 7 = ',2E10.4,' MJ = ',I5,/)
110      FORMAT(' 5 = ',2E10.4,' LAMDA = ',2E10.4,/,
1      ' KAPPA = ',2E10.4,' ZW = ',2E10.4,/,
2      ' COMEGA = ',2E10.4,/)
111      FORMAT(1H0,///,' OMEGA = ',2E10.4,' INDG = ',I5,/)
112      FORMAT(' G = ',2E10.4,' KAPPA'' = ',2E10.4,/,
1      ' L INCREMENT = ',2E10.4,/)

```

```

113  FORMAT(' OM MATRIX IS SINGULAR, DET = ',2E10.4,/)
114  FORMAT(' TYPE IN OMEGA IN COMPLEX FORMAT AND INDQ',/)
115  FORMAT(' MU')
    END
    SUBROUTINE CGELG(RR,RI,AR,AI,M,N,EPS,IER)
C.....CGELG SOLVES A GENERAL SYSTEM OF SIMULTANEOUS
C.....LINEAR EQ'NS WITH COMPLEX COEFFICIENTS AND RHS
C.....BY GAUSSIAN ELIMINATION WITH COMPLETE PIVOTING.
C.....THE COMPLEX COEFFICIENTS AND RHS HAVE DOUBLE
C.....PRECISION REAL AND IMAGINARY PARTS.
C.....R=RR+I*RI IS THE MXN MATRIX OF RHS (DESTROYED).
C.....ON RETURN R CONTAINS THE SOLUTION.
C.....A=AR+I*AI IS THE MXM COEFFICIENT MATRIX (DESTROYED).
C.....EPS IS THE RELATIVE TOLERANCE FOR TEST ON
C.....LOSS OF SIGNIFICANCE (10E-6 TO 10E-7 SUGGESTED FOR SINGLE
C.....PRECISION, 10E-14 TO 10E-16 FOR DOUBLE PRECISION),
C.....SET ON INPUT.
C.....IER IS THE RESULTANT ERROR PARAMETER (0 INDICATES
C.....NO ERROR, -1 INDICATES M<1 OR A PIVOT ELEMENT IS 0,
C.....K IS A WARNING DUE TO A POSSIBLE LOSS OF SIGNIFICANCE
C.....AT ELIMINATION STEP K+1).
C.....MATRICES ARE ASSUMED TO BE STORED COLUMNWISE
C.....WITH REAL AND IMAGINARY PARTS SEPARATED.
    IMPLICIT DOUBLE PRECISION(A-H,O-Z)
    DIMENSION AR(1),AI(1),RR(1),RI(1)
    DMULTR(X1,Y1,X2,Y2)=X1*X2-Y1*Y2
    DMULTI(X1,Y1,X2,Y2)=X1*Y2+X2*Y1
    DIVR(X1,Y1,X2,Y2)=(X1*X2+Y1*Y2)/(X2**2+Y2**2)
    DIVI(X1,Y1,X2,Y2)=(X2*Y1-X1*Y2)/(X2**2+Y2**2)
    IF(M) 23,23,1
C.....SEARCH FOR GREATEST ELEMENT IN MATRIX A
1    IER=0
    PIVR=0.D0
    PIVI=0.D0
    MM=M*M
    NM=N*M
    DO 3 L=1,MM
    TBR=AR(L)
    TBI=AI(L)
    IF(DSQRT(TBR**2+TBI**2)-DSQRT(PIVR**2+PIVI**2)) 3,3,2
2    PIVR=TBR
    PIVI=TBI
    I=L
3    CONTINUE
    TOLR=EPS*PIVR
    TOLI=EPS*PIVI
C.....A(I)=AR(I)+I*AI(I) IS PIVOT ELEMENT.
C.....START ELIMINATION LOOP.
    LST=1
    DO 17 K=1,M
C.....TEST ON SINGULARITY.
    IF(PIVR.EQ. 0.D0 .AND. PIVI.EQ. 0.D0) GO TO 23
4    IF(IER) 7,5,7
5    IF(DSQRT(PIVR**2+PIVI**2)-DSQRT(TOLR**2+TOLI**2)) 6,6,7
6    IER=K-1
7    PIVIR=DIVR(1,D0,0.D0,AR(I),AI(I))
    PIVII=DIVI(1,D0,0.D0,AR(I),AI(I))
    J=(I-1)/M
    I=I-J*M-K
    J=J+1-K
C.....I+K IS ROW=INDEX, J+K COLUMN=INDEX OF PIVOT ELEMENT.

```

```

C.....PIVOT ROW REDUCTION AND ROW INTERCHANGE IN RHS.
DO 8 L=K,NM,M
  LL=L+I
  TBR=DMULTR(PIVIR,PIVII,RR(LL),RI(LL))
  TBI=DMULTI(PIVIR,PIVII,RR(LL),RI(LL))
  RR(LL)=RR(L)
  RI(LL)=RI(L)
  RR(L)=TBR
8  RI(L)=TBI
C.....ELIMINATION TERMINATED.
  IF(K-M) 9,18,18
C.....COLUMN INTERCHANGE IN MATRIX A.
9  LEND=LST+M-K
  IF(J) 12,12,10
10 II=J+M
  DO 11 L=LST,LEND
  TBR=AR(L)
  TBI=AI(L)
  LL=L+II
  AR(L)=AR(LL)
  AI(L)=AI(LL)
  AR(LL)=TBR
11 AI(LL)=TBI
C.....ROW INTERCHANGE AND PIVOT ROW REDUCTION IN MATRIX A.
12 DO 13 L=LST,MM,M
  LL=L+I
  TBR=DMULTR(PIVIR,PIVII,AR(LL),AI(LL))
  TBI=DMULTI(PIVIR,PIVII,AR(LL),AI(LL))
  AR(LL)=AR(L)
  AI(LL)=AI(L)
  AR(L)=TBR
13 AI(L)=TBI
C.....SAVE COLUMN INTERCHANGE INFORMATION
  AR(LST)=DBLE(FLOAT(J))
  AI(LST)=0.DO
C.....ELEMENT REDUCTION AND NEXT PIVOT SEARCH.
  PIVR=0.DO
  PIVI=0.DO
  LST=LST+1
  J=0
  DO 16 II=LST,LEND
  PIVR=-AR(II)
  PIVII=-AI(II)
  IST=II+M
  J=J+1
  DO 15 L=IST,MM,M
  LL=L-J
  AR(L)=AR(L)+DMULTR(PIVIR,PIVII,AR(LL),AI(LL))
  AI(L)=AI(L)+DMULTI(PIVIR,PIVII,AR(LL),AI(LL))
  TBR=AR(L)
  TBI=AI(L)
  IF(DSQRT(TBR**2+TBI**2)=DSQRT(PIVR**2+PIVI**2)) 15,15,14
14 PIVR=TBR
  PIVI=TBI
  I=L
15 CONTINUE
  DO 16 L=K,NM,M
  LL=L+J
  RR(LL)=RR(LL)+DMULTR(PIVIR,PIVII,RR(L),RI(L))
16 RI(LL)=RI(LL)+DMULTI(PIVIR,PIVII,RR(L),RI(L))
17 LST=LST+M

```



```

C.....END OF ELIMINATION LOOP.
C.....BACK SUBSTITUTION AND BACK INTERCHANGE.
18  IF(M=1) 23,22,19
19  IST=MM+M
    LST=M+1
    DO 21 I=2,M
      II=LST-I
      IST=IST-LST
      L=IST-M
      L=DABS(AR(L)+0.5D0)
      DO 21 J=II,NM,M
        TBR=RR(J)
        TBI=RI(J)
        LL=J
        DO 20 K=IST,MM,M
          LL=LL+1
          TBR=TBR-DMULTR(AR(K),AI(K),RR(LL),RI(LL))
          TBI=TBI-DMULTI(AR(K),AI(K),RR(LL),RI(LL))
          K=J+L
          RR(J)=RR(K)
          RI(J)=RI(K)
          RR(K)=TBR
          RI(K)=TBI
20  TBI=TBI-DMULTI(AR(K),AI(K),RR(LL),RI(LL))
    K=J+L
    RR(J)=RR(K)
    RI(J)=RI(K)
    RR(K)=TBR
    RI(K)=TBI
21  RI(K)=TBI
22  RETURN
C.....ERROR RETURN
23  IER=-1
    RETURN
    END
    SUBROUTINE CMPRD(A,B,R,N,M,L)
C.....CMPRD COMPUTES THE COMPLEX MATRIX PRODUCT
C.....A(NXM) X B(MXL) = R(NXL) WHERE THE MATRICES ARE
C.....STORED COLUMNWISE AS VECTORS.
    IMPLICIT COMPLEX(A-H,O-Z)
    DIMENSION A(1),B(1),R(1)
    IR=0
    IK=-M
    DO 10 K=1,L
      IK=IK+M
      DO 10 J=1,N
        IR=IR+1
        JI=J-N
        IB=IK
        R(IR)=(0.0,0.0)
        DO 10 I=1,M
          JI=JI+N
          IB=IB+1
10    R(IR)=R(IR) + A(JI)*B(IB)
    RETURN
    END
    SUBROUTINE CMINV(A,N,D,L,M)
C.....CMINV INVERTS A MATRIX WITH COMPLEX ELEMENTS
C.....BY GAUSS-JORDAN METHOD.
C.....A IS THE INPUT MATRIX, DESTROYED IN COMPUTATION
C.....AND REPLACED BY THE INVERSE.
C.....N IS THE ORDER OF A.
C.....D IS THE RESULTANT DETERMINENT.
C.....L AND M ARE WORK VECTORS EACH OF LENGTH N.
    IMPLICIT COMPLEX(A-H,O-Z)
    DIMENSION A(1),L(1),M(1)
C.....SEARCH FOR LARGEST ELEMENT.
    D=(1.0,0.0)

```

```

      NK=N
      DO 80 K=1,N
      NK=NK+N
      L(K)=K
      M(K)=K
      KK=NK+K
      BIGA=A(KK)
      DO 20 J=K,N
      IZ=N*(J-1)
      DO 20 I=K,N
      IJ=IZ+I
10      IF(CABS(BIGA)-CABS(A(IJ))) 15,20,20
15      BIGA=A(IJ)
      L(K)=I
      M(K)=J
20      CONTINUE
C.....INTERCHANGE ROWS
      J=L(K)
      IF(J=K) 35,35,25
25      KI=K-N
      DO 30 I=1,N
      KI=KI+N
      HOLD=A(KI)
      JI=KI-K+J
      A(KI)=A(JI)
30      A(JI)=HOLD
C.....INTERCHANGE COLUMNS.
35      I=M(K)
      IF(I=K) 45,45,38
38      JP=N*(I-1)
      DO 40 J=1,N
      JK=NK+J
      JI=JP+J
      HOLD=A(JK)
      A(JK)=A(JI)
40      A(JI)=HOLD
C.....DIVIDE COLUMN BY MINUS PIVOT (VALUE OF PIVOT
C.....ELEMENT IS CONTAINED IN BIGA).
45      IF(BIGA .NE. (0.0,0.0)) GO TO 48
46      D=(0.0,0.0)
      RETURN
48      DO 55 I=1,N
      IF(I=K) 50,55,50
50      IK=NK+I
      A(IK)=A(IK)/(-BIGA)
55      CONTINUE
C.....REDUCE MATRIX
      DO 65 I=1,N
      IK=NK+I
      HOLD=A(IK)
      IJ=I-N
      DO 65 J=1,N
      IJ=IJ+N
      IF(I=K) 60,65,60
60      IF(J=K) 62,65,62
62      KJ=IJ-I+K
      A(IJ)=HOLD+A(KJ)+A(IJ)
65      CONTINUE
C.....DIVIDE ROW BY PIVOT
      KJ=K-N
      DO 75 J=1,N

```



```

      KJ=KJ+N
      IF(J=K) 70,75,70
70    A(KJ)=A(KJ)/BIGA
75    CONTINUE
C.....PRODUCT OF PIVOTS
      D=D*BIG
C.....REPLACE PIVOT BY RECIPROCAL
      A(KK)=(1.0,0.0,0.0)/BIGA
80    CONTINUE
C.....FINAL ROW AND COLUMN INTERCHANGE.
      K=N
100   K=(K-1)
      IF(K) 150,150,105
105   I=L(K)
      IF(I=K) 120,120,108
108   JQ=N*(K-1)
      JR=N*(I-1)
      DO 110 J=1,N
      JK=JQ+J
      HOLD=A(JK)
      JI=JR+J
      A(JK)=-A(JI)
110   A(JI)=HOLD
120   J=M(K)
      IF(J=K) 100,100,125
125   KI=K=N
      DO 130 I=1,N
      KI=KI+N
      HOLD=A(KI)
      JI=KI-K+J
      A(KI)=-A(JI)
130   A(JI)=HOLD
      GO TO 100
150   RETURN
      END

```

### I.1.3 Computational Results

The first computational result which we present has a bearing on the effects of multi-wheel interactions. The values of parameters are as follows:

#### Case 1:

$$\begin{aligned}\ell &= 2 \text{ ft}, a = 1 \text{ ft}, p = 2, b = 1 \text{ ft} \\ E &= 30 \times 10^6 \text{ lb/in}^2, m_r(\rho_r) = 34 \text{ lb/ft}, \\ I &= 40 \text{ in}^4, B_r = EI = 8.33 \times 10^6 \text{ lb ft}^2, \eta_r = 0 \\ G &= 0, K = .7 \times 10^5 \text{ lb/in.}, \eta_f = 0.001\end{aligned}$$

This case corresponds to fasteners having a linear stiffness such that the resonance of rail on fasteners is at 100 Hz. No torsional stiffness was assumed. The case was run both with and without the second wheel, taking its impedance to be  $-j\omega M$  with  $M = 1000 \text{ lb}$ . In both cases a force excitation was imposed at the location of the first wheel.

Figure I.5 shows the resulting propagation constants as functions of the nondimensional frequency parameter

$$\Omega = \omega \sqrt{\frac{m_r \ell^4}{B_r}} = (1.29 \times 10^{-3}) \omega$$

It is seen that the wave component corresponding to  $\mu_2$  is rapidly attenuated, while  $\mu_1$  represents the propagating part of the solution.

The case without the second wheel can be easily compared to analytical solutions from Chapter 2.3 for a continuous support model. The continuous and discrete fastener models should agree for frequencies much lower than the frequency at which the bending wavelength is twice the fastener spacing ( $\sim 1200 \text{ Hz}$ ). On this basis the computer solutions were found to agree quite well with the continuous model.

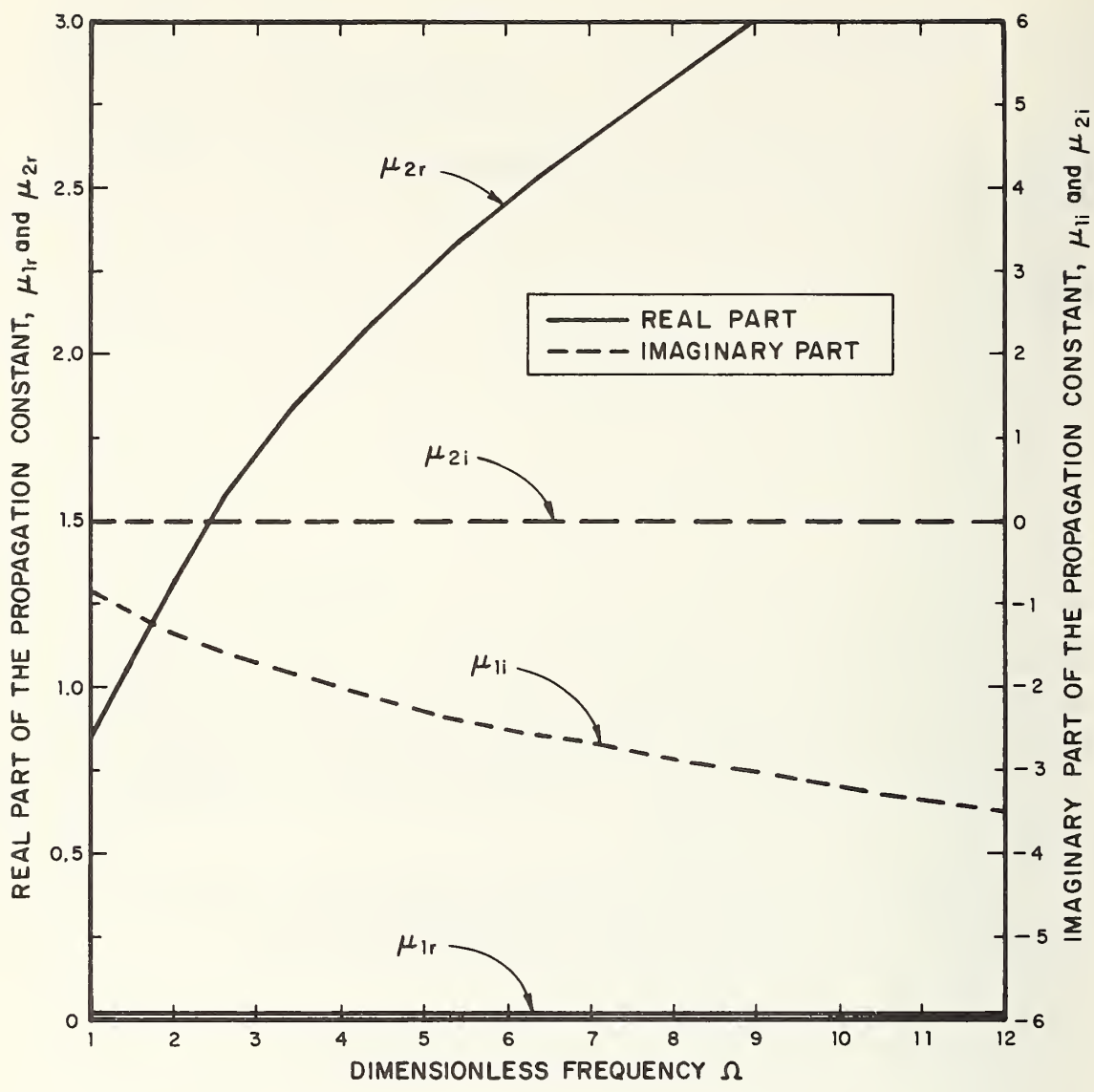


FIG. I.5 PROPAGATION CONSTANTS FOR CASE 1

The real parts of the displacement phasor with and without the second wheel are shown in Fig. I.6 for  $\omega = 10^3$  rad/sec (159 Hz). The plot for the case including the second wheel mass shows that the displacement is nearly zero at the second wheel position. This is not surprising since above the rail-fastener resonance, the wheel impedance is much larger than the driving point impedance of the rail. Thus, the second wheel acts as a nearly rigid pin support. The computer calculations show that the transmission of bending waves by the loading point of the second wheel is quite high. Thus, a large buildup of vibration between truck wheels due to reflections from the wheels is not expected.

We now present a second case which is more characteristic of the rail and fastener on the MBTA Red Line Anderson Bridge.

## Case 2

$$l = 2.5 \text{ ft}, a = 1.25 \text{ ft}, p = 3, b = .75 \text{ ft}$$

$$\text{distance between wheels} = 7 \text{ ft}$$

$$E = 30 \times 10^6 \text{ lb/in}^2$$

$$I = 65 \text{ in}^4, B_r = 13.54 \times 10^6 \text{ lb ft}^2, \eta_r = 0.1$$

$$m_r = 38.3 \text{ lb/ft}, K = .517 \times 10^6 \text{ lb/in.}, \eta_f = 0$$

$$G = 7.89 \times 10^6 \text{ lb-in}$$

The values for rail moment of inertia and density are for RE 115 rail. The fastener stiffness and spacing used here give a rail fastener resonance at 230 Hz. At the time this case was run, the fastener properties were intended to be those of the Liberty fasteners used on the Anderson Bridge. However, in later work we estimated the resonant frequency to be 275 Hz. Thus, the case presented here does not correspond exactly to the case studied in Section 4.2, although we expect the general results to be applicable to both cases.

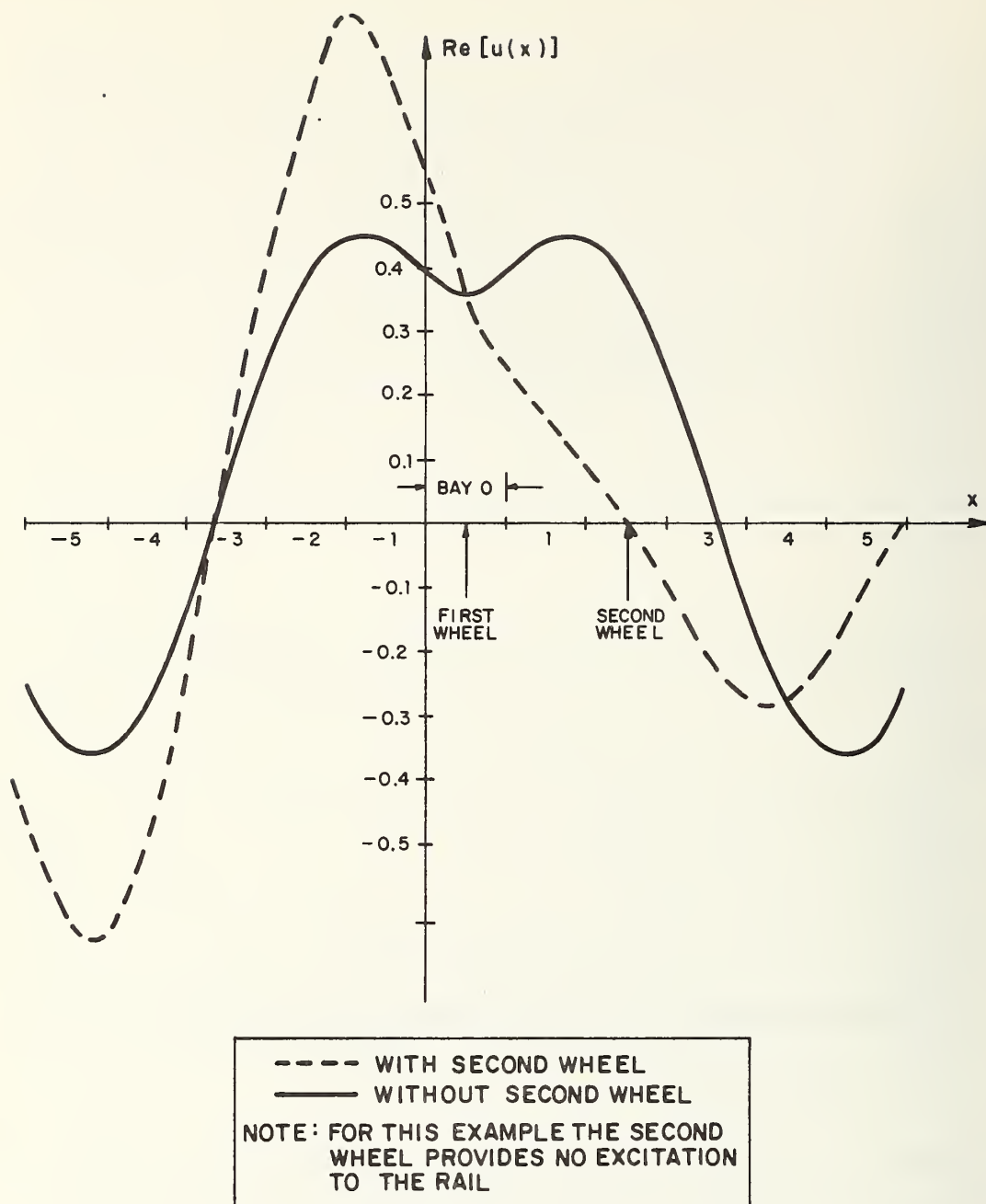


FIG. I.6 REAL PART OF THE DISPLACEMENT PHASOR  $u(x)$   
FOR CASE 1 AT  $\omega = 1000$  RADIANS/SECOND

On the Anderson Bridge, the fasteners are 15-1/2" long. Thus, the fasteners give a torsional stiffness approximately equal to  $KL^2/12$ , where L is the fastener length. The damping loss factors for the rail and the fasteners were set to provide reasonable correspondence between measured data and the predicted rate of attenuation with distance from the excitation point. Although the damping is actually associated with losses in the rail fasteners, we have accounted for it by endowing the rail with a loss factor of 0.1. As discussed in the next section, a better model would allow the fastener damping loss factor to be frequency dependent. However, in its present form the computer program does not allow the damping loss factors to be frequency dependent. Finally, a mass impedance of  $-j\omega M$  with  $M = 1000$  lbs is again used for each of the two wheels, and the first wheel excites the rail through a wheel-rail roughness velocity of unit magnitude.

Figure I.7 shows the propagation constants in this case. One propagation constant corresponds to a rapidly attenuated near-field while the other represents a propagating wave attenuated only by damping. As in the previous case there is no non-propagating band of frequencies above the rail-fastener resonance. In fact, calculation of the propagation constants through the continuous model, see Chapter 2.3, yields results nearly identical to those presented here.

Figures I.8 and I.9 show the acceleration level for the rail,  $10 \log [|\ddot{u}|^2]$  plotted versus x. As might be expected, the propagation away from the wheels shows a near-field dependence for frequencies below the rail fastener resonance. Above this frequency, there is only attenuation due to damping. The large drop-off near the second wheel is due to its large impedance. In reality this drop-off will not occur since the complete solution is the sum of the present one and the rail response due to direct excitation by the second wheel with the first acting as a passive load. Furthermore, it should be noted that at the higher frequencies the rail acceleration shows only a small scale periodicity reflecting the periodic variation of support conditions. Thus, it can be expected that rail vibration will be little affected by the relative position of wheels and fasteners.



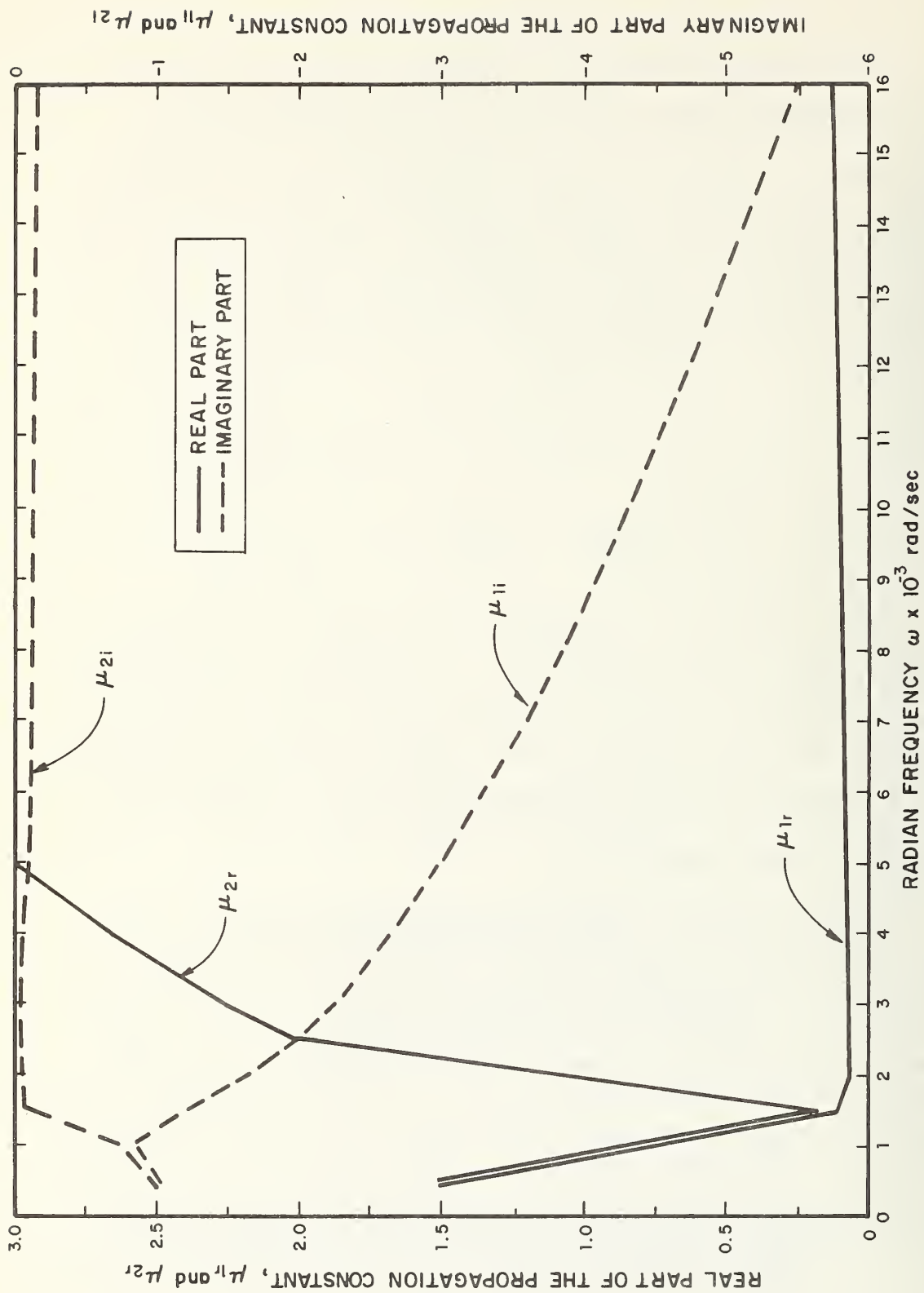


FIG. 1.7 PROPAGATION CONSTANTS FOR CASE 2

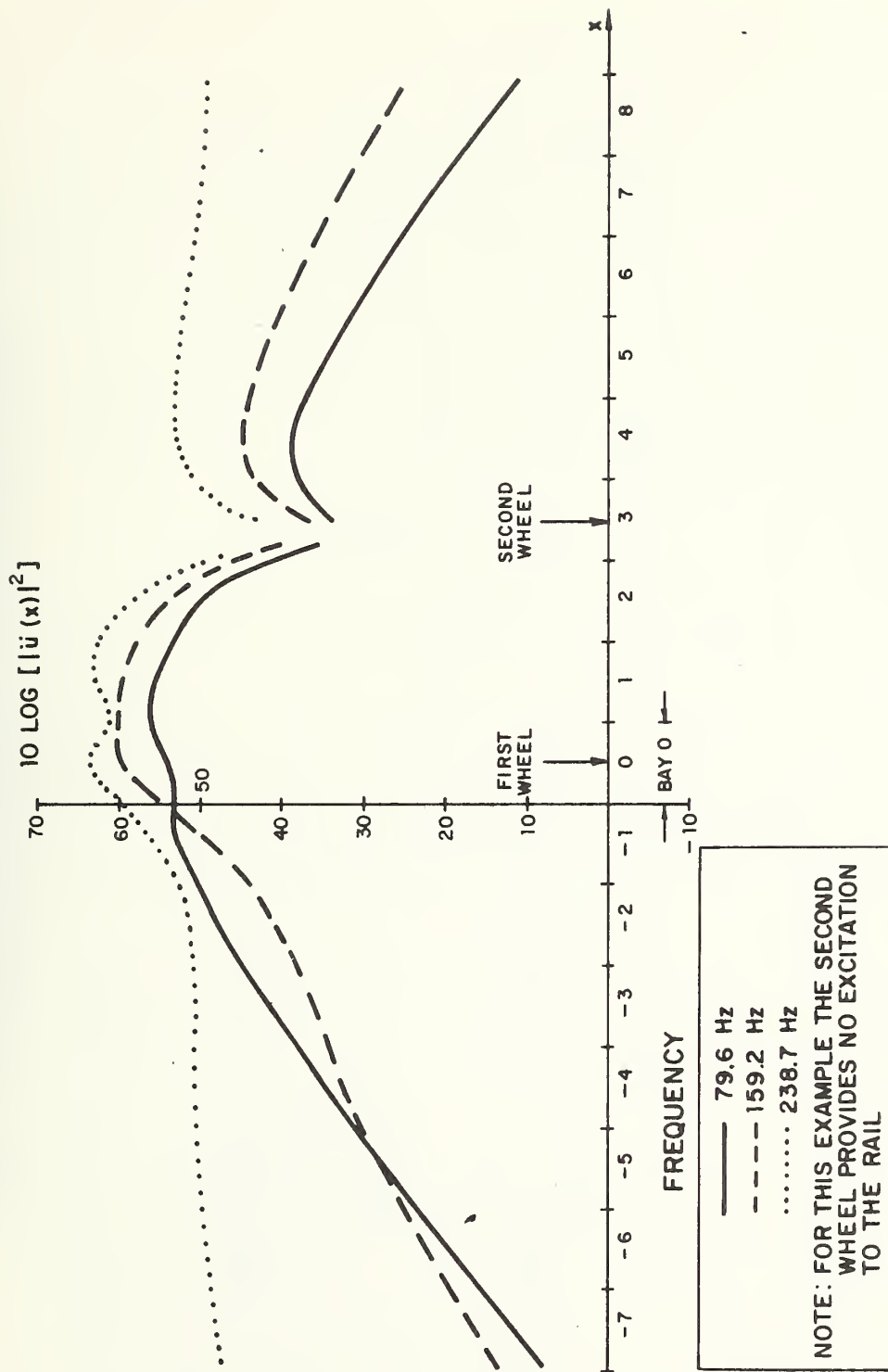


FIG. I.8 SPATIAL DISTRIBUTION OF THE ACCELERATION LEVEL FOR CASE 2 AT THREE FREQUENCIES

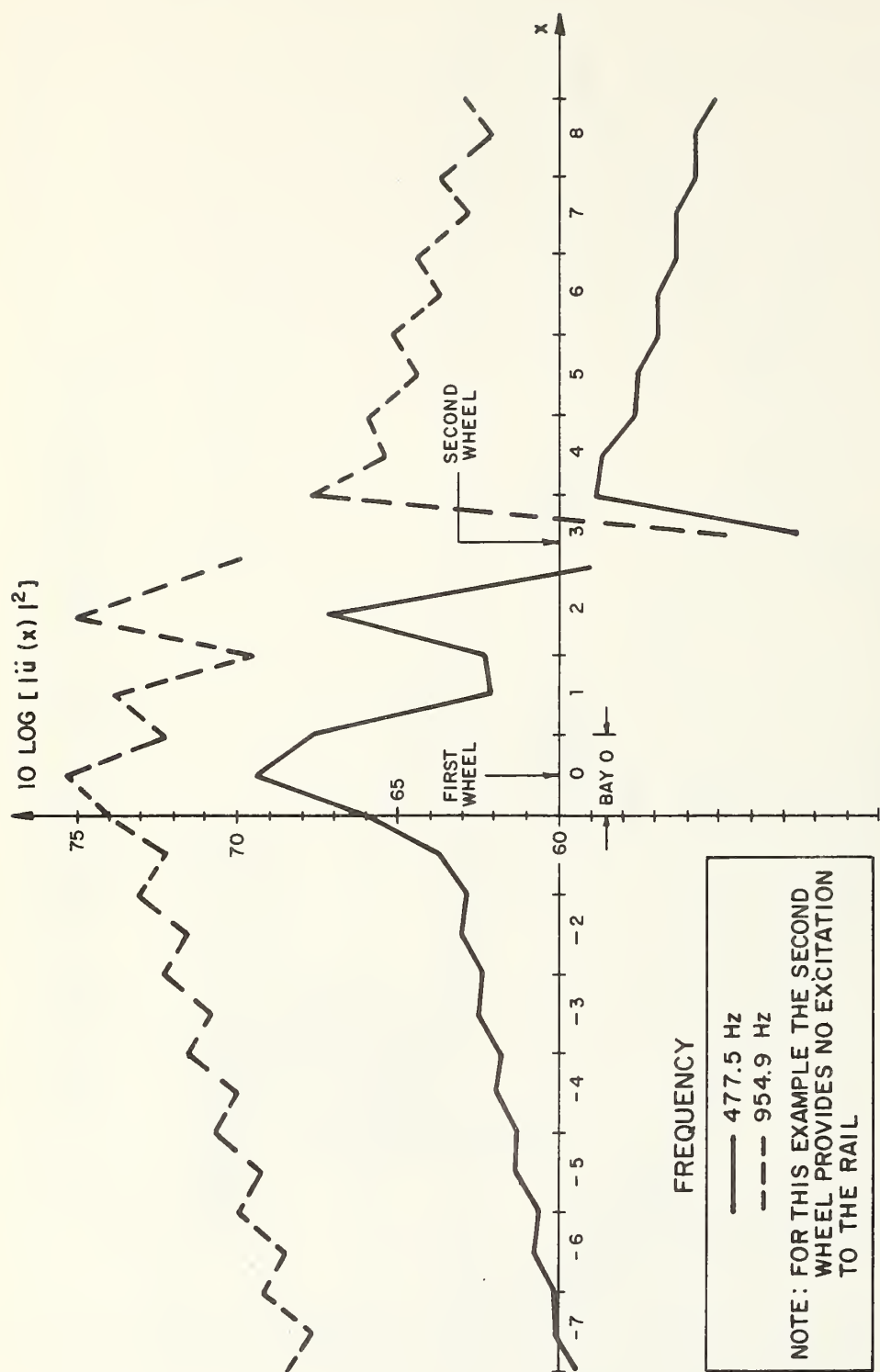


FIG. I.9 SPATIAL DISTRIBUTION OF THE ACCELERATION LEVELS FOR CASE 2 AT TWO HIGH FREQUENCIES

In the above cases, a non-propagating band above the rail-fastener resonance was not found. Thus, in this respect the continuous and discrete models agree. However, in general, the existence of non-propagating bands is not immediately clear. The situation can be sensitive to the ratio of the fastener stiffness to the bending rigidity of the rail, particularly at the frequency at which the bending wavelength is twice the fastener spacing. To check the sensitivity to fastener stiffness, Case 2 was run again, increasing the fastener stiffness by a factor of ten. The propagation constants are shown in Fig. I.10. Here, one of the propagation constants, whose real part was of the order of the damping in Case 2, now shows a hump between  $5.5 \times 10^3$  and  $8 \times 10^3$  rad/sec. This represents a non-propagating band in the relatively narrow frequency range between  $\sim 900$  and  $\sim 1300$  Hz.

From these results we can conclude that for typical rail and fastener properties, the discreteness of fasteners will not appreciably affect the qualitative features of rail vibration.

As a result of these investigations, we can, in summary, draw the following conclusions.

- (1) Vibration buildup between wheels of a truck due to multiple reflections from the wheels does not occur. The effect of one wheel on rail response to direct excitation by another wheel is essentially that of a rigid pin support.
- (2) For typical rail and fastener properties there are no non-propagating frequency bands above the rail-fastener resonance frequency. This means that the large attenuation rates observed may not be explained by wave propagation effects due to the periodic nature of rail fastening.
- (3) The wheel positions relative to fastener locations do not significantly affect rail vibration.

Hence, on the whole, the continuous elastic foundation model of rail fastening is validated, and we recommend use of this simple model in predicting elevated structure noise.

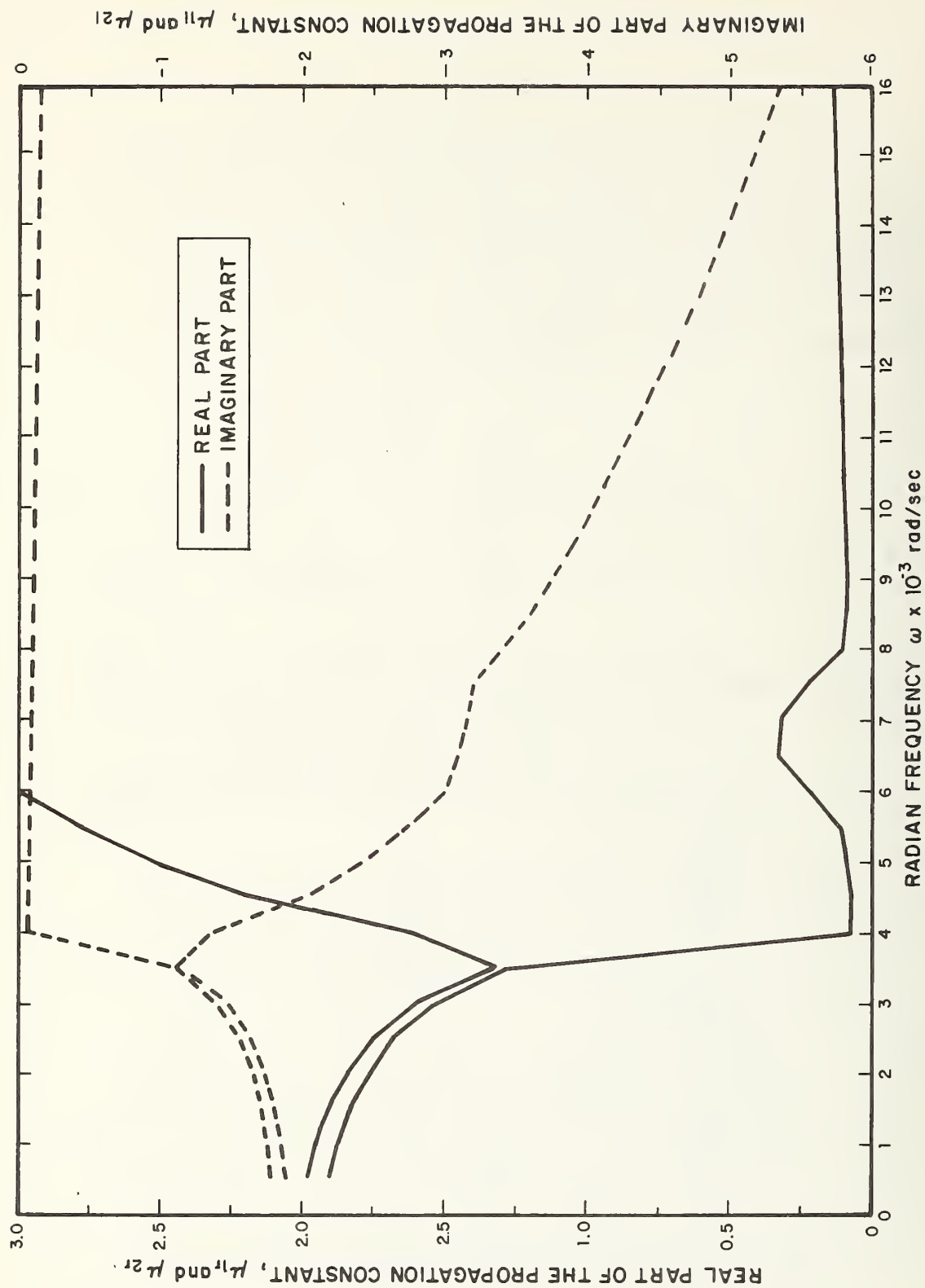


FIG. 1.10 PROPAGATION CONSTANTS FOR THE CASE IN WHICH THE FASTENER STIFFNESS OF CASE 2 IS INCREASED BY A FACTOR OF 10

## 1.2 A Refined Model for Rail Damping

A configuration typical of resilient direct fixation fasteners is shown in Fig. I.11. The fasteners consist of a rubber pad upon which the rail rests and two rubber pads covering the top of the rail foot. These pads are joined by steel covering plates and the whole assemblage is bolted to the supporting structure, as shown. Other resilient fasteners may use different resilient materials and slightly different designs. The only variables of importance in predicting rail vibration are the pad stiffness and damping. It is reasonable to assume that the portion of the fastener which is most effective in both rail support and in the damping of rail vibrations is the section of pad immediately below the rail base, as shown in Fig. I.12. In the following calculations, the fastener stiffness is taken to be essentially the stiffness of this pad. The notations to be used for pad dimensions are indicated in the figure.

To calculate the attenuation of rail vibration due to damping we assume the fastener to be represented by a continuous visco-elastic foundation, as was done for the simple model of Chapter 2.3. The stiffness of the foundation per unit length,  $K_\ell$ , is given by

$$K_\ell = \frac{K}{\ell} \quad (\text{I.37})$$

where  $K$  is the stiffness of a single fastener and  $\ell$  is the fastener spacing. As in Chapter 2.3 the damping of the fastener will be included by letting the fastener stiffness be complex,

$$K' = K (1 + i \eta_f) \quad (\text{I.38})$$

where  $\eta_f$  is the fastener damping loss factor. However, in this Section we will allow the loss factor and stiffness to be



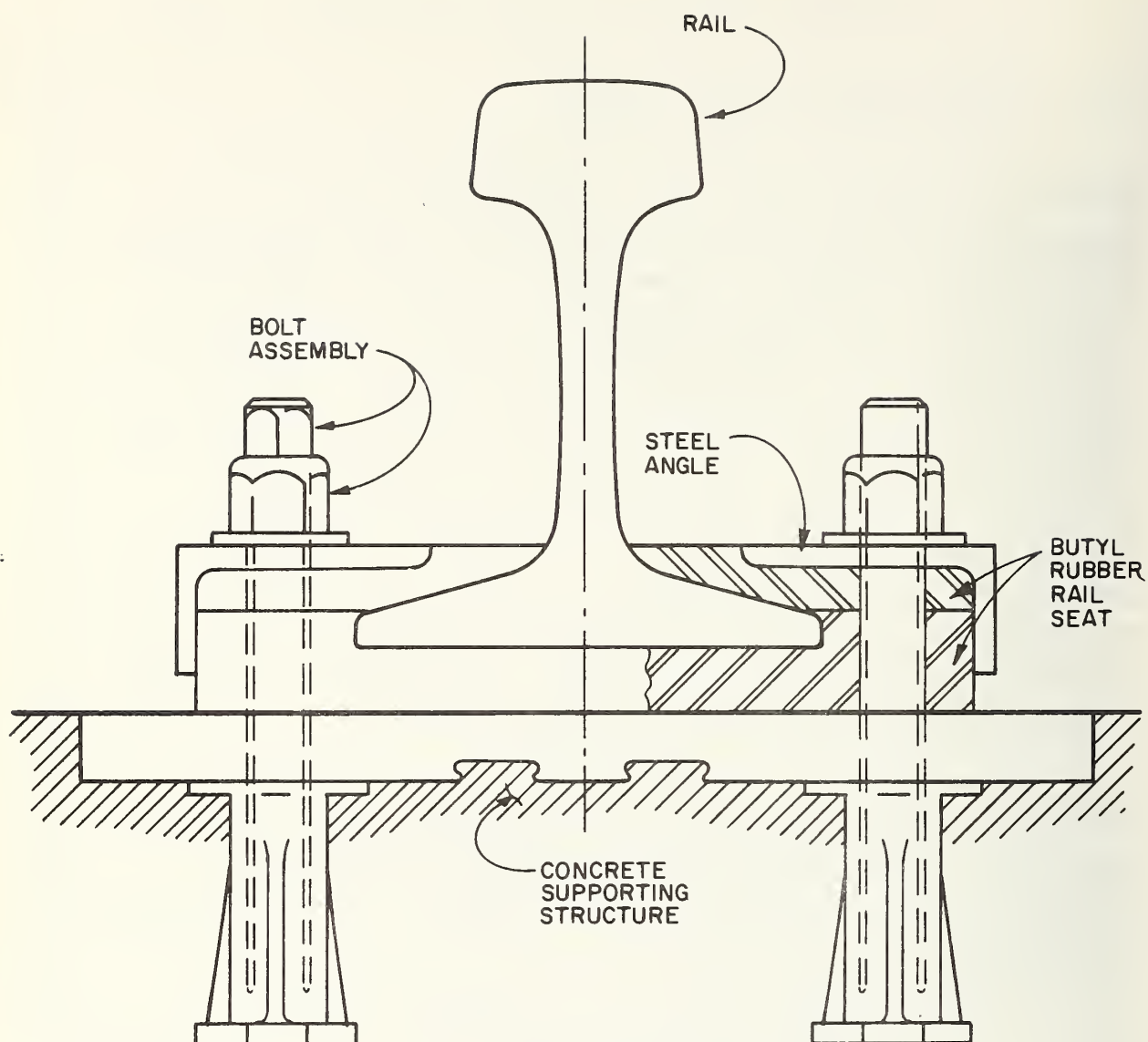


FIG I.11 TYPICAL RAIL FASTENER CONFIGURATION

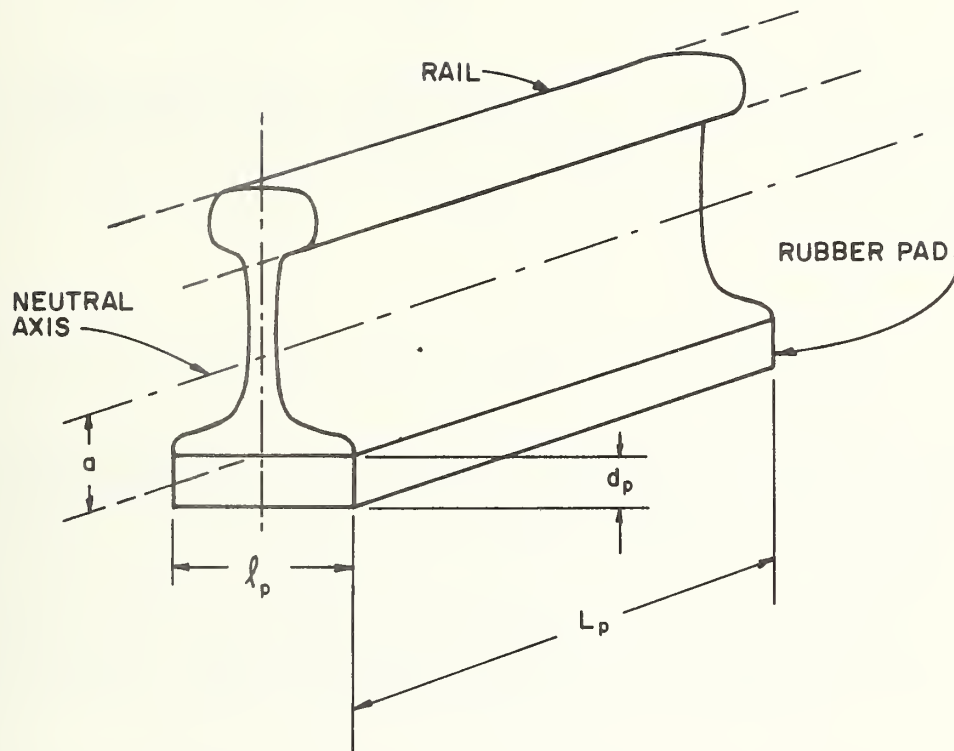


FIG. I.12 SKETCH OF THE RAIL MOUNTED ON THE  
EFFECTIVE LOAD BEARING SECTION OF THE FASTENER PAD

frequency dependent and we will include the effect of shear deformations in the fastener on the damping. We will assume that the frequency of vibration is well above the fundamental resonance frequency of the rail on its fasteners,  $\omega_r$ , where

$$\omega_r^2 = \frac{K_\ell}{m_r} \quad (\text{I.39})$$

and  $m_r$  is the rail mass per unit length. The damping loss factor given in Eq. I.38 relates the time average power dissipated in the fastener,  $W_{f,diss}$ , to the time average energy stored in the fastener,  $E_f$ ,

$$W_{f,diss} = \omega \eta_f E_f \quad (\text{I.40})$$

where  $\omega$  is the radian frequency of vibration. By analogy an effective damping loss factor for the rail and fasteners together,  $\eta_{eff}$ , can be defined such that

$$W_{f,diss} + W_{r,diss} = \omega \eta_{eff} (E_f + E_r) \quad (\text{I.41})$$

where  $W_{r,diss}$  is the time average power dissipated in the rail and  $E_r$  is the energy stored in the rail. With this definition the rate of decay of vibration waves traveling down the rail is [17]

$$\Delta_\lambda = 13.6 \eta_{eff} \text{ dB/wavelength} \quad (\text{I.42})$$

The decay in dB/unit length of rail is found by dividing  $\Delta_\lambda$  by the wavelength. This gives

$$\Delta = 2.16 \eta_{eff} k_m \quad (\text{I.43})$$

where  $k_m$  is the wavelength of the waves,  $k_m = 2\pi/\lambda$ . For the simple model considered in Chapter 2.3 the effective loss factor is given by

$$\eta_{\text{eff}} = \eta_r + \eta_f \frac{\omega_r^2}{\omega^2} \quad (\text{I.44})$$

and the wavenumber,  $k_m$ , is given by

$$k_m^4 \approx \frac{\omega^2 m_r}{B_r} \quad \text{for } \omega \gg \omega_r \quad (\text{I.45})$$

where the loss factors of the fastener,  $\eta_f$ , and the rail,  $\eta_r$ , are considered for the time being to be frequency dependent.

The effect of allowing the loss factors and fastener stiffness to be frequency dependent is to change both the effective damping loss factor and the wavenumber. However, in the work to follow we will take the frequency dependence to be sufficiently small that the wavenumber is unaffected. We will modify Eq. I.39 so that the rail resonance frequency is the solution to the equation

$$\omega_r^2 = \frac{K_\ell(\omega_r)}{m_r} \quad (\text{I.46})$$

where  $K_\ell(\omega_r)$  is the effective fastener stiffness per unit length of rail at  $\omega_r$ . Both of these approximations are valid for typical rail fasteners. Finally, the effective damping loss factor will be found using Eq. I.41. The following dissipation and energy storage mechanisms will be considered for the case in which a vibration wave of the form

$$u(x,t) = \hat{U} e^{-i(k_m x - \omega t)} \quad (\text{I.47})$$

is traveling down the rail.

Vertical compression of the pad: When the rail is loaded by the train wheels, it is pressed firmly to the supporting fastener pad. Thus, a "no-slip" condition can be assumed to hold between rail and pad. The "no-slip" condition requires that the displacement of the upper surface of the pad equal that of the rail base. Primarily, this means that the pad undergoes a periodic vertical displacement of magnitude  $\hat{U} e^{-i(k_m x - \omega t)}$ . The time average mechanical energy in the fastener due to this vertical motion,  $E_{f, \text{compr.}}$ , is simply

$$E_{f, \text{compr.}} = \frac{1}{2} K |\hat{U}|^2 \quad (\text{I.48})$$

Shear of the pad: There is a shear deformation of the fastener pad due to rotation of the rail. The geometry is as indicated in Fig. I.13. To estimate the magnitude of this effect, we assume that the shear is uniformly distributed over the width of the pad. This resulting strain energy in the fastener,  $E_{f, \text{shear}}$ , is

$$E_{f, \text{shear}} = \frac{1}{2} G_p d_p l_p \int_0^{L_p} dx \gamma^2(x) \quad (\text{I.49})$$

where  $G_p$  is the shear modulus of the pad material. The shear angle,  $\gamma$ , is related to the angle of flexure,  $\beta$ , by

$$\gamma = \frac{a}{d_p} \beta = \frac{a}{d_p} \frac{\partial u}{\partial x} = -i k_m \frac{a}{d_p} \hat{U} \quad (\text{I.50})$$

Hence, the time averaged mechanical energy,  $E_{f, \text{shear}}$ , of the fastener due to shear of the pad is

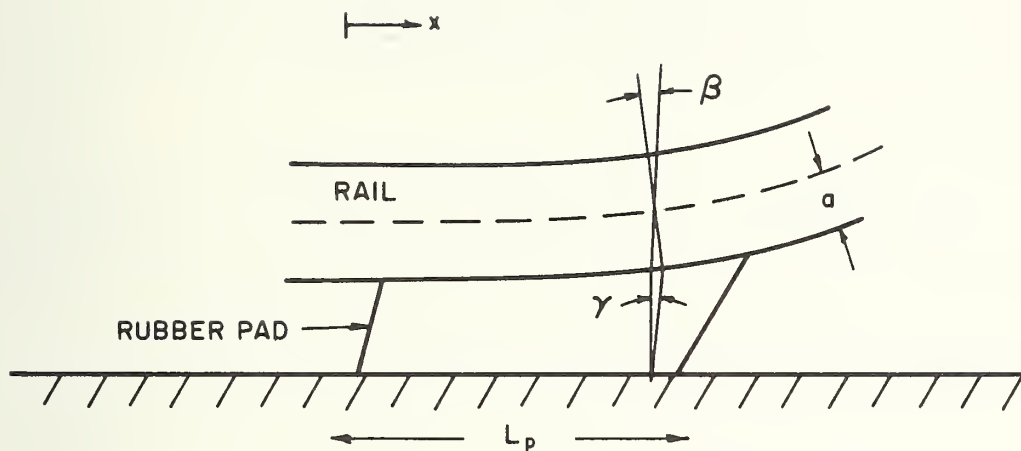


FIG. I.13 SHEAR DEFORMATION IN PAD  
DUE TO RAIL BENDING MOTION



$$E_{f, \text{shear}} \approx \frac{1}{2} G_p d_p \ell_p L_p \left(\frac{a}{d_p}\right)^2 k_m^2 |\hat{U}|^2 \quad (\text{I.51})$$

where it has been assumed that  $\gamma(x)$  is constant over the length, i.e., not a function of  $x$ , of the fastener.

Now we can calculate the energy dissipated by the above two modes of deformation of the pad for each fastener,  $W_{f, \text{diss.}}$ . In Eq. I.40 we set

$$E_f = E_{f, \text{compr.}} + E_{f, \text{shear}} \quad (\text{I.52})$$

If we now let  $\ell$  be the spacing between fasteners, the average energy dissipated in the rail per fastener is

$$W_{r, \text{diss.}} = \omega \eta_r E_r \quad (\text{I.53a})$$

where

$$E_r = \frac{1}{2} B_r k_m^4 \ell |\hat{U}|^2 \quad (\text{I.53b})$$

From Eq. I.41 the effective damping loss factor for the rail and fasteners together is given by

$$\eta_{\text{eff}}/\eta_f = \frac{1 + k_m^2 \frac{G_p}{K} d_p \ell_p L_p \left(\frac{a}{d_p}\right)^2 + \frac{\eta_r}{\eta_f} k_m^4 \frac{B_r}{K_\ell}}{1 + k_m^2 \frac{G_p}{K} d_p \ell_p L_p \left(\frac{a}{d_p}\right)^2 + k_m^4 \frac{B_r}{K_\ell}} \quad (\text{I.54})$$

where  $\eta_f$  is the damping loss factor of the fastener pad material (assumed to be the same for shear and compression).

For typical fastener parameters and rail cross sections, terms in Eq. I.54 involving  $G_p$  are negligible. Thus, the effective damping loss factor may be calculated by assuming only simple compression of the pad,

$$\frac{\eta_{eff}}{\eta_f} \approx \frac{1}{1 + \frac{B_r}{K_\ell} k_m^4} \left[ 1 + \frac{\eta_r}{\eta_f} \left( \frac{B_r}{K_\ell} k_m^4 \right) \right] \quad (I.55)$$

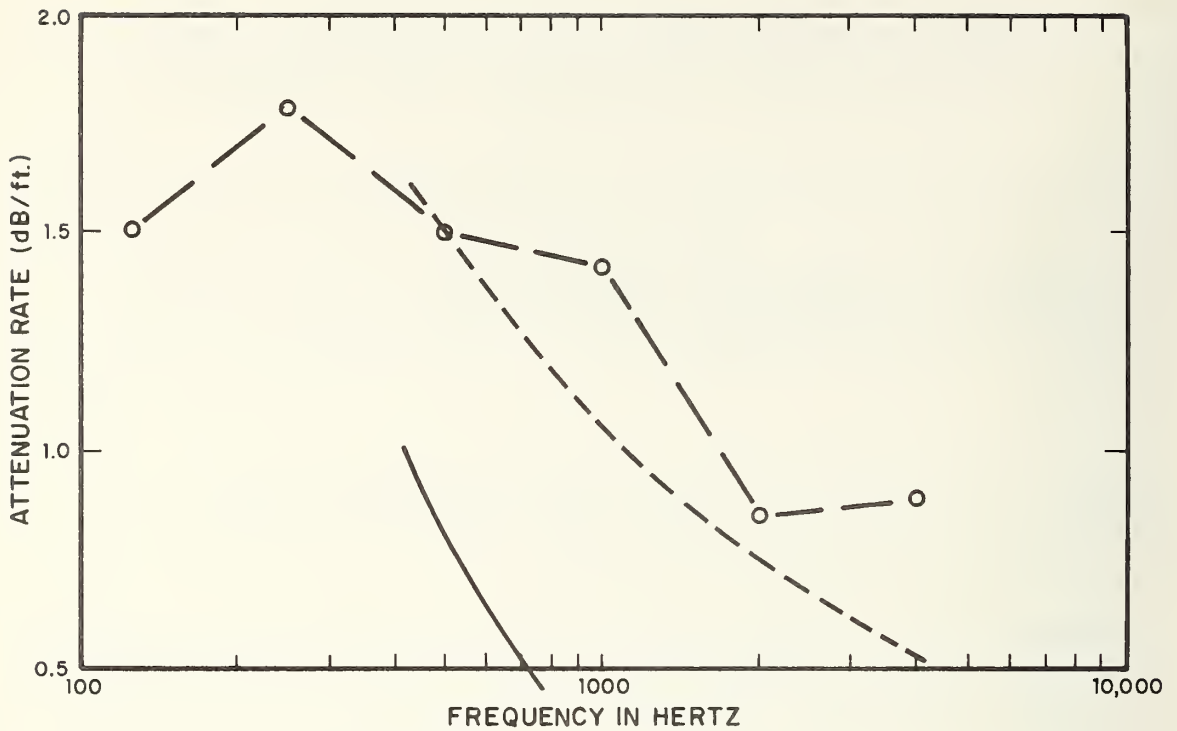
Now we consider the frequency dependence of  $K_\ell$  and  $\eta_f$ . We note that the elastic modulus for many viscoelastic materials display a frequency dependence that gives

$$K_\ell = K_{\ell 1} \left( \frac{\omega}{\omega_r} \right)^{1/2} \quad (I.56a)$$

$$\eta_f = \eta_{f1} \left( \frac{\omega}{\omega_r} \right)^{1/2} \quad (I.56b)$$

where  $K_{\ell 1}$  and  $\eta_{f1}$  are values at  $\omega$  equal  $\omega_r$ , and  $\omega$  is not zero.

As an example we consider the rail (RE 115) and rail fasteners used on the Anderson Bridge of the MBTA. The fastener stiffness is such that the rail/fastener resonance frequency is 275 Hz. The butyl fastener pad damping loss factor at 275 Hz is estimated to be 1.3. The rate of vibration attenuation for the rail for these parameter values is shown in Fig. I.14. Also shown are attenuation rates obtained from measured data and those obtained by taking the fastener stiffness and damping to be frequency independent. It is seen that the relationships of Eq. I.56 yield reasonable agreement with the data.



#### MEASURED VALUES

— — — ○ — — — MBTA RED LINE DATA, RE 115 RAIL,  
LIBERTY FASTENERS

#### PREDICTED VALUES

————— FREQUENCY INDEPENDENT STIFFNESS

$$K_f = 3.55 \times 10^6 \text{ lb./ft./ft.}$$

$$\omega_r = 2\pi \times 275 \text{ rad/sec}$$

$$\eta_f = 1.3$$

----- FREQUENCY DEPENDENT STIFFNESS

$$K_f = K_{f1} \left( \frac{\omega}{\omega_r} \right)^{1/2}$$

$$\eta_f = \eta_{f1} \left( \frac{\omega}{\omega_r} \right)^{1/2}$$

$$K_{f1} = 3.55 \times 10^6 \text{ lb./ft./ft.}$$

$$\eta_{f1} = 1.3$$

$$\omega_r = 2\pi \times 275 \text{ rad/sec}$$

FIG. I.14 PREDICTED AND MEASURED VALUES FOR  
RATE OF ATTENUATION OF THE RAIL VIBRATION

### I.3 Effect of Shear Deformations in the Rail

The simplified model developed in Chapter 2.3 assumes that the rail vibrations are in the form of pure bending. For this case the phase velocity for free bending waves is given by

$$c_b^4 = \frac{\omega^2 B_r}{m_r} \quad (I.57)$$

where  $B_r$  is the bending stiffness of the rail and  $m_r$  is its mass per unit length.

Parameter values for a RE 115 rail cross-section are  $B_r = 2 \times 10^9 \text{ lb-in.}^2$  and  $m_r = 115 \text{ lb/yd}$ . Using these values we find

$$c_b = 146 \sqrt{f} \frac{\text{ft}}{\text{sec}} \quad \text{for RE 115 rail} \quad (I.58)$$

where  $f$  is the frequency in Hz. The wavelength of the bending vibration,  $\lambda_b$ , is simply

$$\lambda_b = \frac{c_b}{f} = \frac{146}{\sqrt{f}} \text{ ft for RE 115 rail} \quad (I.59)$$

At high frequencies, shear deformation of the rail web becomes a significant factor. Rather than being a pure bending motion the rail vibration is due to both bending and shearing of the rail cross-section. To first approximation we can determine the effect of web shear by computing an effective shear wavespeed based on the shear stiffness of the web and the mass of the total rail cross-section.

$$c_s = \sqrt{\frac{G A_w}{m_r}} \quad (I.60)$$

where  $c_s$  is the effective shear wavespeed,  $G$  is the shear modulus of the rail material,  $A_w$  is the cross-sectional area of the rail web and  $m_r$  is the mass per unit length of the rail. For RE 115 rail we find

$$c_s = 5720 \frac{\text{ft}}{\text{sec}} \quad \text{for RE 115 rail} \quad (I.61)$$

At high frequencies, the phase velocity for vibration waves in the rail will equal  $c_s$  rather than  $c_b$ .<sup>\*</sup> An analysis for the intermediate frequencies gives

$$\left(\frac{c}{c_b}\right)^2 = \frac{1}{2} \sqrt{\left(\frac{c_b}{c_s}\right)^4 + 4} - \frac{1}{2} \left(\frac{c_b}{c_s}\right)^2 \quad (I.62)$$

where  $c$  is the phase velocity. From Eq. I.62 we note that the effect of shear deformation is significant only for frequencies above 1500 Hz. Rail vibration at these frequencies is at a comparatively low value and does not contribute significantly to the A-weighted radiated noise levels from the rail or to the vibrational energy transmitted to the track structure. Therefore, we can ignore the effects of shear deformation with no real impact on the accuracy of the prediction model.

---

\*Note at very high frequencies, bending of the rail head and base become important and act to increase the phase velocity. For RE 115 rail this effect is significant above 13,000 Hz.

#### I.4 Effect of a Nonrigid Support Under the Fasteners

In the simplified model we represent the rail support as a continuous visco-elastic foundation on a rigid support. In a realistic case the track structure under the rail fasteners is not rigid. However, we can continue to use the models developed in earlier Sections by replacing the rail fastener stiffness and damping by an effective impedance that takes into account the motion of the track support structure.

The impedance of a continuous visco-elastic foundation on a rigid support,  $Z_f(\omega)$ , is given by

$$Z_f(\omega) = \frac{K_\ell (1 + i \eta_f)}{i \omega} \quad (\text{I.63})$$

where  $K_\ell$  is the foundation stiffness per unit length of rail,  $\omega$  is the radian frequency and  $\eta_f$  is the foundation damping loss factor. When the support structure is not rigid the effective impedance,  $Z$ , becomes both a function of frequency and the wave-number of the rail vibration. The effective impedance is

$$Z(k_x, \omega) = \frac{Z_f(\omega) Z_s(k_x, \omega)}{Z_f(\omega) + Z_s(k_x, \omega)} \quad (\text{I.64})$$

where  $Z_s(k_x, \omega)$  is the impedance of the track support structure and  $k_x$  is the wavenumber. Note that in the limiting case, when the foundation is rigid,  $Z_f = \infty$ , the impedance presented to the rail is the impedance of the track structure. When the foundation is very soft,  $Z_f \approx 0$ , the impedance is equal to the impedance of the fastener.

Two types of track support are of interest for this report: a concrete deck on an elevated structure, and an open deck of



ties on an elevated structure. In the case of elevated structures, we are interested in moderate and high frequencies, above approximately 100 Hz. At these frequencies the impedance of the deck can be modeled by the impedance of an infinitely wide plate in the case of the concrete deck or a series of infinitely wide ties. For the concrete deck

$$Z_s(k_x, \omega) = \frac{4 B_s k_s^2}{\omega} \frac{k_1}{1 - i \frac{k_1}{k_2}} \quad (\text{I.65})$$

where  $B_s$  is the bending stiffness of the deck and

$$k_s^4 = \frac{\omega^2 \rho_s}{B_s} \quad (\text{I.66a})$$

$$k_1 = \sqrt{k_s^2 - k_x^2} \quad \text{if } k_s > k_x \quad (\text{I.66b})$$

$$k_1 = -i\sqrt{k_x^2 - k_s^2} \quad \text{if } k_s < k_x \quad (\text{I.66c})$$

$$k_2 = \sqrt{k_s^2 + k_x^2} \quad (\text{I.66d})$$

and  $\rho_s$  is the mass per unit area of the deck. The wavenumber  $k_s$  is the wavenumber for free bending waves in the concrete deck. For small values of  $k_x$ , the impedance becomes simply the line impedance of an infinite plate,

$$Z_s(k, \omega) = 2(1 + i) \frac{\omega \rho_s}{k_s} \quad (\text{I.67})$$

This impedance consists of a mass term,  $2 i \omega \rho_s / k_s$ , and a damping term,  $2 \omega \rho_s / k_s$ . For typical parameter values (RE 115 rail and 9 inch-thick concrete deck)

$$m_r = 115 \text{ lbs/yd} \quad (\text{I.68a})$$

$$m_{s,\text{eff}} = \frac{12,780}{\sqrt{f}} \text{ lbs/yd} \quad (k_x \ll k_s) \quad (\text{I.68b})$$

For frequencies below 12,350 Hz, the effective support mass is greater than the rail mass. Thus, for the frequency range of interest in this report the concrete deck can be treated as rigid in calculating the rail vibration.

For high wavenumbers the support impedance approaches infinity so that again the deck can be treated as a rigid support.

Wavenumbers very close to  $k_s$  present a problem in that our model using the impedance of an infinite plate is not valid. Effects associated with vehicle speed, column supports, and the finite width of the deck all enter in determining the impedance in this narrow range of wavenumbers. The model of an infinite plate shows the impedance going to zero at  $k_x = k_s$ . This will not happen in the actual case, although the impedance may become small. If the impedance were to become smaller than the impedance of the fastener, then the rail damping due to compression of the fasteners would be greatly reduced. However, this would occur in a very limited frequency range so that we assume the overall effect to be negligible.

When the rails are fastened directly to an open wood tie deck, the representation of the deck impedance is very difficult. In nearly every case the rails are mounted close to the webs of the supporting girders. To first approximation the line impedance of

the ties and girders can be represented simply by the mass per unit length of the girders. We assume that this mass is greater than the mass per unit length of the rail so that the support under the ties can be assumed to be rigid in calculating the rail vibration.

## APPENDIX II

### PREDICTION MODEL FOR LOW FREQUENCIES

At frequencies below the resonance frequency of the rail on its supporting elements (resilient fasteners or wood ties), the vibration of the rail is confined to the region near the excitation point. Freely propagating vibration waves do not exist at these low frequencies. To apply the coupled oscillator approach we must take into account the fact that for each value of wavenumber,  $k_x$ , the modal response for the rail is nonresonant and stiffness controlled, since the frequency is below the modal resonance frequency. To first approximation the forces on the rail are transmitted without attenuation to the deck. However, because of the bending stiffness of the rail the forces which are applied to the rail at discrete points are distributed along a line under the rail.

To use the coupled oscillator approach and Statistical Energy Analysis we calculate the time-average power input to the cross-modes of the deck. Then, we proceed to balance net power input with power dissipated for the deck and for the remaining structural elements. Once the power input to the deck has been found the analysis is similar to that carried out in Sections 3.2 and 3.3, although some of the simplifying assumptions must be re-evaluated. In Section 3.2 we assumed that the interaction between the rail and other elements was dominated by the interaction at the free bending wavenumber,  $k_r$ , for the rail. This assumption is not valid for frequencies below the rail/fastener resonance frequency, since the wavenumber,  $k_r$ , given by Eq. 2.35 is not a real number.

The vibratory response of the rail to a point force excitation can be described in terms of Fourier transform in time and the spatial dimension along the rail. The result is given by

Eq. 2.31. At low frequencies we can ignore the  $\omega^2 m_r$  term in Eq. 2.31 and the fastener damping so that the transform of the rail velocity is given by

$$\hat{V}_r(k_x, \omega) = \frac{i\omega}{K_\ell + k_x^4 B_r} F(\omega) \quad (\text{II.1})$$

where  $k_x$  is the wavenumber,  $\omega$  is the radian frequency,  $K_\ell$  is the effective stiffness of the fasteners per unit length of the rail, and  $B_r$  is the bending stiffness of the rail. The transform of the force applied to the deck,  $\hat{F}_d(k_x, \omega)$ , is given by

$$\hat{F}_d(k_x, \omega) = \frac{K_\ell}{i\omega} \hat{V}_r(k_x, \omega) \quad (\text{II.2})$$

Combining Eqs. II.1 and II.2 we find

$$\frac{\hat{F}_d(k_x, \omega)}{F(\omega)} = \frac{1}{1 + k_x^4 \frac{B_r}{K_\ell}} \quad (\text{II.3})$$

Eq. II.3 shows that the transform of the force on the deck is greatest at low wavenumbers.

In Appendix III we compute the time-average power transmitted from a beam to a plate as a function of wavenumber,  $k_x$ . The calculation is valid regardless of whether the rail response is resonant or nonresonant. The parameter  $s$  in Eq. III.11 for the coupling loss factor is given by

$$s = \frac{k_x}{k_p} \quad (\text{II.4})$$

where  $k_p$  is the free bending wavenumber for the plate. Referring back to Eq. II.3 we note that the transform of the force on the deck is small when  $k_x^4 > K_\ell/B_r$ . Thus, to calculate the power input

to the deck we can use the coupling loss factor given by Eq. III.11 with  $s = 0$  as long as the condition below is met:

$$k_s > (K_l/B_r)^{1/4} \quad (\text{II.5})$$

where from Eq. III.4 b

$$k_s = (\rho_s/D_s)^{1/4} \sqrt{\omega} \quad (\text{II.6})$$

where  $\rho_s$  is the density of the deck per unit area and  $D_s$  is the bending stiffness of the deck.

For the case of a typical concrete slab deck with parameters given in Fig. 4.6 and Table 4.1 the condition given by Eq. II.5 becomes

$$f > 184 \text{ Hz} \quad (\text{II.7})$$

Unfortunately, this condition does not apply at the lowest frequency band of interest which is centered at 63 Hz. Thus, we must divide the low frequency prediction model into two regions. At frequencies below the frequency at which Eq. II.5 is valid, we use the coupling loss factor given by Eq. III.11 with  $k_x = k_s$  or  $s = 1$  to calculate the input power to the deck. At frequencies between the frequency at which Eq. II.5 is valid and the rail/fastener resonance frequency we use Eq. III.11 with  $k_x = 0$  to calculate the input power.



## APPENDIX III

### COMPILATION OF COUPLING LOSS FACTORS

In this Appendix we calculate certain average coupling loss factors which are required to study the vibration transmission in elevated structures. Some of these loss factors have been determined in the literature, but we include here explicit calculations for completeness. In every case the wave calculation procedure as outlined in Ref. 11 will be used. Thus, the results presented are coupling loss factors for the modes of two coupled structures averaged over the separation between their resonance frequencies.

#### Coupled Beam and Plate

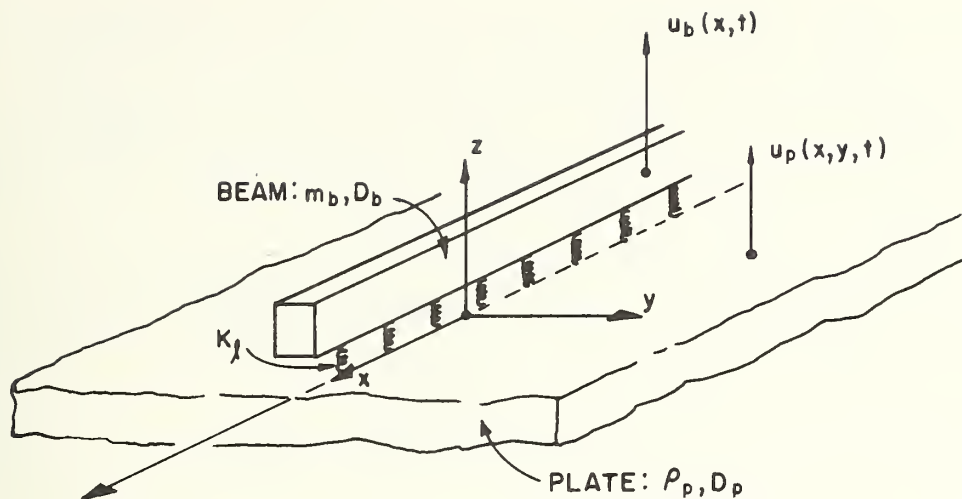
Consider a Bernoulli-Euler beam coupled to a Bernoulli-Euler plate by a continuous elastic foundation, as shown in Fig. III-1. Both the beam and plate are infinite along the x-axis. Although the plate has a finite width, we calculate the average coupling loss factor between the beam and the plate by assuming the plate to be infinite along the y-axis. We proceed by taking a prescribed wave disturbance on the beam of the form

$$u_b(x,t) = \hat{U}_b e^{-i(k_x x - \omega t)} \quad (\text{III.1})$$

The resulting force on the plate,  $f_p(x,t)$ , is denoted as

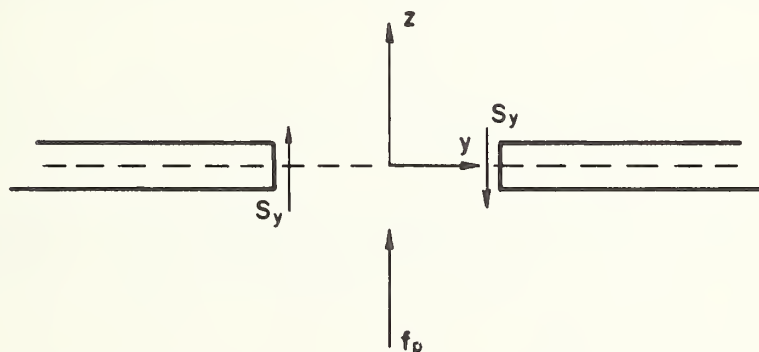
$$f_p(x,t) = \hat{F}_p e^{-i(k_x x - \omega t)} \quad (\text{III.2})$$

where



BEAM & PLATE CONNECTED BY A CONTINUOUS ELASTIC LAYER

- $m_b$  BEAM MASS PER UNIT LENGTH
- $B_b$  BEAM BENDING STIFFNESS,  $D_b = E_b I_b$
- $\rho_p$  PLATE MASS PER UNIT AREA
- $D_p$  PLATE BENDING STIFFNESS,  $D_p = E_p I_p$



SIGN CONVENTION FOR SHEAR FORCES ACTING ON THE TWO HALVES OF THE PLATE

FIG. III.1 COUPLED BEAM AND PLATE

$$\hat{F}_p = K_\ell [\hat{U}_b - \hat{U}_p(y=0)],$$

$\hat{U}_p(y=0)$  is the complex amplitude of the plate displacement at  $y = 0$  and  $K_\ell$  is the foundation stiffness per unit length. Due to symmetry, only the  $y > 0$  portion of the plate need be considered. The plate displacement amplitude obeys the homogeneous plate equation so that for  $y > 0$

$$\hat{U}_p(y) = \hat{U}_{p1} e^{-ik_y y} + \hat{U}_{p2} e^{-\sqrt{k_x^2 + k_p^2} y} \quad (\text{III.3})$$

where

$$k_y^2 = k_p^2 - k_x^2 \quad (\text{III.4a})$$

and  $k_p$  is the free bending-wavenumber for the plate,

$$k_p = (\rho_p/D_p)^{1/4} \sqrt{\omega} \quad (\text{III.4b})$$

and  $\rho_p$  is the plate density per unit area and  $D_p$  is its bending stiffness. The angle,  $\theta$ , given by

$$\sin \theta = k_x/k_p \quad (\text{III.5})$$

is the angle between the direction of propagation of waves in the plate and the normal to the beam-plate junction. Since the force,  $f_p$ , given by Eq. III.2, acts at  $y = 0$ , the boundary conditions for the plate at  $y = 0$  are

$$D_p \left[ \frac{\partial^3 u_p}{\partial y^3} + (2 - \nu) \frac{\partial^3 u_p}{\partial x^2 \partial y} \right] = \frac{f_p}{2} \quad (\text{III.6a})$$

and by symmetry

$$\frac{\partial u_p}{\partial y} = 0 \quad (\text{III.6b})$$

where  $\nu$  is the Poisson's ratio. Substituting Eqs. III.2 and III.3 into Eq. III.4 and solving for  $\hat{U}_{p1}$ , we find

$$\hat{U}_{p1} = \frac{\kappa_{bp} \sqrt{1+s^2}}{\kappa_{bp} \sqrt{1+s^2} + i\sqrt{1+s^2} (2\sqrt{1+s^2} - \kappa_{bp})} \hat{U}_b \quad (\text{III.7})$$

where

$$s = \sin \theta$$

and

$$\kappa_{bp} = K_\ell / (2 D_p k_p^3)$$

Note that  $K_\ell$  and  $\kappa_{bp}$  may be complex to account for damping in the elastic layer.

From Eq. III.7 we now calculate the total power transmitted to the plate. The average power passing through a unit length of wave front is  $\rho_p c_p \omega^2 |\hat{U}_{p1}|^2$ , where  $c_p$  is the bending wave speed for the plate,  $c_p = \omega/k_p$ . Then the total average power from the beam to the plate per unit length of rail is

$$W_{b,p} = 2 \rho_p c_p \omega^2 |\hat{U}_{p1}|^2 \cos \theta \quad (\text{III.8a})$$

or

$$W_{b,p} = \frac{2 \rho_p c_p \omega^2 |\kappa_{bp}|^2 (1+s^2) \sqrt{1+s^2}}{|\kappa_{bp} \sqrt{1+s^2} + i\sqrt{1+s^2} (2\sqrt{1+s^2} - \kappa_{bp})|^2} |\hat{U}_r|^2 \quad (\text{III.8b})$$

where the previous results have been multiplied by 2 to account for both sides of the plate.

The average energy of the beam per unit length is

$$T_b = \frac{1}{2} m_b \omega^2 |\hat{U}_b|^2 \quad (\text{III.9})$$

The average beam to plate coupling loss factor is given by

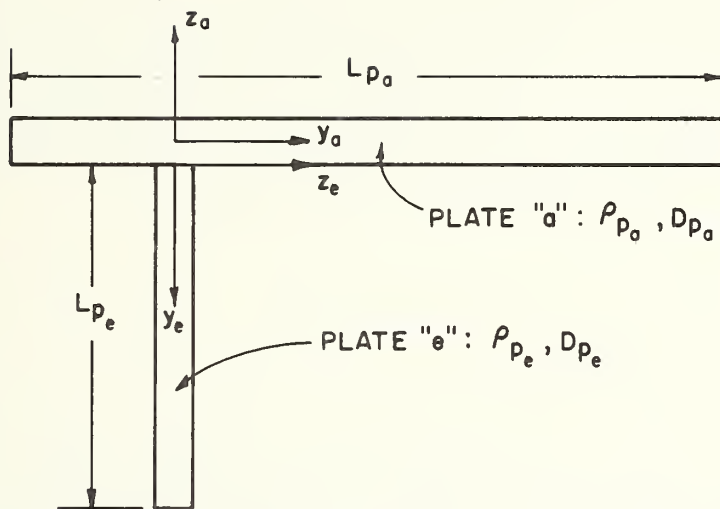
$$\eta_{b,p} = \frac{W_{b,p}}{\omega T_b} \quad (\text{III.10})$$

Substituting Eqs. III.8b and III.9 into Eq. III.10 we find

$$\eta_{b,p} = \frac{\frac{4 \rho_p}{k_p m_b} |\kappa_{bp}|^2 (1+s^2) \sqrt{1-s^2}}{|\kappa_{bp} \sqrt{1+s^2} + i \sqrt{1+s^2} (2\sqrt{1+s^2} - \kappa_{bp})|^2} \quad (\text{III.11})$$

### Coupled Plates - Vibration Transmitted by Moments

Consider two plates "a" and "e" connected through a rigid right-angled junction as shown in Fig. III.2. Both plates are considered infinite along the x-axis. In this section we consider vibration transmission from plate a to plate e due to moments at the junction. In the next section we will consider vibration transmission due to forces at the junction. Although both plates are finite in the y-direction, we calculate the coupling loss factor by assuming plate a to be infinite and plate e to be semi-infinite extending from  $y = 0$  to infinity.



$\rho_{p_i}$  PLATE MASS PER UNIT AREA,  $i = a, e$   
 $D_{p_i}$  PLATE BENDING STIFFNESS,  $i = a, e$

FIG. III.2 TWO PLATES CONNECTED THROUGH A RIGID, RIGHT-ANGLED JUNCTION



Following the wave calculation procedure, we allow bending waves in plate a to impinge on each side of the junction between plates. The incident waves are taken in the form

$$u_{p_a}(x,y,t) = \hat{U}_{a_i} e^{-i(k_y y + k_x x - \omega t)} \quad (\text{III.12})$$

where  $k_y$  is given by Eqs. III.4. The time-averaged power incident on both sides of the junction per unit length is

$$W_{inc} = \rho_{p_a} c_{p_a} \omega^2 \cos \theta |\hat{U}_{a_i}|^2 \quad (\text{III.13})$$

where  $\rho_{p_a}$  is the mass per unit area for plate a,  $c_{p_a}$  is the free bending wavespeed in plate a,  $\omega$  is the frequency and the angle  $\theta$  is given by Eq. III.5.

The incident wave complex amplitude,  $\hat{U}_{a_i}$  can be related to the modal energy,  $T_{p_a}$ , since the vibration associated with a cross-wise (y-direction) normal mode in the plate can be described in terms of waves of equal energy travelling in the +y and -y directions. The time-average modal energy equals the energy per unit length in the x-direction, which is given by

$$T_{p_a} = \frac{1}{2} \rho_{p_a} L_{p_a} \omega^2 |\hat{U}_{a_i}|^2 \quad (\text{III.14})$$

where  $L_{p_a}$  is the width of plate a in the y-direction.

The average coupling loss factor between plate a and plate e is given by

$$\eta_{a,e} = \frac{W_{a,e}}{\omega T_{p_a}} \quad (\text{III.15})$$

where  $W_{a,e}$  is the time-average power transmitted from plate  $a$  to plate  $e$  per unit length along the junction. If we define a transmission coefficient,  $\tau_{a,e}$ , such that

$$W_{a,e} = \tau_{a,e} W_{\text{inc}} \quad (\text{III.16})$$

the average coupling loss factor can be written

$$\eta_{a,e} = \frac{\tau_{a,e}}{k_{p_a} L_{p_a}} \sqrt{1 - \left(\frac{k_x}{k_{p_a}}\right)^2} \quad (\text{III.17})$$

where Eqs. III.4a and III.5 have been used to eliminate  $\theta$ .

To calculate the transmission coefficient, we consider the three semi-infinite plates, joined at right angles, as shown in Fig. III.3. We consider an incident wave at a given frequency,  $\omega$ , and  $x$ -component of wavenumber,  $k_x$ , propagating on plate 1 and determine the resulting bending wave on plate 3. Since only vibration transmission due to moments is being considered, we assume the in-plane motion in each plate to be negligible. Then, the problem is posed solely in terms of out of plane displacements and bending moments at the junction. With the conventions and local plate coordinates as shown in Fig. III.3, the relations between bending moments and displacements at the junction are

$$M_{y_i} = D_{p_a} \left[ \frac{\partial^2 u_i}{\partial y^2} + \nu_{p_a} \frac{\partial^2 u_i}{\partial x^2} \right], \quad i = 1, 2 \quad (\text{III.18a})$$

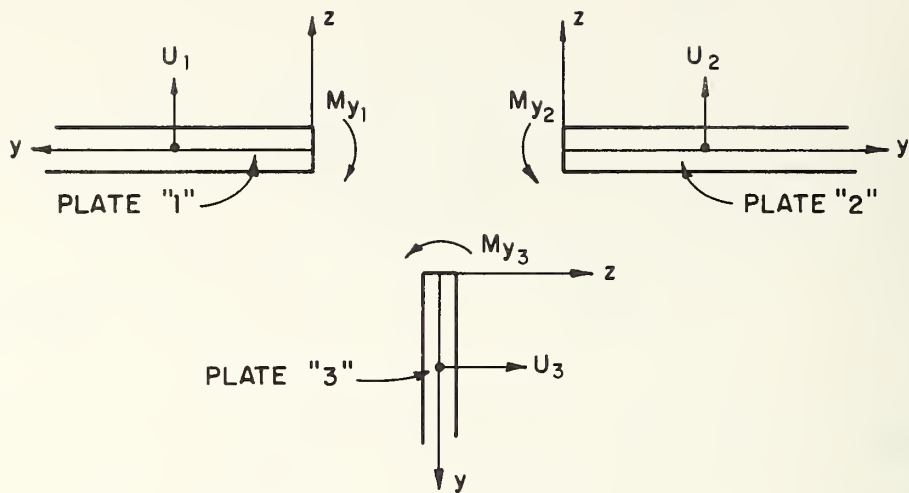


FIG. III. 3 COORDINATE AND MOMENT SIGN CONVENTIONS

$$M_{y_3} = D_{p_e} \frac{\partial^2 u_3}{\partial y^2} + \nu_{p_e} \frac{\partial^2 u_3}{\partial x^2} \quad (\text{III.18b})$$

where  $\nu_{p_a}$  and  $\nu_{p_e}$  are the Poisson ratios for plates a and e. The displacements satisfying the homogeneous plate equations are

$$u_i(x, y, t) = \hat{U}_i(y) e^{-i(k_x x - \omega t)} \quad \text{with } i = 1, 2, 3 \quad (\text{III.19a})$$

where

$$\hat{U}_1(y) = \hat{U}_{1+} e^{-i\sqrt{k_{p_a}^2 - k_x^2} y} + \hat{U}_{1-} e^{i\sqrt{k_{p_a}^2 - k_x^2} y} + \hat{U}_{1_i} e^{\sqrt{k_{p_a}^2 + k_x^2} y} \quad (\text{III.19b})$$

$$\hat{U}_2(y) = \hat{U}_{2+} e^{-i\sqrt{k_{p_a}^2 - k_x^2} y} + \hat{U}_{2-i} e^{-\sqrt{k_{p_a}^2 + k_x^2} y} \quad (\text{III.19c})$$

$$\hat{U}_3(y) = \hat{U}_{3+} e^{-i\sqrt{k_{p_e}^2 - k_x^2} y} + \hat{U}_{3-i} e^{-\sqrt{k_{p_e}^2 + k_x^2} y} \quad (\text{III.19d})$$

In Eqs. III.19  $U_{1+}$  corresponds to incoming waves in plate 1 and is assumed to be known and  $U_{3+}$  corresponds to out-going waves on plate 3. The boundary conditions at  $y = 0$  are

$$u_1 = 0, \quad u_2 = 0, \quad u_3 = 0$$

$$\frac{\partial u_1}{\partial y} = \frac{\partial u_2}{\partial y} = \frac{\partial u_3}{\partial y} \quad (\text{III.20})$$

$$M_{y_1} - M_{y_2} - M_{y_3} = 0$$

The first three relations follow from neglecting in-plane motions and the second three require that the junction angle be preserved. The last condition merely states moment equilibrium.

Substituting Eqs. III.19 into Eqs. III.20 one obtains relations through which  $U_{1i}$ ,  $U_{2-i}$ , and  $U_{3-i}$  may be expressed in terms of the coefficients of the propagating part of the field. Using Eqs. III.18 and Eqs. III.19, the remaining conditions of Eqs. III.20 become

$$U_{1+} [\alpha - i\sqrt{1+s^2}] - U_{1-} [\alpha + \sqrt{1+s^2}] = U_{2+} [\alpha + i\sqrt{1+s^2}] \quad (\text{III.21a})$$

$$U_{2+} [\alpha + i\sqrt{1+s^2}] = U_{3+} [\sqrt{\kappa^2 - s^2} + i\sqrt{\kappa^2 + s^2}] \quad (\text{III.21b})$$

$$W_{1+} + W_{1-} = W_{2+} + \psi W_{3+} \quad (\text{III.21c})$$

where

$$\alpha = \sqrt{1 - \left(\frac{k_x}{k_{p_a}}\right)^2}, \quad s = \frac{k_x}{k_{p_a}} \quad (\text{III.21d})$$

and

$$\psi = \frac{k_{p_e} D_{p_e}}{k_{p_a}^2 D_{p_a}}, \quad \kappa = \frac{k_{p_e}}{k_{p_a}} \quad (\text{III.21e})$$

Finally, Eqs. III.21 may be solved for  $U_{3+}$  in terms of  $U_{1+}$ . Doing this, one arrives at the transmission coefficient,

$$\tau_{a,e} = \psi \left| \frac{U_{3+}}{U_{1+}} \right|^2 \frac{\sqrt{\kappa^2 - s^2}}{\sqrt{1 - s^2}} \quad (\text{III.22})$$

$$\tau_{a,e} = \frac{\psi \sqrt{1-s^2} \sqrt{\kappa^2-s^2}}{\psi^2/2 + \psi [\sqrt{1-s^2} \sqrt{\kappa^2-s^2} + \sqrt{1+s^2} \sqrt{\kappa^2+s^2}] + 2\kappa^2} \quad (\text{III.23})$$

The coupling loss factor for bending waves in plate "a" and bending in plate "e" is

$$\eta_{a,e} = \frac{(\psi/k_{p_a} L_{p_a})(1-s^2) \sqrt{\kappa^2-s^2}}{\psi^2/2 + \psi [\sqrt{1-s^2} \sqrt{\kappa^2-s^2} + \sqrt{1+s^2} \sqrt{\kappa^2+s^2}] + 2\kappa^2} \quad (\text{III.24})$$

### Coupled Plates - Vibration Transmitted by Forces

We consider the same situation as above except that the vibration transmitted by forces at the junction is of interest. We assume that a bending-wave in plate "a" impinges on the junction between the two plates. Defining  $\eta_{a,e_u}$  as the power transmitted by forces at the junction into in-plane motion of plate "e" divided by power incident on the junction one finds that the corresponding coupling loss factor,  $\eta_{a,e_u}$ , is

$$\eta_{a,e_u} = \frac{\tau_{a,e_u}}{k_{p_a} L_{p_a}} \sqrt{1 - \left( \frac{k_x}{k_{p_a}} \right)^2} \quad (\text{III.25})$$



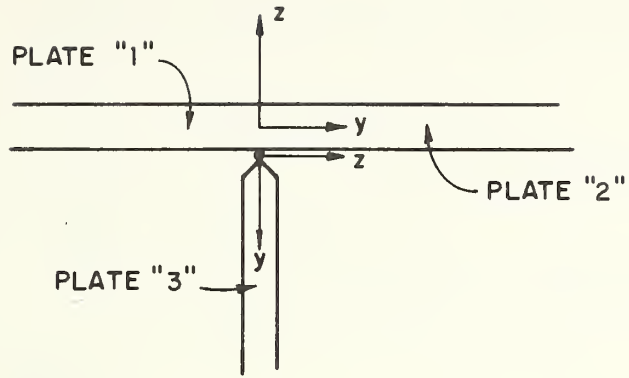
To calculate the transmission coefficient,  $\tau_{a,e_u}$ , we consider three semi-infinite plates as shown in Fig. III.4. It is assumed that the bending rigidity of plate 3 is much less than that of plates 1 and 2. Therefore, for the purpose of calculating the transmission coefficient,  $\tau_{a,e_u}$ , bending moments transmitted to 3 may be neglected so that 3 is essentially pinned to plates 1 and 2. Suppose that an incident bending wave exists on plate 1 and we wish to calculate the resulting in-plane displacement in plate 3. First, since no bending moments are transmitted to 3, there is no bending motion in that plate and consequently the in-plane motions of plates 1 and 2 may be neglected. This being the case, the power delivered to plate 3 is mostly due to vertical forces,  $F_{y_3}$ , so that the in-plane motion of plate 3 may be approximated by longitudinal waves propagating normal to the junction. Then, the only non-zero displacements are the out of plane displacement  $u_1$  and  $u_2$  and the in-plane y-component in plate 3,  $u_{y_3}$ .

We can formulate the problem solely in terms of the bending moments  $M_{y_1}$ ,  $M_{y_2}$ , shear forces  $S_{y_1}$ ,  $S_{y_2}$  and axial force  $F_{y_3}$  at the junction. These forces and moments are related to the displacements by

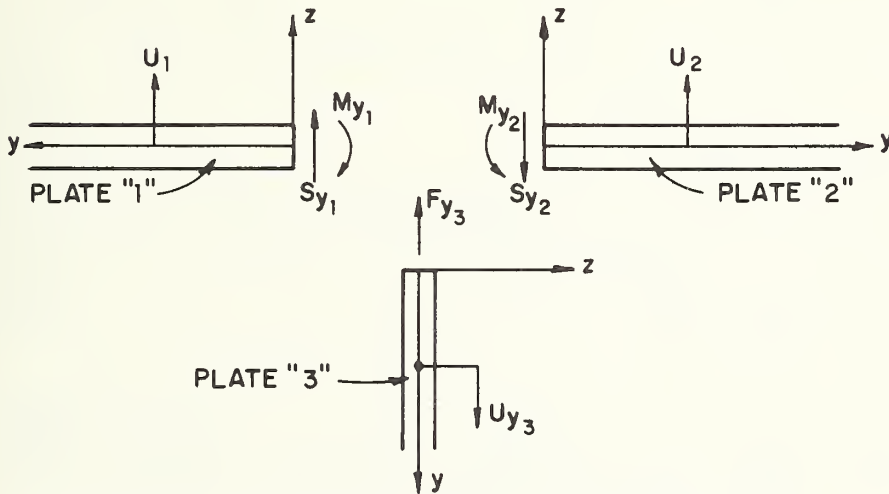
$$M_{y_i} = D_{Pa} \left( \frac{\partial^2 u_i}{\partial y^2} + \nu_{Pa} \frac{\partial^2 u_i}{\partial x^2} \right) \quad (\text{III.26a})$$

$$S_{y_i} = D_{Pa} \left( \frac{\partial^3 u_i}{\partial y^3} + (2 - \nu_{Pa}) \frac{\partial^3 u_i}{\partial x^2 \partial y} \right) \quad i = 1, 2 \quad (\text{III.26b})$$

$$F_{y_i} = c_{l,e}^2 \rho_{Pe} \frac{\partial u_3}{\partial y} \approx - \rho_{Pe} c_{l,e} u_{y_3} \quad (\text{III.26c})$$



IDEALIZED APPROXIMATION FOR CALCULATION OF TRANSMISSION  
OF BENDING WAVES IN PLATE 1 TO LONGITUDINAL WAVES IN PLATE 3  
A PINNED CONNECTION BETWEEN 1 & 2 AND 3 IS ASSUMED



COORDINATE, FORCE AND MOMENT CONVENTIONS USED

FIG. III.4 COORDINATE , MOMENT, AND FORCE SIGN CONVENTIONS

where  $c_{\ell,e}$  is the longitudinal wavespeed in plate 3. The displacements satisfying the wave equations can be written

$$u_i(x,y,t) = \hat{U}_i e^{-i(k_x x - \omega t)} \quad (i = 1, 2) \quad (\text{III.27a})$$

$$u_{y_i}(x,y,t) = \hat{U}_{y_i} e^{-i(k_x x - \omega t)} \quad (\text{III.27b})$$

where

$$\hat{U}_1 = \hat{U}_{1+} e^{-ik_y y} + \hat{U}_{1-} e^{-ik_y y} + \hat{U}_{1i} e^{\sqrt{k_x^2 + k_{pa}^2} y} \quad (\text{III.28a})$$

$$\hat{U}_2 = \hat{U}_{2+} e^{-ik_y y} + \hat{U}_{2i} e^{-\sqrt{k_x^2 + k_{pa}^2} y} \quad (\text{III.28b})$$

$$\hat{U}_{y_3} = \hat{U}_{y,3+} e^{-ik_\ell y} \quad (\text{III.28c})$$

where

$$k_y^2 = k_{pa}^2 - k_x^2 \quad (\text{III.28d})$$

$$k_\ell = \frac{\omega}{c_{\ell,e}} \quad (\text{III.28e})$$

where  $\hat{U}_{1+}$  and  $\hat{U}_{y,3+}$  correspond to the incident bending waves in plate 1 and the out-going longitudinal waves in plate 3, respectively. The boundary conditions at  $y = 0$  are

$$\hat{U}_1 = \hat{U}_2 = -\hat{U}_{y_3}, \quad (\text{III.29a})$$

$$\frac{\partial \hat{U}_1}{\partial y} = \frac{\partial \hat{U}_2}{\partial y} \quad (\text{III.29b})$$

$$S_{y_1} - S_{y_2} + F_{y_3} = 0 \quad (\text{III.29c})$$

$$M_{y_1} - M_{y_2} = 0 \quad (\text{III.29d})$$

Substituting Eqs. III.26 and III.27 into these conditions gives one set of equations which then can be solved for the ratio  $U_{y,3+}$  to  $U_{1+}$ . Then the transmission coefficient  $\tau_{a,e_u}$  is given by

$$\tau_{a,e_u} = \frac{1}{2} \frac{\rho_{p_e} c_{\ell,e} k_{p_a}}{\rho_{p_a} \omega} \left| \frac{\hat{U}_{y,3+}}{\hat{U}_{1+}} \right|^2 \frac{1}{\sqrt{1-s^2}} \quad (\text{III.30a})$$

or

$$\tau_{a,e_u} = \frac{\rho_{p_e} c_{\ell,e} k_{p_a}}{2 \rho_{p_a} \omega \sqrt{1-s^2}} \frac{1-s^4}{(\sqrt{1-s^4} + \frac{\lambda}{4} \sqrt{1+s^2})^2 + \frac{\lambda^2}{16} (1-s^2)} \quad (\text{III.30b})$$

where

$$\lambda = \frac{c_{\ell,e} \rho_{p_e} \omega}{k_{p_a}^3 D_{p_a}} \quad (\text{III.30c})$$

and

$$s = \frac{k_x}{k_{p_a}} \quad (\text{III.30d})$$

Hence, from Eq. III.25, the coupling loss factor  $\eta_{a,e_u}$  between bending in plate "a" and in-plane "e" is

$$\eta_{a,e_u} = \frac{\rho_p c_{l,e}}{2 \rho_p \omega L_p} \frac{1-s^4}{(\sqrt{1-s^4} + \frac{\lambda}{4} \sqrt{1+s^2})^2 + \frac{\lambda^2}{16} (1-s^2)} \quad (\text{III.31})$$

where  $\lambda$  and  $s$  are given by Eqs. III.30c and III.30d.

APPENDIX IV  
REPORT OF INVENTIONS APPENDIX

This report presents the development of a noise prediction model for rail transit elevated structures. After a diligent review of the work performed under this contract it was found that no new inventions, discoveries, or improvements of inventions were made.



## REFERENCES

- [1] Manning, Cann and Fredberg, "Prediction and Control of Rail Transit Noise and Vibration — A State-of-the-Art Assessment," Report No. UMTA-MA-06-0025-74-5, April, 1974, PB233363/AS.
- [2] Hyland, Tocci and Manning, "Noise and Vibration Prediction Models for Floating-Slab Track," Report under preparation by Cambridge Collaborative, Inc., Contract DOT-TSC-643.
- [3] Manning, "Engineering Procedures for Predicting Elevated Structure Noise," Report under preparation by Cambridge Collaborative, Inc., Contract DOT-TSC-643.
- [4] Remington et al, "Wheel/Rail Noise and Vibration," Vol. I--Mechanics of Wheel/Rail Noise Generation; Vol. II--Applications to Control of Wheel/Rail Noise; Report Nos. UMTA-MA-06-0025-75-10 (Vol. I), and UMTA-MA-06-0025-75-11 (Vol. II), May, 1975.
- [5] Bender and Remington, "The Influence of Rails on Train Noise," J. Sound & Vib., Vol. 37, No. 3, pp. 321-334, December, 1974.
- [6] Meisenholder and Weidlinger, "Dynamic Interaction Aspects of Cable-Stayed Guideways for High Speed Ground Transportation," ASME, Paper No. 74-AUT-R., 1974.
- [7] Wilson, "Diablo Test Track Noise and Vibration Measurements," Wilson, Ihrig & Associates, Inc., June, 1967, prepared for Parsons Brinckerhoff-Tudor-Bechtel under contract 3Z4966.
- [8] Bailey and Fahy, "Radiation and Response of Cylindrical Beams Excited by Sound," ASME Paper No. 71-VIBR-84, 1971.
- [9] Morse and Ingard, Theoretical Acoustics, Chapter 7.3, McGraw-Hill Book Co., New York, 1968.

- [10] Blair, March, Moore and Spinka, "MBTA Train Noise from Elevated Structures," Project Report under M.I.T. Course 2.066, May, 1974.
- [11] Lyon, "Statistical Energy Analysis for Designers," M.I.T. Course Notes available from Prof. R. H. Lyon, Massachusetts Institute of Technology, Cambridge, Mass., 1975.
- [12] Scharton and Lyon, "Power Flow and Energy Sharing in Random Vibration," J. Acoust. Soc. Am., Vol. 43, No. 6, pp. 1332-1343, 1968.
- [13] Morse and Ingard, Theoretical Acoustics, Section 9.2, McGraw-Hill Book Co., New York, 1968.
- [14] Serendipity, Inc., "A Study of the Magnitude of Transportation Noise Generation and Potential Abatement, Vol. V — Train System Noise," NTIS — PB 203 186 November, 1970.
- [15] Maidanik, "Response of Ribbed Panels to Reverberant Acoustic Fields," J. Acoust. Soc. Am., 34, (6), p. 809, 1962.
- [16] Anonymous, "Larmbekämpfung an Brücken. Gerauschemessungen an der Brücke Rosenheim," (Noise abatement on bridges. Noise measurements on the Rosenheim Bridge), Office of Research and Experiments, Report No. 2, Question D105, Utrecht, Netherlands, 1966.
- [17] Ungar, "Damping of Panels," Noise and Vibration Control, Edited by L.L. Beranek, McGraw-Hill Book Co., Chapter 14, 1971.



HE 18.5 : A37  
no. DOT-TSC-  
UMTA-75-13

U

BORROWER

*Kenneth M.C.*

Form DOT F 172

DOT LIBRARY



00009374